Title

I. Nuclear Production Reaction and Chemical Isolation Procedure for 240Am II. New Superheavy Element Isotopes: 242Pu(48Ca,5n)285-114

Author

Ellison, Paul Andrew

Publication Date

2011

I. Nuclear Production Reaction and Chemical Isolation Procedure for ^{240}Am
II. New Superheavy Element Isotopes: ^{242}Pu(^{48}Ca,5n)^{285}114

by

Paul Andrew Ellison

A dissertation submitted in partial satisfaction of the
requirements for the degree of
Doctor of Philosophy

in

Chemistry

in the

Graduate Division
of the
University of California, Berkeley

Committee in charge:
Professor Heino Nitsche, Chair
Professor Joseph Cerny
Professor Per Peterson

Fall 2011

I. Nuclear Production Reaction and Chemical Isolation Procedure for ^{240}Am
II. New Superheavy Element Isotopes: ^{242}Pu(^{48}Ca,$5n$)^{285}114

Abstract

I. Nuclear Production Reaction and Chemical Isolation Procedure for ^{240}Am
II. New Superheavy Element Isotopes: ^{242}Pu(^{48}Ca,5n)^{285}114

by

Paul Andrew Ellison
Doctor of Philosophy in Chemistry

University of California, Berkeley

Professor Heino Nitsche, Chair

Part I discusses the study of a new nuclear reaction and chemical separation procedure for the production of ^{240}Am. Thin ^{242}Pu, $^{\mathrm{nat}}$Ti, and $^{\mathrm{nat}}$Ni targets were coincidently activated with protons from the 88-Inch Cyclotron, producing ^{240}Am, ^{48}V, and ^{57}Ni, respectively. The radioactive decay of these isotopes was monitored using high-purity Ge gamma ray detectors in the weeks following irradiation. The excitation function for the $^{242}\mathrm{Pu}(p,3n)^{240}\mathrm{Am}$ nuclear reaction was measured to be lower than theoretical predictions, but high enough to be the most viable nuclear reaction for the large-scale production of ^{240}Am.

Details of the development of a chemical separation procedure for isolating ^{240}Am from proton-irradiated ^{242}Pu are discussed. The separation procedure, which includes two anion exchange columns and two extraction chromatography columns, was experimentally investigated using tracer-level ^{241}Am, ^{239}Pu, and model proton-induced fission products ^{95}Zr, ^{95}Nb, ^{125}Sb, and ^{152}Eu. The separation procedure was shown to have an Am/Pu separation factor of $>2\times10^7$ and an Am yield of $\sim$70%. The separation procedure was found to purify the Am sample from >99.9% of Eu, Zr, Nb, and Sb. The procedure is well suited for the processing of $\sim$1 gram of proton-irradiated ^{242}Pu to produce a neutron-induced fission target consisting of tens of nanograms of ^{240}Am.

Part II describes the use of the Berkeley Gas-filled Separator at the Lawrence Berkeley National Laboratory 88-Inch Cyclotron for the study of the ^{242}Pu(^{48}Ca,5n)^{285}114 nuclear reaction. The new, neutron-deficient, superheavy element isotope ^{285}114 was produced in ^{48}Ca irradiations of ^{242}Pu targets at a center-of-target beam energy of 256 MeV ($E^* = 50$ MeV). The α decay of ^{285}114 was followed by the sequential α decay of four daughter nuclides, ^{281}Cn, ^{277}Ds, ^{273}Hs, and ^{269}Sg. ^{265}Rf was observed to decay by spontaneous fission. The measured α-decay Q-values were compared with those from a macroscopic-microscopic nuclear mass model to give insight into superheavy element shell effects. The ^{242}Pu(^{48}Ca,5n)^{285}114 cross section was $0.6^{+1.3}_{-0.2}$ pb.

I dedicate this dissertation to those who came before me and those who will come after.

That probably means you.

Contents

List of Figures

List of Tables

List of Acronyms

ADC	Analog-to-digital converter
BGS	Berkeley Gas-filled Separator
CFD	Constant fraction discriminator
DGFRS	Dubna gas-filled recoil separator
DOE	Department of Energy
E_n	Neutron energy
E_p	Proton energy
EC	Electron capture
EoB	End of bombardment
EVR	Evaporation residues
f	Fission
FCV	Free column volume
FLNR	Flerov Laboratory of Nuclear Reactions
FP	Fission product
FPD	Focal plane detector
FWHM	Full width at half maximum
GSI	Gesellschaft für Schwerionenforschung mbH
HERL	Heavy Element Research Laboratory
HPGe	High purity germanium
HPLC	High pressure liquid chromatography
IAEA	International Atomic Energy Agency
ID	Implantation detector
JINR	Joint Institute for Nuclear Research
$K\pi I$	Projection of total angular momentum onto nuclear symmetry axis, nuclear spin, and total angular momentum
LANL	Los Alamos National Laboratory
LANSCE	Los Alamos Neutron Science Center
LBNL	Lawrence Berkeley National Laboratory
LSC	Liquid scintillation counting
LSDS	Lead slowing-down spectrometer

MBS	Multi-branch system
MCA	Multichannel analyzer
MWPC	Multiwire proportional counter
n	Neutron
NIM	Nuclear Instrumentation Module
NNSA	National Nuclear Security Administration
ORNL	Oak Ridge National Laboratory
p	Proton
PIPS	Passivated implanted planar silicon
PTD	Punch-through detector
Q_{alpha}	Alpha decay Q-value
ROI	Region of interest
SCFH	Standard cubic feet per hour
SF	Spontaneous fission
SHIP	Separator for heavy ion reaction products
SHV	Save high voltage
SSAAP	Stewardship Science Academic Alliances Program
TAG	Target-Ala-Ghiorso
TASCA	Transactinide separator and chemistry apparatus
ToF	Time of flight
UD	Upstream detector

Acknowledgments

There are many who have shaped the past five years into some of the most enjoyable of my life. The following people are among those responsible for the personal and intellectual growth I've experience here in Berkeley.

First and foremost is my dissertation advisor, Heino Nitsche. Since joining his group in Fall 2006, Heino has believed in, stood by, and stuck up for me during my successes and failures. With the successes, he always made my accomplishments seem extraordinary. With the failures, he made sure the lessons were learned, but not belabored. From Heino I learned much about patience, diplomacy, perseverance, and leadership. I am truly grateful to have had the opportunity to work for and learn from Heino.

I am also indebted to Ken Gregorich for always having an answer to my questions and a solution to my problems. His incredibly comprehensive knowledge of everything related to nuclear chemistry and the 88-Inch Cyclotron was invaluable to the work presented in this dissertation. Ken was always patient and thorough when answering my many questions and always fun to be around, even while waiting for beam at very late hours of the night.

Several postdoctoral fellows have also been instrumental in my education. The first of these is Liv Stavsetra, who I worked closely with during the preparation of the ^{242}Pu targets used in this work. Liv taught me much of what I know about electrodeposition and glovebox chemistry techniques. She was also a good coworker and friend, even under rather stressful conditions. Two other postdoctoral fellows, Zuzana Dvorakova and Julie Champion, provided the majority of the driving force and work behind research presented in Chapter 3. Jan Dvorak was very helpful to me while planning and executing the cyclotron irradiations discussed in this dissertation. Julie, Zuzana, and Jan were also good friends within the group.

I am happy to acknowledge my fellow nuclear chemistry graduate students for their friendship and fellowship. Jacklyn Gates taught me the basics of nuclear and radiochemistry during Spring 2007 Chemistry 146 and has continued teaching me since. The rest of the heavy elementalist throughout my years, Sarah Nelson, Irena Dragojević, Mitch Garcia, and Oliver Gothe have been great to work with, learn from, and in the later most case, teach. The actinide side folk, Mike Calvert, Joey Hu, Tashi Parsons-Moss, Kestrel Schwaiger, and Deborah Wang helped broaden my knowledge of actinide chemistry. The new class, Nick

Esker, Erin Gantz, and Jen Schusterman, have been a pleasure to get to know and impart a bit of my knowledge upon. Erin deserves an extra special thanks for reading this document with a discerning eye for grammar and spelling. Rex Lake also gets a mention in this section for teaching me much more about quantum mechanics, statistical mechanics and many other nuclear and chemical topics than I ever taught him as his GSI in Spring 2008 Chemistry 146. His excellence in derivation can be seen in Appendix D, a section I never would have been able to understand, nonetheless write, if not for his help. Also, an in-depth, off-topic, yet intellectual, conversation with Rex has been the hallmark of a good work day here in building 88.

I have also had the pleasure to work with several outstanding undergraduate students. Several of the results reported in Chapter 3 were obtained in experiments performed by Carolina Fineman-Sotomayor. Joseph McLaughlin, whose work is summarized in Section 2.3.2, has been the ideal undergraduate researcher. He has been enthusiastic, dedicated, self-motivated, and a pleasure to work with. I know his contributions to this work will be only the first of his many research accomplishments.

I would also like to acknowledge the members of my qualifying examination committee: Joe Cerny, Darleane Hoffman, Ken Raymond, and Per Peterson. I appreciate all their questions and their belief that I deserved to be a Ph.D. candidate.

The experiments described in this dissertation would not have been possible without the hard work put in by many dedicated Lawrence Berkeley National Laboratory employees. This includes, but certainly is not limited to, the 88-Inch Cyclotron staff and engineers and the Environment, Health, & Safety division's radiation protection group.

Part II presents work which has been previously published [EGB$^+$10] and is reproduced and elaborated upon with the permission of the coauthors Ken Gregorich, Jill Berryman, Darren Bleuel, Rod Clark, Irena Dragojević, Jan Dvorak, Paul Fallon, Carolina Fineman-Sotomayor, Jacklyn Gates, Oliver Gothe, I-Yang Lee, Walt Loveland, Joseph McLaughlin, Stefanos Paschalis, Marina Petri, Jing Qian, Liv Stavsetra, Mathis Wiedeking, and Heino Nitsche. I am very thankful to these collaborators for their contributions to this work.

Over the past years, I have lived around 2,000 miles away from my immediate family. They have been wonderfully supportive of me and a pleasure to visit back in Wisconsin. Thank you so much for everything you have done.

I am also very grateful for all the folks in Berkeley and Davis who have become dear friends. I have met many excellent, entertaining, kind, and fun people. We have had stressful times in the chemistry library, celebratory times at Dwight & Milvia, calculating times hunched over a board game table, and delicious times enjoying a meal prepared with friends. I am very thankful for all good times.

Finally, Shelby Repinski has played a major role in shaping the last five years. I greatly appreciate her continual support, allowing me to vent when stressed, and giving me something to look forward to every weekend, and, more recently, every day.

The work presented in Part I was funded by the U.S. National Nuclear Security Administration (NNSA), Stewardship Science Academic Alliance program under Contract Nos. DE-FG52-06NA27480 and DE-FG52-10NA29652. The work presented in Part II was funded largely by the Office of High Energy and Nuclear Physics, Nuclear Physics Division, and by the Office of Basic Energy Sciences, Division of Chemical Sciences, Geosciences and Biosciences of the U.S. Department of Energy, under Contract No. DE-AC02-05CH11231. My personal funding came through a NNSA Stewardship Science Graduate Fellowship under contract No. DE- FC52-08NA28752. I must also thank the Krell Institute for doing an excellent job of administering this fellowship and making my life so easy.

Part I

Nuclear Production Reaction and Chemical Isolation Procedure for ^{240}Am

Chapter 1

Introduction

The research presented in Part I of this dissertation was funded through the United States' Department of Energy (DOE) National Nuclear Security Administration (NNSA) Stewardship Science Academic Alliances Program (SSAAP). This program funds academic research in fields pertinent to the United States' science-based stockpile stewardship effort [Jea00]. These fields include the study of materials under extreme conditions, high energy/density physics, and low energy nuclear science. By funding these three areas of research within universities, the NNSA aims to accomplish several goals. First, it is their goal to foster collaboration between the academic community and national laboratories. These collaborations will, in turn, create a stable pipeline through which the national laboratories can recruit scientific research personnel. Second, it is their aim to answer fundamental science questions and develop new experimental techniques and capabilities related to science-based stockpile stewardship.

The following chapters of this dissertation report work done toward characterizing a new nuclear production reaction and chemical isolation procedure for ^{240}Am. This research has been performed as part of the larger research goal of measuring the neutron-induced fission cross section of ^{240}Am. Measurement of this ^{240}Am(n, f) cross section is of interest to the NNSA because of its role in stockpile stewardship and post-detonation nuclear forensics.

1.1 Motivation

Information about a nuclear device's total high energy neutron fluence has historically been determined by measuring the ^{238}Pu/^{239}Pu isotopic ratio present in post-detonation debris. This value is correlated to the number of high energy neutrons released upon detonation because neutrons with a kinetic energy greater than 5.646 MeV can produce ^{238}Pu from ^{239}Pu via the $(n, 2n)$ reaction. This ratio measured in the debris must be corrected for the fact that all plutonium fuel will contain some initial quantity of ^{238}Pu. Thus, knowledge of

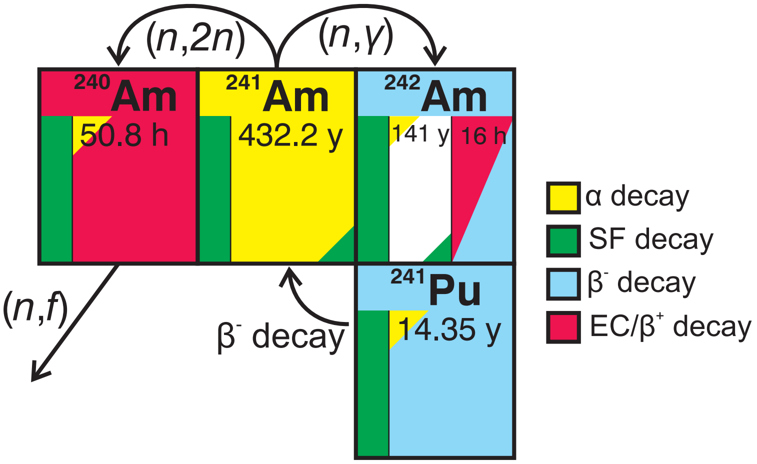

Figure 1.1 The neutron-induced reaction network on ^{241}Am.

the ingoing isotopic composition of the plutonium fuel is necessary for the utilization of this method of measuring the high energy neutron fluence. This condition would not be fulfilled in the event of a hostile detonation. Because information about the location and date of the production of the plutonium fuel can be deduced from the total neutron fluence, it is strongly desirable to have an alternate means of measuring this value. A second failing of this method occurs when the amount of ^{238}Pu produced in the detonation is small compared to the ingoing ^{238}Pu composition, as is the case with low burn-up nuclear devices.

An alternate method for the measurement of high energy neutron fluence utilizes the fact that all plutonium fission fuel contains some amount of ^{241}Pu in its isotopic distribution. This ^{241}Pu decays by β^- emission to ^{241}Am with a 14.4-year half-life. Consequently, all plutonium fuel contains an amount of ^{241}Am proportional to the isotopics of the plutonium fuel and the time since it was last separated from americium. While the total amount of americium is small compared with the plutonium, the enormous amount of neutrons released upon detonation will measurably react with the ^{241}Am in several ways. The two major neutron-induced reactions on ^{241}Am will produce $^{242/242m}$Am in the (n,γ) reaction and, with neutron energies above the 6.645-MeV reaction threshold, ^{240}Am in an $(n,2n)$ reaction. The major neutron-induced nuclear reaction on ^{240}Am produced in this way will be its neutron-induced fission. The neutron-induced reaction network on these americium isotopes is shown in Figure 1.1. If the rates of the ^{241}Am$(n,2n)^{240}$Am, ^{241}Am$(n,\gamma)^{242}$Am, and ^{240}Am(n,f) nuclear reactions are well understood and characterized, then the ^{240}Am/^{241}Am ratio measured from debris can be used to calculate the total high-energy neutron fluence. While the ^{241}Am$(n,2n)^{240}$Am [TAB$^+$08] and ^{241}Am$(n,\gamma)^{242}$Am [JBB$^+$08] reactions have recently been experimentally studied, the ^{240}Am(n,f) reaction has not.

1.2 Previous ^{240}Am(n, f) studies

Accurate neutron-induced reaction cross sections have long been a goal of both experimentalists and theoreticians in the field of nuclear chemistry and physics. These cross sections are extensively used in predicting and simulating nuclear processes, many of which are sensitive tasks such as evaluating the safety and performance of nuclear power plants or performing radiochemical analyses of nuclear explosion debris. It is very desirable to have the most accurate values when evaluating which nuclear reaction cross sections to use in such calculations. Evaluation of available experimental and theoretical data is so important that several national and international groups of nuclear physicists from industry, academia, and government have formed for this purpose. These groups collect and process experimental and theoretical data from nuclear reaction studies and issue recommended cross sections, spectra, angular distributions, fission product yields, photo-atomic and thermal neutron scattering law data. As of Spring 2011, there are five major evaluated nuclear data libraries:

* the United States-based Evaluated Nuclear Data File (ENDF/B-VII.0 [CzH$^+$06, vdM06]), which is overseen by the Cross Section Evaluation Working Group,
* the Joint Evaluated Fission and Fusion Library (JEFF-3.1.1 [SBB$^+$09]), which is overseen by the Organisation for Economic Co-operation and Development's Nuclear Energy Agency,
* the Japanese Evaluated Nuclear Data Library (JENDL-4.0 [SIN$^+$11]), which is overseen by the Nuclear Data Evaluation Center of the Japan Atomic Energy Agency and the Japanese Nuclear Data Committee,
* the Russian evaluated neutron data library (BROND-2.2 [BFI$^+$94]),
* and the Chinese Evaluated Nuclear Data Library (CENDL-3.1 [ZHY$^+$07]), which is overseen by the China Nuclear Data Center in cooperation with the China Nuclear Data Coordination Network.

The data libraries issued by these groups can be searched by users through a web-based interface. As of Spring 2011, the most extensive web-based interface for searching current and archived nuclear data libraries is the Nuclear Data Services page of the International Atomic Energy Agency (IAEA) found at `http://www-nds.iaea.org`.

Compared with other fissionable actinides, experimental research on the ^{240}Am(n, f) cross section is very limited. Because of this, evaluations of the ^{240}Am(n, f) cross sections are only available in two of these major evaluated nuclear data libraries and seven special nuclear data libraries. As of Spring 2011, the nuclear data libraries which contain ^{240}Am(n, f) data are JENDL-4.0 [SIN$^+$11], TENDL-2009 [KRa], TENDL-2010 [KRb], EAF-2010 [SPKF10],

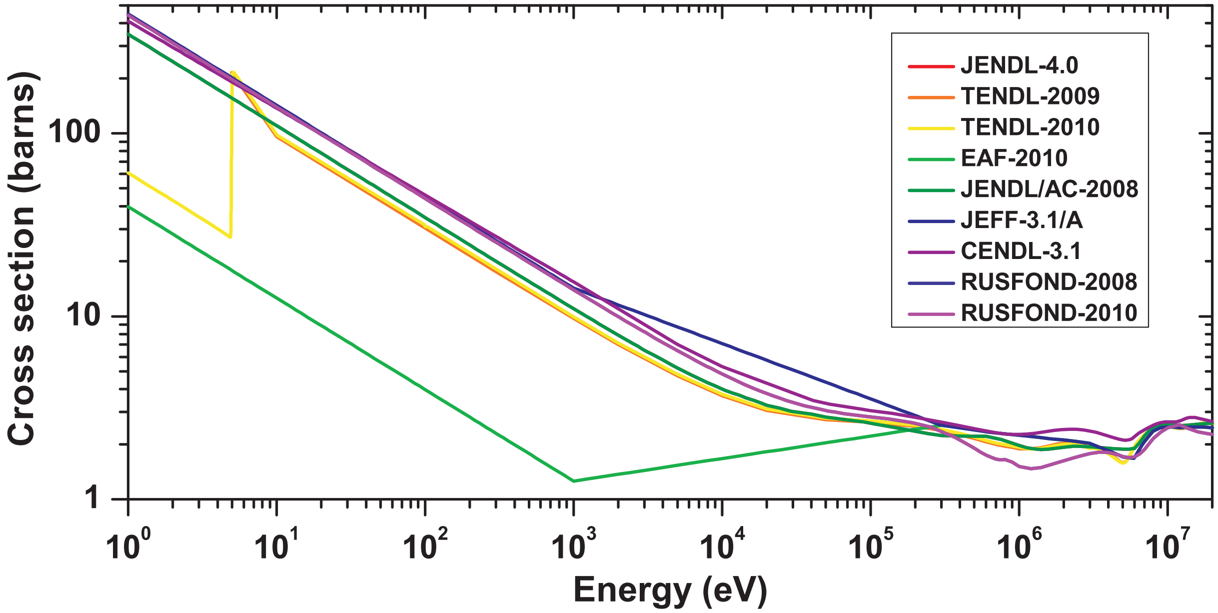

Figure 1.2 Evaluated ^{240}Am(n, f) data from IAEA Nuclear Data Services.

JENDL/AC-2008 [INO$^+$08], JEFF-3.1/A: [SKFK03], CENDL-3.1:[ZHY$^+$07], RUSFOND-2008, and ROSFOND-2010: [NK]. These evaluated ^{240}Am(n, f) cross section "data" are summarized in Figure 1.2.

A recent publication by Rochman *et al.* [RHOS06] reports neutron-induced fission cross section predictions for eight americium isotopes (A = 239 to 244) given by the nuclear reaction model code EMPIRE-2.19 [HCNO$^+$01]. In this publication, the authors compare their predictions with previous experimental, theoretical, and evaluated values for the ^{240}Am(n, f) cross section. This comparison is summarized in Figure 3 of the article (reproduced here as Figure 1.3, original image copyright 2006 by the American Nuclear Society, La Grange Park, Illinois). The top half of Figure 1.3 compares the EMPIRE-2.19 predictions with the evaluated "data" from the JEFF-3.1/A [SKFK03] data file. The bottom half of Figure 1.3 compares the EMPIRE-2.19 predictions with several different simulations for [Mas88, Beh77, KSF84], and all of the limited available experimental measurements of [BW79, BW81, YBB04], the ^{240}Am(n, f) cross section.

The majority of the experimental data reported in this figure has been estimated using the surrogate reaction technique. Using this technique, direct reaction experiments are used to produce the same compound nucleus system as a neutron-induced reaction on a short-lived actinide target. The experimentally-measured direct-reaction-fission-probability data can then be combined with calculated neutron-induced compound nucleus formation cross sections to estimate neutron-induced fission cross sections of short-lived actinide isotopes.

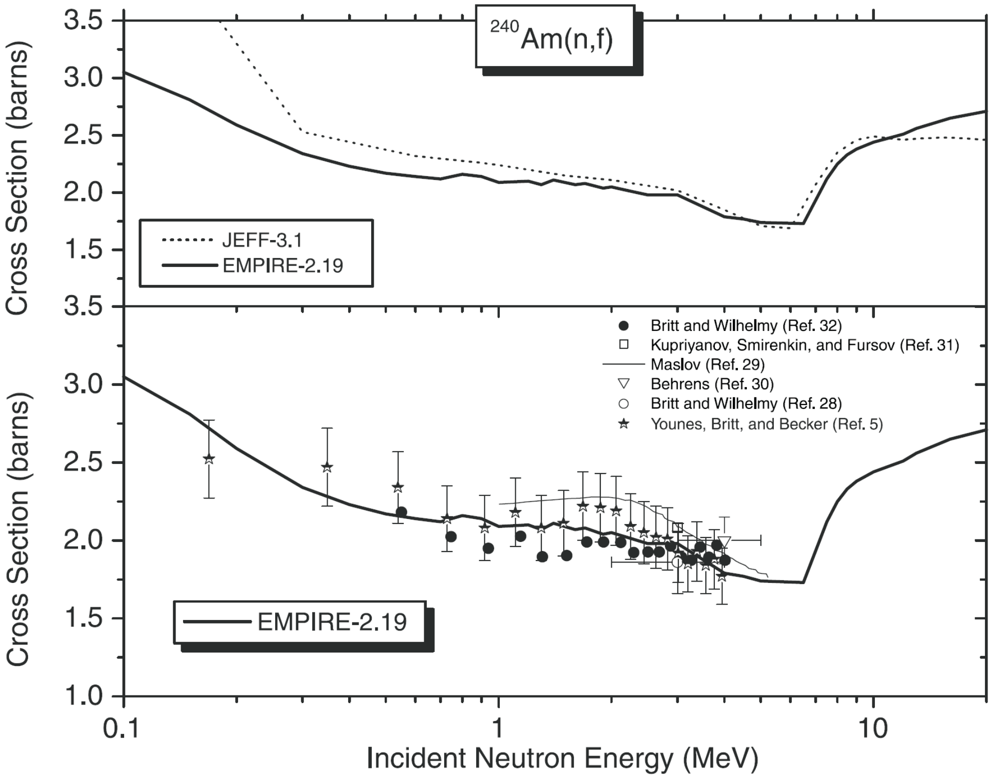

Figure 1.3 Calculated, evaluated, and measured cross sections for ^{240}Am(n, f).

This technique has recently been used to deduce the well established ^{235}U(n, f) cross section in the neutron energy range of $E_n = 0.2 - 2.5$ MeV from surrogate ^{234}U(t, pf) measurements as a proof-of-concept experiment [YB03]. The deduced neutron-induced fission cross sections agree with the evaluated nuclear data file (ENDF/B-VI) [MG96] data to within 10% except for an approximate 20% overshoot in the neutron energy range of 0.2 – 0.5 MeV. This disagreement is attributed to increased uncertainties in both the direct-reaction-fission-probability data and calculated neutron-induced compound nucleus formation cross sections at lower neutron energies.

Estimates of the ^{240}Am(n, f) cross sections were deduced through experimentally measured ^{240}Pu(^{3}He, df) direct-reaction-fission probabilities performed by Gavron *et al.* [GBK+76]. These measured fission probabilities have been used as a surrogate reaction in two studies to estimate the ^{240}Am(n, f) cross section in the neutron energy range of $E_n = 100$ keV – 20 MeV. The results from these estimates are shown in Figure 1.3 as closed circles [BW79] and half-closed stars [YBB04]. These surrogate reaction experimental estimations are useful in that they provide experimentally-based cross section values that have been shown to be accurate within 10 – 20%. However, the utility of these measurements is limited by the fact that their accuracy relies upon estimated neutron-induced compound nucleus formation cross sections and can only be used to estimate cross sections at neutron energies above 100 keV.

The only direct experimental measurement of the ^{240}Am(n, f) cross section that is reviewed by Rochman *et al.* is shown as an open circle at $E_n = 3$ MeV in Figure 1.3. This value is cited as being reported by Britt and Wilhelmy [BW81]; however, this reference does not report any direct measurement of this value. It is likely that this point was measured radiochemically from debris from a nuclear explosion performed as part of the nuclear weapons testing program at the Nevada Test Site and remains only available in classified documents. There are no other reported direct experimental measurements of ^{240}Am(n, f) cross section in peer-reviewed literature as of Spring 2011.

Experimental measurements of the ^{240}Am(n, f) cross section are very limited because they are exceedingly difficult due to the nuclide's relatively short 50.8 hour half-life. This short half-life greatly limits the amount of ^{240}Am it is possible to produce through nuclear reactions. Even small samples of ^{240}Am will emit a significant radiation field posing a health and safety risk. In addition, such a measurement would require a large amount of coordination to minimize the time between the production of the ^{240}Am and its subsequent neutron-induced fission measurement. However, because of the lack of any experimental data at low neutron energies (1 eV – 100 keV), the disagreement of evaluated "data" evident in Fig. 1.2 in the energy range, and the significance of the measurement, it is necessary to overcome these challenges.

1.3 Directly measuring the ^{240}Am(n, f) cross section

Measurement of neutron-induced fission cross sections of targets such as ^{240}Am that can only be made in small quantities is a very difficult task. To compensate for the small amounts of target material in such experiments, a spectrometer with very high neutron flux is necessary. The most promising design of neutron spectrometer for this purpose is that of the lead slowing-down neutron spectrometer.

The concept of the lead slowing-down neutron spectrometer (LSDS) was introduced by Bergman *et al.* in 1955 [BIM^{+}56]. In this article, a neutron spectrometer was constructed by placing a pulsed neutron source inside a large (> 1 m^3) block of high-purity lead. The neutrons produced in the center of the block interact with the lead with largely elastic collisions and are trapped inside for hundreds of microseconds. Because the neutron-lead elastic scattering cross section is energy independent, the neutrons slowed down by these collisions will group with a relatively narrow energy spread. The neutrons gradually slow and the energy spread widens with increasing slowing-down time. Thus, by measuring the time difference between the previous neutron pulse and a detected neutron-induced event, the neutron energy causing the nuclear reaction can be deduced. The number of neutron-induced events as a function of neutron energy can then be measured over a range of neutron energies. Such a spectrometer has the main advantage that there is an enhancement in neutron intensity of 3 – 4 orders of magnitude when compared with a conventional time-of-flight neutron spectrometer. In the early years of the LSDS, such a detector allowed for the usage of relatively inexpensive, low intensity ^{3}H$(^2$H$, n)^4$He neutron sources to perform neutron-induced reaction cross section measurements. When coupled with a high intensity, accelerator-driven, pulsed neutron source, this amplification allows for the measurement of (n, f) cross sections on very small mass targets. One disadvantage of this method is that the best neutron energy resolution ($\Delta E/\bar{E}$) is on the order of 30%. This resolution limit is a result of fluctuations in the neutron path length between collisions and the spread in the energy lost in elastic scattering due to thermal motion of the lead atoms.

Since their introduction in 1955, there have been a number of LSDSs that have been constructed at different laboratories around the world to accomplish several different goals. In the 1960s and 1970s LSDSs were constructed at the University of Tokyo [WSNN70], the Kernforschungzentrum, Karlsruhe [MP64, CW71], and Argonne National Laboratory [Leh70] with the goal of measuring neutron-induced reaction cross sections on fissile material and common nuclear fission products in the 1 eV – 50 keV neutron energy range. Such cross section measurements were important for nuclear reactor design, physics, and dosimetry. It was also proposed around this time to use LSDSs to perform non-destructive fissile material assays of new and spent nuclear fuel assemblies. A LSDS for this purpose was constructed at the University of Wisconsin–Madison. Sawan and Conn [SC74] performed theoretical and experimental studies with this LSDS.

Starting in 1977, several LSDSs have been constructed around more intense neutron sources. The first of these instruments was constructed at the 100-MeV electron linear accelerator (linac) at the Rensselaer Polytechnic Institute by Slovacek *et al.* [SCB$^+$77]. Kobayashi *et al.* [KYY$^+$97] constructed a similar spectrometer on a 46 MeV electron linac at Kyoto University. The center of these two spectrometers contains a tantalum photoneutron target which produces neutrons through the Ta$(e,\gamma)(\gamma,n)$ reaction, giving neutron fluxes on the order of 10^{12} neutrons/s. Using these high neutron fluxes, it has been possible to measure subthreshold neutron-induced fission cross sections on major actinide isotopes such as ^{232}Th [NBSB91], ^{237}Np [YKK$^+$93], and ^{238}U [SCB$^+$77].

Taking advantage of nuclear spallation reactions of high energy protons on a high-Z target, even larger neutron fluxes can be obtained. Recently, several LSDSs have been constructed taking advantage of this. The Transmutation by Adiabatic Resonance Crossing (TARC) project [AAA$^+$02] is a LSDS with neutrons produced at its center by the 2.5- or 3.5-GeV proton beam from the CERN Proton Synchrotron impinging upon lead. The goal of this project is to examine the possibility of destroying long-lived nuclear fission products by neutron capture in a high flux of resonance-energy neutrons. A LSDS is also located along the 209-MeV proton beam at the Institute for Nuclear Research, Russian Academy of Sciences, Moscow [ABGt04]. With neutron fluxes on the order of 10^{13} neutrons/s, several difficult (n,f) cross section measurements have been made on the minor actinide isotopes ^{236}U [ABB$^+$08], ^{242m}Am and ^{245}Cm [ABB$^+$09a], ^{243}Cm [ABB$^+$09b], ^{244}Cm [ABB$^+$10a], and ^{246}Cm [ABB$^+$10b].

The most recently designed LSDS has been coupled to the 800-MeV proton accelerator at the Los Alamos Neutron Science Center (LANSCE). The characteristics of the LSDS at LANSCE have been summarized by Rochman *et al.* [RHD$^+$05]. The LSDS at LANSCE has been specifically designed to perform neutron-induced fission measurements on small amounts of radioactive target material. Spallation neutrons are produced at the center of a 1.2 m x 1.2 m x 1.2 m high-purity lead cube from the interaction of the 800-MeV proton beam with a stopping thickness of tungsten metal. The proton beam is presently limited by radiation safety considerations to an average proton current of 1 μA. During the spallation interaction of 800-MeV protons in tungsten, $13-14$ neutrons are emitted, giving a total neutron flux on the order of $10^{13}-10^{14}$ neutrons/s. The apparatus is situated in a specially designed, well characterized room of the Weapons Neutron Research facility [LBRW90] at LANL. This allows for extensive modeling of the facility using Monte Carlo simulations of the interactions of protons and neutrons with all the surrounding material, giving experimenters an accurate prediction of the neutron flux experienced by the neutron-irradiation samples. Experimental measurements have been performed on very small actinide samples including a 10 nanogram ^{239}Pu target [DRT$^+$07]. Being able to perform neutron-induced fission cross section measurements on such extremely small samples makes the LSDS at LANSCE particularly well suited for the measurement of the ^{240}Am(n,f) cross section. However, the production of an ^{240}Am target with even 10 nanograms of target material is still a major challenge.

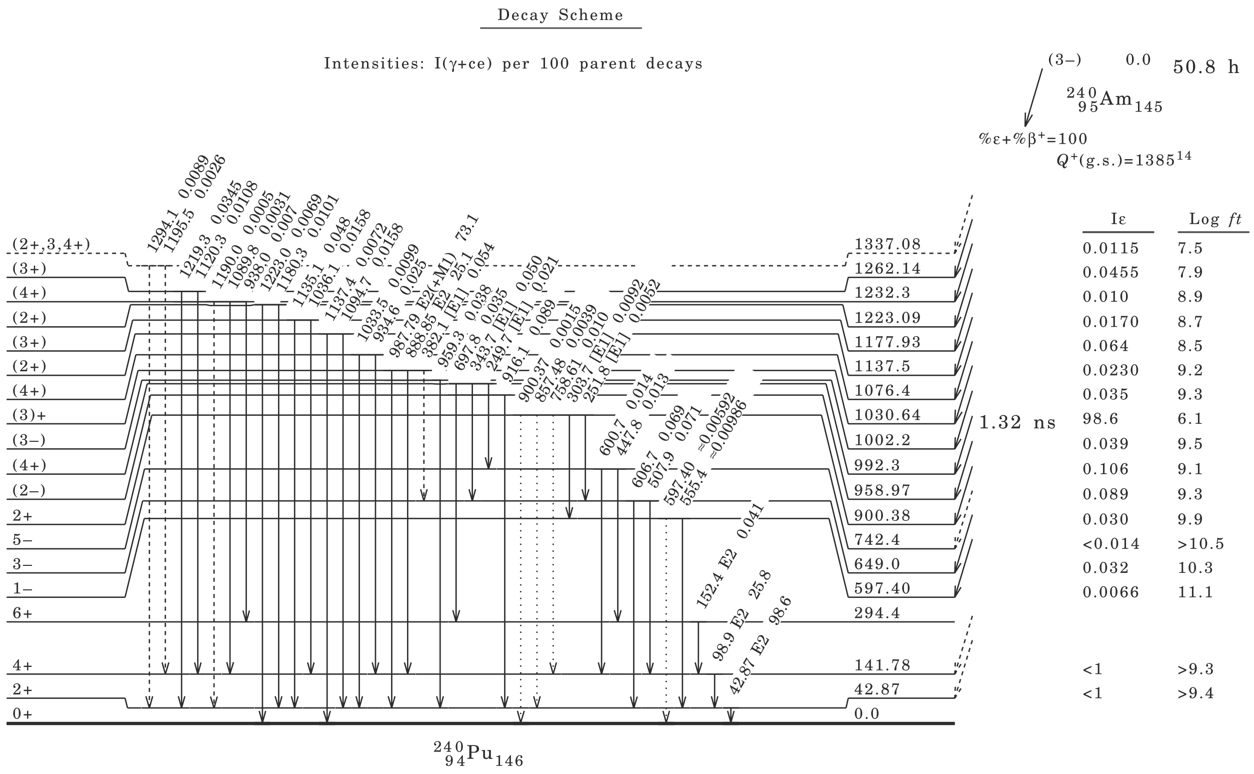

Figure 1.4 ^{240}Am EC/β^+ decay scheme.

1.4 Nuclear properties of ^{240}Am

The identification of the electron capture (EC) decay mode and measurement of the half-life of ^{240}Am was first performed by Seaborg *et al.* [SJM49]. To date, the most detailed experimental study of these properties was performed by Ahmad *et al.* [ABSF72]. This study measured a half-life of 50.8 ± 0.3 hours and yielded detailed γ-ray and conversion electron spectra. Based on the comparative half-life ($\log ft$) values measured for the different electron capture transitions, the ground state spin and parity of ^{240}Am was assigned to a $K\pi I = 3-3$ state composed of the $\frac{5}{2}-[523]$ proton and $\frac{1}{2}+[631]$ neutron orbitals. Using data from this and other experiments, a detailed decay scheme of the EC decay ^{240}Am was summarized by Singh and Browne [SB08]. The ^{240}Am EC decay diagram from this publication is reprinted here as Figure 1.4 with permission from Elsevier.

The alpha decay of ^{240}Am was first observed by Gorman and Asaro [GA70]. In this work, three alpha energy groups were observed with a total branching ratio of $1.9 \times 10^{-4}\%$. The spin and parity of the ^{240}Am ground state based on the α particle energies observed in this publication are in good agreement with those from the electron capture experiments.

Table 1.1 summarizes the observed radiations from ^{240}Am collected by Singh and Browne [SB08] and Browne and Tuli [BT06].

1.5 Nuclear reactions for the production of ^{240}Am

The nuclear reactions discussed in the following section make an exhaustive list of those reported in the literature for the production of ^{240}Am. The maximum reported ^{240}Am-production cross section for each of these reactions is summarized in Table 1.2.

The first reports of the production of ^{240}Am date back to the discovery of americium by Seaborg *et al.* [SJM49]. In this work, ^{240}Am was produced by bombarding ^{239}Pu targets with 19-MeV deuterons and ^{237}Np targets with 32- and 38-MeV helium ions at the University of California Radiation Laboratory's 60-inch cyclotron. The deuteron bombardment of ^{239}Pu was used in many early studies of ^{240}Am, including the confirmation of its approximately 50-hour half-life [SGS50] and detailed investigations of its electron-capture decay [SGH57] and alpha decay [GA70]. Detailed cross section measurements of this and other nuclear reactions for the production of ^{240}Am were measured across the 1950s, 60s and 70s. Cross section measurements were performed for the ^{239}Pu(d, n) [LGG66], ^{239}Pu$(\alpha, p2n)$ [GCCS56], and ^{237}Np(α, n) [LGG66, LA77, FRNA73] production reactions for ^{240}Am.

Several nuclear reactions have also been used to study the spontaneously-fissioning nuclear shape isomer of ^{240}Am. The study of these nuclear reactions began in the 1960s with the discovery that many isotopes of actinide elements had isomeric states decaying by spontaneous fission with half-lives on the picosecond to millisecond time scales [Bri73, Van77]. The study of these isomeric states became a major nuclear physics research topic because it was found that they were shape isomers corresponding to a second minimum in the potential energy curve along the degree of prolate deformation. The spontaneously fissioning isomer ^{240}Am^f has been shown to be produced in the ^{241}Pu$(p, 2n)$ [rBWK67], the ^{238}U(^{7}Li,5n) [BBYK79], and the ^{242}Pu$(p, 3n)$ [BHK$^+$98] nuclear reactions.

In the 1980s and 1990s, production of ^{240}Am was reported as a nuclear reaction product during the study of heavy ion transfer reactions on actinide targets. Starting in the late 1970s, a large number of radiochemical studies were performed examining actinide production in bombardments of actinide targets ranging from uranium to einsteinium with a variety of projectiles ranging from oxygen to uranium. The aim of these studies was to try to systematically understand this class of nuclear reactions, as well as produce new neutron-rich and -deficient actinide isotopes, and possibly even new superheavy elements. Of these many studies, only Welch *et al.* [WMG$^+$87], Gregorich *et al.* [GML$^+$87], and Türler *et al.* [TvGL$^+$92] report the production of ^{240}Am.

More recently, work by Adam *et al.* related to accelerator-driven transmutation of nuclear waste has measured an additional cross section for the production of ^{240}Am [ABB$^+$02]. In this work, ^{241}Am and ^{237}Np targets were irradiated with 0.66-GeV protons and the sub-

Table 1.1 Radiations emitted from radioactive decay of ^{240}Am.

$\gamma-$rays		$x-$rays		$\alpha-$particles	
Energy (keV)	% per Decay	Energy (keV)	% per Decay	Energy (keV)	% per Decay
987.79 *6*	73.2 *10*	103.74 *2*	29.0 *10*	5378 *1*	(1.65 *61*)$\times 10^{-4}$
888.85 *5*	25.1 *4*	99.53 *2*	18.6 *6*	5337 *2*	(2.28 *84*)$\times 10^{-5}$
98.9 *1*	1.49 *4*			5286 *3*	(2.34 *88*)$\times 10^{-6}$
42.87 *4*	0.111 *2*	116.25 *3*	10.8 *4*		
916.1 *2*	0.090 *6*	117.23 *3*			
507.9 *10*	0.072 *6*				
606.7 *10*	0.070 *8*	120.65 *3*	3.80 *15*		
382.1 *10*	0.053 *5*	121.56 *3*			
343.7 *10*	0.049 *5*				
1135.1 *3*	0.049 *3*				
959.3 *3*	0.039 *5*				
697.8	0.035 *8*				
1219.3 *3*	0.035 *2*				
934.6 *5*	0.025 *3*				
249.7 *10*	0.020 *3*				
1094.7 *3*	0.016 *1*				
1036.5 *3*	0.016 *2*				
600.7 *10*	0.014 *6*				
447.8 *10*	0.013 *4*				
152.4 *10*	0.012 *3*				
1120.3 *4*	0.011 *1*				
758.61 *8*	0.0105				
1180.3 *3*	0.0102 *8*				
555.4 *10*	0.01				
1033.5 *3*	0.010 *1*				
303.7 *10*	0.009 *2*				
1294.1 *3*	0.009 *1*				
1137.4 *5*	0.0073 *20*				
938.0 *6*	0.007 *3*				
1223.0 *3*	0.007 *1*				
597.4 *7*	0.006				
251.8 *10*	0.005 *2*				
857.48 *10*	0.004				
1089.8 *10*	0.0031 *6*				
1195.5 *4*	0.0026 *5*				

Table 1.2 Maximum cross sections of ^{240}Am-producing nuclear reactions.

Reaction	Max. cross section (mbarn)	E_{proj} (MeV)	Reference
$^{239}\mathrm{Pu}(\alpha, p2n)$	17 ± 3	50	[GCCS56]
$^{238}\mathrm{Pu}(\alpha, pn)$	15 ± 4	40	[GCCS56]
$^{237}\mathrm{Np}(\alpha, n)$	~ 3	28	[LA77, LGG66, FRNA73]
$^{239}\mathrm{Pu}(d, n)$	~ 13	15	[LGG66]
$^{241}\mathrm{Am}(p, pn)$	46.5 ± 1.1	660	[ABB+02]
$^{249}\mathrm{Cf}(^{136}\mathrm{Xe}, x)$	0.043 ± 0.004	813	[GML+87]
$^{248}\mathrm{Cm}(^{40}\mathrm{Ca}, x)$	0.015 ± 0.007	289	[TvGL+92]
$^{248}\mathrm{Cm}(^{44}\mathrm{Ca}, x)$	0.029 ± 0.008	254	[TvGL+92]
$^{248}\mathrm{Cm}(^{132}\mathrm{Xe}, x)$	0.0854 ± 0.0075	805	[WMG+87]
$^{248}\mathrm{Cm}(^{129}\mathrm{Xe}, x)$	0.0838 ± 0.0075	780	[WMG+87]
$^{241}\mathrm{Am}(\gamma, n)$	201 ± 8	12	[THH+10, WFS92]
$^{241}\mathrm{Am}(n, 2n)$	260 ± 9	12	[TAB+08]
$^{241}\mathrm{Am}(n, 2n)$	440 ± 50	11	[PPK+07]

sequent radioactivities measured through γ-ray spectroscopy. The production of ^{240}Am was observed in the irradiated ^{241}Am target allowing for the measurement of the cross section of the $^{241}\mathrm{Am}(p, pn)^{240}\mathrm{Am}$ at 0.66 GeV.

In the 1990s and 2000s, the production of ^{240}Am through the neutron and photon bombardment of ^{241}Am was investigated. The $^{241}\mathrm{Am}(n, 2n)^{240}\mathrm{Am}$ reaction has been studied with neutron energies 13.4 – 14.9 MeV by Filatenkov *et al.* [FC00], at 14 MeV by Lougheed *et al.* [LWN+02], 8.8 – 11.4 MeV by Perdikakis *et al.* [PPV+06], and 9 – 16 MeV by Tonchev *et al.* [TAB+08]. These measurements agree except in the 10.5 – 11.5 MeV neutron energy range where Perdikakis *et al.* measured a cross section nearly two times larger than Tonchev *et al.*. Future experimental measurements in this neutron energy range are necessary to resolve these conflicting results. The $^{241}\mathrm{Am}(\gamma, n)^{240}\mathrm{Am}$ reaction has been studied with photon energies from 5 – 10 MeV by Watson *et al.* [WFS92] and from 9 – 16 MeV by Tonchev *et al.* [THH+10]. These results agree within reported error bars.

While the $^{242}\mathrm{Pu}(p, 3n)$ reaction has been used to produce the spontaneous fission isomer $^{240}\mathrm{Am}^f$, its cross section for production of the ground state of ^{240}Am has never been measured. This is an unfortunate omission as this reaction has been predicted to have a high ^{240}Am production cross section. Figure 1.5 shows calculated cross sections for the $^{242}\mathrm{Pu}(p, 3n)^{240}\mathrm{Am}$ reaction using the compound nucleus code, JORPL [Alo74] (green triangles) and the cascade-exciton code, CEM03.02 [MGS+05, MPG06] (black squares). Lines are drawn to guide the eye. These ^{240}Am-production cross sections are significantly larger than the majority of those of previously investigated nuclear reactions summarized in Table 1.2.

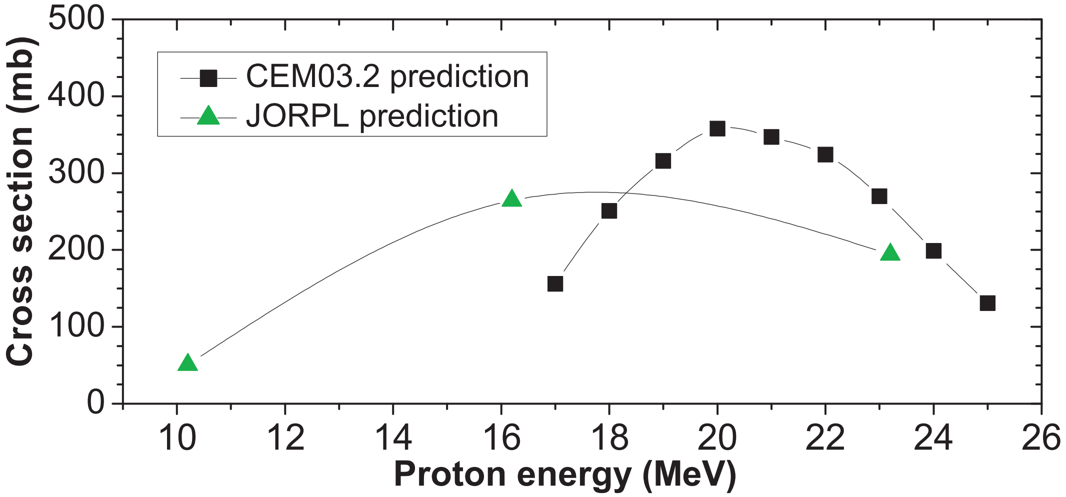

Figure 1.5 Predicted cross sections for ^{242}Pu$(p, 3n)^{240}$Am.

In addition, protons in the 15 – 25-MeV range are relatively accessible in high intensities at a large number of experimental facilities and the low excitation energy of the nuclear reaction results in significantly fewer competing nuclear reaction products. Also, because the ^{240}Am will be produced from a different element, it will be possible to develop a chemical separation procedure to isolate a pure ^{240}Am target from the irradiated target material. Thus, the ^{242}Pu$(p, 3n)^{240}$Am reaction is a very promising reaction for the production of an ^{240}Am LSDS target. It is necessary to perform experimental measurements of the ^{240}Am production cross section through this nuclear reaction before a large-scale ^{240}Am production campaign is performed. This is one of the main goals of the second part of this dissertation.

Chapter 2

Investigation of the ^{242}Pu$(p,3n)^{240}$Am Nuclear Reaction

The total amount of a radioactive species produced by a nuclear reaction is dependent on both the production rate and decay rate of the species. For the case of a stable or long-lived radioactive target being bombarded with a typical intensity ($I = 10^9 - 10^{14}$ / s $\cdot$ cm^2) of ions, the number of target nuclei (N_0) can be regarded as constant over the irradiation period. In this case, the production rate (R) of the species can be regarded as

$$R = N_0\,\sigma\,I \tag{2.1}$$

where σ is the cross sectional probability for its production. Thus, the total number of the radioactive species (N) which has decay constant λ can be shown by

$$dN = R\,dt - \lambda\,N\,dt \tag{2.2}$$

which integrates to

$$N(t) = \frac{R}{\lambda}(1 - e^{-\lambda\,t}) = \frac{N_0\,\sigma\,I}{\lambda}(1 - e^{-\lambda\,t}) \tag{2.3}$$

Because $A = \lambda N$, the cross section for the production of ^{240}Am through the proton irradiation of ^{242}Pu targets ($\sigma_{^{242}\mathrm{Pu}(p,3n)^{240}\mathrm{Am}}$) can thus be represented through the following equation

$$\sigma_{^{242}\mathrm{Pu}(p,3n)^{240}\mathrm{Am}} = \frac{A_{EoB}}{N_{Pu}\,I_p\,(1 - e^{-\lambda\,t})} \tag{2.4}$$

where t is the length of bombardment, A_{EoB} is the activity of ^{240}Am at end-of-bombardment (EoB) in decays per second, N_{Pu} is the thickness of the ^{242}Pu target in atoms per square centimeter, I_p is the total proton beam intensity in protons per second, and λ is the decay rate of ^{240}Am.

Table 2.1 Isotopic composition of ^{242}Pu used to produce nuclear reaction targets.

Plutonium isotope	Isotopic abundance 12/19/1979	Isotopic abundance calculated for 2007
^{238}Pu	0.004%	0.003%
^{239}Pu	0.005%	0.005%
^{240}Pu	0.022%	0.002%
^{241}Pu	0.035%	0.007%
^{242}Pu	99.932%	99.96%
^{244}Pu	0.002%	0.002%

2.1 Production of ^{242}Pu targets

For the measurement of the $^{242}\text{Pu}(p,3n)^{240}\text{Am}$ cross section, targets of a known thickness of isotopically enriched ^{242}Pu are necessary. Such targets were fabricated in the LBNL Heavy Element Research Laboratory (HERL) by electrodeposition from isopropanol using a procedure adapted from Müllen and Aumann [AM74, MA75]. The ^{242}Pu sample used to produce these targets was shipped to LBNL from Oak Ridge National Laboratory (ORNL) in 1987 as part of the Transplutonium Production Program. The shipping document included with the transfer of this sample can be found in Appendix A. According to this document, the sample originated from the Operations Isotopes Enrichment Section of ORNL and was shipped without chemical purification. The plutonium isotopic abundance of the sample as of December 19, 1979 is included in this document. Since 1979, this sample has radioactively decayed ~30 years, causing significant changes to the sample chemical constituents and the plutonium isotopic make up. The majority of these changes have come as a result of the radioactive decay of the short-lived isotope of plutonium, ^{241}Pu with a half-life of 14.35 years. The isotopic abundances of the different plutonium isotopes as of 2011 can be calculated by decay-correcting the abundances reported in the original ^{242}Pu sample shipping document. These values, as well as the original abundances, are shown in Table 2.1.

The major radioactive decay mode of ^{241}Pu is through β^- decay to ^{241}Am. Thus, by 2007, a significant amount of ^{241}Am will have grown into the ^{242}Pu sample. Because it is highly desirable to have pure target material for these nuclear reaction studies, a chemical procedure was used to isolate the plutonium from americium. In addition, the chemical separation was useful for the removal of silicates produced through radiation damage of the quartz container.

Figure 2.1 The boiling/scrubbing apparatus used to prepare ^{242}Pu solutions.

2.1.1 Dissolution and purification of ^{242}Pu

The above discussed ^{242}Pu sample is currently stored as an oxide powder in a glovebox in the LBNL HERL. 154 mg of the oxide powder was weighed and added to 8 mg of NaF in a boiling flask for dissolution. 1.4 mL of 8 M HNO_3 was added to the flask in 100 μL increments while heating. While heating, the boiling flask was attached to the vapor scrubbing system shown in Figure 2.1. The first liquid compartment of this system was filled with water and the second with NaOH. Its purpose was to minimize corrosive nitric acid fumes emitted into the glove box. An additional 18 mg of NaF and 50 μL of 8 M HNO_3 were added and the solution was allowed to boil until all visible powder had dissolved. An additional 250 μL of 8 M HNO_3 was added to the solution and it was allowed to cool. After cooling, 1 mL of 4 M HNO_3 was added resulting in a $\sim$2.5 mL solution with $[PuO_2] \approx 0.2$ M, $[NO_3{}^-] \approx 6.5$ M, and $[Na^+] = [F^-] \approx 0.2$ M. It's also likely that the solution contained some SiO_2 which had been leached from the glass boiling flask by the presence of hydrofluoric acid. The clear nitric acid solution became dark green at the start of the dissolution and went to a very dark brown by the time the solution had cooled.

To characterize the isotopic purity of the dissolved ^{242}Pu sample, it was desirable to measure the alpha particle emission spectrum. A 20 μL sample of the ^{242}Pu stock was taken

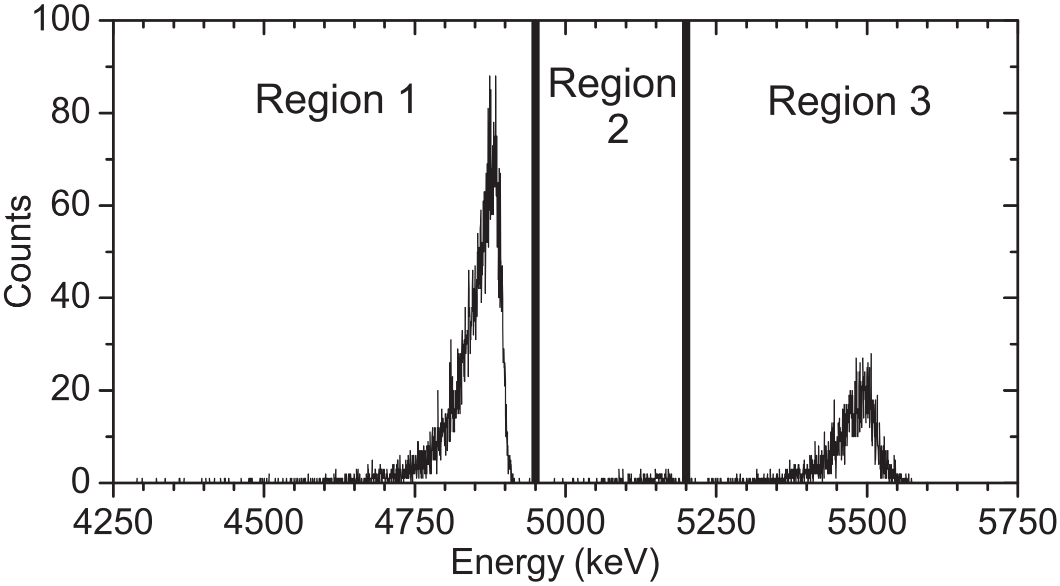

Figure 2.2 Alpha spectrum of the ^{242}Pu solution before chemical purification.

and diluted first by a factor of 50x, and then again by a factor of 100x, resulting in a 5000x dilution. A 10 μL aliquot of this 5000x dilution was pipetted onto a small platinum foil which was subsequently heated for a few seconds in an induction heater. The alpha plate was then counted using a computer setup with an Ortec® TRUMP™-PCI-8K multichannel analyzer (MCA) connected to a Tennelec TC256 alpha spectrometer. The resulting alpha spectrum is shown in Figure 2.2.

There are three discernible peaks in Figure 2.2, each with low energy broadening typical of evaporated alpha plates. The first peak is between 4.25 – 4.95 MeV (denoted Region 1) and is composed of alpha particles from ^{242}Pu, ^{241}Pu, and ^{244}Pu. The small second peak is present between 4.95 – 5.2 MeV (denoted Region 2) and is composed of alpha particles from ^{239}Pu and ^{240}Pu. The third peak is located from 5.2 – 5.6 MeV (denoted Region 3) and is composed of alpha particles from ^{238}Pu and ^{241}Am. Based on the isotopic abundances of the ^{242}Pu sample given in the third column of Table 2.1, as well as the different isotopes' half-lives, alpha decay energies, and branching ratios, a Region 1 to Region 3 count ratio of $\sim$8 would be expected for the pure plutonium stock. In Figure 2.2, we measure a Region 1 to Region 3 count ratio of $\sim$3, as a result of a significant amount of ^{241}Am contamination. In an effort to make the purest ^{242}Pu targets possible, a separation procedure was performed to remove the americium from the plutonium stock.

An anion exchange chromatography procedure was used to purify plutonium from americium. The usage of anion exchange chromatography for the separation of plutonium from americium has been extensively studied [Col65, PK60] and takes advantage of the tendancy of plutonium to form negatively-charged complexes in various concentrations of mineral acids. These complexes are then sorbed to an anion exchanging resin, allowing for the separation from americium and other elements which do not form anionic complexes.

The resin used for the separation procedure was AG 1x8 100 - 200 mesh anion exchange resin from BioRAD. This analytical grade resin is composed of a styrene-divinylbenzene copolymer support matrix functionalized with a quartenary amine anion exchanger. In the 1x8 resin, there are divinylbenzene cross linkages of 8%. The mesh size of 100 - 200 corresponds to a 106 – 180 μm wet bead size. The manufacturer reported capacity for this resin is 1.2 meq/mL wet resin. Prior to use, the resin was conditioned according to the following procedure:

- Resin soaked in 1 M HNO_3 with occasional agitation for 1 hour.
- Acid decanted and resin soaked in water with occasional agitation for 1 hour.
- Water decanted and resin soaked in 1 M NaOH with occasional agitation for 1 hour.
- Base decanted and resin soaked in 1 M HNO_3 with occasional agitation for 1 hour.
- Acid decanted and resin soaked in water with occasional agitation for 30 minutes.
- Water decanted and resin soaked in 1 M NaOH with occasional agitation for 30 minutes.
- Base decanted and resin soaked in 1 M HNO_3 with occasional agitation for 30 minutes.
- Acid decanted and resin soaked in water.

A glass column with a 9 mm inner diameter and 18 cm length, giving a volume of 11.45 mL was used for the separation procedure. The capacity of this column with a 15 cm bed length is 1.57 g of PuO_2, giving the desired safety factor of 10 over the amount of Pu to be loaded. The column was packed with a small amount of glass wool near the tip and on top of the resin. The drop size of the column was measured to be ~50 μL/drop by counting the number of drops needed to fill a graduated cylinder. The column's free column volume (FCV), which is represents the column volume not occupied by resin, was measured to be 5.1 mL by rinsing the column with water while dripping into a beaker containing $AgNO_3$ solution. The number of drops counted between adding the HCl to the top of the column and observing the precipitation of AgCl from the $AgNO_3$ solution determined the FCV.

On the day the Pu/Am separation was to be done, the column was packed as a slurry from aqueous solution and conditioned with 8 M HNO_3. This process was done the day of the separation because a column conditioned with 8 M HNO_3 will begin to form bubbles from the degradation of HNO_3 in the resin bed overnight. After packing, the column was stoppered on top and bottom and transferred into the glovebox in HERL containing the

Figure 2.3 Anion exchange column sorbed with ^{242}Pu.

^{242}Pu solution. Inside the glovebox, the 2 mL of HNO_3 on top of the column was collected in a 30 mL Nalgene bottle. The ~2.5 mL of ^{242}Pu stock was added slowly to the top of the column. This transfer was done with a glass transfer pipette in several aliquots to minimize the volume of ^{242}Pu solution in contact with the column reservoir. With the addition of the plutonium stock, a dark green band formed at the top of the resin and began to spread down the column. Being careful not to allow the column to go dry, 8 M HNO_3 was used in 200 – 300 μL quantities to first rinse the empty boiling flask and then rinse the column reservoir to maximize the transfer of ^{242}Pu. The green plutonium band continued to spread down the column until a total of 4.25 mL of acid had been eluted. The band took up 10 cm of the column's 15 cm bed when it stopped spreading. A photograph of the column with the plutonium sorbed is shown in Figure 2.3.

A total of 7.5 FCVs of 8 M HNO_3 were added to the column to wash the ^{241}Am impurities from the ^{242}Pu. The plutonium was then eluted from the column with the addition of 0.35 M HNO_3. In this less concentrated nitric acid solution, the $Pu^{4+} + NO_3^- \rightleftharpoons Pu(NO_3)_6^{-2}$ equilibrium is shifted to the left, causing the plutonium ions to desorb and elute from the column. After the addition of 3/4 of an FCV of 0.35 M HNO_3 the bottom of the green plutonium band began to visibly move, the resin began to compress, and the top of the resin began to turn yellow. Fractions of 1 – 1.5 mL of the eluting 0.35 M HNO_3 were collected in tubes containing 200 μL of 15.8 M HNO_3. The tubes contained aliquots of concentrated HNO_3 so the eluted plutonium fractions would equilibrate to a solution with ~2 M HNO_3, thus retarding the formation of plutonium polymer. As the green plutonium band reached the bottom of the column, the color of the eluted drops turned from colorless to pink (characteristic of Pu(VI)-nitrato complexes) for a few drops, then to green (characteristic of Pu(IV)-nitrato complexes) and then eventually back to colorless. After the elution of ~5 FCVs of 0.35 M HNO_3, a 10 μL alpha plate was taken of a 1 mL elution fraction. Analysis of this plate showed that it contained ~1 mg of ^{242}Pu. A total of ~9 FCVs of 0.35 M HNO_3 were eluted from the column with the first 25 mL taken in 1 – 1.5 mL fractions.

As evident from the amount of plutonium still being eluted 5 FCVs after the addition of 0.35 M HNO_3, this method of plutonium elution resulted in severe tailing. While this is undesirable, this process was specifically chosen over alternate methods such as elution by reduction to Pu(III) through the addition of a HI/HCl mixture because the electrodeposition process performed significantly better when using a ^{242}Pu stock solution in pure HNO_3.

Two ^{242}Pu stock solutions were made from the plutonium fractions eluted from this column. The first solution was made by collecting and rinsing the six most plutonium-rich fractions (1.6 FCVs total) eluted from the column. A 100x dilution of this solution was taken and 10 μL of this diluted solution was used to prepare an alpha plate. The resulting alpha spectrum is shown as Figure 2.4. The analysis of this alpha plate showed that the stock solution contained a total of 76 mg of ^{242}Pu in a ~7 mL of 2 – 3 M HNO_3. Also, the Region 1 to Region 3 ratio in this spectrum is ~9, which shows a significant decontamination from ^{241}Am.

The second stock solution was prepared by collecting ten additional plutonium-rich fractions (2.5 FCVs total) eluted from the column. A 100x dilution of this stock solution was assayed using liquid scintillation spectroscopy using a Wallac 1414 Liquid Scintillation Counter (LSC). Analysis of the measured radioactivity showed that this second post-separation stock contained 35.1 mg of ^{242}Pu in a total of 12.9 mL of of 2 – 3 M HNO_3. The remaining ~25 mg of ^{242}Pu was presumed to be in the large elution tail or have remained sorbed to the column.

The more concentrated of the two post-separation ^{242}Pu stock solutions was also analyzed by absorption spectrophotometry. Because of differences in electronic structure, solvated and complexed ions with different oxidation states have different light absorption properties. Actinide ions in solution have the tendency to absorb light of specific wavelengths in the visible and near infrared range. The absorption properties of different oxidation states of plutonium are different enough that spectrophotometry can be used to identify various oxidation states of plutonium present in solution. In his 1961 publication [Coh61], Cohen reports the spectra of the various oxidation states of plutonium in non-complexing 1 M $HClO_4$ solutions.

Spectrophotometric data of plutonium solutions were taken in HERL using an Ocean

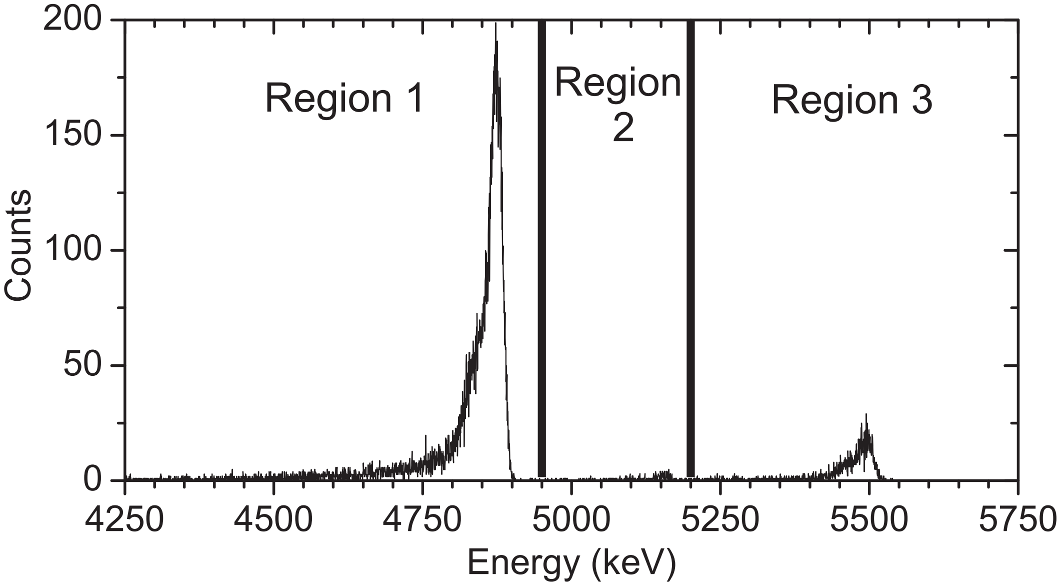

Figure 2.4 Alpha spectrum of the ^{242}Pu solution after chemical purification.

Optics USB2000 fiber optic spectrometer. A diagram of the set up is shown in Figure 2.5. Light from an Ocean Optics LS-1 tungsten halogen light source is passed through a fiber optic cable, through a sample inside a containment glovebox, and then collected using a USB2000 spectrometer. This spectrometer is fitted with a grating that results in a spectral range from 350 – 1000 nm. Transmission of light within this spectral range was measured for the ^{242}Pu stock solution ($S(\lambda)$) and a blank sample containing pure 3 M HNO_3 ($R(\lambda)$). A background dark measurement ($D(\lambda)$) was also taken while blocking the light source prior to the sample. The absorbance for a given wavelength is then calculated by

$$A(\lambda) = -log\left(\frac{S(\lambda) - D(\lambda)}{R(\lambda) - D(\lambda)}\right) \tag{2.5}$$

The absorbance spectrum of the post-separation ^{242}Pu stock solution is shown in Figure 2.6. By comparison of this spectrum with the reference absorbance spectra collected by Cohen [Coh61], details about the oxidation state of the plutonium in solution can be elucidated. The presence of the distinct peak at 470 nm range implies that the solution is largely in the Pu(IV) oxidation state. The lack of a large double or single peak in the 550 – 620 nm range demonstrates the lack of Pu(III) or Pu(V) oxidation states, respectively. The sharp peak at 830 nm signifies the presence of the Pu(VI) oxidation state. According to the Beer-Lambert law, $A = \epsilon\ell c$, where A is the absorbance, ℓ is the path length of the sample, c is the concentration of the species, and ϵ is the extinction coefficient of the species.

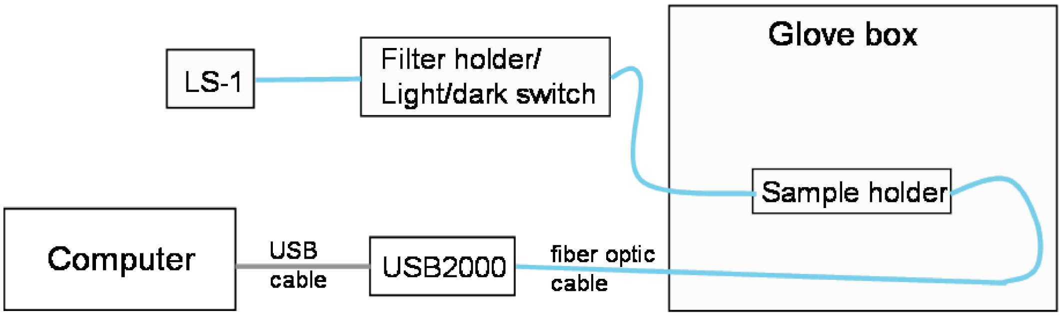

Figure 2.5 Diagram of the absorbance spectrophotometer in HERL.

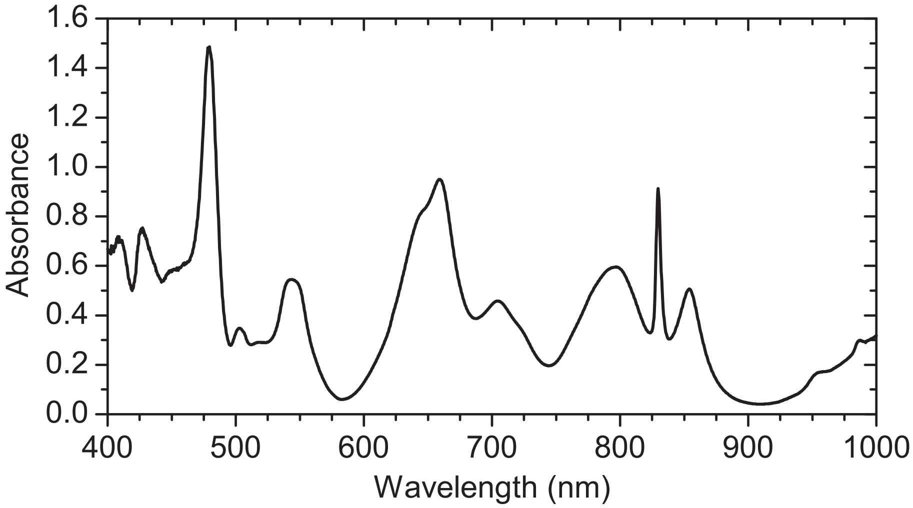

Figure 2.6 Absorbance spectrum of the ^{242}Pu solution after chemical purification.

Assuming the extinction coefficients of the Pu(IV) absorbance at 470 nm and Pu(VI) absorbance at 830 nm are equal to those measured by Cohen, the solution is ∼94% Pu(IV) and ∼6% Pu(VI). The presence of a complexing ligand such as NO_3^+ will significantly affect the absorbance of the solution. Thus, this comparison with the Cohen data taken on plutonium in non-complexing perchloric acid solutions can only be used to qualitatively analyze the plutonium oxidation states in solution.

2.1.2 Preparation and electrodeposition of ^{242}Pu targets

The target backing chosen for the production of targets for the measurement of the $^{242}\mathrm{Pu}(p,3n)^{240}\mathrm{Am}$ cross section was high purity titanium. This metal backing was chosen for several reasons. First, the high strength to weight ratio of titanium makes the handling of very thin titanium foils feasible. Second, the plutonium electrodeposition process that was developed was particularly reproducible with titanium metal backings. Finally, this backing allowed for the use of the well characterized $^{\mathrm{nat}}\mathrm{Ti}(p,xn)^{48}\mathrm{V}$ nuclear reaction to monitor proton dose to the plutonium target.

The titanium used for target production was purchased from the ACF-Metals company based in Tucson, AZ. The 75 mm by 25 mm foils were adsorbed to a thick stainless steel substrate with a $BaCl_2$ release agent. The 0.002 mm thick foils had a titanium purity of 99.995%. For targets prepared for proton-irradiation, the titanium foils were removed from the steel substrate by placing the foil-substrate in an evaporation dish with the foil-side up. The foil-substrate was then covered with water and allowed to sit for ∼30 minutes. Once the foil was completely desorbed from the substrate, it was carefully removed from the dish and allowed to dry. The thin foil could be handled and cut into 2 cm by 2 cm electrodeposition backing squares by placing in the fold of a piece of paper. These squares were then placed inside a 2 cm by 2 cm envelope of 25.4 μm thickness aluminum foil with a 1 cm diameter hole in the center of the top layer. The usage of this Al envelope made the handling of the very thin Ti foils significantly easier, especially when inside a glovebox. A diagram of this foil-envelope configuration is shown in Figure 2.7.

Plutonium was deposited on these target backings using a chimney-type electrodeposition cell. A cross-sectional diagram of the cell is shown on the left of Figure 2.8. The middle and right portion of this figure show photographs of the closed and open cell, respectively. This cylindrical electrodeposition cell is composed of three main segments which are mounted together with a total of six screws. The upper two segments of the cell are made from Kel-F® (polychlorotrifluoroethylene), a machinable, inert fluorocarbon-based polymer and have been fashioned with a 6 mm diameter middle bore. A thin, annular palladium anode is situated between the two segments which are mounted together with three screws. The upper segment has a female SHV connector which has its live wire connected to the Pd anode and its grounding wire routed to come out the bottom of the second segment. When the cell is closed, the ground wire is in contact with the aluminum base. The target backing

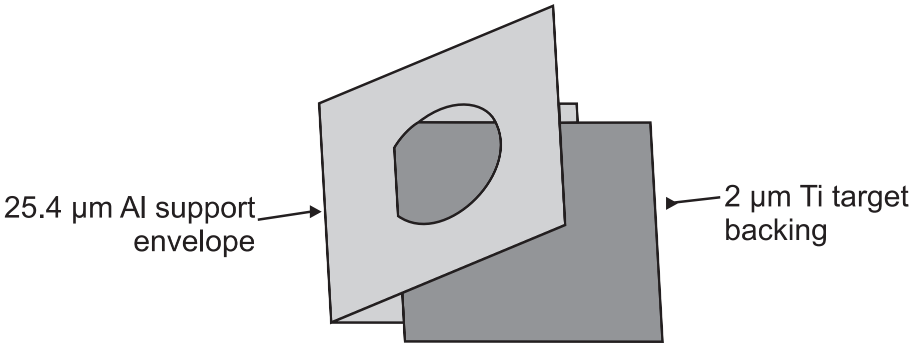

Figure 2.7 Diagram of proton-irradiation-style electrodeposition backings.

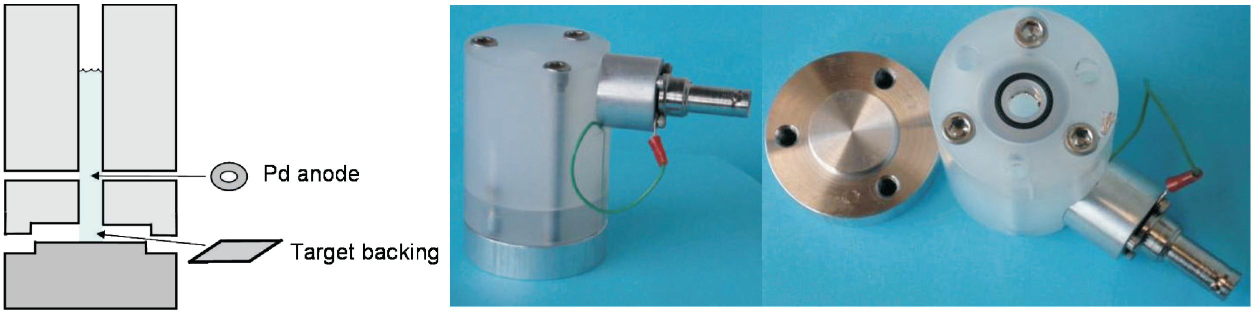

Figure 2.8 Diagram and photographs of the electrodeposition cell for proton-irradiation targets.

is centered on the base which is screwed onto the upper two segments with three screws. An accurate, annotated schematic drawing of the electrodeposition cell is shown in Appendix B.

The electrodeposition cell used for making plutonium targets was located inside a glovebox in HERL. It was supplied with voltage through a coaxial cable feedthrough from a Stanford Research Systems, Inc. PS310 1250 V – 25 W high voltage power supply. This power supply allowed for constant-current electrodepositions by varying the voltage administered to the cell while keeping the current constant. A positive bias was applied to the palladium anode, causing it to attract negatively-charged ions. Positively-charged Pu^{4+} and ${PuO_2}^{2+}$ ions were attracted to the grounded target backing cathode.

The target backings composed of thin Ti foil wrapped in an Al support envelope (see Figure 2.7) were passed into the electrodeposition glovebox inside a pre-labeled, small, hinged, polystyrene box. The target was then centered on the aluminum electrodeposition cell base. Being careful not to shift the target backing or twist the upper part on the base, the cell was closed by lowering the assembled upper two segments onto the base and evenly screwing in three screws. The target backing was conditioned and deposition cell tested by adding 1 mL of Sigma Aldrich® Chromasolv® Plus high-performance liquid chromatography (HPLC) grade isopropanol, connecting the cell to the power supply, and putting increasing voltages across the cell from 10 – 200 V over a period of ∼30 minutes. During the conditioning and testing, it was verified that the deposition cell was not leaking solution. Typical currents of 0.07 – 0.1 mA were observed with 200 V across a cell containing clean isopropanol. After the conditioning, the cell was unplugged, emptied of isopropanol and allowed to dry.

While the electrodeposition cell was tested and conditioned in one glovebox, the electrodeposition solution was prepared in the glovebox which was used to perform the ^{242}Pu dissolution and separation. To prepare the solution, 75 μL of the less concentrated post-separation ^{242}Pu stock (described in Section 2.1.1) was pipetted into the boiling flask of the apparatus shown in Figure 2.1. This aliquot volume of ^{242}Pu stock solution was chosen such that a 600 μg/cm^2 layer of ^{242}Pu would be deposited over a 6 mm diameter circle assuming an 80% transfer/deposition efficiency. The aliquot of ^{242}Pu stock was evaporated over low heat with argon flowing through the boiling flask and scrubber apparatus. To ensure the plutonium was not overheated, the temperature of the sand was monitored and kept below 100°C. Once the solution had evaporated down to a greenish, highly-viscous fluid at the bottom of the flask, the argon gas was detached from the flask, attached to a plastic pipette tip, and used to evaporate the condensed nitric acid on the walls of the boiling flask. After the flask was dried, it was raised from the sand bath and allowed to cool. Once cool, 1 mL of HPLC grade isopropanol was added to the boiling flask and used to dissolve the evaporated ^{242}Pu viscous fluid. The plutonium-isopropanol solution was then immediately transferred to the electrodeposition glovebox using a small glass vial.

After the transfer between gloveboxes, the 1 mL plutonium-isopropanol sample was immediately added to the electrodeposition cell. A thin glass stirring rod was used to agitate the plutonium-isopropanol solution during the deposition. The deposition was begun by slowly applying a voltage to the deposition cell. The voltage was applied and increased in 10 V increments until a current limit of 0.35 mA/cm^2 was reached. The deposition was then allowed to proceed by maximizing the deposition voltage for the current limit. Five ^{242}Pu targets on thin Ti backing foils were deposited and labelled C04, C05, C06, C07, and C08. The deposition times, voltages, and currents are shown in Table 2.2. Typically, the voltages would be increased to ∼50 V before reaching the current limit and then increase to a current-limited maximum (at 0.35 mA/cm^2) of 80 – 120 V over the next several hours of deposition.

Once at the beginning of the deposition procedure and periodically thereafter, a 5 μL aliquot of the plutonium-isopropanol solution was pipetted into a doubly-contained liquid scintillation vial containing 5 mL of MP Biomedicals EcoLume™ liquid scintillation cocktail. The samples were counted using the Wallac 1414 LSC. The activity in the pre-deposition aliquot implied a transfer efficiency of ^{242}Pu from stock solution to electrodeposition cell of 55 – 90%. The large deviation in these numbers is likely a result of poor consistency in the

Table 2.2 Time, voltage and current profile of deposition of five circular ^{242}Pu targets.

C04			C05			C06			C07			C08		
min.	V	mA	min.	V	mA	min.	V	mA	min.	V	mA	min.	V	mA
0	10	0.03	0	10	0.03	0	10	0.02	0	10	0.02	0	10	0.02
1	20	0.05	1	20	0.04	1	20	0.04	1	20	0.03	1	20	0.04
2	30	0.08	2	30	0.06	2	30	0.06	2	30	0.05	2	30	0.05
3	37	0.1	4	40	0.08	4.5	40	0.06	4	40	0.06	3	40	0.07
5	35	0.1	5	50	0.1	6	50	0.09	5	50	0.08	4	50	0.09
7	34	0.1	7	51	0.1	10	61	0.1	6	62	0.1	5	56	0.1
9	35	0.1	9	54	0.1	12	63	0.1	10	66	0.1	10	58	0.1
11	36	0.1	12	57	0.1	14	65	0.1	12	62	0.1	18	62	0.1
13	37	0.1	15	61	0.1	18.5	70	0.1	16	68	0.1	20	64	0.1
15	38	0.1	20	65	0.1	20	71	0.1	20	68	0.1	25	69	0.1
20	38	0.1	25	70	0.1	25	76	0.1	25	71	0.1	33	75	0.1
25	38	0.1	30	74	0.1	30	80	0.1	32	76	0.1	40	80	0.1
30	38	0.1	40	79	0.1	37	86	0.1	40	80	0.1	50	83	0.1
35	38	0.1	50	84	0.1	45	92	0.1	50	85	0.1	55	85	0.1
40	39	0.1	60	87	0.1	55	98	0.1	60	88	0.1	60	87	0.1
50	39	0.1	70	90	0.1	60	100	0.1	70	90	0.1	70	86	0.1
60	39	0.1	83	91	0.1	100	100	0.07	76	92	0.1	85	89	0.1
70	39	0.1	91	88	0.1	110	118	0.1	80	93	0.1	101	90	0.1
80	39	0.1	100	87	0.1	120	117	0.1	95	95	0.1	110	90	0.1
90	39	0.1	110	86	0.1	130	117	0.1	110	96	0.1	121	80	0.1
95	36	0.1	120	87	0.1	140	116	0.1	125	94	0.1	140	86	0.1
100	36	0.1	132	89	0.1	150	116	0.1	140	95	0.1	150	87	0.1
110	36	0.1	140	90	0.1	160	116	0.1	150	92	0.1	170	86	0.1
120	47	0.14	150	92	0.1	172	115	0.1	161	92	0.1	190	86	0.1
125	46	0.14	162	94	0.1	180	114	0.1	172	90	0.1	210	86	0.1
135	46	0.14	170	96	0.1	190	113	0.1	180	89	0.1	230	88	0.1
150	46	0.14	180	97	0.1	200	111	0.1	200	84	0.1	241	87	0.1
165	45	0.14	190	98	0.1	210	108	0.1	220	79	0.1	270	89	0.1
180	45	0.14	200	98	0.1	225	108	0.1	232	75	0.1	285	91	0.1
195	44	0.14	210	99	0.1	240	101	0.1	243	73	0.1			
210	44	0.14	220	100	0.1				254	70	0.1			
225	42	0.14	240	101	0.1									
240	43	0.14	260	101	0.1									
255	44	0.14	280	100	0.1									
270	43	0.14	290	100	0.1									
			315	99	0.1									

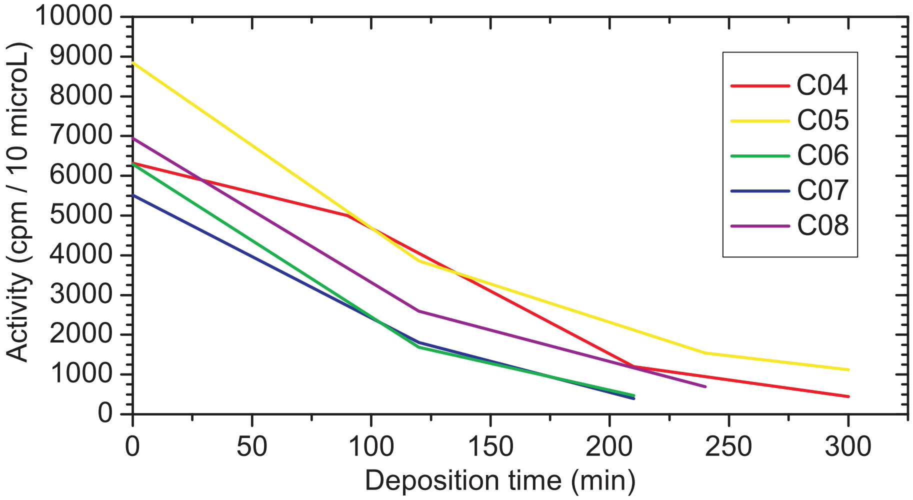

Figure 2.9 Plot of radioactivity in plutonium-isopropanol solutions as a function of time since start of deposition for the five circular ^{242}Pu targets.

isopropanol dissolution and transfer steps. The radioactivity of the plutonium-isopropanol solution as a function of time since the beginning of the deposition for each of the five ^{242}Pu targets is shown in Figure 2.9. The percent deposition as a function of time is fairly consistent between the five targets with half the activity deposited within 60 – 90 minutes and 90% of the activity deposited in 240 – 300 minutes.

After the completion of the deposition process, the voltage was turned off and the plating solution carefully removed from the cell. The cell was allowed to dry for at least 5 minutes and then carefully opened. Damage to the thin Ti backing foil was minimized by removing the three screws evenly while keeping the cell's upper segments stationary on the base. Once the screws were removed, the upper segments were lifted upward without twisting. After the target had fully dried, it was baked using a variac-controlled tube furnace. The target was heated to 100°C for 10 minutes, then to 200°C for 10 minutes, and finally to 300°C for 20 minutes. A photo of a circular ^{242}Pu spot on a thin Ti backing wrapped in an Al support envelope after deposition and baking is shown as Figure 2.10. Measurements of the electrodeposited ^{242}Pu spots show that the deposition spots have a diameter of 7.3 mm rather than 6 mm as anticipated from the cell's bore diameter. This is because, while the bore diameter is 6 mm, the o-ring (seen in black in right-most photo of Figure 2.8) has a inner diameter of 9 mm. The 7.3 mm diameter of the ^{242}Pu deposits is a result of plating solution leaking between the plastic body and aluminum base of the cell.

Figure 2.10 Photograph of deposited and baked 6-mm-diameter ^{242}Pu target on thin Ti wrapped in Al support foil.

2.1.3 Characterization and assembly of ^{242}Pu$(p,3n)^{240}$Am targets

The ^{242}Pu targets discussed in Section 2.1.2 are well suited for proton-irradiation followed by subsequent gamma spectroscopy for the measurement of the ^{242}Pu$(p,3n)^{240}$Am reaction cross section. However, prior to proton irradiation, several important measurements must be made. One such measurement is of N_{Pu}, the thickness of the ^{242}Pu irradiation target in atoms/cm^2.

Measurement of ^{242}Pu thickness

Measurement of the ^{242}Pu thickness was performed by alpha spectroscopy. Alpha spectra of the electrodeposited targets were measured using a flowing-helium-style alpha spectrometer situated inside the electrodeposition glovebox in HERL. The spectrometer was composed of a 10.2 cm diameter, 7 cm long stainless steel pipe. On top of the pipe was an aluminum cap which had been fitted with a gas-flow nipple and an Ortec® C-13 female BNC to male Microdot vacuum feedthrough. A circular Canberra A450-18AM Passivated Implated Planar Silicon (PIPS®) detector with an active diameter of 23.9 mm was connected to the Microdot feed-through inside the housing. When operating, helium gas was flowed into the detector housing at a rate of ~0.5 standard cubic feet per hour (SCFH). At this rate, the air inside the detector was displaced with helium, in which alpha particles have a significantly reduced

Table 2.3 Summary of measured ^{242}Pu target thicknesses.

^{242}Pu target	Before irrad. (μg/cm^2)	After irrad. (μg/cm^2)	After/Before ratio	After irrad. w/mask (μg/cm^2)	During irrad. estimate (μg/cm^2)
C04	327 ± 26	267 ± 22	0.82 ± 0.09	429 ± 34	480 ± 130
C05	220 ± 18	166 ± 13	0.75 ± 0.09	120 ± 10	140 ± 42
C06	296 ± 24	254 ± 20	0.86 ± 0.10	224 ± 18	242 ± 55
C07	235 ± 19	189 ± 15	0.80 ± 0.09	165 ± 13	185 ± 49
C08	305 ± 26	292 ± 22	0.96 ± 0.11	203 ± 34	208 ± 48

energy loss per distance traveled. The PIPS® detector was connected through a short BNC cable to a silicon detector general purpose preamplifier situated just outside the glovebox. The preamp was attached to a Tennelec TC246 NIM amplifier and a 40 V NIM bias supply through a TranLamp 4845D power converter. The signals were then recorded using a computer setup with an Ortec® TRUMP™-PCI-8K multichannel analyzer and Maestro 5.10 software.

Alpha spectra of ^{242}Pu targets were measured by centering the targets underneath the detector housing. A sheet of traced graph paper was used to ensure accurate centering of the targets to within ±1 mm. In this geometry, the ^{242}Pu source is situated (4.8 ± 0.2) cm from the PIPS® detector. The geometric solid angle (I) of a circular detector collecting the emissions of a coaxial circular radioactive source has been shown by Ruby and Rechen [RR68] to be equivalent to the following simple integral expression

$$I = \frac{R_d}{R_s}\int_0^\infty du \cdot u^{-1} e^{-\frac{u \cdot z}{R_s}} J_1(u) J_1\big(\frac{uR_d}{R_s}\big) \tag{2.6}$$

where z is the distance from a detector with radius R_d to a source with radius R_s, $u = kR_s$, and $J_1()$ is the Bessel function of the order unity. The efficiency of the flowing-He alpha spectrometer is 0.0149 according to this equation.

Measurements of the ^{242}Pu targets using the above-described alpha spectrometer were taken before and after proton irradiation. After the irradiation, the targets were also measured with a 4.0 ± 0.2 mm diameter mask centered over the target, giving a measurement of the activity of ^{242}Pu which was proton irradiated. Errors in the thickness measurements were propagated from the statistical counting error and the error in the detector efficiency. The error in the detector efficiency was determined by use of a Monte Carlo simulation with the assumption that the placement of the target was ±1 mm in the horizontal directions and ±2 mm in the vertical direction. The results from these measurements are shown in Table 2.3.

The ^{242}Pu thickness decreased by $5 - 25\%$ between counting before and after irradiation. Because the targets were handled an equal amount before and after irradiation, it is not clear how much ^{242}Pu was actually present for the irradiation. To estimate the average ^{242}Pu thickness during the irradiation, the after-/before-irradiation ratio for each target was used to deduce the ^{242}Pu thickness of the center of the target before irradiation, assuming ^{242}Pu was lost equally over the entire target area. Then, the before- and after-irradiation thicknesses were averaged to get a ^{242}Pu-thickness estimate at the time of the irradiation. Error bars for this averaged during-irradiation estimated thickness were calculated to be large enough that they covered the error bars above the before-irradiation and below the after-irratiation thicknesses. When asymmetric error bars were observed, the error was estimated as the larger of the two. These overly conservative error bars were necessary to quantify the uncertainty in thickness as a result of the decrease in the ^{242}Pu target thickness.

Measurement of proton monitor foil thicknesses

A second quantity necessary for an accurate $^{242}\mathrm{Pu}(p,3n)^{240}\mathrm{Am}$ reaction cross section measurement is the irradiation's total proton dose rate in protons per second, I_p. The total proton dose irradiating the ^{242}Pu targets was measured through the use of proton monitor foils. By including additional metal foils in the ^{242}Pu target stacks that have well characterized proton-induced reaction cross sections, producing easy to detect radionuclides, the total proton dose can be directly monitored. Two appropriate proton-monitor reactions are $^{\mathrm{nat}}\mathrm{Ni}(p,x)$ and $^{\mathrm{nat}}\mathrm{Ti}(p,x)$, which produce the easy-to-detect radionuclides and ^{57}Ni and ^{48}V, respectively. To utilize these beam monitor reactions, the nickel and titanium foils must be well characterized in terms of metal purity and foil thickness.

Thin nickel foils were purchased from the Goodfellow Corporation. The foils were quoted to be 99.95% pure nickel, 0.002 mm thick, 25 mm × 25 mm squares. The thickness of each foil was characterized by careful dimensional/weight analysis. The dimensions of each nickel foil were measured with a Mitutoyo 505-646 dial caliper to an accuracy of ±0.5 mm. This dimensional error is a result of irregularities and roughness in the foil edges, rather than the caliper uncertainty. The mass of each nickel foil was measured with a Mettler Toledo XP205 analytical balance to an accuracy of ±0.05 mg. The thickness of each foil and its associated error was calculated from these two values, assuming a uniform thickness.

As a verification of thicknesses measured in this dimensional/weight analysis, the Ni foil thickness was also determined for one nickel foil by measuring the energy attenuation of alpha particles traveling through the foil. To perform this measurement, a 3-peak (^{239}Pu, ^{241}Am, ^{244}Cm) alpha source was placed underneath the metal foil and counted in a vacuum alpha spectrometer. After traveling through the metal foil, the alpha particles were detected at an energy lower than the characteristic ^{239}Pu, ^{241}Am and ^{244}Cm alpha decay energies. SRIM2003 [Zie04] was used to calculate both the range of full energy ^{241}Am alpha particles and the range of ^{241}Am alpha particles with the measured foil-attenuated energy. The difference in these ranges is the average distance the alpha particles traveled through the metal foil. This average distance is related to the thickness of the foil based on the geometry of the source and alpha spectrometer. When D_{avg} is the average distance a detected alpha particle travels through the foil, Th is the foil thickness, and z is the distance from a point radioactive source to a detector with radius R_d, then

$$\frac{D_{avg}}{Th} = \frac{\int_0^{tan(R_d/z)} \frac{sin(\theta)}{2\,cos(\theta)} d\theta}{\int_0^{tan(R_d/z)} \frac{sin(\theta)}{2} d\theta} \tag{2.7}$$

The Ni foil thickness measured through this alpha attenuation method agreed well with the thicknesses measured through the dimensional/weight analysis.

The titanium foils used as ^{242}Pu electrodeposition backings were also used as beam monitor foils. The titanium foils used were described previously in Section 2.1.2. Two 2.5 cm × 2.5 cm Ti foils similar to those used as target backings were characterized by the same dimensional/weight analysis above described for the Ni foils. Two different 0.002 μm Ti foils from a different batch of foils from ACF-metals were subjected to an alpha energy attenuation analysis as described above. The foils measured by alpha attenuation analysis was approximately 10% thicker than the foils measured by dimensional/weight analysis. This is likely due to the variation in thicknesses in the Ti foil production process. Because the thicknesses of each Ti foil used as proton monitor foils was not independently measured, a large, 20% uncertainty was estimated for the Ti beam monitor foil thicknesses.

Assembly of proton irradiation targets

With the thicknesses of the ^{242}Pu, titanium, and nickel accurately determined, the foils were assembled into their irradiation configuration. To minimize contamination when handling the targets, the ^{242}Pu-deposited titanium foils and nickel foils were wrapped in a 25.4-μm-thick, 2 cm by 2 cm aluminum foil envelope. The foils were ordered such that the beam of protons would first travel through the 25.4 μm Al envelope, then the ^{242}Pu layer, then the Ti backing foil, then the 25.4 μm Al support foil, then the Ni foil, and then the back fold of the Al envelope foil. A diagram demonstrating this ordering of foils is shown in Figure 2.11. In this schematic, beam penetrates the target going into the page.

2.2 Irradiation of ^{242}Pu targets

2.2.1 Description of the irradiation apparatus for the ^{242}Pu$(p,3n)^{240}$Am reaction

The ^{242}Pu targets described in the previous section were irradiated in the Target a la Ghiorso (TAG) irradiation apparatus situated along the Cave 0 beam line of the Lawrence

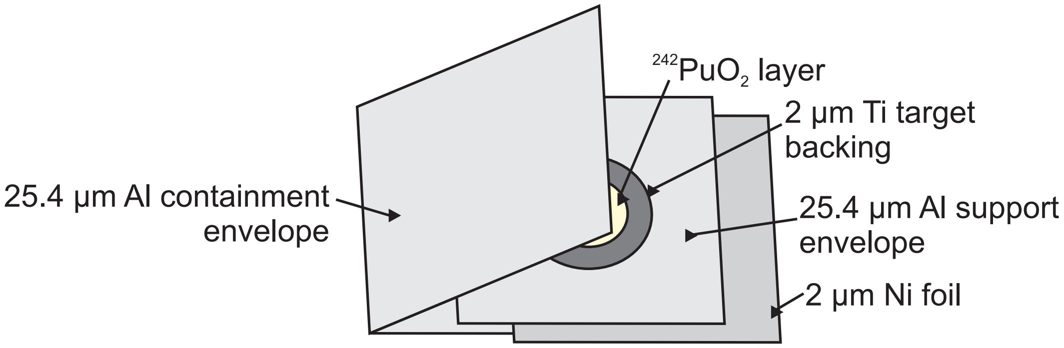

Figure 2.11 Diagram illustrating foil ordering in irradiation targets.

Berkeley National Laboratory's 88-Inch Cyclotron. The TAG irradiation apparatus is an electrically-isolated, water-cooled target holder and beam stop. An annotated photograph of the TAG apparatus is shown in Figure 2.12. Beam enters the figure from the right.

The targets were clamped to a water-cooled beam stop. This configuration of target holder allows for the irradiation of thin foil targets with microampere level beam doses without thermal damage to the targets. A plastic flange electrically isolated the beam stop from the beam line. An annular magnet circled the beam line just upstream from the beam stop to prevent electrons produced at the beam stop from traveling upstream of the plastic flange. This set up allowed for the direct measurement of the beam dose from the current coming from the beam stop. A beam collimator was situated just upstream of the electrically isolated section of the apparatus. This ceramic collimator was sectioned into four segments, each with its own BNC output. Current measurements on each collimator jaw were useful for beam diagnostics during irradiation.

The irradiation targets containing the ^{242}Pu, Ti, and Ni layers wrapped in aluminum containment envelopes were centered on TAG apparatus target holders fabricated from 6063 aluminum alloy. This aluminum alloy was used because of its relatively low level of impurities, leading to little activation resulting from the proton irradiation. The target was held in place using a 6.35-mm-thick clamp ring with a 4.76 mm diameter inner hole. The inner diameter of the clamp ring was designed to be smaller than the plutonium spot size so that the proton beam dose measured for the titanium and nickel foils would be identical to that irradiating the ^{242}Pu. A photograph of a target envelope centered on the TAG block is shown in the left side of Figure 2.13. On the right is a photograph of the assembled TAG target block.

It was also possible to fit the TAG apparatus with a phosphor-coated glass beam stop. This piece was made from 1.27-cm-thick borosilicate glass block which was coated with vacuum grease and covered with type F-65 yellow Rādelin phosphor from United States Radium Corporation. The center of the block was marked by a small carved cross hair on the outside of the block. Figure 2.14 shows the TAG apparatus with the phosphor-coated

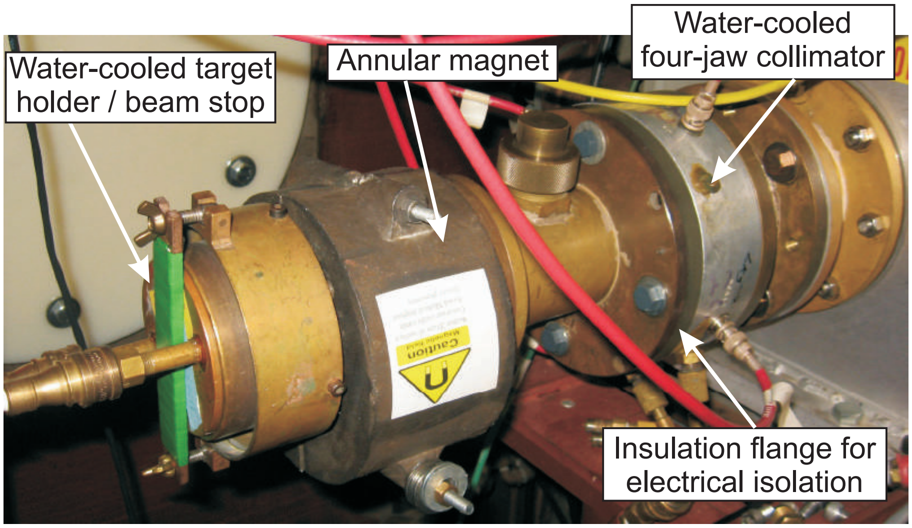

Figure 2.12 Annotated photograph of the TAG apparatus.

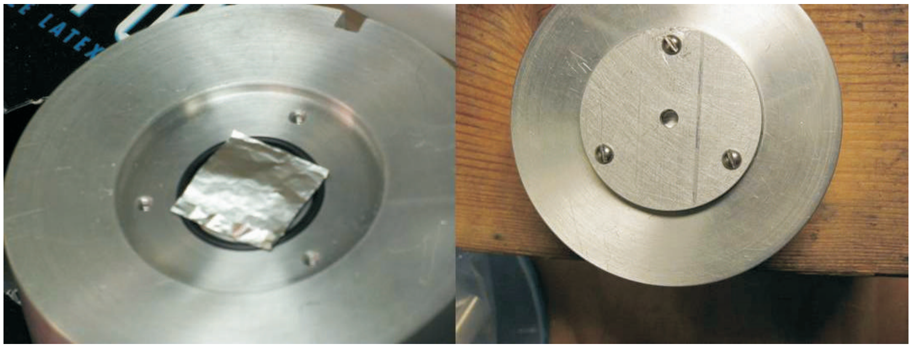

Figure 2.13 Photograph of open and sealed TAG target holder with target foil envelope.

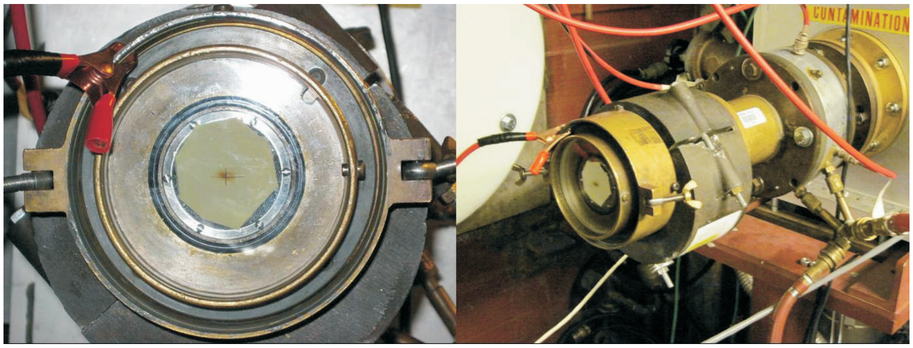

Figure 2.14 Photograph of the TAG tuning beam stop.

beam stop installed. The beam spot at the target position of the apparatus was visualized by the glowing phosphor powder. By placing a video camera focused on the beam spot behind the apparatus, the beam spot was visually tuned to be centered and focused using the upstream bending, switching, and quadrupole magnets. After tuning the ion optics, the glass beam stop was removed and replaced with a ^{242}Pu-target-loaded TAG beam stop for irradiation.

To ensure that the main cyclotron vacuum chamber would not become contaminated with ^{242}Pu target material in the event of a catastrophic target failure, a VAT, Inc. fast-closing shutter valve was installed in the beam line near the exit valve from the cyclotron. This valve would be triggered by a sudden jump in pressure detected by a sensor installed on the beam line near the ^{242}Pu target apparatus. The total time between the initial pressure sensing and the closure of the valve was 17 ms, which is fast enough to stop a room temperature ^{242}Pu atom traveling the 8.2 m from target to valve with velocity according to a one-dimensional Maxwell-Boltzmann distribution.

2.2.2 Measurement of proton irradiation dose

The proton dose delivered to the beam stop was measured in two independent ways. First, the proton dose was directly monitored during the irradiation. Direct current measurements were performed by connecting the TAG beam stop to a model 11X4160P-1 current integrator which was connected to a Canberra 1774 dual scaler. This current detection set up was calibrated by using a Keithley 264 current source to deliver a 1 microampere current to the TAG beam stop.

The second method for measuring the proton dose delivered to the ^{242}Pu targets is performed using titanium and nickel proton monitor foils. Because the proton-induced reaction cross sections for the $^{\mathrm{nat}}\mathrm{Ti}(p,x)^{48}\mathrm{V}$ and $^{\mathrm{nat}}\mathrm{Ni}(p,x)^{57}\mathrm{Ni}$ nuclear reactions have been extensively studied, coincidently irradiating well-characterized titanium and nickel foils with the

^{242}Pu allows for the calculation of the incident proton dose. Characterization of the nickel and titanium proton monitor foils is described in Section 2.1.3.

The IAEA Nuclear Data Services webpage contains a database compiling cross sections for such beam monitor reactions at `http://www-nds.iaea.org/medical` [IAE01]. This database reports recommended values for the $^{\mathrm{nat}}\mathrm{Ti}(p,x)^{48}\mathrm{V}$ and $^{\mathrm{nat}}\mathrm{Ni}(p,x)^{57}\mathrm{Ni}$ nuclear reactions from fitting a large number of selected experimental cross section measurements. The references, data selection criteria, and fitting procedures are described in an IAEA technical document [IAE01]. Unfortunately, this reference does not recommend uncertainties for the cross section values. Because the uncertainties associated with the characterization of foil thicknesses and the detection of the product radionuclides are relatively low, the uncertainty in the proton-monitor-foil measured proton dose is largely determined by these omitted uncertainties in the reaction cross sections. For this reason, it is desirable to have a rigorous and accurate way of characterizing the uncertainty associated with the proton monitor reaction cross sections. The method used for estimating these uncertainties is as follows.

Experimental values were collected from as many references as possible from those selected for use in the IAEA database [IAE01]. Several references that were included in the IAEA database were omitted from this analysis for several reasons. One reason for omission was if the cross section data were only reported as an excitation function plot which was not available in non-vector format image. A second reason for omission was if reaction cross sections were only reported for monoisotopic Ni or Ti. References were also omitted if they were cited from an especially elusive reference. Such hard-to-find references include foreign language PhD theses and other non-journal citations. Three additional references which were published since the IAEA database was compiled were also included in this analysis. Data were taken from a total of seven references for the $^{\mathrm{nat}}\mathrm{Ti}(p,x)^{48}\mathrm{V}$ nuclear reaction [KSM$^+$93, BMR$^+$95, MB80, STT$^+$01, TTSH02, ZAHA06, KKL$^+$09], and nine references for the $^{\mathrm{nat}}\mathrm{Ni}(p,x)^{57}\mathrm{Ni}$ nuclear reaction [BMR$^+$95, MWH78, MB80, SHS$^+$98, STT$^+$01, TTSH02, TSK91, KKL$^+$11, SMA07].

To get an estimate of the best fit cross section and its associated uncertainty for a given proton energy, the data collected above were locally fit with a linear regression weighted by the square of the cross section error of each point. The error in proton energy of each experimental point was ignored in this estimation. The linear regressions were centered about a proton energy of interest (E_0) over a range of ± 1 MeV according to the equation $y = m(x - E_0) + b$, where m and b are the fitting parameters. With this fitting formaism, the b fitting parameter and its fitting error can be interpreted as the best fit cross section and its associated uncertainty. Figure 2.15 shows the selected experimental data in black points and the localized linear regressions performed on these data as colored lines for four proton energies of interest for both the titanium (top) and nickel (bottom) proton monitor reactions.

The best fit cross sections and uncertainties obtained through these fits do not take into account the fact that there is an uncertainty in the proton beam energy delivered from

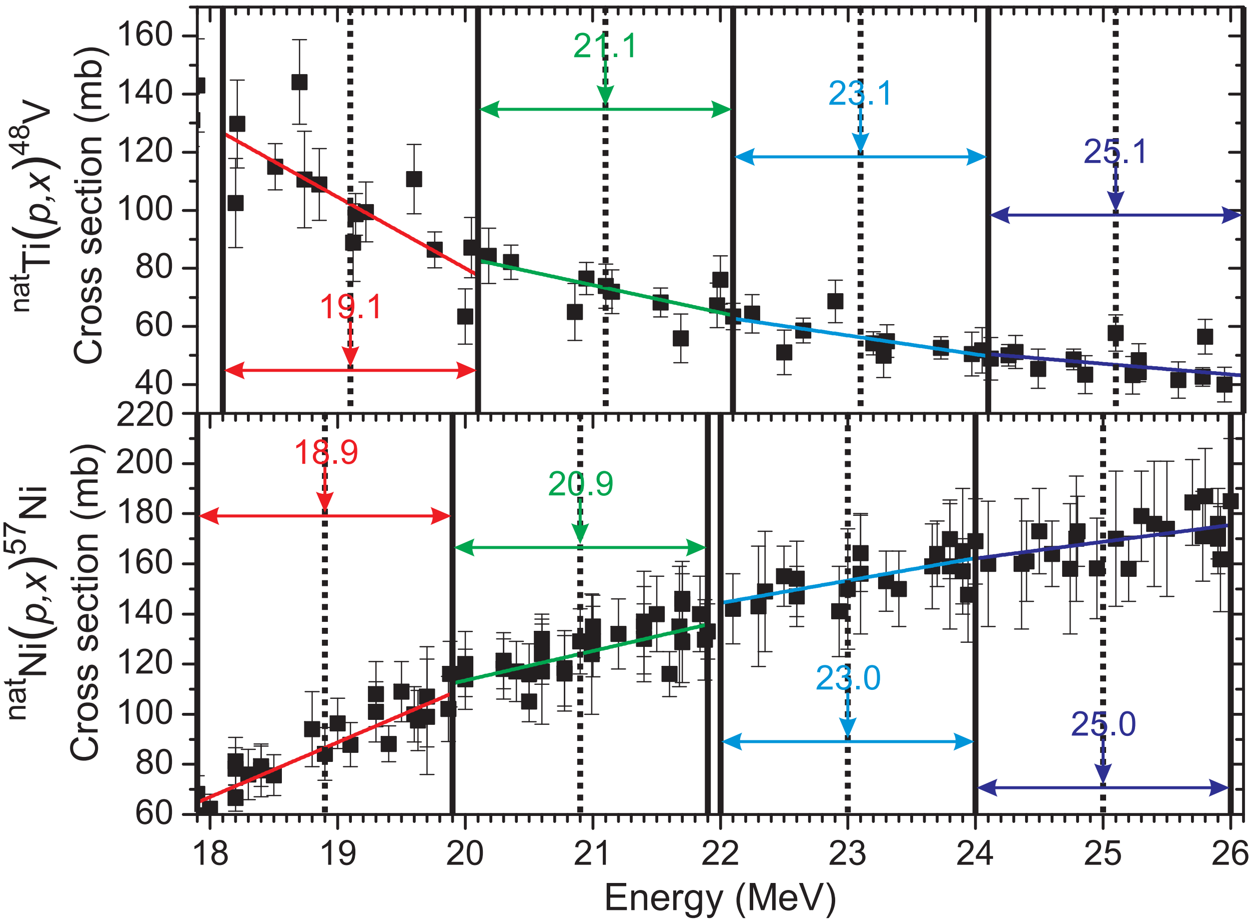

Figure 2.15 Selected experimental data and localized weighted linear fits of proton monitor reaction cross sections.

Table 2.4 Cross sections and associated uncertainties calculated for the $^{\mathrm{nat}}\mathrm{Ti}(p,x)^{48}\mathrm{V}$ and $^{\mathrm{nat}}\mathrm{Ni}(p,x)^{57}\mathrm{Ni}$ nuclear reactions.

Reaction	Proton energy (MeV)	IAEA recommended cross section (mb)	Localized weighted linear fit cross section (mb)
$^{\mathrm{nat}}\mathrm{Ti}(p,x)^{48}\mathrm{V}$	19.1 ± 0.3	104	102 ± 11
	21.1 ± 0.3	73	73 ± 5
	23.1 ± 0.3	56	56 ± 4
	25.1 ± 0.3	46	47 ± 3
$^{\mathrm{nat}}\mathrm{Ni}(p,x)^{57}\mathrm{Ni}$	18.9 ± 0.3	95	87 ± 11
	20.9 ± 0.3	131	124 ± 7
	23.0 ± 0.3	157	153 ± 6
	25.0 ± 0.3	176	169 ± 4

the 88-Inch Cyclotron. This uncertainty is estimated as being ~1.5% of the total beam energy. To account for this ± 0.3 MeV spread in the proton energy, the above discussed linear regression fits of experimental data were performed at $E_0 \pm 0.3$ MeV for each proton energy of interest. The best fit cross section uncertainties were then extracted from the upper/lower uncertainty limits at $E_0 \pm 0.3$ MeV.

The best fit cross sections and uncertainties for the proton beam energies of interest calculated from this procedure are shown in Table 2.4. This table also compares the recommended cross section values [IAE01], and cross sections from the localized weighted linear regression of selected experimental data. While these cross section are in good agreement for the $^{\mathrm{nat}}\mathrm{Ti}(p,x)^{48}\mathrm{V}$ reaction, the localized weighted linear fit cross sections are systematically lower than those the IAEA recommend for the $^{\mathrm{nat}}\mathrm{Ni}(p,x)^{57}\mathrm{Ni}$ reaction. This difference is due to the fact that there were more $^{\mathrm{nat}}\mathrm{Ni}(p,x)^{57}\mathrm{Ni}$ references used in the IAEA document which contained inaccessible cross section data. The cross section values reported in these inaccessible documents were on the whole systematically higher than the rest of the data.

It is worth noting that the uncertainties derived from the localized weighted linear regression analysis are underestimations because the regression does not take into account the error in proton energy of each of these points. This error is reported in nearly all of the selected data to be rather significant, on the order of 0.5 MeV.

2.3 Post-irradiation measurements of targets

The $^{242}\mathrm{Pu}$/Ni/Ti/Al-target-loaded TAG beam stops were irradiated with 0.2 – 1.5 microamperes of protons for 2 – 3.25 hours . The beam stops were allowed to cool for ~15 minutes until the radiation field was below 100 mrem/h at 30 cm, at which point they were

Table 2.5 Details of HP Ge gamma ray spectrometers used in this work.

Make	Model	Bias voltage (V)	Power supply	Amplifier	MCA
Ortec®	GEM 28185-P Pop Top config.	+3000	Ortec® 459	Ortec® 572	TRUMP™-PCI-8K
Oxford Inst.	Model 4011	+2000	Ortec® 459	Ortec® 572	TRUMP™-PCI-8K
Ortec®	GEM 55-P Pop Top config.	+3300	Ortec® DSPEC$^{\text{PLUS}}$™ 16K Channel digital signal processor		
Ortec®	GMX-20190 SL-GMX config.	-2500	Ortec® 459	Tennelec TC244	TRUMP™-PCI-8K

removed from the beam line. Once the radiation field from the face of the beam stop was below 50 mrem/h at 30 cm, the clamp ring and Al-enveloped target stack was removed. The irradiated foil stack was carefully disassembled and the foils individually packaged in a double layered thick plastic bag. Each foil stack was separated into three samples for gamma spectroscopy, one with the ^{242}Pu/Ti foil, one with the Ni foil, and one with the Al envelope and support foil.

2.3.1 Technical details of gamma ray spectrometers.

Details of HPGe gamma ray counters used are shown in Table 2.5. Ortec® GammaVision 32 software was used to control starting, stopping, saving, and clearing spectra taken with these spectrometers.

Calibration of gamma ray spectrometers

The energy and efficiency of the gamma detectors was calibrated using an Eckert & Ziegler Analytics radioactive point source containing ^{241}Am, ^{109}Cd, ^{57}Co, ^{139}Ce, ^{137}Cs, and ^{60}Co. The measured efficiencies and their uncertainties ($\mathrm{eff}_{\mathrm{Meas}} \pm \Delta\mathrm{eff}_{\mathrm{Meas}}$) were calculated and error propagated from the counting error and the uncertainties in the initial activities of the point source. These values were then fit to the equation

$$\mathrm{Eff}_{\mathrm{Best}}(E) = e^{b_1 \cdot E^1 + b_2 \cdot E^0 + b_3 \cdot E^{-1} + b_4 \cdot E^{-2} + b_5 \cdot E^{-3} + b_6 \cdot E^{-4}} \tag{2.8}$$

where $\mathrm{Eff}_{\mathrm{Best}}(E)$ is the best fit efficiency for detecting a gamma ray of energy E and b_1, b_2, b_3, b_4, b_5, and b_6 are fitting parameters. Because of strong covariance between these fitting parameters, it was not possible to calculate the uncertainty in best fit detector efficiency

($\Delta \mathrm{Eff}_{\mathrm{Best}}(\mathrm{E})$) from normal error propagation of the fit uncertainties of these six parameters. As a result, a method involving the generation of many simulated data sets was used to estimate this uncertainty.

The measured gamma ray efficiencies and their uncertainties ($\mathrm{eff}_{\mathrm{Meas}} \pm \Delta \mathrm{eff}_{\mathrm{Meas}}$) were fit to Equation 2.8 and the best fit parameters $[b_{1,\mathrm{best}}, b_{2,\mathrm{best}}, b_{3,\mathrm{best}}, b_{4,\mathrm{best}}, b_{5,\mathrm{best}}, b_{6,\mathrm{best}}]$ were used to calculate the best values for the efficiency at each gamma ray energy present in the gamma ray source ($\mathrm{Eff}_{\mathrm{Best}}(E_{\mathrm{source}})$). The uncertainties in these best efficiency values ($\Delta \mathrm{Eff}_{\mathrm{Best}}(E_{\mathrm{source}})$) was calculated by

$$\Delta \mathrm{Eff}_{\mathrm{Best}}(E_{\mathrm{source}}) = \Delta \mathrm{eff}_{\mathrm{Meas}}(E_{\mathrm{source}}) \left(\frac{\sqrt{\mathrm{Eff}_{\mathrm{Best}}(E_{\mathrm{source}})}}{\sqrt{\mathrm{eff}_{\mathrm{Meas}}(E_{\mathrm{source}})}} \right). \tag{2.9}$$

Simulated efficiency values ($\mathrm{eff}_{\mathrm{MeasSim}}$) were then randomly selected from gaussian distributions with center and deviation of $\mathrm{Eff}_{\mathrm{Fit}} \pm \Delta \mathrm{Eff}_{\mathrm{Fit}}$ for each gamma ray energy in the source. The uncertainty of the simulated efficiency values were calculated by

$$\Delta \mathrm{eff}_{\mathrm{MeasSim}}(E_{\mathrm{source}}) = \Delta \mathrm{Eff}_{\mathrm{Best}}(E_{\mathrm{source}}) \left(\frac{\sqrt{\mathrm{eff}_{\mathrm{MeasSim}}(E_{\mathrm{source}})}}{\sqrt{\mathrm{Eff}_{\mathrm{Best}}(E_{\mathrm{source}})}} \right). \tag{2.10}$$

The $\mathrm{eff}_{\mathrm{MeasSim}}(E_{\mathrm{source}}) \pm \Delta \mathrm{eff}_{\mathrm{MeasSim}}(E_{\mathrm{source}})$ values for each gamma ray energy in the source were then fit with Equation 2.8 to get best fitting parameters for the simulated data set.

This process of fitting simulated data sets generated from $\mathrm{Eff}_{\mathrm{Best}}(E_{\mathrm{source}}) \pm \Delta \mathrm{Eff}_{\mathrm{Best}}(E_{\mathrm{source}})$ was repeated 10,000 times, generating 10,000 sets of best fit parameters of simulated data. The uncertainty in the original best fit parameter ($\Delta \mathrm{Eff}_{\mathrm{Best}}(E_{\mathrm{interest}})$) was then determined for a specific γ-ray energy (E_{interest}) by looking at the distribution of best fit efficiencies generated from the 10,000 different sets of best fit parameters of simulated data sets at E_{interest}. The 68% confidence limits were calculated by integrating this distribution such that 15.9% of the distribution is above the upper efficiency confidence limit and 15.9% is below the lower efficiency confidence limit. To simplify the further propagation of these uncertainties, the larger of the two confidence limits was used to determine $\Delta \mathrm{Eff}_{\mathrm{Best}}(E_{\mathrm{interest}})$ when the confidence interval was asymmetric about $\mathrm{Eff}_{\mathrm{Best}}(E_{\mathrm{interest}})$. A representive plot showing measured gamma ray efficiencies and their uncertainties ($\mathrm{eff}_{\mathrm{Meas}} \pm \Delta \mathrm{eff}_{\mathrm{Meas}}$, squares), as well as the best fit curve and its calculated uncertainty ($\mathrm{Eff}_{\mathrm{Best}}(E) \pm \Delta \mathrm{Eff}_{\mathrm{Best}}(E)$, solid and dotted curves) is shown in Figure 2.16.

Gamma counting procedure of irradiated foils

After irradiation and disassembly, the irradiated ^{242}Pu/Ti foils, Ni foils, and Al foils were counted in the HPGe gamma ray spectrometers. Each foil was counted for a period of several hours, with a Microsoft Windows .job file controlling the starting, stopping, saving, and clearing of the spectra to record many 5 or 10 minute spectra. At the end of this counting

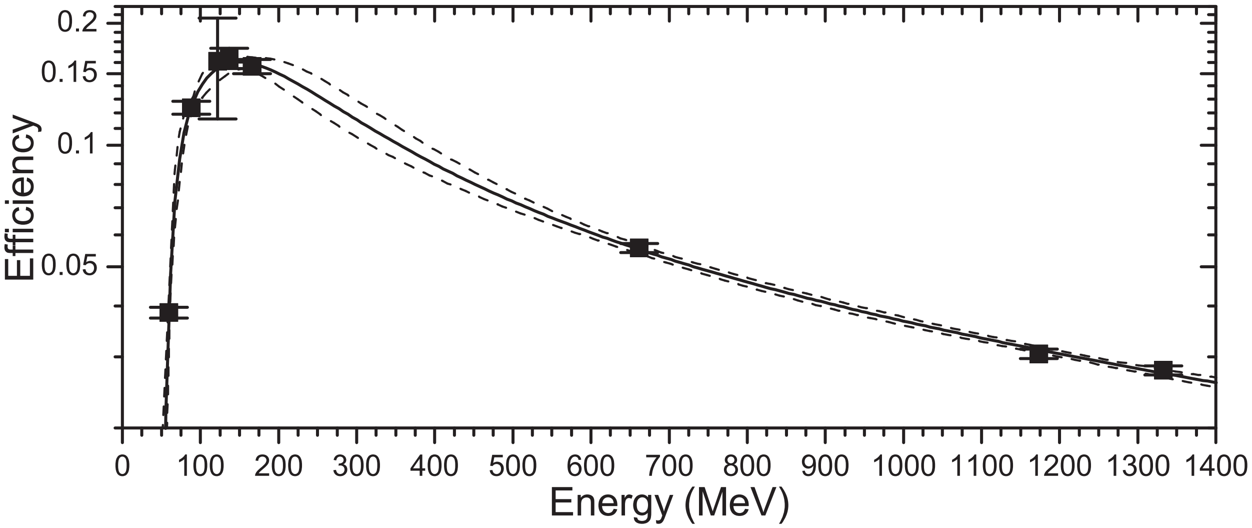

Figure 2.16 Representive plot of measured (square points), best fit (solid line), and confidence intervals (dashed lines) of γ-ray efficiency curve as a function of γ-ray energy.

period, the foils were removed and a different set of foils were counted in the same way. The irradiated foils were counted for a month with continual 5 or 10 minute spectra taken of the periodically exchanged foils.

2.3.2 Analysis of gamma spectra

HPGe gamma ray spectra of all proton-irradiated foils were initially analyzed using Ortec® GammaVision software. Multiple subsequent 5 or 10 minute spectra were summed together to obtain peaks with high counting statistics for identification. A characteristic gamma spectrum obtained from summing 4 hours of measurements 34 hours after irradiation of the ^{242}Pu on a ∼2 μm Ti foil target is shown in Figure 2.17. Peaks from ^{240}Am, the beam monitor reaction product ^{48}V, and other proton-induced reactions on Ti products, ^{44}Sc, ^{46}Sc, and ^{48}Sc are noted. The proton-irradiated Pu/Ti foils also contained peaks from proton-induced ^{242}Pu-fission products and ^{47}Sc. The nickel beam monitor reaction product ^{57}Ni dominated the spectra of irradiated Ni foils, but proton-induced ^{242}Pu-fission products, ^{55,56}Ni, and ^{55,56}Co were also present. The aluminum catcher foils contained proton-induced ^{242}Pu-fission products, ^{57}Ni, ^{55,57}Co, ^{47}Sc, and ^{48}V.

The radionuclides of interest, their half-lives, the energy and intensity of photons used for their identification, and their role in the analysis is summarized in Table 2.6 for all peaks which underwent decay curve analysis. To extract the EoB activity of ^{240}Am, ^{48}V, and ^{57}Ni from the thousands of gamma spectra, the following decay curve analysis procedure was

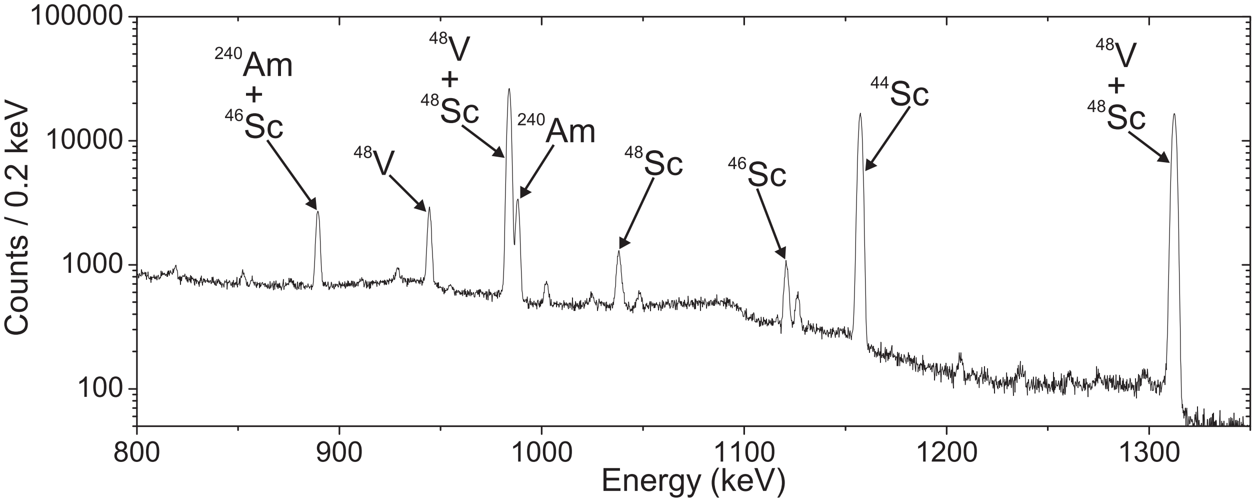

Figure 2.17 Gamma spectrum of proton-irradiated ^{242}Pu on ~2 μm Ti foil.

Table 2.6 Summary of radionuclides which underwent decay curve analysis.

Nuclide	Half-life (h)	E_γ (keV)	I_γ (%)	Role in analysis
^{240}Am	50.8*(3)*	888.80*(5)*	25.1*(4)*	Measurand
^{48}V	15.9735*(25)*	1312.086*(6)*	97.5*(8)*	Proton monitor reaction product
^{57}Ni	35.60*(6)*	1377.63*(3)*	81.7*(16)*	Proton monitor reaction product
^{46}Sc	2011*(1)*	1120.545*(4)*	99.987*(1)*	E_γ = 889.277*(3)*, I_γ = 99.984*(1)*% peak coenergetic with ^{240}Am ROI
^{48}Sc	43.67*(9)*	1037.599*(26)*	97.6*(5)*	E_γ = 1312.096*(6)*, I_γ = 100.1*(5)*% peak coenergetic with ^{48}V ROI

followed.

The net number of counts in a peak of interest was determined through the analysis of a region of interest (ROI) which was defined to encompass the peak and three channels of background on both ends. The size of the ROI was determined for a specific detector/source combination through examination of the high statistics summed spectra. The ROI was broken into three sections: the edge background, the peak background, and the net peak area, as shown in Figure 2.18. The average background counts per channel were calculated by averaging the number of counts in the edge background channels. The average background counts per channel was then used to calculate and subtract the peak background from the gross peak to determine the net peak number of counts. The error in the number of counts from any simple spectrum integration in radioactive decay counting experiments is equal to

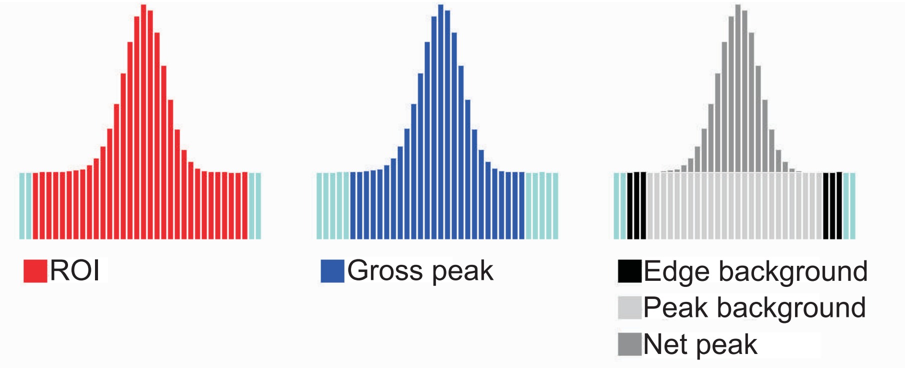

Figure 2.18 Diagram of sections used to determine the net peak area of gamma spectra.

the square root of the number of counts. The error in the net peak number of counts was determined by propagating the error in the gross peak number of counts and from the edge background number of counts.

The decay curve of each radionuclide of interest was fit using the net peak area (N_i) for each of i 5- or 10-minute spectra, the time since the end of bombardment at the beginning of each spectrum (t_i), and the gamma detector live time (τ_i) from each spectrum. The third column in Table 2.6 details which gamma peak was fit for each radionuclide. For the nuclides which exhibited a single exponential decay of their peak of interest (^{57}Ni, ^{48}Sc, and ^{46}Sc), the net peak area from each file was fit to the function

$$N_{fit,i} = \int_{t_i}^{t_i+\tau_i} a_0 e^{-\lambda t'}\, dt' = \frac{a_0}{\lambda} e^{-\lambda t_i}\left(1 - e^{-\lambda \tau_i}\right), \tag{2.11}$$

where λ, the decay constant for the radionuclide and a_0, the expected EoB ($t = 0$) instrument-detected counts per second, were the fitting parameters. The EoB radionuclide activity (A_0) was calculated by

$$a_0 = I_\gamma \epsilon A_0, \tag{2.12}$$

where I_γ is the intensity of the particular gamma emission and ϵ is the gamma detector efficiency at that specific gamma ray energy. Because the half-life of ^{46}Sc is long compared to the length of time the foils were counted, difficulties arose when fitting these data to Equation 2.11. For this nuclide, the net peak areas were divided by the live time of the files and fit to $\frac{N_{exp}}{\tau} = a_0(1 - \lambda t)$, the first order expansion of the decay function.

Equation 2.11 was fit to data by varying a_0 and λ and minimizing the sum of square residuals, defined as

$$\chi^2 = \sum \frac{(N_i - N_{fit})^2}{\sigma_i^2}. \tag{2.13}$$

Minimization was done using a Levenberg-Marquardt algorithm as executed using the Python programming language `leastsq` fuction.

Uncertainty in the fit parameters a_0 and λ was calculated by varying one fit parameter of interest from its least squares value in small steps while keeping all other parameters constant. At each step, χ^2 was minimized by varying the parameters other than the parameter of interest. The quantity "delta chi-squared" was calculated for each step to be $\Delta\chi^2 = \chi^2_{step} - \chi^2_{min}$. The two one-sided 1σ confidence limit for the parameter of interest are defined when $\Delta\chi^2 = 1$. To simplify error propagation, the uncertainty interval was defined as twice the average of the two one-sided 1σ confidence limit.

The ^{240}Am peak at 888.80*(5)* keV and ^{48}V peak at 1312.086*(6)* keV are coenergetic with the ^{46}Sc peak at 889.277*(3)* keV and the ^{48}Sc peak at 1312.096*(6)* keV, respectively. Thus, the decay curve fit directly to the net peak areas from these peaks exhibits a double exponential decay. Instead of directly fitting the net peak areas to a double exponential function, the total EoB activity (A_0) was determined for ^{46}Sc and ^{48}Sc according to the previously described procedures. Using these A_0 values and Equation 2.12 to calculate a_0 for the 889.277*(3)* keV and 1312.096*(6)* keV peaks, Equation 2.11 was then used to calculate the expected number of counts in each ^{240}Am and ^{48}V peak due to ^{46}Sc and ^{48}Sc, respectively. By subtracting these values from the ^{240}Am and ^{48}V net peak areas in a peak-wise, file-wise manner, the total net peak areas due to ^{240}Am and ^{48}V can be extracted for each file. These subtracted net peak areas were then fit according to the above described method for fitting single exponential decays.

Figure 2.19 shows representative best fit curves for a) ^{240}Am, (b) ^{48}V, and (c) ^{57}Ni. The experimental net number of counts per file are shown as black squares. The best fit curve is shown in red. The decay of ^{48}V appears to be non-exponential, in part because the isotope's long half-life ($t_{1/2} \approx 16$ days), and in part because the dead time of the detector was appreciably changing during the measurements taken (0.2 – 0.4) $\times 10^6$ seconds after EoB. Thus, the smaller detector live times at these early times result in a depression in the number of counts. Because the experimental data are fit using Equation 2.11 which takes the detector live time of each file into account, the curve fits the data properly. The decay curve of ^{57}Ni shows a discontinuous jump at about 1 $\times 10^6$ s after EoB because the length of the gamma counting files was changed from 5 minutes per file to 10 minutes per file. Again, Equation 2.11 allows for the proper fitting of the data.

2.4 Results and discussion of ^{242}Pu irradiations

The decay curve analysis described in the previous section was performed on the five proton-irradiated ^{242}Pu/$^{\mathrm{nat}}$Ti foils, $^{\mathrm{nat}}$Ni foils, and Al catcher foils. The EoB activities (A_{EoB}) for ^{48}V and ^{57}Ni are calculated by summing the decay fit values from coincidently irradiated Ti/Ni and Al foils. Data pertaining to the Ti and Ni proton monitor foils for

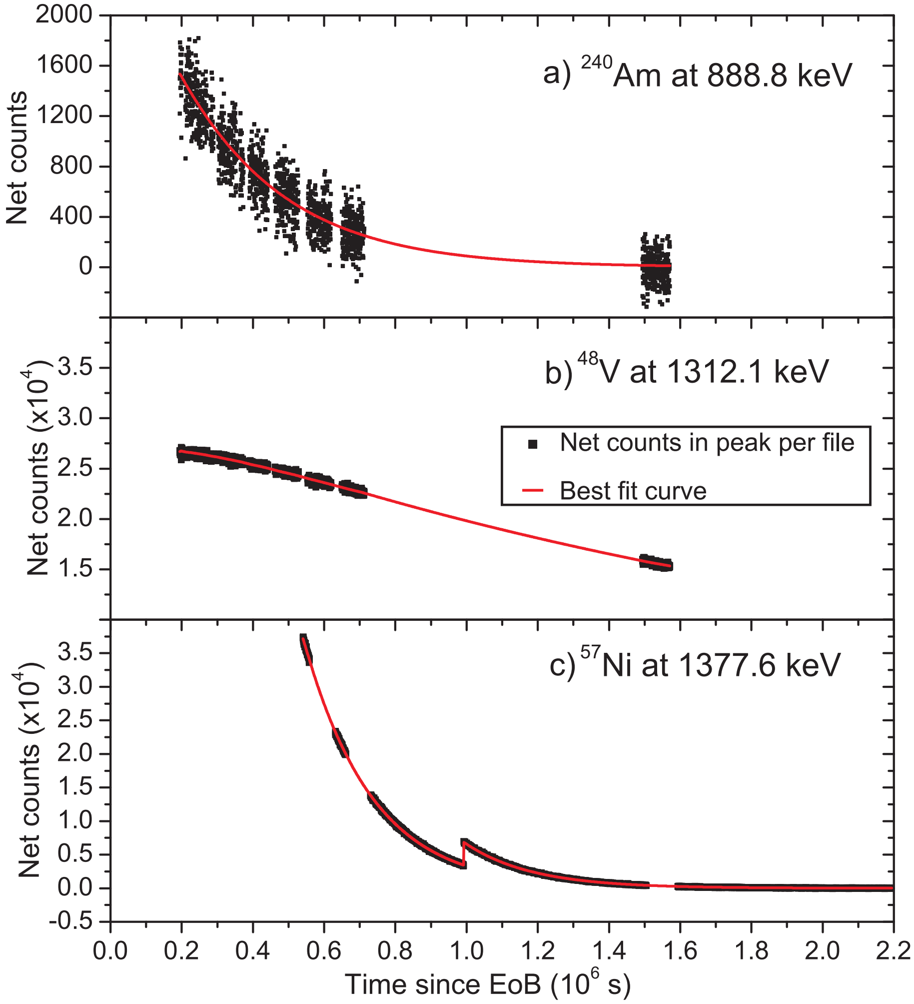

Figure 2.19 Representative best fit curves for background- and $^{46/48}$Sc-subtracted net ^{240}Am, ^{48}V, and ^{57}Ni peaks

Table 2.7 Summary of decay curve analysis results from irradiated proton monitor foils.

Proton monitor reaction	Foil thickness (μg/cm^2)	Proton energy (MeV)	Best fit A_{EoB} (Bq)	Best fit $t_{1/2}$ (h)
$^{\mathrm{nat}}$Ti$(p,xn)^{48}$V	1000 ± 200	19.1 ± 0.3	$(5.50 \pm 0.32)\times 10^3$	401 ± 2
	1000 ± 200	21.1 ± 0.3	$(1.10 \pm 0.16)\times 10^4$	383 ± 1
	1000 ± 200	23.1 ± 0.3	$(4.33 \pm 0.50)\times 10^4$	412 ± 2
	1000 ± 200	23.1 ± 0.3	$(9.63 \pm 0.22)\times 10^3$	400.2 ± 0.5
	1000 ± 200	25.1 ± 0.3	$(8.50 \pm 0.19)\times 10^3$	394.3 ± 0.3
$^{\mathrm{nat}}$Ni$(p,x)^{57}$Ni	1830 ± 50	18.9 ± 0.3	$(9.76 \pm 0.33)\times 10^4$	35.83 ± 0.01
	1580 ± 50	20.9 ± 0.3	$(3.52 \pm 0.12)\times 10^5$	35.78 ± 0.01
	1620 ± 50	23.0 ± 0.3	$(1.455 \pm 0.049)\times 10^6$	35.72 ± 0.01
	1570 ± 50	23.0 ± 0.3	$(3.51 \pm 0.12)\times 10^5$	35.79 ± 0.01
	1580 ± 50	25.0 ± 0.3	$(4.07 \pm 0.13)\times 10^5$	35.79 ± 0.01

each of the five irradiations are shown in Table 2.7. This data includes the proton monitor foil thickness (from characterization discussed in Section 2.1.3), the energy at which the foil was bombarded, the EoB activities, and the best fit ^{48}V/^{57}Ni half-life from the decay curve analysis ($t_{1/2}$). The measured ^{48}V half-lives widely vary and are generally larger than the literature value of 383.36 ± 0.06 h [Bur06]. This is likely due to the presence of background from the numerous ^{242}Pu(p,f) products, that was unable to be distinguished or subtracted. The decay of the ^{48}V peak was fit with linear combinations of exponential decays, but a better fit was unobtainable. The measured ^{57}Ni half-lives agree well with one another, but are systematically larger than the literature value of 35.60 ± 0.06 h [Bha98] by about 0.5%. These disagreements are likely as a result of systematic uncertainties not quantified in the present analysis. The effect of these half-life discrepancies on the measured A_{EoB} values is small compared to other sources of error in the determination of $\sigma_{^{242}\mathrm{Pu}(p,3n)^{240}\mathrm{Am}}$.

The best fit EoB activities (A_{EoB}) for ^{57}Ni and ^{48}V can be used along with the localized weighted linear fit proton monitor reaction cross sections detailed in Table 2.4 and Equation 2.3 to calculate the total proton dose the target received. The proton dose calculated from the Ti and Ni beam monitor foils agree within error bars with the exception of one irradiation. It is most likely that this disagreement is due to a bad estimation of the Ti foil thickness, as this was not explicitly measured for each foil (see Section 2.1.3 for details). Because the Ni foil thickness was measured for each individual foil and there was less background in the Ni foils' gamma spectra, the proton dose from Ni has a smaller error and is more accurate. This proton dose is used along with the ^{242}Pu target thicknesses reported in Table 2.3, the best fit A_{EoB} for ^{240}Am, and Equation 2.4 to calculate the ^{242}Pu$(p,3n)^{240}$Am reaction cross section. The data and results of this calculation are summarized in Table 2.8.

The measured ^{242}Pu$(p,3n)^{240}$Am excitation function (red ×s) is shown compared to pre-

Table 2.8 Summary of decay curve analysis results from irradiated ^{242}Pu.

Proton energy (MeV)	^{242}Pu thickn. (μg/cm^2)	Best fit A_{EoB} (Bq)	Best fit $t_{1/2}$ (h)	Ni proton dose (μA)	Ti proton dose (μA)	$\sigma_{^{240}Am}$ (mb)
19.1 ± 0.3	$140. \pm 42$	518 ± 74	52 ± 2	0.25 ± 0.01	0.19 ± 0.04	35 ± 12
21.1 ± 0.3	242 ± 55	2701 ± 98	48.1 ± 0.4	0.74 ± 0.04	0.6 ± 0.1	36.3 ± 8.5
23.1 ± 0.3	480 ± 130	21800 ± 1000	50.7 ± 0.3	1.50 ± 0.07	1.7 ± 0.3	45 ± 13
23.1 ± 0.3	185 ± 49	$1550. \pm 57$	50.1 ± 0.6	0.60 ± 0.03	0.6 ± 0.1	33.5 ± 9.0
25.1 ± 0.3	208 ± 48	2071 ± 73	52.6 ± 0.7	0.62 ± 0.03	0.6 ± 0.1	38.2 ± 9.1

dicted excitation functions from JORPL [Alo74] (green triangles) and CEM03.02 [MGS$^+$05, MPG06] (black squares) in Figure 2.20. The measured cross section values are lower than predicted by nearly an order of magnitude. However, with the measured 30 – 50 mb cross section, the reaction remains the most promising nuclear reaction for the production of a ^{240}Am(n,f) target, when compared with all other experimentally validated nuclear reactions (see Table 1.2).

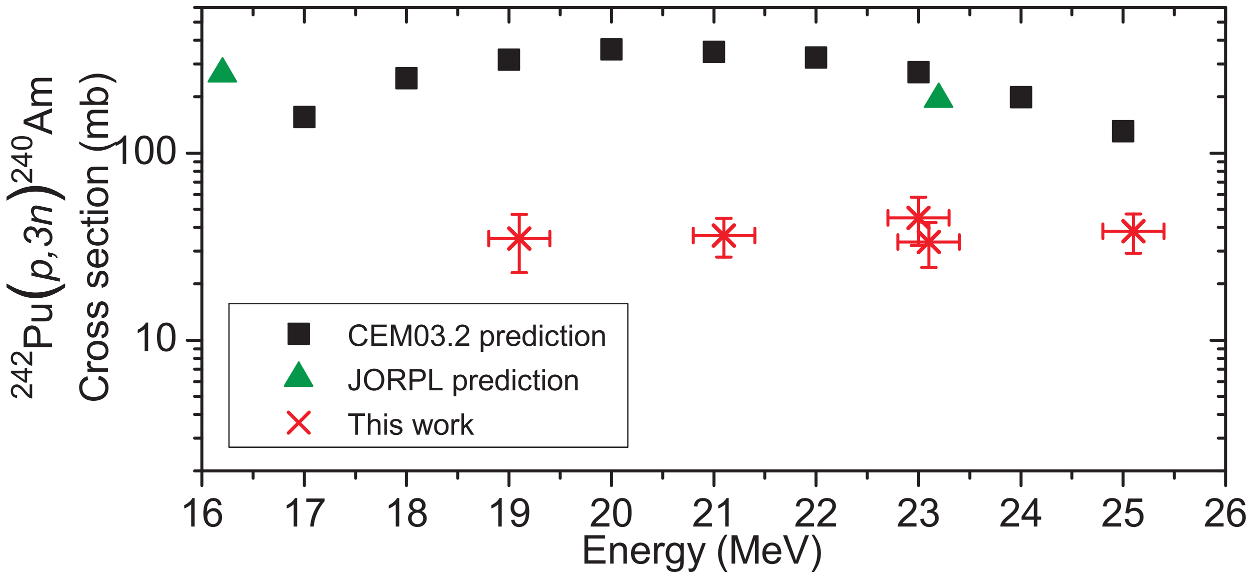

Figure 2.20 Predicted and measured excitation functions for the $^{242}\text{Pu}(p,3n)^{240}\text{Am}$ reaction.

Chapter 3

Development of a Chemical Isolation Procedure for ^{240}Am from Proton-Irradiated ^{242}Pu

In the following chapter, the characteristics of a suitable chemical procedure for producing purified ^{240}Am LSDS target material from proton-irradiated ^{242}Pu are discussed. A proposed separation procedure is described and tested on the tracer-scale with plutonium, americium, and model fission products. Several issues related to the scaling up of the separation procedure for producing a LSDS ^{240}Am(n, f) target are discussed.

3.1 Characteristics of a suitable separation procedure

As discussed in Section 1.3, a successful neutron-induced fission cross section measurement at the LANSCE-coupled LSDS requires at least 20 nanograms of ^{240}Am target material. Assuming a 40 millibarn ^{242}Pu$(p, 3n)^{240}$Am reaction cross section, then irradiating ∼0.5 grams of ^{242}Pu with a 5 microampere proton beam for 3 days will produce about 100 nanograms of ^{240}Am. Because of this fact and the isotope's 50.8 hour half-life, two key characteristics of a chemical procedure for isolating ^{240}Am from proton-irradiated ^{242}Pu will be speed and efficiency. The separation procedure was designed to be completed in one long (8 – 12 hour) work day to minimize losses of ^{240}Am due to radioactive decay. Also, attention has been paid to maximizing the overall americium yield through the procedure.

A third key characteristic of the chemical isolation procedure is the necessity of a very large Am/Pu separation factor. This factor is defined as

$$SF_{\mathrm{Pu/Am}} = \frac{m_{\mathrm{after,Am}} / m_{\mathrm{before,Am}}}{m_{\mathrm{after,Pu}} / m_{\mathrm{before,Pu}}}, \tag{3.1}$$

where $m_{\text{before/after,Am/Pu}}$ is the mass of Am or Pu, which is present in the sample before or after the separation procedure. To benefit the signal to noise ratio in the neutron-induced fission measurement, it is desirable to produce a target containing ten times as much ^{240}Am as ^{242}Pu. Thus a procedure with an Am/Pu separation factor on the order of $10^7 - 10^8$ is necessary to isolate the small amount of ^{240}Am from the bulk ^{242}Pu. Such a large separation factor necessitates the use of several successive steps, each maximized for Am/Pu separation.

A further complication that must be considered when developing an isolation procedure is the separation of ^{240}Am from secondary nuclear reaction products. The most prevalent secondary nuclear reaction that occurs during the proton-bombardment of ^{242}Pu is its proton-induced fission. The products of the proton-induced fission of ^{242}Pu were measured by Ohtsuki *et al.* [ONT$^+$91]. Like all actinide fission products, they are composed of neutron-rich radioactive isotopes with $Z = 36 - 62$. According to a calculation of the dose emitted by these fission products outlined in Section 3.4, the highest dose emitting products are ^{132,133,135}I, ^{97}Zr/Nb, ^{99}Mo, ^{126,129}Sb, ^{140}La, and ^{143}Ce. Because these elements have relatively low Z, they will not cause significant background in the neutron-induced fission measurement of ^{240}Am. They will, however, have a significant radiation dose field, which may pose a health and safety hazard during the handling and processing of proton-irradiated ^{242}Pu. Thus, the effective removal of these high dose fission products is a fourth key characteristic of the ^{240}Am isolation procedure. The very high radiation fields expected from the proton-irradiated ^{242}Pu also define a fifth key characteristic of the ^{240}Am isolation procedure. The procedure must be simple enough that it can be performed in a heavily shielded location such as a lead-lined glovebox or remote manipulator hot cell.

To summarize, the key characteristics of a suitable isolation procedure for producing a ^{240}Am neutron-induced fission target from proton-irradiated ^{242}Pu are as follows.

- Completable within one long (8 – 12 hour) work day
- High americium yield
- Am/Pu separation factor on the order of $10^7 - 10^8$
- Effectively remove high radiation-dose-emitting proton-induced fission products
- Simple enough to be possible under shielded or remote conditions

3.2 Radiochemical separation techniques

The chemistry of plutonium has been studied extensively since the discovery of the element in 1941 [Col65, RCW86]. This is due in large part because of its extremely rich and complicated chemistry. In aqueous solutions, Pu can be found in a total of five oxidation states (III, IV, V, VI, and VII), with the upper three oxidation states present as the plutonyl moiety ($\mathrm{Pu^{V}O_2^{+}}$,$\mathrm{Pu^{VI}O_2^{2+}}$, and $\mathrm{Pu^{VII}O_2^{3+}}$). Under some conditions, up to four of these oxidation states (III, IV, V, and VI) can coexist in solution. The chemical behavior of Pu in solution is closely tied with its oxidation state. Under highly acidic conditions, Pu is predominantly in the $\mathrm{Pu^{IV}}$ and $\mathrm{Pu^{VI}O_2^{2+}}$ oxidation states. If the acid has a complexing counter-ion such as $\mathrm{Cl^-}$ or $\mathrm{NO_3^-}$, then these Pu ions will form anionic complexes such as $\mathrm{Pu^{IV}Cl_6^{2-}}$ or $\mathrm{Pu^{VI}O_2(NO_3)_4^{2-}}$. However, under similar strongly acid conditions, the trivalent Pu oxidation state, which can be formed using a strong reducing agent such as hydroiodic acid or hydroquinone, will not form such anionic complexes.

The chemistry of Am has also been extensively studied, but is significantly less complex [PK60]. Because of its higher effective nuclear charge, the 5f electrons of Am are more contracted and participate less in chemical binding when compared with Pu. Thus, while Am has been observed to take upon higher (IV, V, VI) oxidation states, it is predominantly present in aqueous solutions as $\mathrm{Am^{III}}$. Like the $\mathrm{Pu^{III}}$ ion, $\mathrm{Am^{III}}$ does not form anionic complexes with $\mathrm{NO_3^-}$ or $\mathrm{Cl^-}$ in acidic solutions.

Methods for the separation of plutonium from other actinides (including americium) in spent nuclear fuel have been well studied [Col65, PK60, RCW86]. Many of these same techniques are very suitable as steps in an isolation procedure for ^{240}Am from proton-irradiated plutonium. The following sections elaborate upon several separation methods which were considered for inclusion in the separation procedure, including anion exchange chromatography, solvent extraction, and extraction chromatography.

3.2.1 Anion exchange chromatography

Anion exchange chromatography is a traditional method used for the purification of plutonium from ^{241}Am, which builds up in plutonium samples through the β^--decay of ^{241}Pu [Col65, PK60]. The separation is based on different oxidation state and complexation chemistries of plutonium and americium. In 10 – 12 M HCl or 8 M $\mathrm{HNO_3}$ solutions, the prevalent $\mathrm{Pu^{IV}}$ oxidation state rapidly forms anionic complexes such as $\mathrm{[PuCl_6]^{2-}}$ or $\mathrm{[Pu(NO_3)_6]^{2-}}$, respectively, while $\mathrm{Am^{III}}$ does not. When such a solution is applied to a column containing anion exchange resin, such as Dowex 1 or Bio-Rad® AG 1, the negatively-charged plutonium complexes adsorb to the resin while americium flows through the column bed with the eluent. Later, plutonium is easily recovered by its reduction to $\mathrm{Pu^{III}}$ or through the addition of a low concentration (0.35 M) acid solution, which results in a shifting of the Pu complexation equilibrium away from the anionic complexes. The anion exchange behavior for many other elements in hydrochloric and nitric acids has also been extensively studied [KN56, FB64]. A disadvantage of this method is the fact that the exchange resin has a limited number of sites for the absorption of plutonium, making it cumbersome to scale the process for large amounts of plutonium.

3.2.2 Solvent extraction

Solvent extraction is another traditional method for actinide separation. It has found extensive application on the industrial scale in the reprocessing of spent nuclear fuel (*e.g.* PUREX process). It is based on the fact that the anionic complexes which $\mathrm{Pu^{IV}}$ and $\mathrm{Pu^{VI}}$ form in aqueous nitric acid solutions are selectively extracted by organophosphorus extractants such as tributyl phosphate (TBP) [Bur58] or β-diketones such as 2-thenoyl trifluoro acetone (2-TTA) [CM56], while $\mathrm{Am^{III}}$ is not. After its separation from americium, the plutonium can be stripped from the organic phase by its reduction to $\mathrm{Pu^{III}}$.

Solvent extraction can also be used for the purification of americium from fission products. It is known that actinides form stronger complexes with ligands containing nitrogen and sulfur atoms than do lanthanides. For example, in a system consisting of di-(2-ethylhexyl)phosphoric acid (HDEHP) in decane and diethylenetriaminepentaacetic acid (DTPA) in lactic acid, lanthanides are selectively extracted into the organic phase [KY78]. Recently, in the context of actinide partitioning research, new extraction systems have been developed for the separation of minor actinides (Np, Am, Cm) from lanthanides [GHM+06]. It has been shown that actinides are rapidly and selectively extracted from 1 M HNO_3 by a mixture of a bis-triazin-bispyridine extractant and a malonamide phase transfer reagent. Americium is then back-extracted using a buffered glycolate solution.

In general, solvent extraction is a versatile method and easy to scale up to large amounts of radionuclides. However, solvent extraction also has the disadvantages that it is more labor intensive and generates significant amounts of hazardous/radioactive liquid waste.

3.2.3 Extraction chromotography

A third, more recently developed method for separating actinides and fission products is extraction chromatography [BG74]. This technique combines the versatility and selectivity of solvent extraction with the experimental form factor of anion exchange chromatography. Extraction chromatography resins are composed of macroporous, aliphatic polymer or silica beads. Liquid extractants are present inside the pores of this inert support and serve as the stationary phase for the chromatography. The mobile phase is typically aqueous acid solutions, sometimes containing complexing agents.

Extraction chromatography resins well suited for Am/Pu/FP separations are commercially available from Eichrom Technologies, Inc. These resins are composed of an Amberchrom CG71ms polymer bead support impregnated with a liquid extractant. Two resins that offer high Am/Pu separation factors are the TEVA® resin and the TRU® resin. The TEVA® resin utilizes the aliphatic quaternary amine, tricaprylmethylammonium chloride, or Aliquat·336, extractant [HDC+95] and the TRU® resin utilizes carbamoylphosphine oxide (CMPO) dissolved in TBP [HCD+93]. Like a traditional anion exchange resin, both of these resins bind strongly to anionic Pu complexes present in moderate to concentrated HCl or

HNO_3 solutions. Because americium does not form anionic complexes in acids, it sorbs very weakly to the resin. The TEVA resin exhibits exceptionally low sorption of Am, making it ideal when high americium yield is necessary.

Extraction chromatography can also be used to isolate americium from trivalent lanthanides. Aliquat·336 has been shown to selectively extract americium from lanthanides in the presence of thiocyanate ions (SCN^-) [Moo64]. This is due to the fact that SCN^- ions will selectively form Aliquat·336-extractable complexes with Am because of its larger, more diffuse 5f valence orbitals. This chemistry has been adopted to an extraction chromatographic procedure involving the TEVA® resin loaded with 1 M NH_4SCN and 0.1 M HCOOH by Horwitz [HDC+95]. Under these conditions, americium is sorbed to the column and trivalent lanthanides are selectively eluted. The americium is eluted with the addition of 0.25 M HCl, by shifting the Am^{III} complexation equilibrium away from the SCN^- complexes.

Extraction chromatography is a very versatile technique and yields very high separation factors in the isolation of americium from plutonium. However, its capacity for plutonium is even smaller than anion exchange chromatography, making it ill-suited for the processing of plutonium on the gram-scale.

3.2.4 Proposed Am/Pu/FP separation procedure

A schematic of the proposed separation procedure for isolating ^{240}Am from proton-irradiated ^{242}Pu is shown as Figure 3.1. The procedure starts with the dissolution of the irradiated plutonium oxide powder. Traditionally, the most effective conditions for the dissolution of PuO_2 are 4 – 12 M HNO_3 in the presence of a small concentration (0.02 M) of fluoride ion for complexation [Bar77]. The solution will then be evaporated to dryness to remove volatile fission products such as iodine and xenon, as well as to allow for the re-dissolution of the nitrate salt in a solution appropriate for the following separation procedure.

The first two steps of this procedure involve anion exchange columns utilizing a high capacity, highly cross-linked, strong base, anion exchange resin such as Dowex™1x8 or Bio-Rad AG®1x8. The Bio-Rad AG®1x8, 100 - 200 mesh used is composed of quaternary ammonium ion exchange sites functionalized to a polymer support of divinylbenzene cross-linked with styrene. An 8% cross-linked resin was chosen because of its higher capacity for ions and tendancy to expand and shrink less upon the addition of different elution solutions as compared to lower cross-linked resins. These advantages are balanced by a higher cross-linked resin's tendency to have smaller pore sizes and therefore slower exchange kinetics. A resin mesh of 100 – 200 was used, giving bead diameters of 75 – 150 μm. According to Bio-Rad documentation, the resin has a minimum wet capacity of 1.2 milliequivalents/mL. These first two anion exchange steps can be performed by loading the Pu/Am solution in, and eluting the Am with, either 8 M HNO_3 or 10 M HCl. The hydrochloric acid has the advantage that it is more effective than nitric acid at forming anionic complexes with the high dose fission product elements, resulting in more effective isolation of Am from these

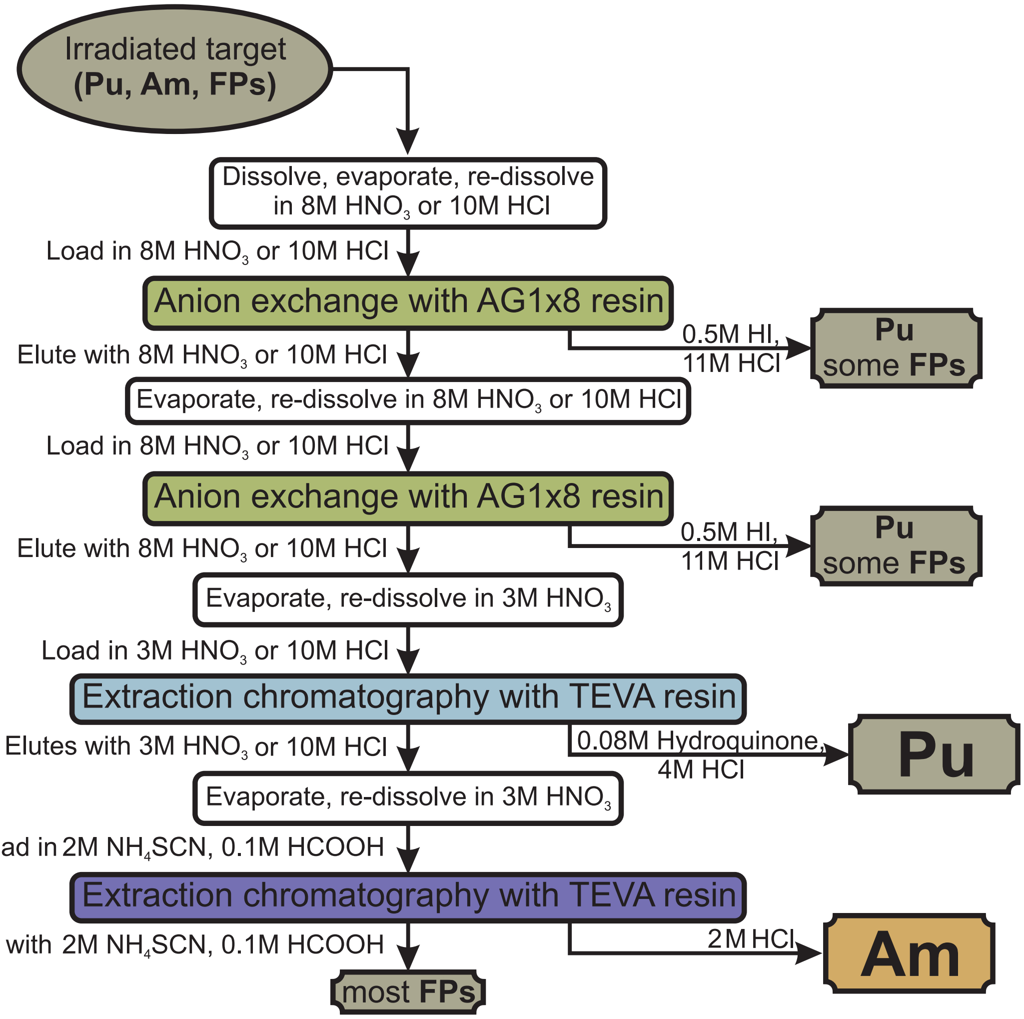

Figure 3.1 Diagram of proposed Am/Pu/FP separation procedure.

elements. Nitric acid has the advantage that a lower molarity can be used. After the Am is washed from the column, the Pu can be reduced to Pu(III) and eluted using a solution with a 0.5 M HI, 11 M HCl solution. This anion exchange procedure is performed twice to remove the bulk of the Pu from the ^{240}Am sample. Solvent extraction was not chosen for these initial steps because of strict limitations which effectively prohibit the generation of mixed radioactive/hazardous liquid waste at LANL.

The third step in the procedure involves an extraction chromatography column using the Eichrom TEVA resin. Like the preceeding anion exchange columns, this extraction chromatography column can be prepared using in either nitric or hydrochloric acid. Under 3 M HNO_3 or 10 M HCl, Pu selectively forms anion complexes which tightly bind to the resin, allowing Am to selectively elute. These conditions offer Am/Pu separation factors on the order of 10^5 [HDC$^+$95]. After the Am is washed from the column, the Pu can be reduced to Pu(III) and eluted using a solution of 0.08 M hydroquinone and 4 M HCl. This step's very effective Pu removal is balanced by the resin's relatively small capacity for Pu. According to Horwitz [HDC$^+$95], the TEVA resin has an experimental wet resin capacity of 0.223 milliequivalents/mL of bed volume, only a fifth of that for the anion exchange resin used. For this reason, this extraction chromatography step is used as a final, highly effective Pu-removal step.

The fourth and final step in the separation procedure is focused on the removal of the remaining high-dose fission products, including trivalent lanthanides which have very similar chemistry to Am. This step again utilizes an extraction chromatography column using the TEVA resin. However, this second TEVA column is loaded in a solution of 2 M NH_4SCN and 0.1 M HCOOH. Under these thiocyanate/formic acid conditions, Am selectively forms anionic complexes due to its larger, more diffuse valence orbitals, causing it to stick to the TEVA resin. Most remaining high-dose fission products, including trivalent lanthanide elements are eluted from the column under these conditions. Americium can then be eluted with 2 M HCl.

3.3 Tracer-scale experiments of proposed separation procedure

The separation procedure proposed in Section 3.2.4 was experimentally tested on the tracer scale (10^2 – 10^6 Bq) using the relatively long-lived radionuclides ^{241}Am, ^{239}Pu, and model fission products ^{152}Eu ($t_{1/2}$ = 13.5 y), ^{95}Zr ($t_{1/2}$ = 64.0 d), ^{95}Nb ($t_{1/2}$ = 35.0 d), and ^{125}Sb ($t_{1/2}$ = 2.76 y). The chemicals used were at least reagent grade purity from a variety of distributors including Riedel-de Haën, Fluka, and Sigma Aldrich. Depending on the radionuclide of interest, the activity in the loading and elution solutions was determined by gamma ray spectroscopy, alpha spectroscopy, and/or LSC. An uncertainty of 5% can be assumed for measurements of loading and eluted activities due to standard counting and pipetting errors.

The preparation of resin and column packing was performed similar to that described in Section 2.1.1 with a few differences. While the Bio-Rad 1x8, 100 - 200 mesh anion exchange resin was prepared as described, the TEVA resin was only pre-conditioned with non-radioactive loading solution prior to use. Also, the free column volume (FCV), which is defined as the column volume not occupied by resin, was not experimentally determined for each experiment. The FCV volume for anion exchange columns was estimated as 50% of the column bed volume. The FCV for the TEVA resin columns was estimated as 68% of the column bed volume, as reported by Horwitz *et al.* [HDC+95]. The columns used were glass with a reservoir top and a platinum tip to assure a small and reproducible drop volume.

3.3.1 Tracer-scale experiments involving Am and Pu

A number of separation experiments were performed developing and testing the various steps of the proposed separation using tracer levels of ^{241}Am and ^{239}Pu. These experiments were performed in a glovebox. For the first two experiments, ^{239}Pu stock solutions were prepared by hydroxide precipitation from perchlorate acid solutions [Col65]. For subsequent experiments, ^{239}Pu stock solutions were prepared from the Pu-rich fractions from these first two columns. The ^{241}Am for these experiments was obtained from stock solutions in hydrochloric or nitric acid. Loading solutions for the columns were prepared by adding a measured amount of ^{239}Pu and ^{241}Am stock solutions to the boiling flask of a scrubbing apparatus similar to that described in Section 2.1.1. The solution was evaporated and redissolved in the appropriate acid solution for loading onto the separation column. The loading solution was carefully loaded onto a pre-conditioned and prepared column in small quantities to avoid losses and tailing of the radioactivity due to wall absorption on the column reservoir. The column washing solution was first used to rinse the boiling flask before addition to the column to increase the efficiency of transfer of radioactivity from flask to column. After the addition of the radioactivity, the eluent from the column was collected in fractions with volumes of 1 – 3 FCVs.

Several important lessons were learned during the development experiments. One such lesson was that a significant amount (estimated at 1 – 5%) of the radioactivity in a solution was left adhered to its boiling flask or vial, depending on its size and how carefully it was rinsed. This fact is important for estimating the losses of the separation procedure. It is also very important when preparing loading solutions for subsequent columns using the same boiling flask. For example, when a separation procedure reduces the amount of Pu in the eluent by a factor of 100 – 10,000, it is important not to add this solution back to its boiling flask which contains 1% of the initial Pu activity. A second lesson from the development of the separation procedure was that it is important to control the Pu oxidation state in the column loading solutions. When using nitric acid solutions, the oxidation state can be held at Pu(IV) by adding a small amount of sodium nitrite ($NaNO_2$) to the loading solution. Care must be taken when using $NaNO_2$ because it will often evolve gas when added to solutions. Gas evolution has also been observed when a solution containing $NaNO_2$ comes in contact with hydroquinone. A column loaded with a solution containing $NaNO_2$ must be thoroughly washed with a nitrite-free solution before eluting with hydroquinone as this gas evolution can easily disrupt the resin bed.

These separation experiments developing the steps of the procedure were culminated in series of experiments where ~1 nanogram of Am was separated in three steps from ~1 milligram of Pu. The experimental details of these three separation columns are given in Table 3.1. Elution from these columns were collected in fractions with volumes of 100 – 600 μL. The total activity in each loading solution and elution fraction was measured by LSC of 5- or 10-μL aliquots from the fraction. Details of the liquid scintillant and the LSC can be found in Section 2.1.2. 5- or 10-μL alpha plates were taken of two of the loading solution and Am elution fractions. These plates were counted in an alpha spectrometer and the ratio of the number of counts in the ^{239}Pu peak at 5.15 MeV and the ^{241}Am peak at 5.49 MeV was used to determine the fraction of the total radioactivity due to ^{239}Pu and ^{241}Am.

First anion exchange step of 1 mg Pu / 1 ng Am separation procedure

The first step of this procedure used a 2 mm diameter, 68 mm bed length platinum-tipped glass column. This column was loaded with Bio-Rad AG®1x8, 100 - 200 mesh anion exchange resin which had been conditioned with 8 M HNO_3. The column's FCV was estimated as half the bed volume, ~100 μL. The loading solution was prepared by evaporating an aliquot of ^{239}Pu stock solution and ^{241}Am stock solution in a boiling flask. The salts were then redissolved in 100 μL of 8 M HNO_3 and transferred to a plastic tube. The boiling flask was rinsed with two 100 μL aliquots of 8 M HNO_3, which were also transferred to the tube. A single grain (~3 mg) of $NaNO_2$ was added to the loading solution to control the oxidation state of Pu. A 2000 times dilution of this loading solution was prepared and assayed by LSC and alpha spectroscopy indicating that the loading solution had a total activity of 2.0 x 10^6 Bq. The Pu/Am mass ratio was so high that the majority of alpha counts in the 5.5 MeV range were due to ^{238}Pu, which was present in the Pu sample at an unknown, but very small, isotopic abundance. Thus, the total activity of ^{241}Am in the loading solution was not accurately determined, but was known to be on the order of 100 Bq due to the volume and concentration of Am stock solution used for its preparation. These activities correspond to roughly 0.9 mg of ^{239}Pu and 0.8 ng of ^{241}Am in the loading solution.

After the addition of the loading solution, the column was washed with 6 FCVs of 8 M HNO_3 and then with 6 FCVs of 10 M HCl. The Pu was then reductively eluted with 5 FCVs of 0.5 M HI, 11 M HCl solution.

The eluent from this column was collected over ten fractions. The first two fractions eluted from the column (470 μL) contained a total ^{241}Am activity of 118 Bq. The third

Table 3.1 Details of 1 mg/1 ng Am/Pu separation columns.

Column dimensions (mm)	Resin	Free column volume	Loading solution	Washing / elution solution	Loading activity (Bq)	
					^{241}Am	^{239}Pu
$\varnothing_{\text{bed}} = 2$ $\mathscr{L}_{\text{bed}} = 68$	AG 1x8	100 μL	~3 mg $NaNO_2$ in 300 μL 8 M HNO_3	620 μL 8 M HNO_3, then 650 μL 10 M HCl, then 500 μL 0.5 M HI 11 M HCl	120	2.0×10^6
$\varnothing_{\text{bed}} = 2$ $\mathscr{L}_{\text{bed}} = 68$	AG 1x8	100 μL	~3 mg $NaNO_2$ in 300 μL 8 M HNO_3	750 μL 10 M HCl, then 400 μL 0.5 M HI 11 M HCl	115	1.4×10^3
$\varnothing_{\text{bed}} = 2$ $\mathscr{L}_{\text{bed}} = 55$	TEVA	120 μL	~2 mg $NaNO_2$ in 150 μL 3 M HNO_3	300 3 M HNO_3, then 600 μL 4 M HCl, then 600 μL 4 M HCl, 0.08 M hydroquinone	68	230

fraction (370 μL) was deduced to contain <12.5 Bq of ^{241}Am by a HPGe gamma ray spectrometric analysis comparing it with the first two fractions. A small fraction of the Pu was also observed to elute from the column under loading and washing conditions. The first two eluted fractions, which contained >90% of the ^{241}Am, contained ~0.06% of the Pu which had been loaded on the column. A total of 1% of the loaded Pu was eluted under the loading and washing conditions, the large majority eluting in the third and fourth fraction.

The majority of the Pu was then reductively eluted into the 6th – 11th fractions (2.36 mL, total). Due to the unknown ^{238}Pu isotopics in the Pu sample, it was not possible to determine the amount of Am in fractions containing significant amounts of Pu. Thus, it was not possible to accurately determine the extent of tailing in the elution of Am. However, based on the gamma spectroscopy measurements of the first three fractions, the tailing was expected to be negligible beyond the third fraction. Because of this, the Am yield in the first two fractions was estimated as >90% and their Am/Pu separation factor as defined in Equation 3.1 was measured to be ~1.5 x 10^3.

Second anion exchange step of 1 mg Pu / 1 ng Am separation procedure

The second step of this procedure used the same 2 mm diameter, 68 mm bed length, platinum tipped glass column. The column was repacked with fresh, 8 M HNO_3-conditioned Bio-Rad AG®1x8, 100 - 200 mesh anion exchange resin. The loading solution was prepared by evaporating the first two elution fractions from the previous anion exchange column. The salts were then redissolved in 100 μL of 8 M HNO_3 and transferred to a plastic tube. The boiling flask was rinsed with two 100 μL aliquots of 8 M HNO_3, which were also transferred to the tube. A single grain (~3 mg) of $NaNO_2$ was added to the loading solution to control the oxidation state of Pu. According to the LSC/alpha analysis of the solutions combined to make this loading solution, 1.2 x 10^3 Bq of ^{239}Pu and 120 Bq of ^{241}Am were present. However, after preparation, the loading solution was assayed using LSC and measured to have a total activity of 1.5 x 10^3 Bq, indicating a significant amount of radioactivity was picked up from the boiling flask during its preparation as a loading solution.

A nearly identical loading, washing, and elution procedure was performed with the exception that this second anion exchange column was not washed with 8 M HNO_3. After the addition of the loading solution, the column was washed with 7 FCVs of 10 M HCl to elute the ^{241}Am. The Pu was then reductively eluted with 4 FCVs of 0.5 M HI, 11 M HI solution.

The eluent from this column was collected over eight fractions. The first three fractions eluted from the column (580 μL) contained a total ^{241}Am activity of 106 Bq. The first (280 μL) and second (115 μL) of these fractions were largely free of Pu with ^{241}Am accounting for 91% and 97% of their alpha activity, respectively. The third fraction (190 μL) contained a significant amount of Pu contamination with only 15% of the fraction's activity from ^{241}Am. This third fraction contained a total of ~6% of the total amount of ^{239}Pu activity loaded on the column. This fraction also contained a significant amount of ^{241}Am, nearly 20% of that which eluted in the first two fractions. It is not clear why such a significant portion of the Pu eluted in this third fraction. The fourth (390 μL) and fifth fractions (215 μL) did not contain much radioactivity with activities of 15 and 4.5 Bq, respectively. This activity was deduced to be predominantly Pu based on the pattern of Am/Pu activity ratios in the first three fractions.

The majority of the Pu was then reductively eluted into the sixth, seventh, and eighth fractions (1.15 mL, total). Because alpha spectra were not taken of the fourth and fifth fractions, it was not possible to determine the extent of the Am elution tailing. Assuming the ^{241}Am activity content in these fractions was the same as in fraction 3 and that all the Am was eluted in the first five fractions, the total Am yield in the first three fractions was estimated to be 97% and their Am/Pu separation factor was measured to be $\sim$14.

TEVA chromatography step of 1 mg Pu / 1 ng Am separation procedure

The third step of this procedure used a 2 mm diameter, 55 mm bed length platinum-tipped glass column. The column was loaded with Eichrom TEVA resin which had been conditioned with 3 M HNO_3. The column's FCV was calculated to be $\sim$120 μL. The loading solution was prepared by evaporating the first three elution fractions from the second anion exchange column. The salts were then redissolved in 70 μL of 8 M HNO_3 and transferred to a plastic tube. The boiling flask was rinsed with two 70 μL aliquots of 8 M HNO_3, which were also transferred to the tube. A single grain ($\sim$3 mg) of $NaNO_2$ was added to the loading solution to control the oxidation state of Pu. This loading solution was then assayed by LSC and alpha spectroscopy. The loading solution was measured to have a total ^{241}Am activity of 80 Bq and a total ^{239}Pu activity of 320 Bq in 210 μL of 8 M HNO_3. These activities correspond to 140 ng of ^{239}Pu and 0.6 ng of ^{241}Am in the loading solution.

A total of 150 μL of the loading solution (containing 68 Bq of ^{241}Am and 230 Bq of ^{239}Pu) was loaded onto the column, followed by washing with 2.5 FCVs of 3 M HNO_3 and then 5 FCVs of 4 M HCl. The Pu was then reductively eluted with 7 FCVs of 4 M HCl / 0.08 M hydroquinone solution.

The eluent was collected over six fractions. The first two fractions eluted from the column (310 μL) contained a total ^{241}Am activity of 65 Bq. The first (160 μL) and second (150 μL) of these fractions were largely free of Pu with ^{241}Am accounting for 100% and 96% of their alpha activity, respectively. The third (165 μL) and fourth (600 μL) fractions were largely free of radioactivity with activities of 2.6 and 0.3 Bq. Based on the lack of Pu observed in the first two fractions, it is likely that the low activity in the third and fourth fractions are due to tailing in the Am elution.

The majority of the Pu was then reductively eluted into the fifth and sixth fractions (900 μL, total). Assuming all the ^{241}Am eluted in the first four fractions, the total Am yield in the first two fractions was estimated to be 96% and the Am/Pu separation factor was measured to be >220. It was only possible to determine a lower limit for the Am/Pu separation factor for this last step because Pu was below detection limits in the Am elution fractions.

Summary of 1 mg Pu / 1 ng Am separation procedure

Overall the separation procedure was very successful. However, the anion exchange steps seem to have some serious limitations. While ∼90% of the Am is effectively eluted in the first 4 FCVs washed from the column, it appears that ∼0.05% of the loaded Pu will co-elute in these fractions. This problem is exacerbated in the fifth and sixth FCV of washing which contains the remaining 10% of the loaded Am and 1 – 6% of the loaded Pu. This creates a significant dilemma in the number of washing FCVs to collect from the anion exchange columns. Collecting 4 FCVs will maximize the separation factor but limit Am yield to ∼90%. Collecting 6 FCVs will result in an Am yield of ∼97%, but give a significantly lower Pu/Am separation factors. The TEVA extraction chromatography step was extremely successful with 96% of the Am eluting in the first 4 FCVs with no observable Pu contamination.

Table 3.2 summarizes the results from the three-step separation procedure isolating 0.8 ng of ^{241}Am from 0.9 mg of ^{239}Pu. The Am efficiency and Am/Pu separation factor for the whole procedure was calculated by taking the product of the values for the individual steps. With an estimated 95% recovery percentage of Am during the dissolution and each fraction collection/evaporation step, this overall efficiency is >68%. If the overall Am/Pu separation factor is calculated using the initial activity of Pu/Am added to the first column and the activity eluted from the final column, the calculated factor is lower, $>6.4 \times 10^5$. This disagreement is due to the fact that when the Am-rich fractions were collected and evaporated between each step they would pick up ^{239}Pu and ^{241}Am from the boiling flask.

The lower limit separation factor measured in this 1 mg Pu / 1 ng Am separation procedure is significantly lower than that needed for the ^{240}Am-isolation procedure. As there was no detectable Pu present in the americium fraction after the procedure, the separation factor is likely significantly higher than this limit. The separation procedure will need to be scaled up to involve a significantly larger initial plutonium and americium activities to elucidate the actual separation factor for the procedure.

3.3.2 Tracer-scale experiments with Zr, Nb, Sb, and Eu

Experiments were also performed to elucidate the behavior of high-dose fission products on the developed Am/Pu separation procedure. These experiments were performed using tracer levels of ^{95}Nb, ^{95}Zr, ^{152}Eu, and in some cases ^{125}Sb, which serve as longer-lived proxies for the high dose fission products ^{97}Zr/Nb, ^{126,129}Sb, ^{140}La, and ^{143}Ce. The activities of the various radionicludes in the loading solutions, elution fractions, and post-separation columns were determined by HPGe gamma ray spectroscopy using the detectors described

Table 3.2 Summary of 1 mg Pu / 1 ng Am separation procedure

Separation step	FCVs collected for Am fraction	Am yield	Am/Pu separation factor
Anion exchange column #1	4	>90%	~1.5 x 10^3
Anion exchange column #2	6	97%	~14
TEVA extraction column	2.5	96%	>220
Full procedure	–	>79%	>4.6 x 10^6

in Section 2.3.1. ^{95}Zr was identified through its 54.5% intensity gamma ray at 756.73 keV, ^{95}Nb through its 99.8% intensity gamma ray at 765.81 keV, ^{152}Eu through its 28.4% intensity gamma ray at 121.78 keV, and ^{125}Sb through its 17.9% intensity gamma ray at 600.60 keV.

Separation procedures with Eu, Zr, Nb, and Sb were performed using 80 – 200 μL bed volume glass columns fitted with Pt tips to minimize drop volume to 5 – 10 μL. ^{95}Zr and ^{95}Nb in 6 M HCl was purchased from PerkinElmer Life and Analytical Sciences and ^{125}Sb in 6 M HCl from Eckert & Ziegler Analytics. Loading solutions were prepared by adding aliquots of radionuclide stock solutions to a small vial and evaporating to dryness using a heat lamp and had varying radionuclide activities of 15 – 150,000 Bq. The evaporant was then redissolved in the acid solution appropriate for the separation procedure. The separation procedures performed were very similar to those described in Section 3.3.1. However, the procedures differed in several ways. First, the procedures performed with Bio-Rad AG®1x8 anion exchange resin were performed using 10 M HCl as the loading and washing solution. Also, the procedures which utilized a reductive step (either with HI/HCl solution as with anion exchange, or hydroquinone as with the first TEVA step) had a crystal ~2 mg of NH_2OH added to the column as the reducing agent was added. This prevented the immediate oxidation of the reducing agent by trace amounts of HNO_3 which may be still present on the column. The following sections contain a summary and discussion of the results of each of these model fission product elements on the developed ^{240}Am isolation procedure.

Results and discussion of behavior of Zr in ^{240}Am isolation procedure

Zirconium exists exclusively as the +4 oxidation state in solution. However, because the Zr^{4+} ion has a very strong tendency to undergo hydrolysis and polymerization reactions, its behavior in aqueous solution is quite complicated [Ste60]. Fortunately, Zr's hydrolysis tendency decreases at the high acidities used in the ^{240}Am isolation procedure [JK56]. Zirconium has been observed to sorb strongly to anion exchange resins in > 9 M HCl ($K_d \approx 10^3$), presumably as $ZrCl_{5-6}^{(1-2)-}$ complexes, with no observed sorption below 6 M HCl [HIL51]. The anion exchange resin sorption of zirconium from nitric acid is significantly less, peaking at ~5 M HNO_3 with a K_d of only 1 – 10 [FB64]. As anionic Zr complexes have been observed to

Table 3.3 Summary of results of Zr behavior in separation procedure.

Resin	Zr activity loaded (Bq)	Loading solution	% Zr eluted w/ loading	Elution solution	% Zr eluted w/ elution
AG 1x8	1400	10 M HCl	**6**	0.5M HI/11 M HCl then 0.5 M HCl	21 then 38
AG 1x8	1.0×10^3	10 M HCl	**58**	2 mg NH_2OH w/ 0.5M HI/11 M HCl	14
AG 1x8	100	10 M HCl	**70**	2 mg NH_2OH w/ 0.5M HI/11 M HCl	30
TEVA	100	2 mg $NaNO_2$ w/ 3 M HNO_3 then 4 M HCl	**61** then 28	0.08 M hydroquinone/ 4 M HCl	5.5
TEVA	260	2 mg $NaNO_2$ w/ 3 M HNO_3	**83**	0.08 M hydroquinone/ 4 M HCl	6.2
TEVA	5.0×10^3	2 M NH_4SCN/ 0.1 M HCOOH	78	2 M HCl	**2**
TEVA	115	2 M NH_4SCN/ 0.1 M HCOOH	32	2 M HCl	**17**

be extracted from >7 M HCl solutions by Aliquat·336 [SW70, PFRPRL06], it is likely that the TEVA resin would provide adequate Am/Zr separation at high HCl concentrations. No experimental studies of Zr with Aliquat·336 or TEVA have been made using nitric acid, but because nitrate ion does not complex with Zr well (as observed in anion exchange studies), very little Zr/Aliquat·336/TEVA interaction would be expected in HNO_3. The behavior of Zr in the presence of NH_4SCN/HCOOH solutions has not been previously studied.

The results from seven tracer-scale experiments examining the behavior of Zr on the different steps of the separation procedure are summarized in Table 3.3. The unaccounted percentage of Zr activity for each column was left adsorbed to the column material at the end of the chromatography experiment. The bolded percentages of Zr elution highlight the percentage of Zr which would elute in the Am-containing fractions of the separation step.

Three total experiments were performed examining the behavior of Zr in the anion exchange chromatography steps of the ^{240}Am isolation procedure. The latter two experiments were performed sequentially, with the loading solution of the third experiment prepared by evaporating and redissolving the hypothetically-Am-containing fractions from the second experiment. In addition, the first experiment was performed with Zr freshly purchased from PerkinElmer Life and Analytical Sciences. The results for this first experiment matched those expected from the discussion in the previous paragraph with only 6% of Zr eluting with the 10 M HCl loading/washing solution (in the Am fractions) and 21% eluting with the reductive 0.5 M HI, 11 M HCl solution. An additional 38% of Zr was then eluted with 0.5 M HCl and 35% left on the column. The second and third experiment was performed using Zr from the same stock solution ~1 year later. These two experiments had significantly different results with a large portion of the Zr eluting with 10 M HCl loading/washing solution. This drastic change in the behavior of Zr is possibly due to changes in complexation or speciation of Zr during the year-long storage of the stock solution in 6 M HCl.

Two experiments were performed examining the behavior of Zr on the first TEVA extraction chromatography step of the ^{240}Am isolation procedure. The results of these experiments are shown in the fourth and fifth rows of Table 3.3. The majority of Zr eluted with with the 3 M HNO_3 loading/washing solution (in the Am fractions), with a small portion eluting with the reductive 0.08 M hydroquinone / 4 M HCl solution, and the remainder sorbed to the column. These experiments agree with the results expected from literature showing that Zr will poorly sorb to the TEVA resin because it does not form anionic nitrato complexes.

Two experiments were also performed examining the behavior of Zr on the second TEVA step of the procedure. The results are shown in the bottom two rows of Table 3.3. The results of these two experiments disagreed significantly. The large variation in the results from these two experiments is not yet well understood and will require future separation experiments to clarify.

Results and discussion of behavior of Nb in ^{240}Am isolation procedure

Niobium exists primarily in the +5 oxidation state as complex ions in solution, although it can be reduced to the tetra- and trivalent states with strong reducing agents. Like zirconium, niobium's aqueous chemistry is complicated by its tendency to undergo hydrolytic polymerization and colloid formation, which is minimized in the presence of strong complexing agents such as fluoride (F^-) or oxalate ($C_2O_4^-$) or high concentrations of more weakly complexing acids such as HCl [Ste61]. Niobium has been observed to sorb strongly to anion exchange resins in >8 M HCl ($K_d \approx 10^3$), presumably as $NbOCl_{4-6}^{(1-2)-}$ complexes, with significantly weaker sorption with 2 – 6 M HCl [HIL51]. It is only slightly sorbed to anion exchange resins from HNO_3 solutions [FB64]. As anionic Nb complexes have been observed to be strongly extracted from >6 M HCl solutions by Aliquat·336 [PKS$^+$99], it is likely that the TEVA resin would provide adequate Am/Nb separation at high HCl concentrations. No experimental studies of Nb with Aliquat·336 have been made using nitric acid, but because nitrate ion does not complex with Nb (as observed in anion exchange studies), very little Nb/Aliquat·336/TEVA interaction would be expected in HNO_3. The behavior of Nb in the presence of NH_4SCN/HCOOH solutions has not been previously studied.

Table 3.4 Summary of results of Nb behavior in separation procedure.

Resin	Nb activity loaded (Bq)	Loading solution	% Nb eluted w/ loading	Elution solution	% Nb eluted w/ elution
AG 1x8	2300	10 M HCl	**2.6**	0.5M HI/11 M HCl then 0.5 M HCl	1 then 75
AG 1x8	$4.0{\times}10^3$	10 M HCl	**2**	2 mg NH_2OH w/ 0.5M HI/11 M HCl	13
AG 1x8	40	10 M HCl	**51**	2 mg NH_2OH w/ 0.5M HI/11 M HCl	43
TEVA	15	2 mg $NaNO_2$ w/ 3 M HNO_3 then 4 M HCl	**50** then 16	0.08 M hydroquinone/ 4 M HCl	3.5
TEVA	360	2 mg $NaNO_2$ w/ 3 M HNO_3	**88**	0.08 M hydroquinone/ 4 M HCl	1.6
TEVA	$6.0{\times}10^3$	2 M NH_4SCN/ 0.1 M HCOOH	44	2 M HCl	**9.5**
TEVA	80	2 M NH_4SCN/ 0.1 M HCOOH	4.5	2 M HCl	**2**

The results from seven tracer-scale experiments examining the behavior of Nb on the different steps of the separation procedure are summarized in Table 3.4. The unaccounted percentage of Nb activity for each column was left adsorbed to the column material at the end of the chromatography experiment. The bolded percentages of Nb elution highlight the percentage of Nb which would elute in the Am-containing fractions of the separation step.

Three total experiments were performed examining the behavior of Nb on the anion exchange chromatography steps of the ^{240}Am isolation procedure. The latter two experiments were performed sequentially, with the loading solution of the third experiment prepared by evaporating and redissolving the hypothetically-Am-containing fractions from the second experiment. In addition, the first experiment was performed with Nb recently purchased from PerkinElmer Life and Analytical Sciences. The results for this first experiment matched those expected from the discussion in the previous paragraph with only 3% of Nb eluting with the 10 M HCl loading/washing solution (in the Am fractions) and 1% eluting with the reductive 0.5 M HI, 11 M HCl solution. 75% of Nb was then eluted with 0.5 M HCl and 21% left on the column. The second and third experiment was performed using Nb from the same stock solution ∼1 year later. The second experiment had relatively similar results to the first, with 2% of Nb eluting with the 10 M HCl loading/washing solution (in the Am fractions), 13% eluting with the reductive 0.5 M HI, 11 M HCl solution, and 85% staying on the column. However, the third experiment exhibited significantly different results with 51% of Nb eluting with the 10 M HCl loading/washing solution (in the Am fractions), 43% eluting with the reductive 0.5 M HI, 11 M HCl solution, and only 6% staying on the column. This disagreement in results could possibly be due to changes in the complexation or speciation of a a small fraction of Nb atoms during the year-long storage of the stock solution in 6 M HCl, or as a result of the very small Nb activity (40 Bq) loaded onto the third experiment's column.

Two experiments were performed examining the behavior of Nb on the first TEVA extraction chromatography step of the ^{240}Am isolation procedure. The results of these experiments are shown in the fourth and fifth rows of Table 3.4. The majority of of Nb eluted with with the 3 M HNO_3 loading/washing solution (in the Am fractions), with a small portion eluting with the reductive 0.08 M hydroquinone / 4 M HCl solution, and the remainder sorbed to the column. These experiments agree with the inference that Nb will poorly sorb to the TEVA resin because it does not form anionic nitrato complexes.

Two experiments were also performed examining the behavior of Nb on the second TEVA step of the procedure. The results are shown in the bottom two rows of Table 3.4. The large variation in the results from these two experiments is not yet well understood and will require future separation experiments to clarify.

Results and discussion of behavior of Eu in ^{240}Am isolation procedure

The chemistry of europium is straightforward and similar to the other lanthanide elements. In solution, these elements all are stable in the +3 oxidation state and behave as hydrated trivalent ions. These trivalent ions do not form anionic complexes with Cl^- or HNO_3^-, so they do not sorb to anion exchange or TEVA resins at any acid concentration. In addition, lanthanides have been observed not to form complexes under NH_4SCN/HCOOH conditions, resulting in no interaction with TEVA resin [HDC$^+$95].

The results from four tracer-scale experiments examining the behavior of Eu on the different steps of the separation procedure are summarized in Table 3.5. The unaccounted percentage of Eu activity for each column was left adsorbed to the column material at the end of the chromatography experiment. The bolded percentages of Eu elution highlight the percentage of Eu which would elute in the Am-containing fractions of the separation step.

Two experiments were performed examining the behavior of Eu on the anion exchange chromatography steps of the ^{240}Am isolation procedure. The results of both of these experiments matched those expected from the discussion in the previous paragraph with 99% of Eu eluting with the 10 M HCl loading/washing solution (in the Am fractions), 1% eluting with the reductive 0.5 M HI, 11 M HCl solution. No Eu activity was left on the column.

Table 3.5 Summary of results of Eu behavior in separation procedure.

Resin	Eu activity loaded (Bq)	Loading solution	% Eu eluted w/ loading	Elution solution	% Eu eluted w/ elution
AG 1x8	1.5×10^5	10 M HCl	**99**	2 mg NH_2OH w/ 0.5M HI/11 M HCl	1
AG 1x8	3.2×10^4	10 M HCl	**99**	2 mg NH_2OH w/ 0.5M HI/11 M HCl	1
TEVA	5.0×10^4	2 mg $NaNO_2$ w/ 3 M HNO_3	**99**	0.08 M hydroquinone/ 4 M HCl	0.4
TEVA	5.3×10^3	2 M NH_4SCN/ 0.1 M HCOOH	95	2 M HCl	**2**

One experiment was performed examining the behavior of Eu on the first TEVA extraction chromatography step of the ^{240}Am isolation procedure. In this experiment, 99% of Eu eluted eluted with the 3 M HNO_3 loading/washing solution (in the Am fractions), <1% eluted with the reductive 0.08 M hydroquinone / 4 M HCl solution, and <1% stayed on the column. An experiment was also performed examining the behavior of Eu on the second TEVA step of the procedure. In this experiment, 95% of Eu eluted with the 2 M NH_4SCN, 0.1 M HCOOH loading/washing solution, 2% eluted with 2 M HCl (in the Am fractions), and 3% stayed on the column. This TEVA step performed as intended, separating the lanthanide activities from the americium.

Results and discussion of behavior of Sb in ^{240}Am isolation procedure

Antimony can exist in a wide variety of oxidation states, including -3 as SbH_3, +3 as Sb_2O_3, and +5 as Sb_2O_5. In aqueous solution, it typically exists as complexed ions in the +3 and +5 oxidation states. The sorption of antimony to anion exchange resin is very dependent on this oxidation state of Sb in solution. For example, in 10 M HCl solutions, Sb (V) will sorb strongly to anion exchange resin ($K_d > 10^5$), presumably as $SbCl_6^-$, while Sb (III) will sorb only moderately ($K_d \approx 10-100$), presumably as $SbCl_{4-6}^{(1-3)-}$ [KN56]. Sb has not been observed to sorb to anion exchange resins from HNO_3 solutions [FB64]. As anionic Sb complexes have been moderately extracted from 10 M HCl solutions by Aliquat·336 [NL00], the TEVA resin to would be expected to provide some Am/Sb separation at these HCl concentrations. While Aliquot·336 was observed not to extract Sb from 0.001 M HNO_3 solutions [MLMR03], there are no literature reports of its behavior from more concentrated nitric acid solutions where Sb would be more likely to form extractable anionic nitrato complexes. However, because

Table 3.6 Summary of results of Sb behavior in separation procedure.

Resin	Eu activity loaded (Bq)	Loading solution	% Eu eluted w/ loading	Elution solution	% Eu eluted w/ elution
TEVA	25	2 mg $NaNO_2$ w/ 3 M HNO_3 then 4 M HCl	**78** then 11	0.08 M hydroquinone/ 4 M HCl	0
TEVA	100	2 M NH_4SCN/ 0.1 M HCOOH	74	2 M HCl	**13**

nitrate ions do not complex with Sb (as observed in anion exchange studies), very little Sb/Aliquat·336/TEVA interaction would be expected in HNO_3. The behavior of Sb in the presence of NH_4SCN/HCOOH solutions has not been previously studied.

The results from two tracer-scale experiments examining the behavior of Sb on the different steps of the separation procedure are summarized in Table 3.6. The unaccounted percentage of Sb activity for each column was left adsorbed to the column material at the end of the chromatography experiment. The bolded percentages of Sb elution highlight the percentage of Sb which would elute in the Am-containing fractions of the separation step.

While no experiments were performed examining the behavior of Sb on the anion exchange steps of the ^{240}Am isolation procedure, one experiment was performed studying its behavior on the first TEVA step. In this experiment, 89% of Sb eluted with the 3 M HNO_3 loading/washing solution (in the Am fractions), none eluted with the reductive 0.08 M hydroquinone / 4 M HCl solution, and 10% stayed on the column. This result implies that Sb does not form anionic nitrato complexes in 3 M HNO_3. An experiment was also performed examining the behaivor of Sb on the second TEVA step of the procedure. In this experiment, 74% of Sb eluted with the 2 M NH_4SCN, 0.1 M HCOOH loading/washing solution, 13% eluted with 2 M HCl (in the Am fractions), and 12% stayed on the column. This result implies that Sb does not form anionic thiocyanato complexes in 2 M NH_4SCN, 0.1 M HCOOH solution and thus this step would provide some Sb/Am separation.

Conclusions from tracer scale Zr, Nb, Eu, and Sb separations

The previous sections discuss the behavior of the high dose fission products Zr, Nb, Eu, and Sb in the separation procedure designed to isolate ^{240}Am from proton-irradiated ^{242}Pu. One major conclusion from this work is that for the procedure to do an adequate job of isolating Am from Zr, Nb, and Sb, the anion exchange and first TEVA separation steps must be performed in 10 M HCl as opposed to 3 M HNO_3. Under these conditions, Zr, Nb, and Sb all form anionic chloro complexes which are sorbed by the resin, allowing for their separation from Am. A second conclusion is that care must be taken to prevent the formation of Zr and Nb polynuclear hydrolysis products by keeping the pH of the solutions below 1. To accomplish this, the dissolved target material should be kept under high concentration HCl after dissolution. If the ^{240}Am isolation procedure is performed with attention paid to these two important conclusions, it will effectively reduce the amount of high dose fission products in the ^{240}Am sample by a factor of 10 - 100. Finally, because of some discrepancies in the results from these separation steps, a series of duplicated experiments should be performed to verify the behavior of these radionuclides in the separation procedures in both 10 M HCl and 3 M HNO_3.

3.3.3 Discussion of expected behavior of Mo/Tc in separation

Molybdenum-99 is a proton-induced fission fragment of ^{242}Pu which β^- decays with a 66.0 hour half-life to ^{99m}Tc which decays by isomeric transition with a 6 hour half-life to the relatively long-lived isotope, ^{99}Tc. According to calculations detailed in Section 3.4, a total of $\sim$11% of the gamma dose emitted from the proton-irradiated ^{242}Pu target 24 hours after irradiation will come from the radioactive decay of ^{99}Mo and ^{99m}Tc. Unfortunately, because of lack of availability of easy-to-detect, relatively long-lived radionuclides, it was not possible to perform tracer-level studies of the behavior of Mo and Tc on the developed ^{240}Am isolation procedure. Fortunately, the radiochemistry of Mo and Tc has long been studied and documented in the literature [SB60, And60]. This section discusses the expected behavior of these important elements on each proposed chemical separation step.

Molybdenum has a total of six oxidation states: 0, +2, +3, +4, +5, and +6. In aqueous solution, its most common state is the +6 state in the form of the oxygenated anion. Because of this wide variety of oxidation states, molybdenum has a very complicated chemistry. On strongly basic anion exchange resins such as Dowex 1 or Bio-Rad®AG 1, Mo has been observed to sorb strongly under 10 M HCl conditions [MP54, BBPF59, KNM55, HOW56], but not adsorb under 8 M HNO_3 conditions [FB64]. Thus, the two anion exchange steps of the ^{240}Am isolation procedure would only be effective at isolating Am from Mo if performed under HCl conditions. The behavior of Mo with the Aliquat·336 extractant in nitric acid media has also been studied [JAOS03]. While Mo is observed to have a ten times larger affinity for the ligand than Am, it remains unclear whether the difference is large enough to enable their separation with a 3 M HNO_3 TEVA® resin column. The behavior of Mo on a 10 M HCl TEVA® resin column has not been reported in the literature.

Technetium exists largely in two oxidation states while in solution: the 7+ state as the pertechnetate ion (TcO_4^-) or volatile technetium heptoxide (Tc_2O_7) and the 4+ state as a complexed cation. On strongly basic anion exchange resins such as Dowex 1 or Bio-Rad®AG 1, Tc has been observed to sorb strongly under 10 M HCl conditions [HOW56], but not under 8 M HNO_3 conditions [FB64]. Thus, like Mo, the two anion exchange steps of the ^{240}Am isolation procedure would only be effective at isolating Am from Tc if performed under HCl conditions. The behavior of Tc with the Aliquat·336 extractant in nitric acid media has also been studied [LL99]. In these studies, Tc was observed to have a very large affinity for the Aliquat·336 extractant compared with Am. Thus, the 3 M HNO_3 / TEVA® resin separation step would be expected to be effective at isolating Am from Tc. The behavior of Tc on a 10 M HCl TEVA® resin column has not been reported in the literature.

3.4 Scaling the separation for ^{240}Am(n, f) target production

The above described separation procedure for isolating ^{240}Am from proton-irradiated ^{242}Pu was developed and tested on the milligram of Pu scale. Several important factors will need to be considered when planning for the scaling-up of this procedure to isolate tens of nanograms of ^{240}Am from hundreds of milligrams of ^{242}Pu. One such consideration is the volume of separation columns that will be needed for the large scale separation. When using anion exchange chromatography as the first bulk separation step, enough resin will be needed to fully exchange all the Pu ions. Thus, with a 500 mg ^{242}Pu target material and accounting for a safety factor of 10x, a column containing 34 mL of wet anion exchange resin will be necessary. To minimize losses of ^{240}Am in the procedure, the volumes of this and subsequent columns will need to be carefully calculated and minimized. Also, the number of times that the ^{240}Am fraction is transferred between containers will necessarily be kept to a minimum to reduce losses due to absorption to the container walls.

Another important consideration when scaling up the separation procedure will involve how the 500 mg of ^{242}Pu will be contained during the irradiation. These targetry considerations are beyond the scope of this thesis, but will likely have a significant impact on the separation procedure. For example, if it is necessary to dissolve some of the targetry containment along with the ^{242}Pu target material, an additional separation step may be necessary for the isolation of ^{240}Am from the targetry containment material.

A third very important scaling consideration is that of the radiation dose fields emitted by the proton-irradiated ^{242}Pu. This consideration is especially important because the radiation fields produced in this irradiation may be a significant health and safety hazard for the scientists performing the separation, unless careful considerations are given. A significant portion of the irradiated target's radiation field will be coming from the ^{240}Am itself. The γ dose (D_γ, rad/hr) from ^{240}Am can be calculated according Shleien *et al.* [SLAB91] to be

$$D_\gamma = 0.53 \cdot \left(\frac{n_\gamma A E_\gamma}{d^2} \right), \tag{3.2}$$

where A is the activity of nuclide in Ci, E_γ is the energy of photon in MeV, and d is the distance from the source in meters. For 100 nanograms of ^{240}Am, this dose is 155 mrad/h at 30 cm.

The γ and β radiation dose fields from the proton-induced fission products of ^{242}Pu will also be significant. These radiation fields can be calculated using a measurement of the mass distribution of $^{242}\mathrm{Pu}(p, f)$ fission products by Ohtsuki *et al.* [ONT+91]. Using the cross sections reported in this publication, the activity of each fission product was calculated according to Equation 2.3. The γ dose (D_γ, rad/hr) from each fission product was then calculated according to Equation 3.2 and the β dose (D_β, rad/hr) according to

$$D_\beta = 27.9 \cdot \left(\frac{n_\beta A}{d^2}\right), \tag{3.3}$$

where n_β is the intensity of the β emission from Shleien *et al.* [SLAB91]. An analysis according to this method yields a gamma dose of 0.11 rad/h at 30 cm after one day of cooling, and 0.065 rad/h after two days and a beta dose of 11.2 rad/h at 30 cm after one day of cooling, and 6.8 rad/hr after two days.

The radiation fields from the proton-induced fission products can be estimated in a second way. This way estimates the total number of fission events from the ratio of the overall $^{242}\mathrm{Pu}(p, f)$ cross section to $^{242}\mathrm{Pu}(p, 3n)$ cross section. Unfortunately, this value has not been experimentally measured for ^{242}Pu. However, information about this ratio can be inferred from similar studies on other actinide isotopes. McCormick and Cohen [MC54] measured a $(p, f)/(p, 3n)$ cross section ratio of ∼2 for ^{232}Th and Tewes [Tew55] measured it to be ∼40 for ^{238}U. With an assumed $^{242}\mathrm{Pu}(p, f)/^{242}\mathrm{Pu}(p, 3n)$ cross section ratio of 40 and the measured $^{242}\mathrm{Pu}(p, 3n)^{240}\mathrm{Am}$ cross section of 40 millibarns, an expected 10^{16} fissions would occur during an irradiation of 0.5 grams of ^{242}Pu with a 5 microampere proton beam for 3 days. Based on process experience at Los Alamos, the fission products from this many fission events would produce a radiation field of 32 rad/hr at 30 cm after one day of cooling, and 10 R/hr after two days [Vie08].

The above discussed radiation fields are important to consider not only because of their health and safety hazard, but because they will directly affect the separation through radiolytic damage of resins. The process of radiolysis and its effects on radioactive material separations has been reviewed recently by Mincher *et al.* [MM09, MMM09]. The two primary problems caused by radiolysis with anion exchange resins are a decrease in the resin's capacity and in the production of gas, which can disturb the resin bed of the column [Pil86b]. This reference remarks that strongly basic anion exchangers of quaternary ammonium base type are the least radiation stable of the polymeric styrene-DVB resins after absorbing ionizing radiation doses above 10^4 Gray (1 Gy = 1 J/kg = 100 rad = 100 rem for β/γ). This reference also give a G-value of 0.6 for the production of CO_2 by radiodamaged Dowex 1x4 resin in 7 M HNO_3. This G-value is equal to the amount of CO_2 formed per 100 eV of absorbed radiation. The extent to which an ion exchange resin's capacity is decreased as a result of radiation dose is summarized from many references for different resins by Pillay [Pil86a]. This reference collects data from many varied radiolytic studies of the Dowex 1x8 resin. Most of these studies report the loss of exchange capacity after the resin had absorbed an integral dose of $\sim 10^6$ Gy. At these dose levels, the resin exhibited a loss of exchange capacity from 5 – 60%.

The stability of extraction chromatographic resins composed of liquid-liquid extractants surrounding polymer beads has also been studied by Chiarizia and Horwitz [CH00] In this publication, the Dipex extraction chromatography resins were irradiated with 2.5×10^5 – 2×10^6 Gy of absorbed dose. At 2.5×10^5 Gy, the resin's affinity for some ions changed by up to ∼15%. However, the acid/base dependency of the distribution ratios remain unchanged, indicating that the exchanging functional groups are remaining intact. The capacity of the resin may also be adversely affected by radiolysis. The capacity of the Dipex-2 resin was decreased by 24% after receiving 2.5×10^5 Gy of dose.

A radiation field of 32 rad/hr at 30 cm will be $\sim1.2\times10^3$ Gy/hr at 0.5 centimeter, a typical distance for column chromatography. Assuming a column run time of 1 hour, the resin would then absorb about 1.2×10^3 Gy of adsorbed dose. The volume of CO_2 (calculated using the G-value from [Pil86b]) that is expected to be produced if 34 mL of wet Bio-Rad 1 resin were to absorb this dose is 68 μL of CO_2 gas. It is not likely that this volume of CO_2 is enough to disrupt the resin bed of a 34 mL column. Also, while it is likely that there would be some decrease in capacity for the anion exchange and TEVA resins, it is likely that this will be below 10%, as the expected dose to the resin is significantly lower than the dose levels studied in the above discussed references.

3.5 Summary of Part I

Chapter 1 introduces background related to investigating a new production reaction and purification procedure for ^{240}Am. It begins with the motivation behind the measurement of this isotope's neutron-induced fission cross section at low (1 eV – 100 keV) neutron energies. It goes on to discuss the nuclear reactions previously used to produce ^{240}Am. Because none of these reactions are suitable for producing enough material for a neutron-induced fission target, a new nuclear reaction for the production of ^{240}Am was investigated. The $^{242}\mathrm{Pu}(p, 3n)^{240}$Am nuclear reaction was selected because of its high predicted ^{240}Am production cross section.

Chapter 2 discusses the first experimental studies of the $^{242}\mathrm{Pu}(p, 3n)^{240}$Am nuclear reaction performed at the LBNL 88-Inch Cyclotron. Cross sections on the order of 40 millibarns were measured for the production of ^{240}Am. While these cross sections are lower than predicted, this nuclear reaction remains the most viable for producing a target of tens of nanograms of ^{240}Am for a LSDS neutron-induced fission cross section measurement.

Chapter 3 summarizes the characteristics of the necessary chemical procedure for isolating tens of nanograms of ^{240}Am from hundreds of milligrams of proton-irradiated ^{242}Pu. Such an effective separation procedure is necessary for the production of pure ^{240}Am target material for a neutron-induced fission cross section measurement. A suitable separation procedure is introduced, discussed, and experimentally tested using tracer-scale ^{239}Pu, ^{241}Am, and model fission products ^{95}Zr, ^{95}Nb, ^{125}Sb, and ^{152}Eu. Future work will verify the separation factors and Am yields necessary to use the separation procedure for the isolation of tens of nanograms of ^{240}Am from hundreds of milligrams of proton-irradiated ^{242}Pu.

Part II

New Superheavy Element Isotopes: ^{242}Pu(^{48}Ca,$5n$)^{285}114

Chapter 4

Introduction

Part I of this dissertation discusses research investigating a new production reaction and purification procedure for producing ^{240}Am. This research utilized several nuclear chemistry techniques to pursue the applied goal of working towards performing a nuclear reaction cross section measurement applicable to the fields of post-detonation nuclear forensics and science-based nuclear stockpile stewardship. In Part II of this dissertation, many of these same techniques, including molecular deposition of plutonium, low energy ion bombardment, and identification of radioactive isotopes through nuclear spectroscopic techniques, are used to pursue the goal of exploring the limits of nuclear stability.

One of the fundamental goals of chemists throughout history has been the study of the chemical properties of the elements and how the similarities and differences in their behavior can be understood. These goals date back to the 1600s when Hennig Brand performed the first chemical discovery of an element by isolating phosphorus from urine [Wee33]. The first progress in organizing the elements by their relative weights and chemical properties was performed by Johann Döbereiner [Pra50]. As early as 1817, Döbereiner identified the existence of"triads" of elements which exhibit similar chemical behavior and have the property that the atomic weight of the middle element closely matched the average of the atomic weights of the two other elements. These observations helped lay the groundwork for what became the periodic table of the chemical elements, which was first described in a relatively modern form by Dmitri Ivanovich Mendeleev in the late 1869 [Men69]. The most recent shift in the way the chemical elements are tabulated came with Glenn T. Seaborg's discovery of the transuranium elements and his reorganization of the periodic table [Sea46].

Work in this same vein continues today with experiments performed by nuclear chemists investigating the physical and chemical properties of the transactinide elements. The transactinide elements are those elements with $Z \geq 104$ which begin under the transition metals in the seventh row of the periodic table as shown highlighted in Figure 4.1. The elements highlighted in blue, connected with the main body of the periodic table, are elements which have been recognized as discovered by the International Union of Pure and Applied Chemistry

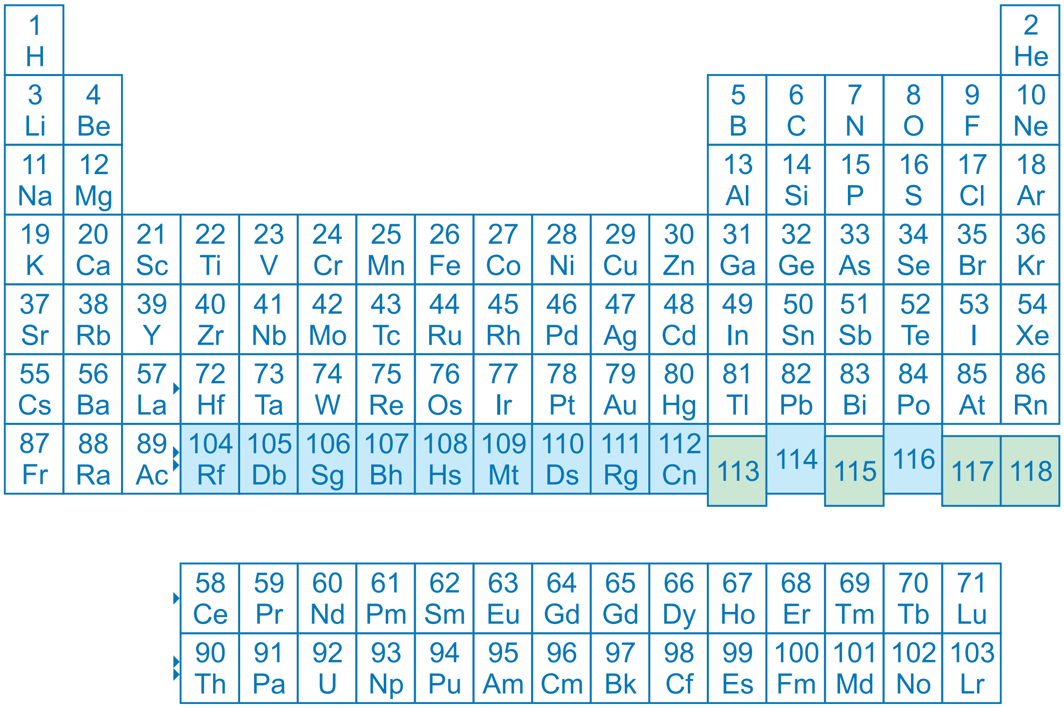

1 H																	2 He
3 Li	4 Be											5 B	6 C	7 N	8 O	9 F	10 Ne
11 Na	12 Mg											13 Al	14 Si	15 P	16 S	17 Cl	18 Ar
19 K	20 Ca	21 Sc	22 Ti	23 V	24 Cr	25 Mn	26 Fe	27 Co	28 Ni	29 Cu	30 Zn	31 Ga	32 Ge	33 As	34 Se	35 Br	36 Kr
37 Sr	38 Rb	39 Y	40 Zr	41 Nb	42 Mo	43 Tc	44 Ru	45 Rh	46 Pd	47 Ag	48 Cd	49 In	50 Sn	51 Sb	52 Te	53 I	54 Xe
55 Cs	56 Ba	57 La	72 Hf	73 Ta	74 W	75 Re	76 Os	77 Ir	78 Pt	79 Au	80 Hg	81 Tl	82 Pb	83 Bi	84 Po	85 At	86 Rn
87 Fr	88 Ra	89 Ac	104 Rf	105 Db	106 Sg	107 Bh	108 Hs	109 Mt	110 Ds	111 Rg	112 Cn	113	114	115	116	117	118
			58 Ce	59 Pr	60 Nd	61 Pm	62 Sm	63 Eu	64 Gd	65 Gd	66 Dy	67 Ho	68 Er	69 Tm	70 Tb	71 Lu	
			90 Th	91 Pa	92 U	93 Np	94 Pu	95 Am	96 Cm	97 Bk	98 Cf	99 Es	100 Fm	101 Md	102 No	103 Lr	

Figure 4.1 Periodic table of the elements

(IUPAC) / International Union of Pure and Applied Physics (IUPAP) Transfermium Working Group (TWG) [RGH+93, KNPV01, KNPV03, BGK+09, BKN+11]. Those highlighted in green and slightly removed from the main table have been claimed but not confirmed.

The study of the transactinide elements is a very difficult pursuit because the elements are produced very rarely in heavy-ion-induced nuclear reactions. In extreme cases, these production rates are so low as to require months of accelerator time to observe a single atom. In addition, the large amount of other reaction products results in an enormous background from which transactinides must be physically or chemically separated before detection. Also, all identified transactinide isotopes are radioactive with relatively short half-lives, generally from tens of milliseconds to tens of seconds, requiring elaborate nuclear detection setups for their identification. The particle accelerators, chemical/physical isolation apparatuses, and detection setups necessary for their identification are generally expensive and exist only in a small number of institutions around the world, including Berkeley, the GSI Helmholtzzentrum für Schwerionenforschung in Darmstadt, Germany, the Flerov Laboratory of Nuclear Reactions (FLNR) at the Joint Institute for Nuclear Research (JINR) in Dubna, Russia, and the Institute of Physical and Chemical research (RIKEN) in Saitama, Japan. These limitations make the field of study small and competitive, with controversy surrounding many of the major discoveries.

Studying the chemistry of the transactinide elements is especially difficult. Low production rates and short half-lives necessitate chemical studies which employ simple and fast separation techniques such as liquid or gas chromatography or liquid-liquid extraction coupled to detection setups which can detect and determine chemical information at an atom-at-a-time scale. Matthias Schädel has recently reviewed the state of the chemistry of the superheavy elements [Sch06]. The physics and chemistry of the transactinide elements are closely intertwined because nuclear reactions for the production of a transactinide element must always be discovered and well characterized before they can be used to effectively study the element's chemistry. The work in this part of the dissertation focuses on studying the production nuclear reaction for a new isotope of element 114. Studying this nuclear reaction furthers the fundamental understanding of the stability of the transactinide elements and the nuclear reactions which produce them, concepts necessary for future transactinide chemical studies.

4.1 Parent-daughter correlation technique for identifying transactinide elements

The first three transactinide elements, rutherfordium, dubnium, and seaborgium, were discovered in essentially contemporaneous experiments performed at Berkeley and JINR in Dubna in the late 1960s and early 1970s. Credit for the discovery of the elements is shared for Rf and Db, while it is given solely to Berkeley for Sg [RGH$^+$93]. The experiments involved nuclear reactions such as the following:

$$^{13}_{6}\mathrm{C} + ^{249}_{98}\mathrm{Cf} \longrightarrow ^{259}_{104}\mathrm{Rf} + 3\,^{1}_{0}\mathrm{n}, \tag{4.1}$$

$$^{15}_{7}\mathrm{N} + ^{249}_{98}\mathrm{Cf} \longrightarrow ^{260}_{105}\mathrm{Db} + 4\,^{1}_{0}\mathrm{n}, \tag{4.2}$$

$$^{18}_{8}\mathrm{O} + ^{249}_{98}\mathrm{Cf} \longrightarrow ^{263}_{106}\mathrm{Sg} + 4\,^{1}_{0}\mathrm{n}. \tag{4.3}$$

In these experiments, nuclear reaction products were collected and monitored for α or spontaneous fission (SF) radiation. The results from Berkeley were especially convincing because of their sensitivity to detecting α-decay parent-daughter relationships. In these experiments, the Berkeley group would transport the nuclear reaction products onto a rotating target wheel which would periodically step to place the nuclear reaction products in front of a series of α detectors. After measuring α particles from atoms deposited on the wheel, the wheel detectors were shuttled off to be placed face-to-face with a second set of detectors to monitor the decay of radioactivity which had been ejected from the nuclear reaction deposits on the wheel onto the face of the wheel detectors. This technique allowed for the connection of the suspected $^{259}_{104}\mathrm{Rf}$ decays with the previously known decay half-life and energy of $^{255}_{102}$No [GNH$^+$69]. This technique was also used to identify the $^{263}_{106}$Sg-$^{259}_{104}$Rf-$^{255}_{102}$No parent-daughter-granddaughter relationship in the Sg discovery experiment [GNA$^+$74].

The parent-daughter correlation identification technique has significant advantages in the study of the transactinide elements. First, experiments benefit from a decreased sensitivity to background because the random rate of correlated series of alpha decays is significantly lower than the random rate for single events. In addition, this technique allows for the stepwise expansion of the chart of the nuclides, using the decay properties of nuclides which have been solidly established to determine those for a previously unknown nuclide. This technique has become a heavily used standard in the field of transactinide element studies.

4.2 Nuclear reactions for producing transactinide elements

The nuclear reactions used in these early studies involved the bombardment of highly radioactive actinide targets with low-Z projectile ions at energies that produced compound nuclei with such an excitation energy that 3 – 6 neutrons were evaporated. This type of nuclear reaction for the production of transactinides has been since deemed "hot fusion" because of the high excitation energy with which the compound nucleus is formed. This class of nuclear reaction is in contrast with a second class which were first observed in 1975 by Oganessian *et al.* [OIDT75]. This second class of reactions involved bombardments of stable Pb and Bi targets with medium mass ($Z \geq 20$) projectiles at energies that produced compound nuclei with low excitation energies such than only 1 – 3 neutrons were evaporated. These reactions have been deemed "cold fusion" reactions because of the low excitation energy of the produced compound nucleus.

Starting in the mid-1970s, important contributions to the field of transactinide physics and chemistry were made by the GSI Helmholtzzentrum für Schwerionenforschung in Darmstadt, Germany. Through the use of the velocity filter SHIP (Separator for Heavy Ion Products) [MFH$^+$79], coupled to the GSI UNILAC heavy-ion linear accelerator, they were able to produce, isolate, and identify six new transactinide elements, Bh [MHH$^+$81, MAH$^+$89], Mt [MAH$^+$82, MRH$^+$84, MHH$^+$88], Hs [MAF$^+$84, MAB$^+$87], Ds [HNH$^+$95c, Hof03], Rg[HNH$^+$95a, HHA$^+$02], and Cn [HNH$^+$96, HHA$^+$02] using the following nuclear reactions, respectively:

$$^{54}_{24}\mathrm{Cr} + {}^{209}_{83}\mathrm{Bi} \longrightarrow {}^{262}_{107}\mathrm{Bh} + {}^{1}_{0}\mathrm{n}, \tag{4.4}$$

$$^{58}_{26}\mathrm{Fe} + {}^{209}_{83}\mathrm{Bi} \longrightarrow {}^{266}_{109}\mathrm{Mt} + {}^{1}_{0}\mathrm{n}, \tag{4.5}$$

$$^{58}_{26}\mathrm{Fe} + {}^{208}_{82}\mathrm{Pb} \longrightarrow {}^{265}_{108}\mathrm{Hs} + {}^{1}_{0}\mathrm{n}, \tag{4.6}$$

$$^{62}_{28}\mathrm{Ni} + {}^{208}_{82}\mathrm{Pb} \longrightarrow {}^{269}_{110}\mathrm{Ds} + {}^{1}_{0}\mathrm{n}, \tag{4.7}$$

$$^{64}_{28}\mathrm{Ni} + {}^{209}_{83}\mathrm{Bi} \longrightarrow {}^{272}_{111}\mathrm{Rg} + {}^{1}_{0}\mathrm{n}, \tag{4.8}$$

$$^{70}_{30}\mathrm{Zn} + {}^{208}_{82}\mathrm{Pb} \longrightarrow {}^{277}_{112}\mathrm{Cn} + {}^{1}_{0}\mathrm{n}. \tag{4.9}$$

Most recently, a team of scientists using the gas-filled recoil separator GARIS at RIKEN in Saitama, Japan have claimed the production of element 113 in the cold fusion irradiation of $^{209}_{83}$Bi with $^{70}_{30}$Zn [MMK$^+$04, MMK$^+$07].

Cross sections for both hot and cold fusion reactions drop rapidly with increasing Z of the product. Hot fusion reaction cross sections for elements 104 – 110 drop 4 –5 orders of magnitude to hundreds of femtobarns. Cross sections for the above discussed cold fusion reaction producing element 113 are measured to be on the order of tens of femtobarns, requiring accelerator time for months to years to complete an experiment.

Starting in the late-1970s, researchers began using the doubly-magic ^{48}Ca isotope as the projectile in the irradiation of actinide targets to attempt to make transactinide elements. ^{48}Ca beams were used due to the fact that this isotope is especially neutron-rich, allowing access to a previously unreachable area of neutron-rich transactinide elements which nears the predicted spherical shell closure at $Z = 114$, $N = 184$ [MPS01, MHPS03, MPS03]. In addition, the isotope's large negative mass excess allows for the production of compound nuclei with low excitation energies compared with other hot fusion reactions. Because of this fact, irradiation of actinide targets with ^{48}Ca beams have been deemed "warm fusion" reactions.

The investigation of ^{48}Ca irradiations of actinide targets in the 1970s and 1980s only yielded upper limits for cross sections of transactinide production [HLW$^+$77], [IHN$^+$78, OBB$^+$78, AAB$^+$85]. These studies implemented both chemical and physical separation techniques to look for a transactinide products with a large range of half-lives. Only recently have experimental techniques become sensitive enough to observe nuclear reaction products produced with the small cross sections of ^{48}Ca-irradiations of actinide targets. The production of neutron-rich isotopes of element 112, 113, 114, 115, 116, 117 and 118 were first observed in ^{48}Ca bombardments of actinide targets at JINR in Dubna in the late 1990s and 2000s [Oga07, OAB$^+$10]. The recoils from these nuclear reactions were detected using the Dubna gas-filled recoil separator (DGFRS) to physically isolate and identify the nuclear reaction product of interest from other reaction products and unreacted beam. The cross sections observed for the production of transactinide elements in ^{48}Ca-bombardments of actinide targets are significantly higher than those expected from extrapolation of the hot fusion cross section trends. Figure 4.2 details this trend by plotting experimental cross section measurements for $3n$ (red squares), $4n$ (yellow circles), and $5n$ (blue triangles) reaction cross sections for the production of transactinide elements (see Appendix C for references). The arrows are drawn to guide the eye to the cross section trends for hot fusion reactions using light projectiles from C to S and actinide targets. The cross sections for ^{48}Ca plus actinide targets producing $Z > 111$ do not follow this trend and are on the order of picobarns.

The nuclear reaction products of these warm fusion reactions are much more neutron rich compared with the nuclear reaction products of other hot and cold fusion reactions.

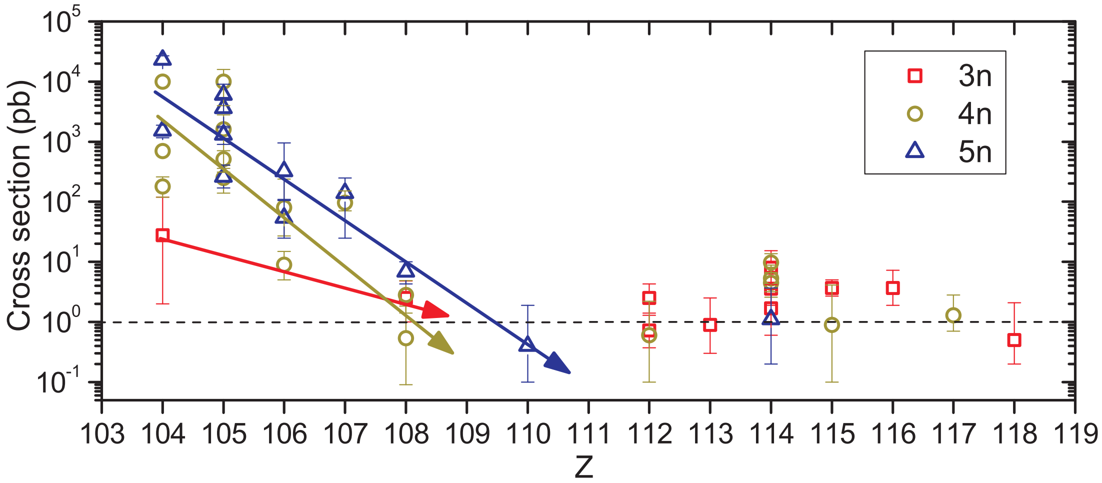

Figure 4.2 Experimental hot and warm fusion reaction cross sections as a function of atomic number of the product

Thus, they do not alpha decay into previously discovered isotopes of lighter transactinide elements, causing significant problems with assigning the observed correlated alpha decay chains to a specific nuclide. The final assignments as summarized in [Oga07] were only determined after an in depth analysis of the results from irradiation of various isotopes of U, Np, Pu, Am, Cm, Bk, and Cf at a variety of compound nucleus excitation energies. The body of six new elements and 52 new isotopes discovered through this work now form a self consistent island of isotopes at the heaviest, most neutron-rich end of the chart of the nuclides. However, until an explicit mass or atomic number measurement of one of these isotopes is performed, it is still possible that the entire island may shift by one or two units of Z or A.

4.3 Details of previous element 114 studies

The production of element 114 at the DGFRS was first reported as a result of the ^{244}Pu(^{48}Ca,3n)^{289}114 nuclear reaction [OUL+99]. This work reported one correlated α-decay chain attributed to the decay of ^{289}114 and its daughters ^{285}Cn and ^{281}Ds, followed by the spontaneous fission of ^{277}Hs with reported lifetimes of 21 s, 15.4 min, 1.6 min, and 16.5 min, respectively. Soon after this first report, the decay of ^{288}114 was reported based on the observation of two correlated α-decay chains, complosed of nuclides with significantly shorter lifetimes than those previously reported [OUL+00a]. These two decays were seemingly corroborated as similar decay properties were observed in the daughter of one event assigned to ^{292}116 produced in the ^{48}Ca bombardment of ^{248}Cm [OUL+00b].

Table 4.1 Decay properties of element 114 isotopes and their daughters.

Z	A	Decay mode, branch (%)	Half-life	Reference
114	289	α	$2.1^{+0.8}_{-0.4}$ s	[DSY+10]
	288	α	$0.69^{+0.17}_{-0.11}$ s	[DSY+10]
	287	α	$0.48^{+0.16}_{-0.09}$ s	[Oga07]
	286	α: 50, SF: 50	$0.13^{+0.04}_{-0.02}$ s	[Oga07]
112	285	α	29^{+11}_{-6} s	[DSY+10]
	284	SF	99^{+24}_{-16} ms	[DSY+10]
	283	α: 100, SF: ≤ 10	$3.8^{+1.2}_{-0.7}$ s	[Oga07]
	282	SF	$0.82^{+0.30}_{-0.18}$ ms	[Oga07]
110	281	α: 9^{+16}_{-7}, SF: 91^{+7}_{-16}	13^{+5}_{-3} s	[DSY+10]
	279	α: 10, SF: 90	$0.20^{+0.05}_{-0.04}$ s	[Oga07]
108	277	SF	3^{+15}_{-1} ms	[DSY+10]
	275	α	$0.19^{+0.22}_{-0.07}$ s	[Oga07]
106	271	α: 70, SF: 30	$1.9^{+2.4}_{-0.6}$ min	[Oga07]
104	267	SF	$1.3^{+2.3}_{-0.5}$ h	[Oga07]

More recently, detailed studies of the ^{242}Pu(^{48}Ca,$3-4n$)^{287,286}114 [OUL+04a] and ^{244}Pu (^{48}Ca,3-5n)^{289,288,287}114 nuclear reactions [OUL+04b] performed with the DGFRS have led to the reassignment of the decay chains originally attributed to ^{288}114. Because the original decay properties observed for ^{289}114 [OUL+99] were not reproduced, the ^{288}114 chains reported in [OUL+00a] were reassigned to ^{289}114. Multiple events with new α-decay and SF decay properties were observed and assigned to ^{286}114, ^{287}114 [OUL+04a], and ^{288}114 [OUL+04b]. The assignments of these observed chains were corroborated with production of the Cn daughters in ^{48}Ca-irradiations of ^{238}U and production of the α-decaying parent isotopes, $^{290-294}$116, in ^{48}Ca-irradiations of ^{245,248}Cm. The results of these irradiations and the interpretations of the results are summarized in [Oga07]. Maximum cross sections for the $3n$ and $4n$ evaporation products with ^{244}Pu targets were measured to be $1.7^{+2.5}_{-1.1}$ and $5.3^{+3.6}_{-2.1}$ picobarn, respectively, and for the $3n$ and $4n$ evaporation products with ^{242}Pu targets to be $3.6^{+3.4}_{-1.7}$ and $4.5^{+3.6}_{-1.9}$ picobarn, respectively.

The decay properties, cross sections and assignments of these isotopes of element 114 have been independently verified in ^{48}Ca irradiations of ^{242}Pu and ^{244}Pu targets using the Berkeley Gas-filled Separator (BGS) at Berkeley and the TransActinide Separator and Chemistry Apparatus (TASCA) He-filled recoil separator at GSI, respectively [SGD+09, EGB+10, DSY+10, GDS+11]. Table 4.1 shows the verified decay properties from [Oga07, DSY+10].

Chapter 5

Experimental Setup: Berkeley Gas-filled Separator

The experiment described in Part II of this dissertation was performed using the Berkeley Gas-filled Separator (BGS) at the LBNL 88-Inch Cyclotron. The BGS has been described in detail previously [Fol04, FGD$^+$04, GGL$^+$03, GLP$^+$05, LGP$^+$02]. It uses three magnets to achieve physical separation of energetic ions based on their differing magnetic rigidities in dilute helium gas. Using this instrument, complete-fusion evaporation residues (EVRs) can be isolated from the deluge of unreacted projectile ions, transfer and other unwanted nuclear reaction products.

The BGS is shown schematically in Figure 5.1. The beam enters the BGS target box (upper left of Figure) after traveling through a triplet of quadrupole focusing magnets, a collimator, and a 1 meter acoustic delay line. The latter of these pre-BGS features was installed just outside the BGS target chamber along with a pressure sensor for the fast-closing shutter valve described in Section 2.2 to protect the cyclotron from contamination with radioactive target material in the event of a target or beamline failure. Upon entering the target box, the ion beam passes through a through a 45 ± 5 μg/cm^2 carbon window separating the 67-Pa He gas inside BGS from the beam-line vacuum.

5.1 Targets

Once inside the target chamber, the beam passes through one of several types of targetry compatible with BGS. This targetry includes 2 cm diameter stationary targets, and rotating target wheels with 35.6-cm and 9.5-cm diameters. Because of more effective cooling, the rotating target wheels are able to withstand significantly higher beam intensity (on the order of a particle microampere) compared with the stationary targets (10 – 100 particle nanoamperes).

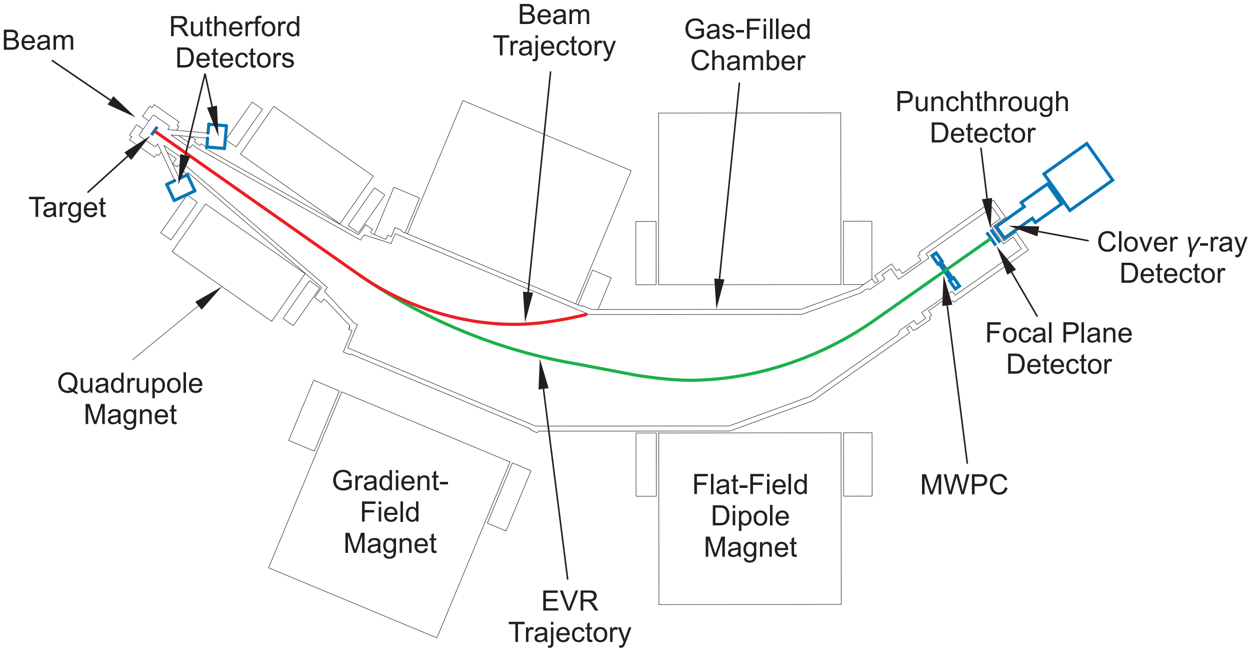

Figure 5.1 Schematic of Berkeley Gas-filled Separator

For irradiations of ^{242}Pu targets in the BGS, a new transuranium target facility was designed and assembled. This facility consisted of a ventilated glovebox, shown on the left in Figure 5.2, which was installed on top of the BGS target box. Inside, a cassette containing the ^{242}Pu target wheel was mounted through the glovebox floor into the beam line. The cassette, shown open on the right in Figure 5.2, was assembled in a fumehood, and then closed for transport into the BGS transuranium target facility glovebox. Once inside the glovebox, several small covers were removed, opening holes in the cassette large enough for beam to travel through the target and nuclear reaction products to travel out. This facility allowed for handling the relatively radioactive target nuclide ^{242}Pu with very limited risk for radioactive contamination of the externals of BGS. These controls for external contamination control complimented the previously described acoustic delay line and fast-closing shutter valve which controlled the spread of internal cyclotron plutonium contamination.

The target wheel inside the cassette was composed of four banana-shaped target segments mounted on the periphery of a 9.5-inch diameter wheel. Each target segment was composed of a 2 – 2.4 μm Ti foil supported by a 16-mil stainless steel frame around a 5.5 cm^2 banana-shaped opening. ^{242}Pu was electrodeposited from isopropanol solutions in a procedure very similar to that discussed in Section 2.1. The electrodeposition cell used to produce these banana-shaped segments is shown on the left and middle of Figure 5.3. As apparent in the figure, the deposition solution reservoir, which is made from polyethyl

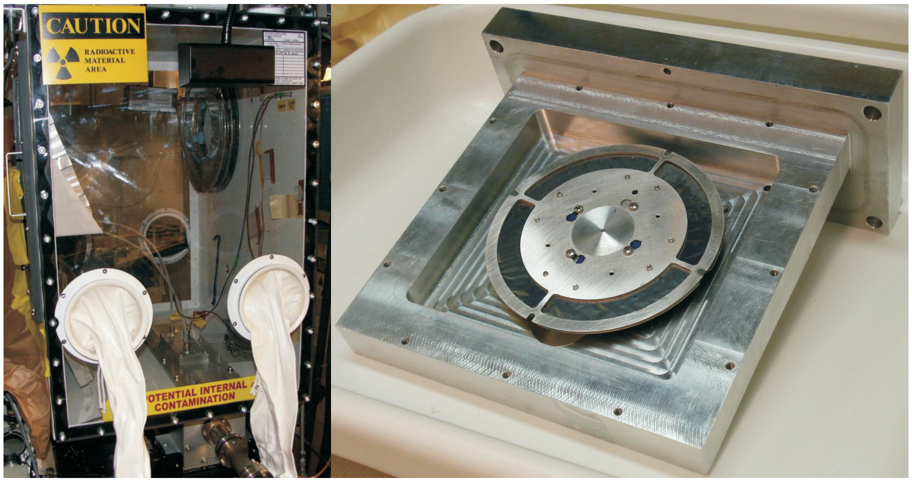

Figure 5.2 Photographs of the ventilated glovebox and target cassette, parts of the new BGS transuranium target facility.

ether ketone, is situated between the target backing on a grounded aluminum plate and a palladium anode which is biased with positive voltage.

The isopropanol deposition solutions used in this larger electrodeposition cell were prepared identically to those described in Section 2.1 with the exception that a larger quantity of evaporated ^{242}Pu stock was dissolved in 23 mL of isopropanol. A small teflon-coated stir bar was placed inside plating solution reservoir and used to agitate the plating solution for 1 minute at 10 minute intervals during the electrodeposition process. When electrodepositing these larger targets, voltage was ramped up over 10 – 15 minutes to a maximum 150 – 200 V. These voltage limited depositions resulting in currents of 2 – 3 mA (0.35 – 0.55 mA/cm^2).

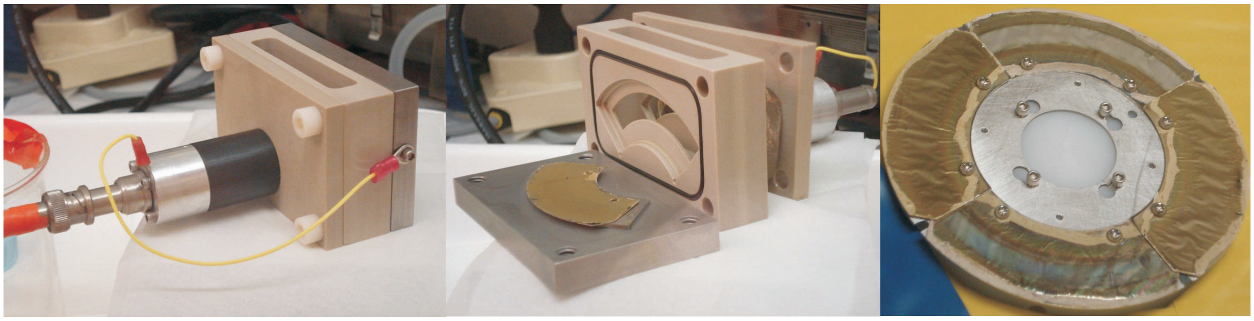

Figure 5.3 Photographs of the banana-shaped ^{242}Pu target electrodeposition cell and assembled target wheel.

Electrodepositions were performed for 180 – 300 minutes until the radioactivity in the plating solution had dropped to one tenth of the initial activity. After deposition, the targets were baked as previously described in Section 2.1. The right photo shows the assembled ^{242}Pu target wheel with two irradiated (white) and two non-irradiated (metallic) ^{242}Pu targets.

5.2 Magnets

After passing through the targets, the ion beam and nuclear reaction products are transported into the main magnet chamber of the BGS with the momentum of the beam. The nuclear reaction products studied in the BGS generally have very small, sub-nanobarn reaction cross sections. Thus, the very small number of nuclear reaction products of interest must be physically separated from the large amount of unreacted beam and unwanted nuclear reaction products for detection. The BGS accomplishes this separation based on the ion's differing magnetic rigidity.

When charged particles travel through magnetic fields, they experience the Lorentz force as described by $\vec{F} = q(\vec{v} \times \vec{B})$, where $\vec{F}$ is the force vector, q is the charge on the particle, $\vec{v}$ is the velocity vector of the particle, and $\vec{B}$ is the magnetic field vector. For particles traveling perpendicular to a magnetic field, as, on average, particles in the BGS are, this equation can be written in its scalar form, $F = qvB$. As the Lorentz force causes the charged particles to follow a curved path, this force is also equal to the centripetal force equation, $F = (mv^2)/\rho$, where m is the mass of the particle and ρ is the radius of curvature. Setting these two force equations equal to each other and performing a simple algebraic rearrangement gives $B\rho = mv/q$. This quantity of $B\rho$ is called the magnetic rigidity of a charged particle. Because the radius of curvature of the BGS is well defined by its physical geometry, changing the magnetic field inside BGS allows for the selection of ions at the focal plane based on their magnetic rigidity.

As shown in the BGS schematic in Figure 5.1, the first of three magnets is a quadrupole magnet which vertically focuses and horizontally defocuses the particles. Placing the quadrupole magnet immediately after the target chamber results in the BGS having an relatively large angular acceptance for nuclear reaction products, 45 msr. However, because this focusing magnet is so far away from the focal plane detector, the image at the focal plane has a large vertical distribution, necessitating a large focal plane detector.

After the focusing quadrupole magnet, the particles enter the gradient-field dipole magnet and then the flat-field dipole magnet. It is in these sections of the BGS that particles with different magnetic rigidities are separated based on their horizontal dispersion. The BGS has a target – focal plane bend angle of 70°, resulting in very large horizontal dispersion of different magnetic rigidities. Changing the magnetic rigidity settings of the BGS by 1% results in moving the focal plane image horizontally about 1.8 cm.

5.2.1 Magnetic rigidity of ions in helium

The ions traveling through the BGS are separated by their differing magnetic rigidities equal to mv/q. The mass can be obtained from mass tables or estimated as the nuclide's mass number. The velocity can easily be calculated from the kinematics of the nuclear reaction. The charge, however, is a more complicated matter. Nuclear reaction products recoil out of the target with a variety of charge states [ND68]. If the BGS were operated as a vacuum separator, each of these charge states would require a different magnet setting to traverse the separator and reach the focal plane. However, the BGS is filled with 67 Pa of helium. When energetic ions travel through the helium-filled chamber, they undergo a large number of charge-exchanging collisions. These collisions rapidly cause the ion to take upon a well defined average charge state, $\bar{q}$. This results in the nuclear reaction products traversing the separator with magnetic rigidity equal to $mv/\bar{q}$.

The average charge state, $\bar{q}$, of heavy ions in dilute He has been measured and summarized by Ghiorso *et al.* [GYL$^+$88]. This work observed a general $\bar{q} \propto vZ^{1/3}$ trend with significant sinusoidal deviations due to electronic shell effects of the ions. Gregorich *et al.* measured the average charge state of ions with $Z = 99 - 111$ with the BGS [GLP$^+$05] and, together with data from [GYL$^+$88, Arm, WB73], made a global fit to $\bar{q}$, including a sinusoidal correction for the shell structure of the stripped ion. Because this correction involves assumptions about electronic shell structure, it is only applicable for ions in the sixth and seventh periods of the periodic table. If $x = (v/v_0)Z^{1/3}$ where $v_0 = 2.1877 \times 10^6$ m/s is the Bohr velocity, this fitting equation is

$$\bar{q} = mx + b + d\sin\left(\frac{2\pi}{32}\Big(Z - \big(mx+b\big) - f\Big)\right), \tag{5.1}$$

where the best fit parameters were $m = 0.641$, $b = -0.235$, $d = 0.517$, and $f = 74.647$. At ion velocities where $(v/v_0) < 1.6$, this fitting equation requires an additional empirical linear correction factor equal to

$$q_{\text{slow}}(v/v_0 < 1.6) = \frac{\bar{q}(v/v_0 = 1.6) - 2.5}{1.6}(v/v_0) + 2.5. \tag{5.2}$$

Figure 5.4 shows the effectiveness of this fitting equation for experimental data. The open black squares are data taken at Berkeley, Dubna, and Julich [Arm]. The open red circles are data taken using the BGS [GLP$^+$05]. The open green triangles are data taken by Wittkower and Betz [WB73]. The closed blue square is from the TASCA He-filled recoil separator at GSI [DSY$^+$10]. As observed in this plot, this fitting parameterization does a good job of fitting the experimental data, especially in intermediate x of 8 – 13. One exception to this is the closed blue point from the experimental study of element 114 isotopes produced in ^{48}Ca-bombardment of ^{244}Pu targets using TASCA [DSY$^+$10]. In this study, element 114 was observed to have a magnetic rigidity of (2.29 ± 0.11) Tm, while the above described fitting

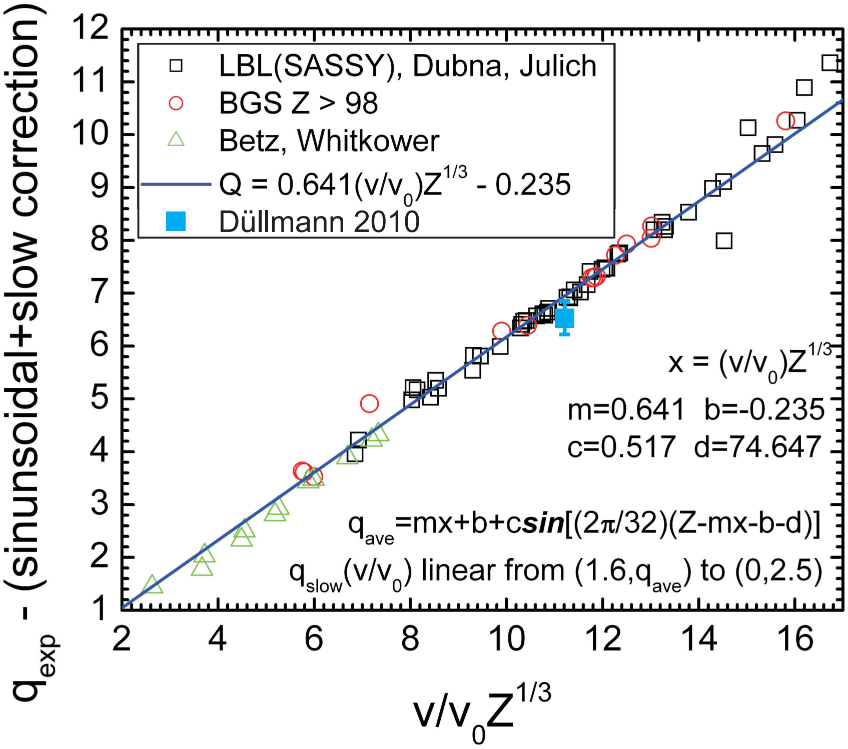

Figure 5.4 Experimental average charge of heavy ions passing through dilute helium corrected by several factors.

equation predicts the significantly lower element 114 EVR magnetic rigidity of 2.15 Tm. With the BGS's large dispersion, this 6.5% difference in magnetic rigidity results in a significant 13 cm difference in focal plane image location.

Once the average charge state, $\bar{q}$, is estimated or measured, the magnetic rigidity for the particle can easily be calculated as $B\rho = mv/\bar{q}$. The current (in A) for the three BGS magnets can be calculated with the following equations as a function of $B\rho$ and the experimentally determined optimal ratio, $R = I(\mathrm{M2})/I(\mathrm{M1}) = 1.5$ [Dra09].

$$I(\mathrm{Q1}) = 795 B\rho \,\frac{\mathrm{A}}{\mathrm{T\cdot m}} \tag{5.3}$$

$$I(\mathrm{M1}) = \frac{B\rho}{0.002467 + 0.002016R}\,\frac{\mathrm{A}}{\mathrm{T\cdot m}} \tag{5.4}$$

$$I(\mathrm{M2}) = \frac{B\rho}{\dfrac{0.002467}{R} + 0.002016} \frac{\mathrm{A}}{\mathrm{T} \cdot \mathrm{m}} \tag{5.5}$$

These equations assume a linear relationship between magnetic field strength and magnet current. This assumption is good except when a magnet reaches saturation, resulting in the trend deviating from linearity. Gregorich has collected data using a Hall probe to monitor the effects of saturation inside the BGS magnets [Gre]. These data are used to correct the above method for calculating magnet currents for $B\rho >\sim 2.15$ Tm.

The efficiency (ϵ) of the BGS for transporting EVRs of interest from the target to the focal plane detector can be estimated using a Monte Carlo simulation which has been detailed previously [GGL+03]. Based on the comparison of the size and shape of the modeled and experimental focal plane distributions of the ^{48}Ca + $^{206-208}$Pb reactions, an uncertainty of $\Delta\epsilon/\epsilon = 10\%$ for $v/v_0 >\approx 2.0$ and $\Delta\epsilon/\epsilon = 30\%$ for $v/v_0 < 1.6$ has been estimated for the BGS efficiencies calculated in this manner [GLP+05].

5.3 Multiwire proportional counter

A multiwire proportional counter (MWPC) was placed in the flight path of compound nucleus EVRs traveling between the BGS magnets and the focal plane detector. The MWPC was composed of 3 wire grid planes made from 0.4 mil diameter gold-plated tungsten wire wound around 1.5 mm thick printed circuit boards. Outer grids were connected to ground and the inner grid was baised to +520 V to serve as an anode for ionized particles. The open front and back of the MWPC were covered with thin plastic films, typically made from 0.5 – 2 μm polypropylene or Mylar, which were sealed to the MWPC with vacuum grease. The MWPC was filled with 370-Pa isobutane controlled through a MKS Instruments, Inc. differential pressure control system composed of a model MKS223B differential pressure valve, MKS type 250B controller, and MKS0248A valve. Two photos of the MWPC inside the BGS detector chamber are shown in Figure 5.5.

MWPC analog signals and MWPC – focal plane time of flight (ToF) signals were used to tag focal plane events resulting from the implantation of particles from the BGS. This allowed for discrimination between these implantation events and events resulting from particles emitted from radioactive decay of focal-plane-implanted atoms. This tagging resulted in a significant reduction in background in the focal plane detector's α-particle spectrum.

5.4 Focal plane detector

After traveling through the MWPC, compound nucleus EVRs reach the focal plane detector (FPD). The FPD, which has been previously described in detail [Fol04, FGD+04], is shown in Figure 5.6 and is composed of three detectors, the implantation detector (ID),

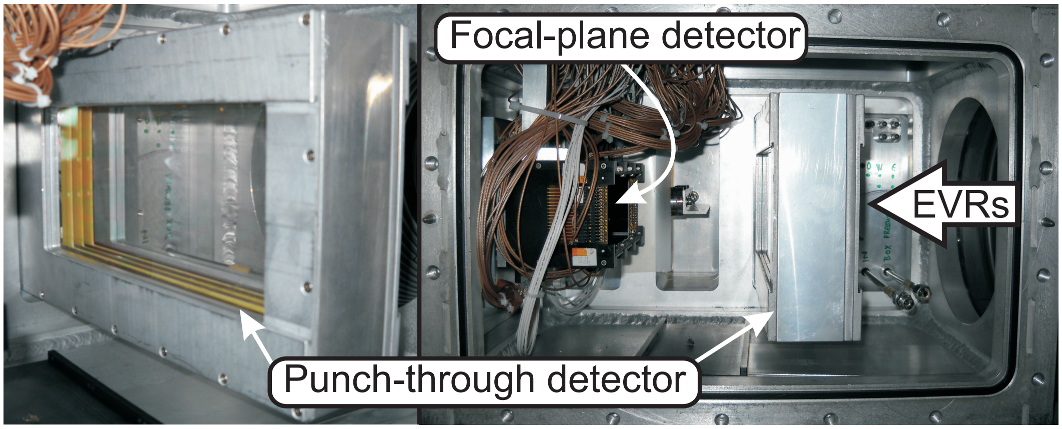

Figure 5.5 Photographs of multiwire proportional counter in the BGS detector chamber.

the punch-through detector (PTD), and the upstream detector (UD). Each of these detectors is composed of a number of 6 cm × 6 cm Si cards each divided into 16 strips. Each card is made from 300-μm-thick Si on a 1500-Å Al layer. The strips are biased at +30 – 40 V, most using a 64 channel CAEN SY403 high voltage power supply.

The ID is the primary detector located perpendicular to the incoming EVRs. It is composed of three 16-vertical-strip Si detector cards, giving 48 strips for horizontal position resolution. Charge is collected from both ends of each strip, allowing for the determination of the vertical position of the signal by resistive charge division [AR76]. The ID is used to detect implantations of EVRs and their subsequent alpha and SF decays. The efficiency to detect full energy α particles emitted from implanted EVRs is 51%.

The PTD is composed of three additional Si detector cards mounted immediately behind the ID. The PTD is wired such that charge is collected from four adjacent strips at one end, resulting in 12 non-position sensitive strips. Signals in the PTD are generally due to light, low-ionizing particles, typically as a result of elastic scattering of He nuclei from the BGS or nuclear reactions from the Ta beam stop. These particles, which are a significant source of background, travel from the BGS, through the main ID depositing 1 – 10 MeV, and then leave a signal in the PTD. Signals in the PTD are then used to veto coincident signals in other detectors.

The UD is constructed from eight Si detector cards mounted perpendicular and upstream to the ID. The Si cards are mounted such that the strips are perpendicular to the ID and wired similarly to the PTD such that charge is collected from four adjacent strips at one end. The result is a five-sided-box configuration with 32 non-position-sensitive sectors along the periphery of the box. The UD gives the FPD additional coverage to detect α particles and spontaneous fission fragments emitted from EVRs implanted in the ID and results in an

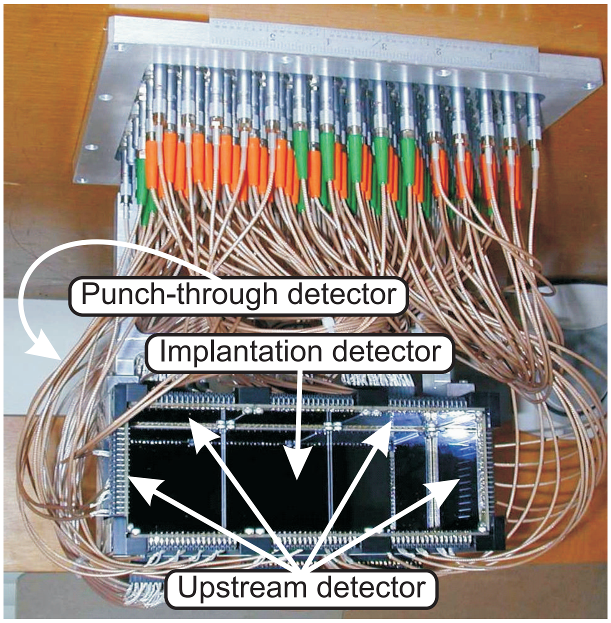

Figure 5.6 Photograph of BGS FPD. A 6-inch ruler sits at the top of the photo for scale.

additional 25% efficiency for detecting α particles.

The energy is calibrated for the ID and UD using a four-peak α source containing ^{146}Gd, ^{239}Pu, ^{241}Am, and ^{244}Cm. The α peaks of a spectrum of summed overall positions and all strips have a FWHM of 55 keV. The vertical position of α-particle implantations from this source is calibrated for the ID in a procedure similar to that detailed by Folden [Fol04]. The vertical position resolution is proportional to $1/E$ and on the order of 0.2 – 0.4 mm for the detection of a full energy α particle. The energy is not calibrated for the PTD; all above-threshold signals in the PTD are used to veto coincident signals in other detectors.

5.5 Clover gamma ray detector

The FPD was situated as close as possible to the back of the detector chamber. A standard high purity germanium (HPGe) Clover detector [DBT^{+}99] was mounted immediately outside the 2-mm-thick Al back wall of the vacuum chamber. The detector consisted of four, coaxial, 70 mm long, 50 mm diameter, n-type HPGe diodes attached to a cryostat. The energy is calibrated for the Ge detector using an Eckert & Ziegler Analytics radioactive point source containing ^{241}Am, ^{109}Cd, ^{57}Co, ^{139}Ce, ^{137}Cs, and ^{60}Co.

5.6 Rutherford detectors and cross section calculations

The nuclear reactions studied using the BGS usually involve bombarding high-Z targets ($Z \geq 82$) with medium-Z projectiles ($8 \leq Z \leq 36$). Under these irradiation conditions, a significant fraction of the projectile beam interacts with the target through elastic scattering caused by the electrostatic repulsion of the projectiles by the heavy, high-Z target nuclei. Two silicon photodiode detectors (model XRA, Detection Technology, Inc.) were mounted 27° from the beam axis to detect Rutherford scattered projectile ions. Between the target and the detectors were four metal grid attenuators which reduced the total transmission of particles and a circular collimator with 4.78 mm diameter. The total distance between the target and collimators was 292 mm.

The cross section for this so-called Rutherford scattering is well characterized as a function of scattering angle, projectile energy, and Z and A of the target and projectile. The differential Rutherford scattering cross section for a finite mass target is given by Segré [Seg77] to be:

$$\frac{d\sigma_{Ruth}}{d\omega} = \left[\frac{e^2 Z_p Z_t}{4\pi\epsilon_0(2E_{lab})}\right]^2 \cdot \frac{1}{sin^4\theta} \cdot \frac{\left[cos\theta \pm \sqrt{1-\left(\frac{A_p}{A_t}\right)^2 \cdot sin^2\theta}\right]^2}{\sqrt{1-\left(\frac{A_p}{A_t}\right)^2 \cdot sin^2\theta}}, \tag{5.6}$$

with the charge of the electron, e, equal to 1.602176×10^{-19} C, the permittivity of free space, ϵ_0, equal to 1.418597×10^{-39} $\mathrm{C^2/(MeV\ fm)}$, the atomic number of the projectile and target, Z_p, and Z_t, respectively, the lab-frame projectile energy, E_{lab}, in MeV, the lab-frame scattering angle of the Rutherford detectors, θ, and the atomic mass of the projectile and target, A_p and A_t, respectively. For $A_p < A_t$, only the plus sign is used before the square root. When $A_p > A_t$, the cross section is given by the sum of both the expression using a plus sign and the expression using the minus sign.

Using this differential cross section and the total detected number of Rutherford scattered projectile ions ($N_{Ruth,obs}$), the product of the target thickness and integrated beam dose can be calculated according to:

$$N_t I t = \frac{N_{Ruth,obs}}{\frac{d\sigma_{Ruth}}{d\omega}(\Omega/scaledown)}, \tag{5.7}$$

where N_t is the areal target density, I is the beam intensity, t is the length of irradiation, Ω is the solid angle subtended by the collimator in steradian, and *scaledown* is the reduction factor due to the metal grid attenuators. Based on the geometry of the target, detectors and metal grid attenuators, $\Omega = (2.1 \pm 0.2) \times 10^{-4}$. The reduction factor due to the metal grid attenuators was measured to be $scaledown = 1348 \pm 20$ by comparing the ratio of rutherford-scattered beam particle events to focal plane events with and without attenuators in the ^{207}Pb(^{48}Ca,2n)^{253}No reaction.

With this measured value for the product of the target thickness and integrated beam dose (N_tIt), the cross section for a nuclear reaction of interest (σ_{rxn}) can be easily calculated from the number of observed decay chain events ($N_{obs,rxn}$) and the BGS separation/detection efficiency ($\epsilon_{det,rxn}$) to be

$$\sigma_{rxn} = \frac{N_{obs,rxn}}{\epsilon_{det,rxn} N_t It}. \tag{5.8}$$

Systematic uncertainties are present in a number of the values necessary for the measurement of a nuclear reaction cross section, including E_{lab}, θ, *scaledown*, and Ω. Combining these uncertainties with the estimated 10% error in the BGS separation efficiency discussed in Section 5.2 through standard error propagation methods results in a systematic uncertainty of ~12% for nuclear reaction cross section measurements with $v/v_0 \approx 2 - 2.5$.

5.7 Data acquisition and analysis

The signals produced in the FPD are transported outside the detection chamber, immediately into standard preamplifiers, and then to a data acquisition shack. The signals are then processed by a CAEN N568B amplifier which splits the signal to a "fast out" and a low-gain and a high-gain "slow out" signals. The "fast out" signal is routed to a MSU 1806 constant fraction discriminator (CFD). If the signal is above the CFDs pre-calibrated noise threshold, it triggers an event in the Multi-Branch System (MBS), a data acquisition system developed by the data acquisition group at GSI [EK00]. The minimum time between two consecutive events is 13 μs and subsequent signals separated by 13 – 100 μs are stored as "subevents". When the "fast out" signals a trigger event, the low-gain and high-gain "slow out" signals were sent to CAEN V785 analog-to-digital converters (ADCs) and those above a predefined noise threshold are digitized. In addition, the ADCs digitize processed analog signals from the Rutherford detectors, MWPC, and HPGe Clover detectors and the ToF between signals in the various detectors through the use of a time-to-amplitude conversion module. When the ADCs are readout during the recording of an event, various timing scalers and bit registers are coincidently recorded.

The MBS runs on a PowerPC real-time processor board RIO2 computer located in the same VME crate as the ADCs, timing scalers, and bit registers. The MBS handles user inputted keyboard commands, data buffering, writing data to disk, file handling, and networking. In addition, the MBS can be programmed through user-written software to control data readout, on-line data analysis tools such as histogramming, event building, and the fast (~140 μs) shutoff of the beam in response to a series of time-correlated events. By using this fast beam shutoff tool, the alpha decays of longer-lived decay chain daughters can be searched for in the absence of the higher background rates present when the beam was on.

Off-line data analysis is performed by several independently developed C++ computer routines. One data analysis routine utilizes the ROOT object-oriented data analysis framework [ABB$^+$09c]. ROOT is used to sort, calibrate and plot the data, as well as search for time and position correlated events through the implementation of C++ code containing ROOT-specific commands.

Chapter 6

Production of ^{285}114 in the ^{242}Pu(^{48}Ca,5n) Nuclear Reaction

6.1 Motivation

The UC, Berkeley / LBNL Heavy Element Nuclear and Radiochemistry Group has long played an important role in the study of the physics and chemistry of the superheavy elements. With the production and installation of the ^{242}Pu target wheel discussed in Section 5.1, the Berkeley Gas-filled Separator (BGS) was well suited to perform the first experimental verification of element 114 in the ^{242}Pu(^{48}Ca,$3-4n$) nuclear reactions reported by the DGRFS group at FLNR [OUL^{+}04a]. This experiment, conducted in January 2009, confirmed the decay properties reported for ^{286}114 and ^{287}114 and was the first independent verification of element 114 [SGD^{+}09].

This ^{48}Ca irradiation of ^{242}Pu targets was performed at a compound nucleus excitation energy of $E^{*} = 41$ MeV. This excitation energy was chosen to maximize the reaction cross section for both the 3 and the 4 neutron evaporation products, ^{287}114 and ^{286}114, respectively. When performed at $E^{*} = 50$ MeV, the fusion products from the ^{48}Ca bombardment of ^{242}Pu would require the evaporation of 4 or 5 neutrons to de-excite the compound nucleus. At these energies, the expected fusion-evaporation products would be ^{286}114 and the new, neutron-deficient isotope ^{285}114.

The motivation for performing such higher energy ^{48}Ca bombardments of ^{242}Pu targets was two-fold. First, as described in detail in Section 6.1.2, the predicted new-isotope product ^{285}114 was expected to α decay through a total of six new isotopes. The elucidation of these five new α-decay energies would provide insight into the accuracy of modern predictions of the shell stucture of the heaviest elements. Secondly, these isotopes would be the most neutron-deficient even-Z isotopes observed in ^{48}Ca bombardments of actinide targets. This fact makes their discovery an important stepping stone in the effort to connect the island of isotopes produced in ^{48}Ca irradiations of actinide targets with the rest of the chart of the nuclides.

6.1.1 Predicted ^{242}Pu(^{48}Ca, $5n$)^{285}114 nuclear reaction cross section.

The cross section for the ^{242}Pu(^{48}Ca, $5n$)^{285}114 nuclear reaction was estimated in several ways. Essentially all modern theories [SSWW05, ZIO03, ASKB03, AAS04a, AAS04b, FJFL06, Ari07] predicting heavy element formation cross sections are understood through a three-step approach. The total formation cross section is the product of a capture cross section, σ_{cap}, which is the probability the target and projectile nuclei will come into contact and become trapped in their mutual Coulomb + nuclear energy potential, a compound nucleus formation probability, P_{CN}, which is the probability for the di-nuclear capture configuration to proceed to a spherical compound nucleus, and a survival probability, P_{surv}, which is the probability for the compound nucleus to de-excite through several stages of neutron evaporation in competition with fission. While this theory has trouble predicting the magnitude of the cross section for some reactions because of systematic errors in these last two terms, the theory is thought to more accurately predict the *ratios* of P_{CN} and P_{surv} for neighboring nuclides at similar excitation energies.

The ^{242}Pu(^{48}Ca, $5n$)^{285}114 reaction cross section at $E^* = 50$ MeV can be quantitatively calculated from the experimentally measured ^{242}Pu(^{48}Ca, $4n$)^{286}114 reaction cross section at $E^* = 40$ MeV and calculated values for the $5n/4n$ ratios of capture cross sections (σ_{cap}), compound nucleus formation probabilities (P_{CN}) and survival probabilities (P_{surv}). The survival probability is calculated as the product of two terms: P_{xn}, the probability that there will be exactly x stages of neutron evaporation for a given excitation energy, and $\prod_{i=0}^{x}(\Gamma_n/\Gamma_{tot})$, the product of probabilities that the excited compound nucleus will de-excite by neutron emission as opposed to fission at each of the x stages. Multiplying the product of these four factors by the experimentally measured ^{242}Pu(^{48}Ca, $4n$)^{286}114 cross section gives an approximation of the ^{242}Pu(^{48}Ca, $5n$)^{285}114 reaction cross section. Table 6.1 summarizes the results and details for each of these four calculated ratios and the overall cross section. The calculation predicts a cross section of 0.5 – 1.3 pb for the ^{242}Pu(^{48}Ca, $5n$)^{285}114 nuclear reaction.

A second statistical model for predicting superheavy element formation cross sections has been developed by Zagrebaev *et al.* [ZIO03, Zag04]. This theory has been extensively used for predicting ^{48}Ca + actinide nuclear reaction cross sections and effectively reproduces those measured for the ^{242,244}Pu(^{48}Ca, $3-4n$)$^{286-289}$114 nuclear reactions. However, the effectiveness of the theory at predicting $5n$ evaporation product cross sections has not been rigorously validated because there has been only one $5n$ evaporation event observed in ^{48}Ca bombardments of actinide targets [OUL$^+$04b]. This event was reported in the bombardment

Table 6.1 Predicted cross section ratios for ^{48}Ca + ^{242}Pu $5n/4n$ reactions.

Factor	Value	Details
$\frac{\sigma_{cap}(5n,\ E^* = 50\ \text{MeV})}{\sigma_{cap}(4n,\ E^* = 40\ \text{MeV})}$	0.95	Calculated using Appendix A from [SSWW05] assuming a critical angular momentum of $40\hbar$ [MSPG80].
$\frac{P_{CN}(5n,\ E^* = 50\ \text{MeV})}{P_{CN}(4n,\ E^* = 40\ \text{MeV})}$	1.6	Calculated using Appendix A from [SSWW05]. Higher excitation energies result in an increased probability that shape fluctuations lead to the formation of a compound nucleus.
$\frac{P_{5n}(E^* = 50\ \text{MeV})}{P_{4n}(E^* = 40\ \text{MeV})}$	0.9	Assumed to be slightly less than one. Higher excitation energies have a smaller likelihood of de-exciting with exactly the desired number of neutrons.
$\frac{\prod_{i=0}^{x}\Big(\Gamma_n/\Gamma_{tot}(5n,\ E^* = 50\ \text{MeV})\Big)}{\prod_{i=0}^{x}\Big(\Gamma_n/\Gamma_{tot}(4n,\ E^* = 40\ \text{MeV})\Big)}$	0.09 – 0.24	Estimated by comparing the Γ_n/Γ_{tot} ratio for the last four stages of neutron emission in the $5n$ reaction with all four stages in the $4n$ reaction. Each Γ_n/Γ_{tot} stage will be at about the same excitation energy with the compound nucleus differing by one neutron. The geometric mean of this ratio of ratios ($\frac{\Gamma_n/\Gamma_{tot}(E^*,N)}{\Gamma_n/\Gamma_{tot}(E^*,N+1)}$) has been experimentally measured in the superheavy element region to be $\sim$0.83 [CIM83, DSE66, SGN68] and calculated theoretically to be 0.65 [SSWW08, MS94, Rei81, MS74]. The total $5n/4n$ ratio is the product of this value and the Γ_n/Γ_{tot} of the first neutron evaporation step at $E^* = 50$ MeV, which, based on experimental experience, is estimated as 0.5.
$\sigma_{tot}(5n,\ E^* = 50\ \text{MeV})$	**0.5 – 1.3 pb**	Product of above four ratios and experimentally measured 4 pb cross section for the ^{242}Pu(^{48}Ca, $4n$)^{286}114 reaction [Oga07].

Table 6.2 Predicted ^{285}114 decay properties.

Isotope	Q_α (MeV)	$t_{1/2,\alpha}$ (s)	$t_{1/2,SF}$ (s)	Expected decay property
^{285}114	10.85	0.013	130	α decay
^{281}Cn	10.13	0.21	49	α decay
^{277}Ds	10.15	0.042	340	α decay
^{273}Hs	9.75	0.11	62,000	α decay
^{269}Sg	8.68	34	830,000	α decay
^{265}Rf	7.66	21,000	7,600	SF decay

of ^{244}Pu targets at $E^* = 53$ MeV by Oganessian *et al.* and gave a $5n$ cross section of $1.1^{+2.6}_{-0.9}$ pb [OUL$^+$04b]. At this excitation energy, Zagrebaev's theory predicts a ^{244}Pu(^{48}Ca, $5n$)^{287}114 cross section of ∼0.5 pb [Zag04]. While this cross section agrees within the large one-event error bars, it is a factor of two lower than the measurement. Zagrebaev's theory predicts a cross section of 0.3 pb for the ^{242}Pu(^{48}Ca, $5n$)^{285}114 reaction at $E^* = 50$ MeV [Zag10].

6.1.2 Predicted decay properties of ^{285}114

The predicted decay properties of ^{285}114 and its daughters shown in Table 6.2 were calculated through the following method. First, several different nuclear mass predictions and extrapolations were used to calculate α-decay Q-values. By comparing the α-decay Q-values each reference predicted for the known isotopes ^{286}114, ^{287}114, ^{288}114, ^{289}114 and their daughters, the mass extrapolations by Audi *et al.* [AWT03] were found to produce more accurate values than the mass predictions from Myers and Światecki [MS94], Muntian *et al.* [MPS03], and Möller *et al.* [MNMŚ95]. Alpha decay systematics were then used to calculate the nuclides' α-decay half-lives. The systematics from Parkhomenko and Sobiczewski [PS05] were found to better replicate the observed α-decay half-lives of ^{286}114, ^{287}114, ^{288}114, ^{289}114 and their daughters, when compared with the systematics from Hatsukawa *et al.* [HNH90] and Denisov and Khudenko [DK09].

Spontaneous fission half-lives were predicted for even-even superheavy element isotopes by Smolańczuk *et al.* [SanSS95]. The unhindered even-odd partial SF half-lives for ^{285}114 and its daughters were interpolated by taking the geometric mean (the square root of the product) of neighboring even-even isotopes. As reviewed by Hoffman [Hof89], even-odd spontaneously-fissioning atomic nuclei exhibit significantly longer half-lives due to their unpaired neutron. These hindrance factors for spontaneous fission are typically on the order of 10^3 – 10^9. The spontaneous fission half-lives calculated in Table 6.2 were calculated with an estimated SF hindrance factor of 10^3.

This method predicts α decay with sub-second half-lives for ^{285}114, ^{281}Cn, ^{277}Ds, and ^{273}Hs. ^{269}Sg is predicted to α decay with a half-life on the order of 30 s. The decay chain is then predicted to terminate with the spontaneous fission of ^{265}Rf with a long half-life on the order of 2 h. Such a decay chain is ideal for studying in the BGS as it has many, rapid, subsequent alpha decays which provide a very identifiable signal.

6.2 Experimental Conditions

The LBNL Advanced Electron Cyclotron Resonance ion source [Xie98] was used to produce beams of ^{48}Ca$^{11+/10+}$. The 88-Inch Cyclotron accelerated the ^{48}Ca to 273 MeV with typical intensities of 300 particle nanoamperes. A total beam dose of 3.1 x 10^{18} ^{48}Ca ions was delivered over 22.8 effective days of irradiation. At the entrance to the BGS, the ion beam passed through a 45 μg/cm^2 carbon window separating beamline vacuum from the 67-Pa He gas inside. The beam then passed through the titanium target backing foil followed by the ^{242}PuO$_2$ target material. Targets were prepared by electrodeposition from isopropanol solutions as described in Section 5.1. Four target segments with 440, 340, 320, and 270 μg/cm^2 of ^{242}Pu (>99% purity) on 2.4-μm Ti backing foils were mounted on a 9.5-cm diameter wheel. The energy loss in the entrance window and targets was calculated using SRIM2003 [Zie04]. The four target segments had calculated center-of-target beam energies of 255.5, 256.0, 256.1, and 256.3 MeV, respectively, with target thickness weighted average center-of-target beam energy of 255.9 MeV and compound nucleus excitation energy of 50.1 MeV [AWT03, MS94]. The systematic error in the cyclotron beam energy is 1%. The ^{48}Ca ion beam lost 2.5 - 4.1 MeV upon passing through the ^{242}PuO$_2$ target layer. The target wheel was rotated at ~12 Hz to disperse the heat of the beam. Elastically-scattered ^{48}Ca ions were recorded by the rutherford detectors and used to monitor the product of beam dose and target thickness as described in Section 5.6.

Compound nucleus EVRs recoiled from the target with the momentum of the beam. The BGS separated these from unreacted beam and other reaction products by their differing magnetic rigidities in helium. The magnetic rigidity of element-114 EVRs in ~70-Pa He was recently measured to be $B\rho = 2.28$ Tm [SGD$^+$09, DSY$^+$10]. The magnet settings were set as described in Section 5.2 used for this magnetic rigidity. The transmission efficiency for an EVR to reach the focal plane detector was calculated using a Monte Carlo simulation of trajectories through the BGS combined with experimentally measured efficiencies. The calculated efficiency for ^{285}114 EVRs was 69%.

In the focal plane area of the BGS, EVRs traveled through the MWPC before implanting in the focal plane detector (FPD). The MWPC had 1.5 μm Mylar upstream and 0.8 μm polypropylene downstream windows. Analog signals from the MWPC were used along with the time-of-flight between the MWPC and FPD to distinguish implantation events from radioactive decay events in the FPD. The FPD's 48 vertical strip implantation detector (ID) provided horizontal position resolution. Vertical position was measured by resistive charge division within each strip and reported as the distance from the vertical center of the detector. Events above center are reported with positive distances. Error in this position was experimentally determined to be $\sigma_y(E_{ID}) = 2600\ (keV \cdot mm)/E_{ID}$ for the energy range of α particles. Events depositing less than 2 MeV in the ID had an additional vertical position uncertainty due to integral non-linearity in the low end of the ADC range. Because fission energies were measured in a separate set of amplifiers and ADCs, 1.5 mm was added to the vertical position uncertainty for fission events. The upstream detector (UD) located upstream and perpendicular to the ID allowed for the reconstruction of α-decay and fission events that only deposited partial energy in the ID. The overall efficiency was approximately 75% for detecting full-energy α particles (either entirely in the ID or ID-UD reconstructed) and 100% for detecting at least one fragment from a SF decay of an implanted atom. The punch-through detector (PTD) mounted immediately behind the ID detected and identified events from low-ionizing particles passing through the ID. The HPGe Clover gamma ray detector was situated outside the vacuum chamber directly behind the ID. The efficiency for detecting superheavy element X-rays was simulated using a Monte Carlo algorithm to be approximately 13% for an assumed recoil distribution centered on the ID.

The MBS data acquisition system was programmed to implement a fast beam shutoff to minimize the effect of randomly correlated unrelated events appearing like element 114 element decay chains. Upon detection of an EVR-like event [$5 < E(\text{MeV}) < 20$, ID only, anti-coincident with punch-throughs, coincident with MWPC] followed within 10 seconds by an α-like event [$8 < E(\text{MeV}) < 12$, ID only or ID-UD reconstructed, anti-coincident with punch-throughs and MWPC] in the same detector position, the beam was shut off for 10 seconds to allow for the detection of subsequent α particles in the resulting low-background environment. If a subsequent α-like event was detecting during the beam-off period, MBS was programmed to shut off beam until manually reset. A total of 51 EVR-α beam shutoffs were implemented, during which no subsequent correlated α particles were detected.

6.3 Results

Element-114 atoms were identified by detecting time- and position-correlated events corresponding to their implantation and subsequent radioactive decay chain, terminating with the detection of a SF event. Figure 6.1 and Table 6.3 contain the times, energies and positions of the two correlated decay chains observed in the experiment. The $B\rho$ column reports the magnetic rigidity corresponding to the strip in which the decay chain was detected. Based on a comparison with predicted decay properties, the first event was assigned to the decay of ^{285}114 and its daughters. This decay chain consisted of a 15.97 MeV EVR-like event followed 0.181 s later by a 1.64 MeV escape-like event [$0.5 < E(\text{MeV}) < 2$, ID only, anti-coincident with punch-throughs and MWPC] indicative of an α-decay event in which the α particle escaped from the front of the five-sided detector box. The chain continued with four subsequent α-like events after 140 ms, 8.21 ms, 346 ms, and 185 s with energies of

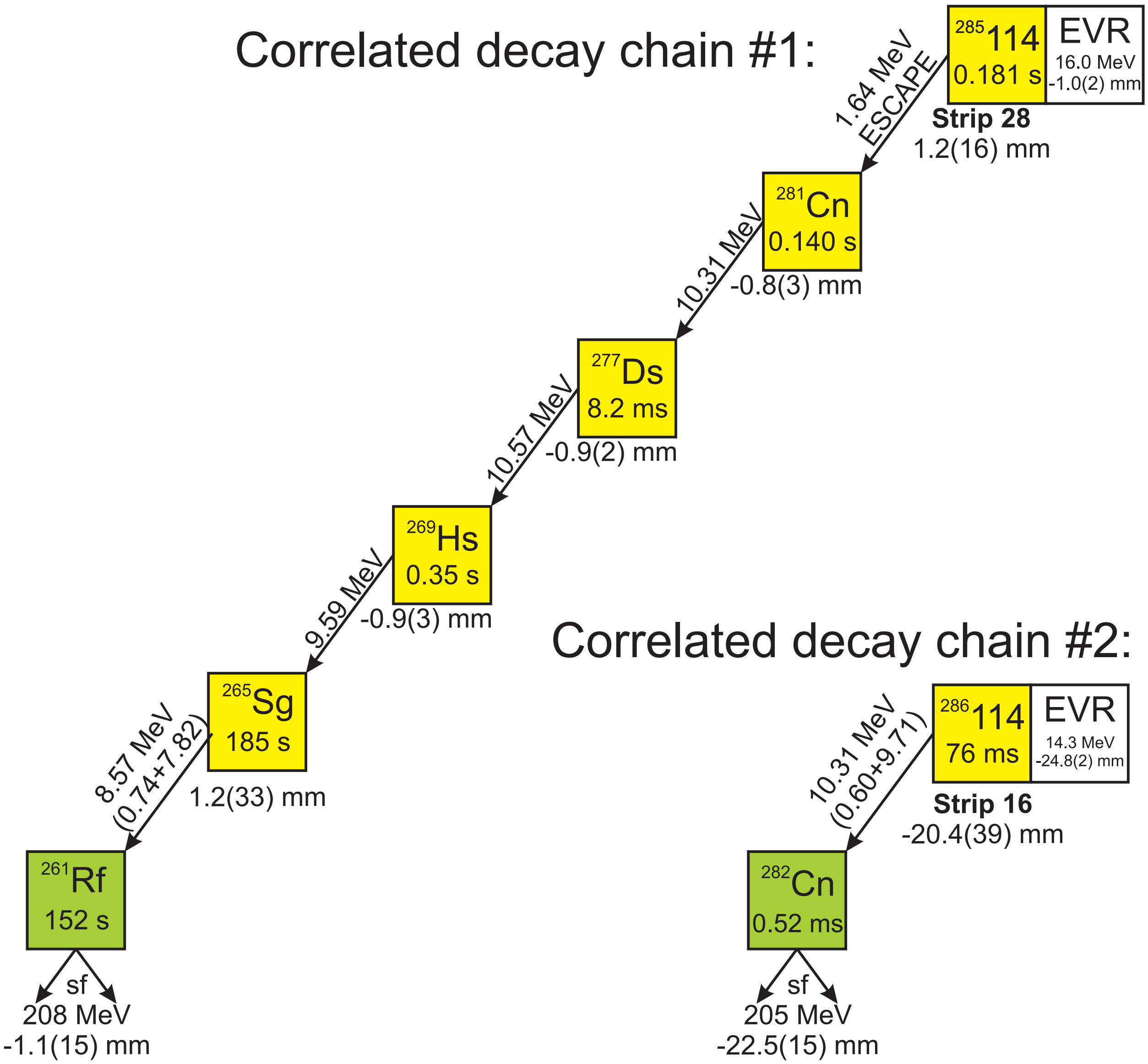

Figure 6.1 Element-114 decay chains observed in ^{48}Ca irradiation of ^{242}Pu

Table 6.3 Observed element-114 decay chains.

Interpretation	E (MeV)	Δt (s)	Pos (mm)	$B\rho$ (Tm)
EVR - strip 28	15.97(4)		-1.0(2)	2.26(3)
^{285}114 α decay	1.64(10)^{1}	0.181	1.2(16)	
^{281}Cn α decay	10.31(4)	0.140	-0.8(3)	
^{277}Ds α decay	10.57(4)	0.00821	-0.9(2)	
^{273}Hs α decay	9.59(4)	0.346	-0.9(3)	
^{269}Sg α decay	8.57(10)^{2}	185	1.2(33)	
^{265}Rf SF decay	208.1	152	-1.1(15)	
EVR - strip 16	14.37(4)		-24.8(2)	2.31(3)
^{286}114 α decay	10.31(10)^{3}	0.0760	-20.4(39)	
^{282}Cn SF decay	205.4	0.000522	-22.5(15)	

[1] Escape α particle depositing only partial energy in ID.
[2] Reconstructed from 0.742 MeV in ID and 7.823 MeV in UD.
[3] Reconstructed from 0.600 MeV in ID and 9.705 MeV in UD.

10.31, 10.57, 9.59, and 8.57 MeV, which are interpreted as the successive α decays of $^{281}_{112}$Cn, $^{277}_{110}$Ds, $^{273}_{108}$Hs, and $^{269}_{106}$Sg, respectively. The final α-like event in this chain was reconstructed from a 0.742 MeV signal in the ID and a 7.823 MeV signal in the UD. The decay chain terminated 152 seconds later with a 208.1 MeV SF-like event [E(MeV) > 80, ID only or ID-UD reconstructed, anti-coincident with punch-throughs and MWPC] interpreted as the SF of $^{265}_{104}$Rf. The vertical positions of the events in this chain agree well. This α-decay chain did not implement a fast beam shutoff because, with the online ID calibration that was being used at the time, the vertical position of the recoil-like event was greater than 3σ away from the α-like events. After the detection of this event, a new calibration with lowered ADC thresholds was performed which gave the reported positions for the events. As the first detected full-energy α-like event is similar in energy and lifetime to the decay of ^{286}114, one may postulate that the 1.64-MeV event was a random correlation and the decay chain was that of ^{286}114 decaying through a previously unobserved α branch of ^{282}Cn. This is unlikely to be the case because (i) based on the random rate of escape-like events, the probability to observe a randomly correlated event in the 0.32 s between the recoil and first α-like event was 0.0070, (ii) the observed lifetime for the event that would be assigned to the α decay of ^{282}Cn was ten times the published half-life for the nuclide [Oga07], and (iii) SF was observed for all of the previous detections of ^{282}Cn [Oga07, SGD^{+}09].

The second observed decay chain was assigned to the decay of ^{286}114 and ^{282}Cn. The chain consisted of a 14.37 MeV EVR-like event followed 76 ms later by a 10.31 MeV α-like event which was reconstructed from 0.600 MeV in the ID and 9.705 MeV in the UD. This

EVR-α signal pair implemented a 10-second fast beam shut off. A 205.4 MeV SF-like event occurred 0.52 ms later. The decay energies and lifetimes of this event agreed very well with the published decay properties of ^{286}114 [Oga07] ($t_{1/2}$ = 0.13 s; 50% 10.19 MeV α decay, 50% SF) and ^{282}Cn ($t_{1/2}$ = 0.82 ms; 100% SF). The SF-like events for both decay chains were each observed with two coincident γ-rays, reinforcing their assignments as SF events. No γ rays were observed coincident with any of the correlated α- or escape-like events.

6.3.1 Calculation of number of expected random decay chains

The numbers of expected decay chains made from coincidences of unrelated events matching the decay properties of ^{285}114 or ^{286}114 were estimated. To simplify the calculation, all events were assumed to be evenly distributed over the ID and the rates were constant at their average values. During the experiment, the rate of EVR-like events for the whole array was 0.38 Hz and the rate of α-like events was 0.011 Hz. A total of 9 SF-like events were observed (only 3 with $E(\text{MeV}) > 101$). The probability that N events occur within an interval of t seconds, given a random rate of R counts per second is given by the Poisson probability distribution and is equal to

$$P(n, R, t) = \frac{(R \cdot t)^n e^{-}(R \cdot t)}{n!} \tag{6.1}$$

The number of expected random ^{285}114-like decay chains was calculated by multiplying the 9 SF-like events by the probability that they were correlated within 20 hours to at least one EVR-like and three α-like events with the additional requirement that at least one of the α lifetimes was less than 3 s. Using this very general schematic of a ^{285}114-like event, the number of random correlations was calculated to be 9.2 x 10^{-4}. The number of random ^{286}114-like event chains with an EVR-like event followed by an α-like event and a SF-like event within 10 times the published half-lives (1.3 s for 0.13-s ^{286}114 and 8.2 ms for 0.82-ms ^{282}Cn) was calculated to be 1.7 x 10^{-9}. These simplified overestimations do not consider event order or α-decay systematics [PS05]. Because these numbers are very low, it is unlikely that either of the event chains were attributable to a random correlation of unrelated events.

6.4 Discussion

Figure 6.2 shows theoretical predictions and experimental measurements of excitation functions for the ^{242}Pu(^{48}Ca,2-5n)$^{285\text{-}288}$114 reactions. Open points represent experimental measurements using the DGRFS [Oga07], closed points represent measurements using the BGS [SGD$^+$09, EGB$^+$10], and curves represent theoretical predictions [Zag04, Zag10]. Green squares represent 3n, blue triangles represent 4n, and orange diamonds represent 5n cross section measurements. The cross sections measured at the compound nucleus excitation

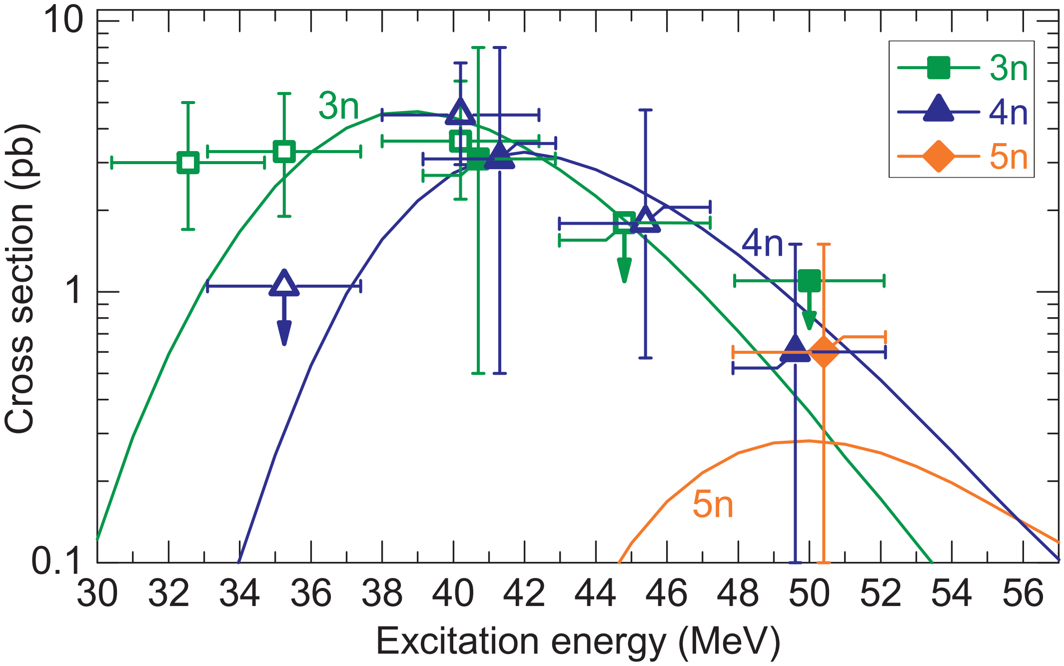

Figure 6.2 Measurements and predictions of excitation functions of the ^{242}Pu(^{48}Ca,2-5n)$^{288\text{-}285}$114 nuclear reactions.

energy $E^* = 50$ MeV for the 4n and 5n products in this work are $0.6^{+1.3}_{-0.2}$ pb, each. Error bars are a 68% confidence interval with minimal length and highest probability density calculated according to the methods of Brüchle [Brü03] which estimates confidence limits using a Bayesian statistical approach assuming a uniform prior function. The confidence intervals can also be overestimated using a classical statistics approach according to the methods of Schmidt *et al.* [SSPC84] to be $0.6^{+1.3}_{-0.5}$ pb. A more detailed discussion of the calculation of low statistics error limits can be found in Appendix D The non-observation of a 3n evaporation product gave an 84% confidence upper limit for the ^{242}Pu(^{48}Ca,3n)^{287}114 reaction of 1.1 pb. This cross section measured for the 5n reaction is larger than Zagrebaev's predictions [Zag10] by a factor of two, although agreeing within the classical confidence limits. As a similar experimental/theoretical cross section discrepancy was observed for the ^{244}Pu(^{48}Ca,5n)^{287}114 reaction [OUL$^+$04b], it is possible that the predictions by Zagrebaev are systematically underestimating the 5n cross section, although current data cannot say so with statistical certainty.

Figure 6.3 compares theoretical alpha decay Q-values from Muntian *et al.* [MPS01, MHPS03, MPS03] shown as small, open, connected circles with experimental measurements (see Appendix E for references) of even-Z isotopes' α-decay Q-values shown as large, closed circles, plotted against their number of neutrons. Predicted neutron shell closures appear as local minima in the curves. Predicted proton shell closures appear as larger gaps between subsequent even-Z isotope curves. A detailed ground-state to ground-state Q-value was unavailable for many of the odd-N experimental Q-values including those of the current work. In these cases, the α-decay Q-value was approximated by the recoil-corrected α-decay energy. Because the α-decay energy for ^{285}114 was not observed, the recoil-corrected α-decay energy was deduced from the observed lifetime and α-decay systematics as outlined by Parkhomenko and Sobiczewski [PS05]. By comparing the trend of discrepancies between experimental points and their theoretical counterparts, it is possible to evaluate how well the theoretical predictions model the shell effects that govern the stability of the transfermium elements. While the α-decay Q-values measured in the current work agree well with predictions for Hs and Ds, the discrepancies in Sg, Cn, and element 114 highlight interesting deviations from the theoretical treatment of shell structure. First, the Q-value measured for ^{269}Sg ($N = 163$) is significantly higher than predicted. Similarly, the α-decay Q-value from ^{267}Sg ($N = 161$), of which one decay has been observed by Dvorak *et al.* [DBC$^+$06, DBC$^+$08], was measured to be above the predicted value. These observed discrepancies imply that the theory may overestimate the strength of the $N = 162$ deformed shell closure for $Z = 106$ or underestimate it for $Z = 104$. Secondly, the α-decay Q-values observed for ^{281}Cn ($N = 169$) and ^{285}114 ($N = 171$) are significantly below their respective predicted values. This observation agrees well with the trend of other Cn and element-114 isotopes and may be either an experimental indication that the $Z = 114$ shell closure predicted around $N = 184$ extends to nuclides with neutron numbers significantly lower than predicted or a result of a systematic overestimation of α-decay Q-values for nuclides with $169 < N < 174$. The observed spontaneous fission lifetime of 152 s for ^{265}Rf is between the previously observed spontaneous fission half-lives of neighboring odd-N isotopes ^{263}Rf ($t_{1/2}$ = 8 s [DBC$^+$06, DBC$^+$08]) and ^{267}Rf ($t_{1/2}$ = 1.3 h [Oga07]). Table 6.4 shows the decay properties of all element 114 isotopes and their daughters, including those reported in the current work. Error bars for the half-lives of ^{285}114 and its daughters were calculated according to Schmidt *et al.* [SSPC84].

The six new isotopes reported here are more neutron-deficient than any previously observed even-Z superheavy element isotope [Oga07, HAA$^+$07, SGD$^+$09, DSY$^+$10]. Figure 6.4 shows the six new isotopes highlighted in orange among the upper end of the chart of the nuclides. Their discovery is an important step towards linking the six new superheavy elements and 52 new isotopes produced in ^{48}Ca bombardments of actinide targets (highlighted in red) to the main body of the chart of nuclides (highlighted in blue). The successful bridging of this gap would provide a necessary proof for unambiguous proton- and neutron-number assignments for these new isotopes.

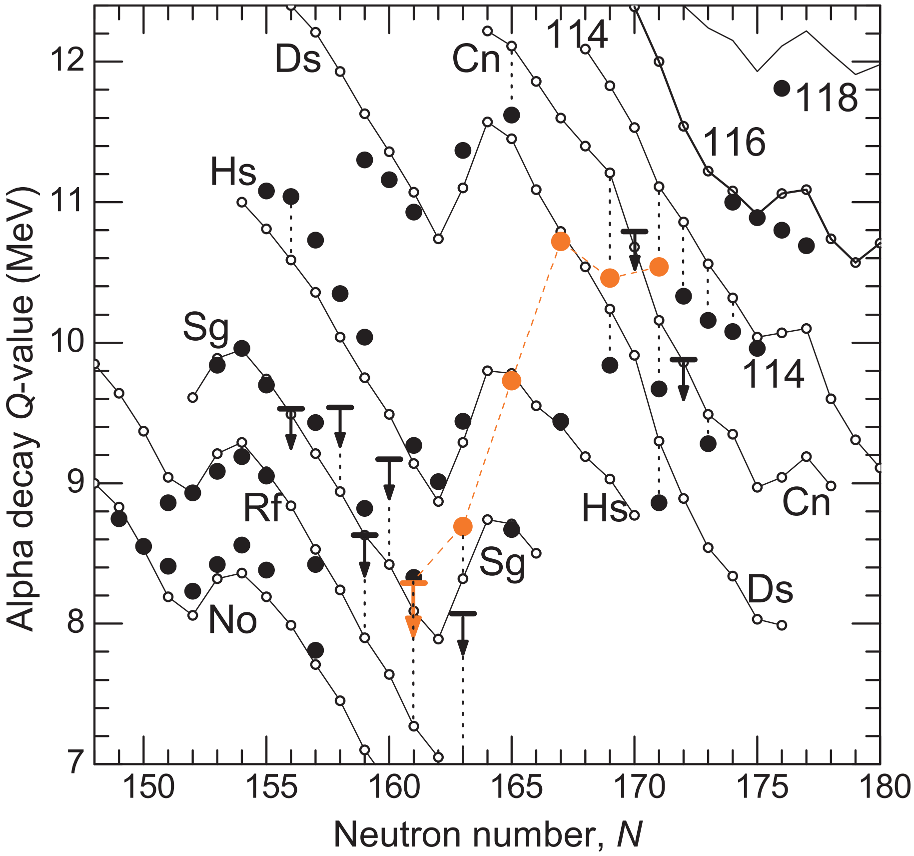

Figure 6.3 Comparison of experimental and theoretical α-decay Q-values versus neutron numbers for even-Z transfermium elements.

Table 6.4 Decay properties of element 114 isotopes and their daughters, including current work.

Z	A	Decay mode, branch (%)	Half-life	Reference
114	289	α	$2.1^{+0.8}_{-0.4}$ s	[DSY$^+$10]
	288	α	$0.69^{+0.17}_{-0.11}$ s	[DSY$^+$10]
	287	α	$0.48^{+0.16}_{-0.09}$ s	[Oga07]
	286	α: 50, SF: 50	$0.13^{+0.04}_{-0.02}$ s	[Oga07]
	285	α	$0.13^{+0.6}_{-0..06}$ s	Current work [EGB$^+$10, SSPC84]
112	285	α	29^{+11}_{-6} s	[DSY$^+$10]
	284	SF	99^{+24}_{-16} ms	[DSY$^+$10]
	283	α: 100, SF: ≤ 10	$3.8^{+1.2}_{-0.7}$ s	[Oga07]
	282	SF	$0.82^{+0.30}_{-0.18}$ ms	[Oga07]
	281	α	97^{+500}_{-40} ms	Current work [EGB$^+$10, SSPC84]
110	281	α: 9^{+16}_{-7}, SF: 91^{+7}_{-16}	13^{+5}_{-3} s	[DSY$^+$10]
	279	α: 10, SF: 90	$0.20^{+0.05}_{-0.04}$ s	[Oga07]
	277	α	5.7^{+30}_{-3} ms	Current work [EGB$^+$10, SSPC84]
108	277	SF	3^{+15}_{-1} ms	[DSY$^+$10]
	275	α	$0.19^{+0.22}_{-0.07}$ s	[Oga07]
	273	α	$0.24^{+1}_{-0.1}$ s	Current work [EGB$^+$10, SSPC84]
106	271	α: 70, SF: 30	$1.9^{+2.4}_{-0.6}$ min	[Oga07]
	269	α	130^{+600}_{-60} s	Current work [EGB$^+$10, SSPC84]
104	267	SF	$1.3^{+2.3}_{-0.5}$ h	[Oga07]
	265	SF	110^{+500}_{-50} s	Current work [EGB$^+$10, SSPC84]

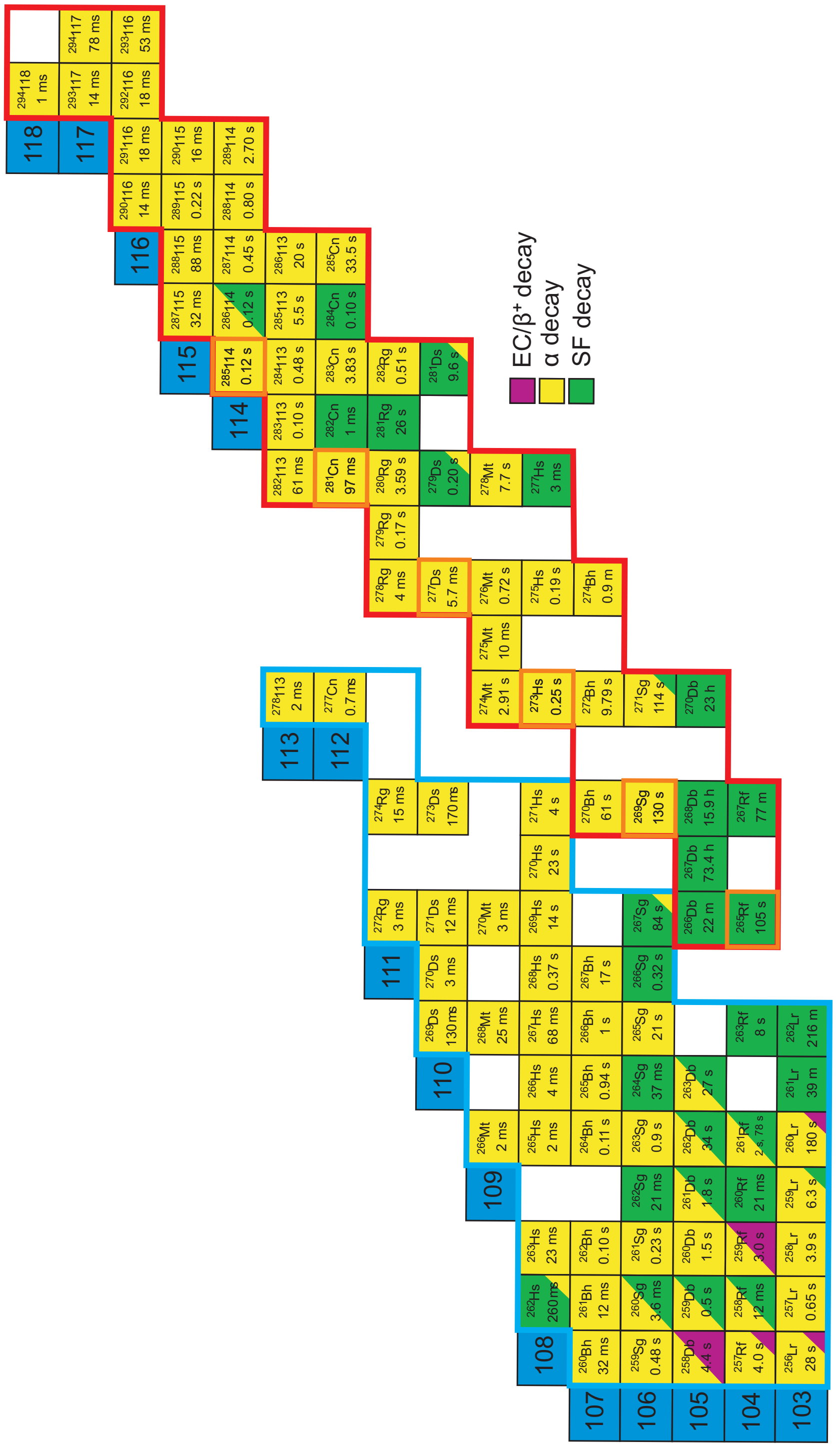

Figure 6.4 New superheavy element isotopes among the upper end of the chart of the nuclides.

6.5 Summary of Part II

Chapter 4 introduces experimental studies of the transactinide elements. It begins by giving a brief history of the discovery of the chemical elements. It then discusses the parent-daughter correlation technique which has been used to unambiguously identify the nuclear properties of transactinide element isotopes. The chapter goes on to discuss the different types of nuclear reactions used to produce transactinide elements. Finally, details of element 114 studies are discussed, including summaries of all nuclear reaction used for the production of the four previously observed element 114 isotopes and their nuclear decay properties.

Chapter 5 discusses the BGS, the apparatus used for the isolation and detection of the element 114 isotopes observed in the current work. Experimental details are given regarding the nuclear reaction targets, magnets, magnet settings, and detector array. Details are given related to the calculation of nuclear reaction cross sections as a function of the number of Rutherford-scattered particles detected in off-beam axis silicon detectors. Details of the data acquisition system and data analysis procedures are also given.

Chapter 6 motivates the study of the new isotope ^{285}114. The chapter discusses predictions of the cross section for its production in the ^{242}Pu(^{48}Ca,5n)^{285}114 nuclear reaction, as well as predictions for the nuclear decay properties of this isotope and its daughters. The results of the experiment are discussed, including the observation of one event of ^{285}114 and its radioactive decay daughters ^{281}Cn, ^{277}Ds, ^{273}Hs, ^{269}Sg, and ^{265}Rf. The measured α-decay Q-values are compared with those from a macroscopic-microscopic nuclear mass model to give insight into superheavy elements shell effects. The ^{242}Pu(^{48}Ca,5n)^{285}114 nuclear reaction cross section is measured to be $0.6^{+1.3}_{-0.2}$ pb.

References

[AAA+02] A. Abánades, J. Aleixandre, S. Andriamonje, A. Angelopoulos, A. Apostolakis, H. Arnould, E. Belle, C. A. Bompas, D. Brozzi, J. Bueno, S. Buono, F. Carminati, F. Casagrande, P. Cennini, J. I. Collar, E. Cerro, R. Del Moral, S. Díez, L. Dumps, C. Eleftheriadis, M. Embid, R. Fernández, J. Gálvez, J. García, C. Gelès, A. Giorni, E. González, O. González, I. Goulas, D. Heuer, M. Hussonnois, Y. Kadi, P. Karaiskos, G. Kitis, R. Klapisch, P. Kokkas, V. Lacoste, C. Le Naour, C. López, J. M. Loiseaux, J. M. Martínez-Val, O. Méplan, H. Nifenecker, J. Oropesa, I. Papadopoulos, P. Pavlopoulos, E. Pérez-Enciso, A. Pérez-Navarro, M. Perlado, A. Placci, M. Poza, J. P. Revol, C. Rubbia, J. A. Rubio, L. Sakelliou, F. Salda na, E. Savvidis, F. Schussler, C. Sirvent, J. Tamarit, D. Trubert, A. Tzima, J. B. Viano, S. Vieira, V. Vlachoudis, and K. Zioutas. Results from the TARC experiment: spallation neutron phenomenology in lead and neutron-driven nuclear transmutation by adiabatic resonance crossing. *Nuclear Instruments and Methods in Physics Research Section A: Accelerators, Spectrometers, Detectors and Associated Equipment*, 478(3):577 – 730, 2002.

[AAB+85] P. Armbruster, Y. K. Agarwal, W. Brüchle, M. Brügger, J. P. Dufour, H. Gäggeler, F. P. Hessberger, S. Hofmann, P. Lemmertz, G. Münzenberg, K. Poppensieker, W. Reisdorf, M. Schädel, K. H. Schmidt, J. H. R. Schneider, W. F. W. Schneider, K. Sümmerer, D. Vermeulen, G. Wirth, A. Ghiorso, K. E. Gregorich, D. Lee, M. Leino, K. J. Moody, G. T. Seaborg, R. B. Welch, P. Wilmarth, S. Yashita, C. Frink, N. Greulich, G. Herrmann, U. Hickmann, N. Hildebrand, J. V. Kratz, N. Trautmann, M. M. Fowler, D. C. Hoffman, W. R. Daniels, H. R. von Gunten, and H. Dornhöfer. Attempts to produce superheavy elements by fusion of ^{48}Ca with ^{248}Cm in the bombarding energy range of 4.5-5.2 MeV/u. *Phys. Rev. Lett.*, 54(5):406–409, Feb 1985.

[AAS04a] G. G. Adamian, N. V. Antonenko, and W. Scheid. Isotopic trends in the production of superheavy nuclei in cold fusion reactions. *Phys. Rev. C*, 69(1):011601, Jan 2004.

[AAS04b] G. G. Adamian, N. V. Antonenko, and W. Scheid. Unexpected isotopic trends in synthesis of superheavy nuclei. *Phys. Rev. C*, 69(1):014607, Jan 2004.

[ABB$^+$02] J. Adam, A. Balabekyan, R. Brandt, V. Dzhelepov, S. Gustov, V. Kalinnikov, M. Krivopustov, I. Mirokhin, J. Mrazek, R. Odoj, V. Pronskikh, O. Savchenko, A. Sosnin, A. Solnyshkin, V. Stegailov, and V. Tsoupko-Sitnikov. Investigation of the formation of residual nuclei from radioactive ^{237}Np and ^{241}Am targets in reactions with 660-MeV protons. *Physics of Atomic Nuclei*, 65:763–775, 2002. 10.1134/1.1481467.

[ABB$^+$08] A. Alekseev, A. Bergman, A. Berlev, E. Koptelov, B. Samylin, A. Trufanov, B. Fursov, and V. Shorin. Cross section for the subthreshold fission of ^{236}U. *Physics of Atomic Nuclei*, 71:1351–1360, 2008. 10.1134/S1063778808080048.

[ABB$^+$09a] A. Alekseev, A. Bergman, A. Berlev, E. Koptelov, B. Samylin, A. Trufanov, B. Fursov, and V. Shorin. ^{242m}Am and ^{245}Cm neutron fission cross sections. *Atomic Energy*, 106:133–140, 2009. 10.1007/s10512-009-9142-1.

[ABB$^+$09b] A. Alekseev, A. Bergman, A. Berlev, E. Koptelov, B. Samylin, A. Trufanov, B. Fursov, and V. Shorin. ^{243}Cm neutron fission cross section. *Atomic Energy*, 107:110–115, 2009. 10.1007/s10512-009-9204-4.

[ABB$^+$09c] I. Antcheva, M. Ballintijn, B. Bellenot, M. Biskup, R. Brun, N. Buncic, Ph. Canal, D. Casadei, O. Couet, V. Fine, L. Franco, G. Ganis, A. Gheata, D. Gonzalez Maline, M. Goto, J. Iwaszkiewicz, A. Kreshuk, D. Marcos Segura, R. Maunder, L. Moneta, A. Naumann, E. Offermann, V. Onuchin, S. Panacek, F. Rademakers, P. Russo, and M. Tadel. ROOT – A C++ framework for petabyte data storage, statistical analysis and visualization. *Computer Physics Communications*, 180(12):2499 – 2512, 2009. 40 YEARS OF CPC: A celebratory issue focused on quality software for high performance, grid and novel computing architectures.

[ABB$^+$10a] A. Alekseev, A. Bergman, A. Berlev, E. Koptelov, B. Samylin, M. Svirin, A. Trufanov, B. Fursov, and V. Shorin. Cross section for the subbarrier fission of ^{244}Cm. *Physics of Atomic Nuclei*, 73:1487–1498, 2010. 10.1134/S1063778810090036.

[ABB$^+$10b] A. Alekseev, A. Bergman, A. Berlev, E. Koptelov, B. Samylin, A. Trufanov, B. Fursov, and V. Shorin. Cross section for ^{246}Cm subbarrier fission. *Physics of Atomic Nuclei*, 73:1645–1655, 2010. 10.1134/S1063778810100029.

[ABGt04] A.A. Alekseev, A.A. Bergman, and O.N. Goncharenko *et al.* In *Proceedings of the International Seminar on Interactions of Neutrons with Nuclei, ISISNN-12 (7th: 2004: Dubna, Russia)*, page 237, 2004.

[ABSF72] I. Ahmad, R. F. Barnes, R. K. Sjoblom, and P. R. Fields. Electron capture decay of ^{240}Am. *Journal of Inorganic and Nuclear Chemistry*, 34(11):3335 – 3343, 1972.

[Alo74] J.R. Alonso. Synthesis of transuranic elements in charged particle reactions. In *Gmelin Handbuch der Anorganischen Chemie*, volume 7b, page 28. Verlag

Chemie GmbH, Weinheim, Germany, 1974.

[AM74] D.C. Aumann and G. Müllen. Preparation of targets of Ca, Ba, Fe, La, Pb, Tl, Bi, Th and U by electrodeposition from organic solutions. *Nuclear Instruments and Methods*, 115(1):75 – 81, 1974.

[And60] Edward Anders. The radiochemistry of technetium. Tech. Rep. NAS-NS 3021, National Academy of Sciences, National Research Council, 1960. Available at `http://library.lanl.gov/radiochemistry/index.htm`.

[AR76] J. L. Alberi and V. Radeka. Position sensing by charge division. *IEEE Transactions on Nuclear Science*, 23(1):251 –258, Feb 1976.

[Ari07] Y. Aritomo. Possibility of synthesizing a doubly magic superheavy nucleus. *Phys. Rev. C*, 75(2):024602, Feb 2007.

[Arm] P. Armbruster. (private communication).

[ASKB03] Y. Abe, C. Shen, G. Kosenko, and D. Boilley. Theory of fusion for superheavy elements. *Physics of Atomic Nuclei*, 66:1057–1064, 2003.

[AWT03] G. Audi, A. H. Wapstra, and C. Thibault. The 2003 atomic mass evaluation: (II). Tables, graphs and references. *Nuclear Physics A*, 729(1):337 – 676, 2003. The 2003 NUBASE and Atomic Mass Evaluations.

[Bar77] G. Scott Barney. The kinetics of plutonium oxide dissolution in nitric/hydrofluoric acid mixtures. *Journal of Inorganic and Nuclear Chemistry*, 39(9):1665 – 1669, 1977.

[BBPF59] L. R. Bunney, N. E. Ballou, Juan. Pascual, and Stephen. Foti. Quantitative radiochemical analysis by ion exchange. Anion exchange behavior of several metal ions in hydrochloric, nitric, and sulfuric acid solutions. *Analytical Chemistry*, 31(3):324–326, 1959.

[BBYK79] C. E. Bemis, J. R. Beene, J. P. Young, and S. D. Kramer. Optical isomer shift for the spontaneous-fission isomer $^{240}\mathrm{Am}^{m}$. *Phys. Rev. Lett.*, 43(25):1854–1858, Dec 1979.

[Beh77] J. W. Behrens. Systematics of neutron-induced-fission cross sections in the MeV range. *Phys. Rev. Lett.*, 39(2):68–71, Jul 1977.

[BFI$^+$94] A.I. Blokhin, B.I. Fursov, A.V. Ignatyuk, V.N. Koshcheev, E.V. Kulikov, B.D. Kuzminov, V.N. Manokhin, and M.N. Nikolaev. In *Proceedings of the International Conference on Nuclear Data for Science and Technology (7th: 1994: Gatlinburg, Tennessee)*, volume 2, page 695, 1994.

[BG74] T. Braun and G. Ghersini, editors. *Extraction chromatography.* Elsevier, New York, New York, 1974.

[BGK$^+$09] R.C. Barber, H.W. Gäggeler, P.J. Karol, H. Nakahara, E. Vardaci, and E. Vogt. Discovery of the element with atomic number 112 (IUPAC Technical Report). *Pure and Applied Chemistry*, 81(7):1331 – 1343, 2009.

[Bha98] M. R. Bhat. Nuclear data sheets for A = 57. *Nuclear Data Sheets*, 85(3):415 – 536, 1998.

[BHK$^+$98] H. Backe, M. Hies, H. Kunz, W. Lauth, O. Curtze, P. Schwamb, M. Sewtz, W. Theobald, R. Zahn, K. Eberhardt, N. Trautmann, D. Habs, R. Repnow, and B. Fricke. Isotope shift measurements for superdeformed fission isomeric states. *Phys. Rev. Lett.*, 80(5):920–923, Feb 1998.

[BIM$^+$56] A.A. Bergman, A.I. Isacoff, I.D. Muring, F.L. Shapiro, I.V. Shtranikh, and M.V. Cazarnovsky. A neutron spectrometer based on measuring the slowing-down time of neutrons in lead. In *Proceedings of International Conference on the Peaceful Uses of Atomic Energy (1st: 1955: Geneva, Switzerland)*, volume 4, pages 135 – 146. United Nations, New York, 1956.

[BKN$^+$11] R.C. Barber, P.J. Karol, H. Nakahara, E. Vardaci, and E.W. Vogt. Discovery of the elements with atomic numbers greater than or equal to 113 (IUPAC Technical Report). *Pure and Applied Chemistry*, 83(7):1485–1498, 2011.

[BMR$^+$95] R. Bodemann, R. Michel, R. Rösell, U. Herpers, B. Holmqvist, H. Conde, and P. Malmborg. Production of radionuclides from target elements ($22 \leq Z \leq 29$) by proton-induced reactions up to 100 MeV. In S.M. Qaim, editor, *Progress Report on Nuclear Data Research in the Federal Republic of Germany for the Period April 1, 1994 to March 31, 1995*, volume NEA/NSC/DOC(95)10, INDC(Ger)-040, Jül-3086, 1995.

[Bri73] H. C. Britt. Properties of fission isomers. *Atomic Data and Nuclear Data Tables*, 12(5):407 – 414, 1973.

[Brü03] W. Brüchle. Confidence intervals for experiments with background and small numbers of events. *Radiochimica Acta*, 91(2-2003):71–80, 2011/05/25 2003.

[BT06] E. Browne and J.K. Tuli. Nuclear data sheets for a = 236. *Nuclear Data Sheets*, 107(10):2649 – 2714, 2006.

[Bur58] L. L. Burger. Uranium and plutonium extraction by organophosphorus compounds. *The Journal of Physical Chemistry*, 62(5):590–593, 1958.

[Bur06] T.W. Burrows. Nuclear data sheets for A = 48. *Nuclear Data Sheets*, 107(7):1747 – 1922, 2006.

[BW79] H.C. Britt and J.B. Wilhelmy. Simulated (n, f) cross sections for exotic actinide nuclei. *Nucl. Sci. Eng.*, 72(2):222–229, Nov 1979.

[BW81] H.C. Britt and J.B. Wilhelmy. Simulated (n, f) cross sections for exotic actinide nuclei. Tech. Rep. LA-UR-79-614, Los Alamos National Laboratory, 1981.

[CH00] R. Chiarizia and E.P. Horwitz. Radiolytic stability of some recently developed ion exchange and extraction chromatographic resins containing diphosphonic acid groups. *Solvent Extraction and Ion Exchange*, 18:109–132, 2000.

[CIM83] E.A. Cherepanov, A.S. Iljinov, and M.V. Mebel. Systematics of the effective ratio (Γ_n/Γ_f) of neutron emission and fission partial widths for transcurium nuclei. *Journal of Physics G: Nuclear Physics*, 9(8):931, 1983.

[CM56] J.G. Cuninghame and G.L. Miles. The separation of plutonium by extraction with thenoyltrifluoracetone (TTA). *Journal of Inorganic and Nuclear Chemistry*, 3(1):54 – 63, 1956.

[Coh61] Donald Cohen. The absorption spectra of plutonium ions in perchloric acid solutions. *Journal of Inorganic and Nuclear Chemistry*, 18:211 – 218, 1961.

[Col65] G.H. Coleman. The radiochemistry of plutonium. Tech. Rep. NAS-NS 3058, National Academy of Sciences, National Research Council, 1965. Available at `http://library.lanl.gov/radiochemistry/index.htm`.

[CW71] Jen-Chang Cou and H. Werle. (n, γ)-cross section measurements of ^{99}Tc, Eu, Sm, and Fe in the energy range 1 eV to 50 keV with a slowing-down time spectrometer. *Journal of Nuclear Energy*, 27:811 – 823, 1971.

[CzH$^+$06] M.B. Chadwick, P. Obložinský, M. Herman, N.M. Greene, R.D. McKnight, D.L. Smith, P.G. Young, R.E. MacFarlane, G.M. Hale, S.C. Frankle, A.C. Kahler, T. Kawano, R.C. Little, D.G. Madland, P. Moller, R.D. Mosteller, P.R. Page, P. Talou, H. Trellue, M.C. White, W.B. Wilson, R. Arcilla, C.L. Dunford, S.F. Mughabghab, B. Pritychenko, D. Rochman, A.A. Sonzogni, C.R. Lubitz, T.H. Trumbull, J.P. Weinman, D.A. Brown, D.E. Cullen, D.P. Heinrichs, D.P. McNabb, H. Derrien, M.E. Dunn, N.M. Larson, L.C. Leal, A.D. Carlson, R.C. Block, J.B. Briggs, E.T. Cheng, H.C. Huria, M.L. Zerkle, K.S. Kozier, A. Courcelle, V. Pronyaev, and S.C. van der Marck. ENDF/B-VII.0: Next generation evaluated nuclear data library for nuclear science and technology. *Nuclear Data Sheets*, 107(12):2931 – 3060, 2006. Evaluated Nuclear Data File ENDF/B-VII.0.

[DacGD$^+$09] I. Dragojević, K. E. Gregorich, Ch. E. Düllmann, J. Dvorak, P. A. Ellison, J. M. Gates, S. L. Nelson, L. Stavsetra, and H. Nitsche. New isotope ^{263}Hs. *Phys. Rev. C*, 79(1):011602, Jan 2009.

[DBC$^+$06] J. Dvorak, W. Brüchle, M. Chelnokov, R. Dressler, Ch. E. Düllmann, K. Eberhardt, V. Gorshkov, E. Jäger, R. Krücken, A. Kuznetsov, Y. Nagame, F. Nebel, Z. Novackova, Z. Qin, M. Schädel, B. Schausten, E. Schimpf, A. Semchenkov, P. Thörle, A. Türler, M. Wegrzecki, B. Wierczinski, A. Yakushev, and A. Yeremin. Doubly magic nucleus $^{270}_{108}$Hs$_{162}$. *Phys. Rev. Lett.*, 97(24):242501, Dec 2006.

[DBC$^+$08] J. Dvorak, W. Brüchle, M. Chelnokov, Ch. E. Düllmann, Z. Dvorakova, K. Eberhardt, E. Jäger, R. Krücken, A. Kuznetsov, Y. Nagame, F. Nebel, K. Nishio, R. Perego, Z. Qin, M. Schädel, B. Schausten, E. Schimpf, R. Schuber, A. Semchenkov, P. Thörle, A. Türler, M. Wegrzecki, B. Wierczinski, A. Yakushev, and A. Yeremin. Observation of the $3n$ evaporation channel in the complete hot-fusion reaction ^{26}Mg+^{248}Cm leading to the new superheavy nuclide ^{271}Hs. *Phys. Rev. Lett.*, 100(13):132503, Apr 2008.

[DBT$^+$99] G. Duchêne, F. A. Beck, P. J. Twin, G. de France, D. Curien, L. Han, C. W. Beausang, M. A. Bentley, P. J. Nolan, and J. Simpson. The clover: a new generation of composite Ge detectors. *Nuclear Instruments and Methods in Physics Research Section A: Accelerators, Spectrometers, Detectors and Associated Equipment*, 432(1):90 – 110, 1999.

[DEJ+99] R. Dressler, B. Eichler, D. T. Jost, D. Piguet, A. Türler, Ch. Düllmann, R. Eichler, H. W. Gäggeler, M. Gärtner, M. Schädel, S. Taut, and A. B. Yakushev. Production of ^{262}Db ($Z = 105$) in the reaction ^{248}Cm(^{19}F, $5n$). *Phys. Rev. C*, 59(6):3433–3436, Jun 1999.

[DK09] V.Yu. Denisov and A.A. Khudenko. α-decay half-lives: Empirical relations. *Phys. Rev. C*, 79(5):054614, May 2009.

[Dra09] I. Dragojević. Systematic studies of nuclear fusion reactions at low excitation energies with ^{208}Pb targets and projectiles differing by two neutrons. Thesis, Universtity of California, Berkeley, 2009.

[DRT+07] Y. Danon, C. Romano, J. Thompson, T. Watson, R.C. Haight, S.A. Wender, D.J. Vieira, E. Bond, J.B. Wilhelmy, J.M. O'Donnell, A. Michaudon, T.A. Bredeweg, T. Schurman, D. Rochman, T. Granier, T. Ethvignot, J. Taieb, and J.A. Becker. Measurements with the high flux lead slowing-down spectrometer at LANL. *Nuclear Instruments and Methods in Physics Research Section B: Beam Interactions with Materials and Atoms*, 261(1-2):953 – 955, 2007.

[DSE66] E.D. Donets, V.A. Shchegolev, and V.A. Ermakov. Reactions involving evaporation of several neutrons on bombardment of U^{238} by accelerated ions of O^{18}, F^{19}, and Ne^{22}. *Soviet Journal of Nuclear Physics*, 2(6):723 – 731, Jun 1966.

[DSY+10] Ch. E. Düllmann, M. Schädel, A. Yakushev, A. Türler, K. Eberhardt, J. V. Kratz, D. Ackermann, L.-L. Andersson, M. Block, W. Brüchle, J. Dvorak, H. G. Essel, P. A. Ellison, J. Even, J. M. Gates, A. Gorshkov, R. Graeger, K. E. Gregorich, W. Hartmann, R.-D. Herzberg, F. P. Heßberger, D. Hild, A. Hübner, E. Jäger, J. Khuyagbaatar, B. Kindler, J. Krier, N. Kurz, S. Lahiri, D. Liebe, B. Lommel, M. Maiti, H. Nitsche, J. P. Omtvedt, E. Parr, D. Rudolph, J. Runke, B. Schausten, E. Schimpf, A. Semchenkov, J. Steiner, P. Thörle-Pospiech, J. Uusitalo, M. Wegrzecki, and N. Wiehl. Production and decay of element 114: High cross sections and the new nucleus ^{277}Hs. *Phys. Rev. Lett.*, 104(25):252701, Jun 2010.

[EGB+10] P. A. Ellison, K. E. Gregorich, J. S. Berryman, D. L. Bleuel, R. M. Clark, I. Dragojević, J. Dvorak, P. Fallon, C. Fineman-Sotomayor, J. M. Gates, O. R. Gothe, I. Y. Lee, W. D. Loveland, J. P. McLaughlin, S. Paschalis, M. Petri, J. Qian, L. Stavsetra, M. Wiedeking, and H. Nitsche. New superheavy element isotopes: ^{242}Pu(^{48}Ca,$5n$)^{285}114. *Phys. Rev. Lett.*, 105(18):182701, Oct 2010.

[EK00] H.G. Essel and N. Kurz. The general purpose data acquisition system MBS. *IEEE Transactions on Nuclear Science*, 47(2):337 –339, Apr 2000.

[FB64] J.P. Faris and R.F. Buchanan. Anion exchange characteristics of the elements in nitric acid and nitrate solutions and application in trace element analysis.

Tech. Rep. ANL-6811, Argonne National Laboratory, 1964.

[FC98] Gary J. Feldman and Robert D. Cousins. Unified approach to the classical statistical analysis of small signals. *Phys. Rev. D*, 57(7):3873–3889, Apr 1998.

[FC00] A. Filatenkov and S. Chuvaev. Measurement of cross sections for the reactions ^{241}am$(n, 2n)$ and ^{241}am$(n, 3n)$. *Physics of Atomic Nuclei*, 63:1504–1510, 2000. 10.1134/1.1312883.

[FGD$^+$04] C. M. Folden, K. E. Gregorich, Ch. E. Düllmann, H. Mahmud, G. K. Pang, J. M. Schwantes, R. Sudowe, P. M. Zielinski, H. Nitsche, and D. C. Hoffman. Development of an odd-Z-projectile reaction for heavy element synthesis: ^{208}Pb(^{64}Ni,n)^{271}Ds and ^{208}Pb(^{65}Cu,n)^{272}111. *Phys. Rev. Lett.*, 93(21):212702, Nov 2004.

[FJFL06] Zhao-Qing Feng, Gen-Ming Jin, Fen Fu, and Jun-Qing Li. Production cross sections of superheavy nuclei based on dinuclear system model. *Nuclear Physics A*, 771:50 – 67, 2006.

[Fol04] C.M. Folden. Development of odd-Z-projectile reactions for transactinide element synthesis. Thesis, Universtity of California, Berkeley, 2004.

[FRNA73] Alain Fleury, F. H. Ruddy, M. N. Namboodiri, and John M. Alexander. Excitation functions for spallation products and fission isomers in ^{237}Np$(^4He, xn)^{241-x}$Am reactions. *Phys. Rev. C*, 7(3):1231–1237, Mar 1973.

[GA70] D. J. Gorman and F. Asaro. Alpha decay of ^{240}Am. *Phys. Rev. C*, 2(6):2406–2408, Dec 1970.

[GAC$^+$10] R. Graeger, D. Ackermann, M. Chelnokov, V. Chepigin, Ch. E. Düllmann, J. Dvorak, J. Even, A. Gorshkov, F. P. Heßberger, D. Hild, A. Hübner, E. Jäger, J. Khuyagbaatar, B. Kindler, J. V. Kratz, J. Krier, A. Kuznetsov, B. Lommel, K. Nishio, H. Nitsche, J. P. Omtvedt, O. Petrushkin, D. Rudolph, J. Runke, F. Samadani, M. Schädel, B. Schausten, A. Türler, A. Yakushev, and Q. Zhi. Experimental study of the ^{238}U(^{36}S,$3-5n$)$^{269-271}$Hs reaction leading to the observation of ^{270}Hs. *Phys. Rev. C*, 81(6):061601, Jun 2010.

[GBK$^+$76] A. Gavron, H. C. Britt, E. Konecny, J. Weber, and J. B. Wilhelmy. Γ_n/Γ_f for actinide nuclei using $(^3\mathrm{He}, df)$ and $(^3\mathrm{He}, tf)$ reactions. *Phys. Rev. C*, 13(6):2374–2384, Jun 1976.

[GCCS56] Richard A. Glass, Robert J. Carr, James W. Cobble, and Glenn T. Seaborg. Spallation-fission competition in heaviest elements; Helium-ion-induced reactions in plutonium isotopes. *Phys. Rev.*, 104(2):434–447, Oct 1956.

[GDS$^+$11] J. M. Gates, Ch. E. Düllmann, M. Schädel, A. Yakushev, A. Türler, K. Eberhardt, J. V. Kratz, D. Ackermann, L.-L. Andersson, M. Block, W. Brüchle, J. Dvorak, H. G. Essel, P. A. Ellison, J. Even, U. Forsberg, J. Gellanki, A. Gorshkov, R. Graeger, K. E. Gregorich, W. Hartmann, R.-D. Herzberg, F. P. Heßberger, D. Hild, A. Hübner, E. Jäger, J. Khuyagbaatar, B. Kindler, J. Krier, N. Kurz, S. Lahiri, D. Liebe, B. Lommel, M. Maiti, H. Nitsche,

J. P. Omtvedt, E. Parr, D. Rudolph, J. Runke, H. Schaffner, B. Schausten, E. Schimpf, A. Semchenkov, J. Steiner, P. Thörle-Pospiech, J. Uusitalo, M. Wegrzecki, and N. Wiehl. First superheavy element experiments at the GSI recoil separator TASCA: The production and decay of element 114 in the ^{244}Pu(^{48}Ca,$3-4n$) reaction. *Phys. Rev. C*, 83(5):054618, May 2011.

[GGD+06] K. E. Gregorich, J. M. Gates, Ch. E. Düllmann, R. Sudowe, S. L. Nelson, M. A. Garcia, I. Dragojević, C. M. Folden III, S. H. Neumann, D. C. Hoffman, and H. Nitsche. New isotope ^{264}Sg and decay properties of $^{262-264}$Sg. *Phys. Rev. C*, 74(4):044611, Oct 2006.

[GGG+08] J. M. Gates, M. A. Garcia, K. E. Gregorich, Ch. E. Düllmann, I. Dragojević, J. Dvorak, R. Eichler, C. M. Folden, W. Loveland, S. L. Nelson, G. K. Pang, L. Stavsetra, R. Sudowe, A. Türler, and H. Nitsche. Synthesis of rutherfordium isotopes in the ^{238}U(^{26}Mg, xn)$^{264-x}$Rf reaction and study of their decay properties. *Phys. Rev. C*, 77(3):034603, Mar 2008.

[GGL+03] K.E. Gregorich, T.N. Ginter, W. Loveland, D. Peterson, J.B. Patin, C.M. Folden, D.C. Hoffman, D.M. Lee, H. Nitsche, J.P. Omtvedt, L.A. Omtvedt, L. Stavsetra, R. Sudowe, P.A. Wilk, P.M. Zielinski, and K. Aleklett. Cross-section limits for the ^{208}Pb(^{86}Kr,n)^{293}118 reaction. *The European Physical Journal A - Hadrons and Nuclei*, 18:633–638, 2003.

[GHM+06] Andreas Geist, Clément Hill, Giuseppe Modolo, Mark R. St, J. Foreman, Michael Weigl, Klaus Gompper, and Michael J. Hudson. 6,6'-bis(5,5,8,8-tetramethyl-5,6,7,8-tetrahydro-benzo[1,2,4]triazin-3-yl) [2,2']bipyridine, an effective extracting agent for the separation of americium(III) and curium(III) from the lanthanides. *Solvent Extraction and Ion Exchange*, 24:463 – 483, 2006.

[GLP+05] K. E. Gregorich, W. Loveland, D. Peterson, P. M. Zielinski, S. L. Nelson, Y. H. Chung, Ch. E. Düllmann, C. M. Folden III, K. Aleklett, R. Eichler, D. C. Hoffman, J. P. Omtvedt, G. K. Pang, J. M. Schwantes, S. Soverna, P. Sprunger, R. Sudowe, R. E. Wilson, and H. Nitsche. Attempt to confirm superheavy element production in the Ca^{48}+U^{238} reaction. *Phys. Rev. C*, 72(1):014605, Jul 2005.

[GML+87] Kenneth E. Gregorich, Kenton J. Moody, D. Lee, Wing K. Kot, Robert B. Welch, Philip A. Wilmarth, and Glenn T. Seaborg. Actinide production in ^{136}Xe bombardments of ^{249}Cf. *Phys. Rev. C*, 35(6):2117–2124, Jun 1987.

[GNA+74] A. Ghiorso, J. M. Nitschke, J. R. Alonso, C. T. Alonso, M. Nurmia, G. T. Seaborg, E. K. Hulet, and R. W. Lougheed. Element 106. *Phys. Rev. Lett.*, 33(25):1490–1493, Dec 1974.

[GNH+69] A. Ghiorso, M. Nurmia, J. Harris, K. Eskola, and P. Eskola. Positive identification of two alpha-particle-emitting isotopes of element 104. *Phys. Rev. Lett.*, 22(24):1317–1320, Jun 1969.

[GQF+01] Z.G. Gan, Z. Qin, H.M. Fan, X.G. Lei, Y.B. Xu, J.J. He, H.Y. Liu, X.L. Wu, J.S. Guo, X.H. Zhou, S.G. Yuan, and G.M. Jin. A new alpha-particle-emitting isotope ^{259}Db. *The European Physical Journal A - Hadrons and Nuclei*, 10:21–25, 2001.

[Gre] K.E. Gregorich. (private communication).

[GSN67] Albert Ghiorso, Torbjorn Sikkeland, and Matti J. Nurmia. Isotopes of element 102 with mass 251 to 258. *Phys. Rev. Lett.*, 18(11):401–404, Mar 1967.

[GYL+88] A. Ghiorso, S. Yashita, M.E. Leino, L. Frank, J. Kalnins, P. Armbruster, J.-P. Dufour, and P.K. Lemmertz. Sassy, a gas-filled magnetic separator for the study of fusion reaction products. *Nuclear Instruments and Methods in Physics Research Section A: Accelerators, Spectrometers, Detectors and Associated Equipment*, 269(1):192 – 201, 1988.

[HAA+07] S. Hofmann, D. Ackermann, S. Antalic, H. Burkhard, V. Comas, R. Dressler, Z. Gan, S. Heinz, J. Heredia, F. Heßberger, J. Khuyagbaatar, B. Kindler, I. Kojouharov, P. Kuusiniemi, M. Leino, B. Lommel, R. Mann, G. Münzenberg, K. Nishio, A. Popeko, S. Śaro, H. Schött, B. Streicher, B. Sulignano, J. Uusitalo, M. Venhart, and A. Yeremin. The reaction ^{48}Ca + ^{238}U $\rightarrow$ ^{286}112 studied at the GSI-SHIP. *The European Physical Journal A - Hadrons and Nuclei*, 32:251–260, 2007.

[HCD+93] E. Philip Horwitz, Renato Chiarizia, Mark L. Dietz, Herbert Diamond, and Donald M. Nelson. Separation and preconcentration of actinides from acidic media by extraction chromatography. *Analytica Chimica Acta*, 281(2):361 – 372, 1993.

[HCNO+01] M. Herman, R. Capote-Noy, P. Oblozinský, A. Trkov, and V. Zerkin. Recent development and validation of the nuclear reaction code EMPIRE. In K. Shibata, editor, *Proc. Int. Conf. Nuclear Data for Science and Technology*, volume 1, page 116, Tsukuba, Japan, 2001. Atomic Energy Society of Japan.

[HDC+95] E. Philip Horwitz, Mark L. Dietz, Renato Chiarizia, Herbert Diamond, Sherrod L. Maxwell, and Matthew R. Nelson. Separation and preconcentration of actinides by extraction chromatography using a supported liquid anion exchanger: application to the characterization of high-level nuclear waste solutions. *Analytica Chimica Acta*, 310(1):63 – 78, 1995.

[Hel84] O. Helene. Errors in experiments with small numbers of events. *Nuclear Instruments and Methods in Physics Research Section A: Accelerators, Spectrometers, Detectors and Associated Equipment*, 228(1):120 – 128, 1984.

[Heß10] Fritz-Peter Heßberger. (private communication), 2010.

[HHA+01] S. Hofmann, F.P. Heßberger, D. Ackermann, S. Antalic, P. Cagarda, S. Ćwiok, B. Kindler, J. Kojouharova, B. Lommel, R. Mann, G. Münzenberg, A.G. Popeko, S. Śaro, H.J. Schött, and A.V. Yeremin. The new isotope ^{270}110 and its decay products ^{266}Hs and ^{262}Sg. *The European Physical Journal A -*

Hadrons and Nuclei, 10:5–10, 2001.

[HHA$^+$02] S. Hofmann, F.P. Heßberger, D. Ackermann, G. Münzenberg, S. Antalic, P. Cagarda, B. Kindler, J. Kojouharova, M. Leino, B. Lommel, R. Mann, A.G. Popeko, S. Śaro, J. Uusitalo, and A.V. Yeremin. New results on elements 111 and 112. *The European Physical Journal A - Hadrons and Nuclei*, 14:147–157, 2002. 10.1140/epja/i2001-10119-x.

[HHA$^+$04] F. P. Heßberger, S. Hofmann, D. Ackermann, P. Cagarda, R. D. Herzberg, I. Kojouharov, P. Kuusiniemi, M. Leino, and R. Mann. Alpha-gamma decay studies of ^{251,253}No and their daughter products ^{247,249}Fm. *The European Physical Journal A - Hadrons and Nuclei*, 22:417–427, 2004.

[HHN$^+$97] F.P. Heßberger, S. Hofmann, V. Ninov, P. Armbruster, H. Folger, G. Münzenberg, H.J. Schött, A.G. Popeko, A.V. Yeremin, A.N. Andreyev, and S. Śaro. Spontaneous fission and alpha-decay properties of neutron deficient isotopes $^{257-253}$104 and ^{258}106. *Zeitschrift für Physik A Hadrons and Nuclei*, 359:415–425, 1997.

[HHS$^+$09] F. Heßberger, S. Hofmann, B. Streicher, B. Sulignano, S. Antalic, D. Ackermann, S. Heinz, B. Kindler, I. Kojouharov, P. Kuusiniemi, M. Leino, B. Lommel, R. Mann, A. Popeko, Š. Šáro, J. Uusitalo, and A. Yeremin. Decay properties of neutron-deficient isotopes of elements from $Z = 101$ to $Z = 108$. *The European Physical Journal A - Hadrons and Nuclei*, 41:145–153, 2009.

[HIL51] E. H. Huffman, G. M. Iddings, and R. C. Lilly. Anion exchange of zirconium, hafnium, niobium and tantalum in hydrochloric acid solutions. *Journal of the American Chemical Society*, 73(9):4474–4475, 1951.

[HKK$^+$11] H. Haba, D. Kaji, H. Kikunaga, Y. Kudou, K. Morimoto, K. Morita, K. Ozeki, T. Sumita, A. Yoneda, Y. Kasamatsu, Y. Komori, K. Ooe, and A. Shinohara. Production and decay properties of the 1.9-s isomeric state in ^{261}Rf. *Phys. Rev. C*, 83(3):034602, Mar 2011.

[HLW$^+$77] E. K. Hulet, R. W. Lougheed, J. F. Wild, J. H. Landrum, P. C. Stevenson, A. Ghiorso, J. M. Nitschke, R. J. Otto, D. J. Morrissey, P. A. Baisden, B. F. Gavin, D. Lee, R. J. Silva, M. M. Fowler, and G. T. Seaborg. Search for superheavy elements in the bombardment of ^{248}Cm with ^{48}Ca. *Phys. Rev. Lett.*, 39(7):385–389, Aug 1977.

[HNH90] Yuichi Hatsukawa, Hiromichi Nakahara, and Darleane C. Hoffman. Systematics of alpha decay half-lives. *Phys. Rev. C*, 42(2):674–682, Aug 1990.

[HNH$^+$95a] S. Hofmann, V. Ninov, F. P. Heßberger, P. Armbruster, H. Folger, G. Münzenberg, H. J. Schött, A. G. Popeko, A. V. Yeremin, A. N. Andreyev, S. Śaro, R. Janik, and M. Leino. The new element 111. *Zeitschrift für Physik A Hadrons and Nuclei*, 350:281–282, 1995. 10.1007/BF01291182.

[HNH$^+$95b] S. Hofmann, V. Ninov, F. P. Heßberger, P. Armbruster, H. Folger, G. Münzenberg, H. J. Schött, A. G. Popeko, A. V. Yeremin, A. N. Andreyev,

S. Śaro, R. Janik, and M. Leino. Production and decay ^{269}110. *Zeitschrift für Physik A Hadrons and Nuclei*, 350:277–280, 1995.

[HNH$^+$95c] S. Hofmann, V. Ninov, F. P. Heßberger, P. Armbruster, H. Folger, G. Münzenberg, H. J. Schött, A. G. Popeko, A. V. Yeremin, A. N. Andreyev, S. Śaro, R. Janik, and M. Leino. Production and decay of ^{269}110. *Zeitschrift für Physik A Hadrons and Nuclei*, 350:277–280, 1995. 10.1007/BF01291181.

[HNH$^+$96] S. Hofmann, V. Ninov, F.P. Heßberger, P. Armbruster, H. Folger, G. Münzenberg, H.J. Schött, A.G. Popeko, A.V. Yeremin, S. Śaro, R. Janik, and M. Leino. The new element 112. *Zeitschrift für Physik A Hadrons and Nuclei*, 354:229–230, 1996. 10.1007/s002180050036.

[Hof89] Darlene C. Hoffman. Spontaneous fission properties and lifetime systematics. *Nuclear Physics A*, 502:21 – 40, 1989.

[Hof03] S. Hofmann. Synthesis and properties of superheavy elements. *Journal of Nuclear and Radiochemical Sciences*, 4(1):R1–R13, 2003.

[HOW56] E.H. Huffman, R.L. Oswalt, and L.A. Williams. Anion-exchange separation of molybdenum and technetium and of tungsten and rhenium. *Journal of Inorganic and Nuclear Chemistry*, 3(1):49 – 53, 1956.

[IAE01] Charged particle cross-section database for medical radioisotope production: diagnostic radioisotopes and monitor reactions. Tech. Doc. IAEA-TECDOC-1211, International Atomic Energy Agency, 2001. Database and information available at `http://www-nds.iaea.org/medical`.

[IHN$^+$78] J. D. Illige, E. K. Hulet, J. M. Nitschke, R. J. Dougan, R. W. Lougheed, A. Ghiorso, and J. H. Landrum. Search for volatile superheavy elements from the reaction ^{248}Cm + ^{48}Ca. *Physics Letters B*, 78(2-3):209 – 212, 1978.

[INO$^+$08] O. Iwamoto, T. Nakagawa, N. Otuka, S. Chiba, K. Okumura, and G. Chiba. JENDL actinoid file 2008 and plan of covariance evaluation. *Nuclear Data Sheets*, 109(12):2885 – 2889, 2008. Special Issue on Workshop on Neutron Cross Section Covariances June 24-28, 2008, Port Jefferson, New York, USA.

[Jam85] F. James. Comment on: "Errors in experiments with small numbers of events". *Nuclear Instruments and Methods in Physics Research Section A: Accelerators, Spectrometers, Detectors and Associated Equipment*, 240(1):203 – 204, 1985.

[JAOS03] M. Johansson, J. Alstad, J. P. Omtvedt, and G. Skarnemark. A comparision of the extraction of carrier-free ^{176,177}W and ^{99}Mo with that of U, Th, Am, Cm, La, Ce, Tm, Yb, Lu and Hf into Aliquat 336 in toluene from nitric, phosphoric, and sulphuric acid media. *Radiochimica Acta*, 91(6):351–356, 2003.

[Jay68] Edwin T. Jaynes. Prior probabilities. *IEEE Transactions on Systems Science and Cybernetics*, SSC-4(3), September 1968.

[JBB$^+$08] M. Jandel, T. A. Bredeweg, E. M. Bond, M. B. Chadwick, R. R. Clement, A. Couture, J. M. O'Donnell, R. C. Haight, T. Kawano, R. Reifarth, R. S. Rundberg, J. L. Ullmann, D. J. Vieira, J. B. Wilhelmy, J. M. Wouters, U. Agvaanluvsan, W. E. Parker, C. Y. Wu, and J. A. Becker. Neutron capture cross section of ^{241}Am. *Phys. Rev. C*, 78(3):034609, Sep 2008.

[Jea00] R. Jeanloz. Science-based stockpile stewardship. *Phys. Today*, 53:44–50, Dec 2000.

[JK56] James S. Johnson and Kurt A. Kraus. Hydrolytic behavior of metal ions. VI. Ultracentrifugation of zirconium(IV) and hafnium(IV); effect of acidity on the degree of polymerization. *Journal of the American Chemical Society*, 78(16):3937–3943, 1956.

[KGZ$^+$92] J. V. Kratz, M. K. Gober, H. P. Zimmermann, M. Schädel, W. Brüchle, E. Schimpf, K. E. Gregorich, A. Türler, N. J. Hannink, K. R. Czerwinski, B. Kadkhodayan, D. M. Lee, M. J. Nurmia, D. C. Hoffman, H. Gäggeler, D. Jost, J. Kovacs, U. W. Scherer, and A. Weber. New nuclide ^{263}Ha. *Phys. Rev. C*, 45(3):1064–1069, Mar 1992.

[KKL$^+$09] M.U. Khandaker, K. Kim, M.W. Lee, K.S. Kim, G.N. Kim, Y.S. Cho, and Y.O. Lee. Investigations of the $^{\mathrm{nat}}\mathrm{Ti}(p,x)^{43,44m,44g,46,47,48Sc,48}\mathrm{V}$ nuclear processes up to 40 MeV. *Applied Radiation and Isotopes*, 67(7-8):1348 – 1354, 2009.

[KKL$^+$11] Mayeen Uddin Khandaker, Kwangsoo Kim, Manwoo Lee, Kyung Sook Kim, and Guinyun Kim. Excitation functions of (p,x) reactions on natural nickel up to 40 MeV. *Nuclear Instruments and Methods in Physics Research Section B: Beam Interactions with Materials and Atoms*, 269(10):1140 – 1149, 2011.

[KN56] K. Kraus and F. Nelson. In *Proceedings of International Conference on the Peaceful Uses of Atomic Energy (1st: 1955: Geneva, Switzerland)*, volume 7, page 113. United Nations, New York, 1956.

[KNM55] Kurt A. Kraus, Frederick Nelson, and George E. Moore. Anion-exchange studies. XVII. molybdenum(VI), tungsten(VI) and uranium(VI) in HCl and HCl-HF solutions. *Journal of the American Chemical Society*, 77(15):3972–3977, 1955.

[KNPV01] P.J. Karol, H. Nakahara, B.W. Petley, and E. Vogt. On the discovery of the elements 110-112 (IUPAC Technical Report). *Pure and Applied Chemistry*, 73(6):959 – 967, 2001.

[KNPV03] P.J. Karo, H. Nakahara, B.W. Petley, and E. Vogt. On the claims for discovery of elements 110, 111, 112, 114, 116, and 118 (IUPAC Technical Report). 75(10):1601 – 1611, 2003.

[KRa] A.J. Koning and D. Rochman. TENDL-2009: TALYS-based evaluated nuclear data library. Database and information available at `http://www.talys.eu/tendl-2009`.

[KRb] A.J. Koning and D. Rochman. TENDL-2010: TALYS-based evaluated nuclear data library. Database and information available at `http://www.talys.eu/tendl-2010`.

[KSF84] V.M. Kupriyanov, G.N. Smirenkin, and B.I. Fursov. Systematics of neutron cross sections and other characteristics of the fission of transuranium nuclei. *Sov. J. Nucl. Phys.*, 39(2):176–186, Feb 1984.

[KSM+93] P. Kopecky, F. Szelecsényi, T. Molnár, P. Mikecz, and F. Tárkányi. Excitation functions of (p, xn) reactions on ^{nat}Ti: Monitoring of bombarding proton beams. *Applied Radiation and Isotopes*, 44(4):687 – 692, 1993.

[KY78] V. Kosyakov and E. Yerin. Separation of transplutonium and rare-earth elements by extraction with HDEHP from DTPA solutions. *Journal of Radioanalytical and Nuclear Chemistry*, 43:37–51, 1978.

[KYY+97] Katsuhei Kobayashi, Shuji Yamamoto, Akihiro Yamanaka, Yoshihiro Nakagome, Yoshiaki Fujita, Satoshi Kanazawa, and Itsuro Kimura. Characteristics of the Kyoto University Lead Slowing-down Spectrometer (KULS) coupled to an electron linac. *Nuclear Instruments and Methods in Physics Research Section A: Accelerators, Spectrometers, Detectors and Associated Equipment*, 385(1):145 – 156, 1997.

[LA77] S. Y. Lin and John M. Alexander. Reactions of ^{237}Np with ^{4}He near the interaction barrier. *Phys. Rev. C*, 16(2):688–693, Aug 1977.

[LBRW90] P.W. Lisowski, C.D. Bowman, G.J. Russell, and S.A. Wender. The Los Alamos National Laboratory spallation neutron sources. *Nucl. Sci. Eng.*, 106:208 – 218, 1990.

[Leh70] Wayne K. Lehto. Fission cross-section ratio measurements of ^{239}Pu and ^{233}U to ^{235}U from 0.24 to 24 keV. *Nucl. Sci. Eng.*, 39:361–367, 1970.

[LGG66] R.M. Lessler, W.M. Gibson, and R.A. Glass. Radiative capture, particle emission and fission in heavy nuclei. *Nuclear Physics*, 81(2):401 – 416, 1966.

[LGL+96] M. R. Lane, K. E. Gregorich, D. M. Lee, M. F. Mohar, M. Hsu, C. D. Kacher, B. Kadkhodayan, M. P. Neu, N. J. Stoyer, E. R. Sylwester, J. C. Yang, and D. C. Hoffman. Spontaneous fission properties of ^{262}Rf. *Phys. Rev. C*, 53(6):2893–2899, Jun 1996.

[LGL+98] M. R. Lane, K. E. Gregorich, D. M. Lee, B. Wierczinski, C. A. McGrath, M. B. Hendricks, D. A. Shaughnessy, D. A. Strellis, E. R. Sylwester, P. A. Wilk, and D. C. Hoffman. Production cross sections of ^{261}Ha from the ^{250}Cf(^{15}N,4n) and ^{243}Am(^{22}Ne,4n) reactions. *Phys. Rev. C*, 58(6):3413–3418, Dec 1998.

[LGP+02] W. Loveland, K. E. Gregorich, J. B. Patin, D. Peterson, C. Rouki, P. M. Zielinski, and K. Aleklett. Search for the production of element 112 in the ^{48}Ca+^{238}U reaction. *Phys. Rev. C*, 66(4):044617, Oct 2002.

[LL99] A. Landgren and J.-O. Liljenzin. Extraction behavior of technetium and actinides in the aliquat-336/nitric acid system. *Solvent Extraction and Ion Exchange*, 17(6):1387 – 1401, 1999.

[LLO+94] Yu. A. Lazarev, Yu. V. Lobanov, Yu. Ts. Oganessian, V. K. Utyonkov, F. Sh. Abdullin, G. V. Buklanov, B. N. Gikal, S. Iliev, A. N. Mezentsev, A. N. Polyakov, I. M. Sedykh, I. V. Shirokovsky, V. G. Subbotin, A. M. Sukhov, Yu. S. Tsyganov, V. E. Zhuchko, R. W. Lougheed, K. J. Moody, J. F. Wild, E. K. Hulet, and J. H. McQuaid. Discovery of enhanced nuclear stability near the deformed shells $N = 162$ and $Z = 108$. *Phys. Rev. Lett.*, 73(5):624–627, Aug 1994.

[LLO+96] Yu. A. Lazarev, Yu. V. Lobanov, Yu. Ts. Oganessian, V. K. Utyonkov, F. Sh. Abdullin, A. N. Polyakov, J. Rigol, I. V. Shirokovsky, Yu. S. Tsyganov, S. Iliev, V. G. Subbotin, A. M. Sukhov, G. V. Buklanov, B. N. Gikal, V. B. Kutner, A. N. Mezentsev, K. Subotic, J. F. Wild, R. W. Lougheed, and K. J. Moody. α decay of $^{273}110$: Shell closure at $N = 162$. *Phys. Rev. C*, 54(2):620–625, Aug 1996.

[LWN+02] R. W. Lougheed, W. Webster, M. N. Namboodiri, D. R. Nethaway, K. J. Moody, J. H. Landrum, R. W. Hoff, R. J. Dupzyk, J. H. McQuaid, R. Gunnink, and E. D. Watkins. ^{239}Pu and ^{241}Am $(n, 2n)$ cross-section measurements near $En = 14$ MeV. *Radiochim. Acta*, 90:833–843, 2002.

[MA75] G. Müllen and D.C. Aumann. Preparation of targets of Np, Pu, Am, Cm and Cf by electrodeposition from organic solutions. *Nuclear Instruments and Methods*, 128(3):425 – 428, 1975.

[MAB+87] G. Münzenberg, P. Armbruster, G. Berthes, H. Folger, F. P. Heßberger, S. Hofmann, J. Keller, K. Poppensieker, A. B. Quint, W. Reisdorf, K. H. Schmidt, H. J. Schött, K. Sümmerer, I. Zychor, M. E. Leino, R. Hingmann, U. Gollerthan, and E. Hanelt. Observation of the isotopes $^{264}108$ and$^{265}108$. *Zeitschrift für Physik A Hadrons and Nuclei*, 328:49–59, 1987. 10.1007/BF01295182.

[MAF+84] G. Münzenberg, P. Armbruster, H. Folger, P. F. Heßberger, S. Hofmann, J. Keller, K. Poppensieker, W. Reisdorf, K. H. Schmidt, H. J. Schött, M. E. Leino, and R. Hingmann. The identification of element 108. *Zeitschrift für Physik A Hadrons and Nuclei*, 317:235–236, 1984. 10.1007/BF01421260.

[MAH+82] G. Münzenberg, P. Armbruster, F. P. Heßberger, S. Hofmann, K. Poppensieker, W. Reisdorf, J. H. R. Schneider, W. F. W. Schneider, K. H. Schmidt, C. C. Sahm, and D. Vermeulen. Observation of one correlated α-decay in the reaction ^{58}Fe on^{209}Bi$\rightarrow^{267}$109. *Zeitschrift für Physik A Hadrons and Nuclei*, 309:89–90, 1982. 10.1007/BF01420157.

[MAH+89] G. Münzenberg, P. Armbruster, S. Hofmann, F. P. Heßberger, H. Folger, J. G. Keller, V. Ninov, K. Poppensieker, A. B. Quint, W. Reisdorf, K. H. Schmidt, J. R. H. Schneider, H. J. Schött, K. Sümmerer, I. Zychor, M. E. Leino, D. Ackermann, U. Gollerthan, E. Hanelt, W. Morawek, D. Vermeulen, Y. Fujita, and T. Schwab. Element 107. *Zeitschrift für Physik A Hadrons and Nuclei*, 333:163–175, 1989. 10.1007/BF01565147.

[Mas88] V. M. Maslov. Fission cross sections of americium isotopes. *Atomic Energy*, 64:478–482, 1988. 10.1007/BF01124585.

[MB80] R. Michel and G. Brinkmann. On the depth-dependent production of radionuclides ($44 \leq \mathrm{A} \leq 59$) by solar protons in extraterrestrial matter. *Journal of Radioanalytical and Nuclear Chemistry*, 59(2):467–510, 1980.

[MC54] G. H. McCormick and B. L. Cohen. Fission and total reaction cross sections for 22-MeV protons on Th^{232}, U^{235}, and U^{238}. *Phys. Rev.*, 96(3):722–724, Nov 1954.

[Men69] D.I. Mendeleev. *Journal of the Russian Chemical Society*, 1:60 – 77, 1869.

[MFH$^+$79] G. Münzenberg, W. Faust, S. Hofmann, P. Armbruster, K. Güttner, and H. Ewald. The velocity filter ship, a separator of unslowed heavy ion fusion products. *Nuclear Instruments and Methods*, 161(1):65 – 82, 1979.

[MG96] Victoria McLane and Cross Section Evaluation Working Group. ENDF-201 ENDF/B-VI summary documentation. Tech. Rep. BNL-NCS-17541 (ENDF-201), 1996.

[MGS$^+$05] S.G. Mashnik, K.K. Gudima, A.J. Sierk, M. Baznat, and N.V. Mokhov. CEM03.01 user manual. Tech. Rep. LA-UR-05-7321, Los Alamos National Laboratory, 2005.

[MHH$^+$81] G. Münzenberg, S. Hofmann, F. P. Heßberger, W. Reisdorf, K. H. Schmidt, J. H. R. Schneider, P. Armbruster, C. C. Sahm, and B. Thuma. Identification of element 107 by α correlation chains. *Zeitschrift für Physik A Hadrons and Nuclei*, 300:107–108, 1981. 10.1007/BF01412623.

[MHH$^+$88] G. Münzenberg, S. Hofmann, F. P. Heßberger, H. Folger, V. Ninov, K. Poppensieker, A. B. Quint, W. Reisdorf, H. J. Schött, K. Sümmerer, P. Armbruster, M. E. Leino, D. Ackermann, U. Gollerthan, E. Hanelt, W. Morawek, Y. Fujita, T. Schwab, and A. Türler. New results on element 109. *Zeitschrift für Physik A Hadrons and Nuclei*, 330:435–436, 1988. 10.1007/BF01290131.

[MHPS03] I. Muntian, S. Hofmann, Z. Patyk, and A. Sobiczewski. Properties of heaviest nuclei. *Acta Physica Polonica B*, 34(4):2073 – 2082, 2003.

[MLMR03] B. Mukhopadhyay, S. Lahiri, K. Mukhopadhyay, and A. Ramaswami. Separation of carrier-free $^{111}\mathrm{In}$, $^{116,117}\mathrm{Te}$ and $^{116,116m,117}\mathrm{Sb}$ from a $^{11}\mathrm{B}$-induced silver target. *Journal of Radioanalytical and Nuclear Chemistry*, 256:307–310, 2003. 10.1023/A:1023949704339.

[MM09] Bruce J. Mincher and Stephen P. Mezyk. Radiation chemical effects on radiochemistry: A review of examples important to nuclear power. *Radiochimica Acta*, 97(9):519–534, 2011/06/14 2009.

[MMK$^+$04] Kosuke Morita, Kouji Morimoto, Daiya Kaji, Takahiro Akiyama, Sin ichi Goto, Hiromitsu Haba, Eiji Ideguchi, Rituparna Kanungo, Kenji Katori, Hiroyuki Koura, Hisaaki Kudo, Tetsuya Ohnishi, Akira Ozawa, Toshimi Suda, Keisuke Sueki, HuShan Xu, Takayuki Yamaguchi, Akira Yoneda, Atsushi Yoshida, and YuLiang Zhao. Experiment on the synthesis of element 113 in the reaction $^{209}\mathrm{Bi}(^{70}\mathrm{Zn},n)^{278}113$. *Journal of the Physical Society of Japan*, 73(10):2593–2596, 2004.

[MMK⁺07] Kosuke Morita, Kouji Morimoto, Daiya Kaji, Takahiro Akiyama, Sin ichi Goto, Hiromitsu Haba, Eiji Ideguchi, Kenji Katori, Hiroyuki Koura, Hidetoshi Kikunaga, Hisaaki Kudo, Tetsuya Ohnishi, Akira Ozawa, Nozomi Sato, Toshimi Suda, Keisuke Sueki, Fuyuki Tokanai, Takayuki Yamaguchi, Akira Yoneda, and Atsushi Yoshida. Observation of second decay chain from $^{278}113$. *Journal of the Physical Society of Japan*, 76(4):045001, 2007.

[MMK⁺09] Kosuke Morita, Kouji Morimoto, Daiya Kaji, Hiromitsu Haba, Kazutaka Ozeki, Yiki Kudou, Nozomi Sato, Takayuki Sumita, Akira Yoneda, Takatoshi Ichikawa, Yasuyuki Fujimori, Sin ichi Goto, Eiji Ideguchi, Yoshitaka Kasamatsu, Kenji Katori, Yikiko Komori, Hiroyuki Koura, Hisaaki Kudo, Kazuhiro Ooe, Akira Ozawa, Fuyuki Tokanai, Kazuaki Tsukada, Takayuki Yamaguchi, and Atsushi Yoshida. Decay properties of ^{266}Bh and ^{262}Db produced in the ^{248}Cm + ^{23}Na reaction. *Journal of the Physical Society of Japan*, 78(6):064201, 2009.

[MMM09] Bruce J. Mincher, Giuseppe Modolo, and Stephen P. Mezyk. Review article: The effects of radiation chemistry on solvent extraction: 1. Conditions in acidic solution and a review of TBP radiolysis. *Solvent Extraction and Ion Exchange*, 27:1–25, 2009.

[MNMŚ95] P. Möller, J.R. Nix, W.D. Myers, and W.J. Światecki. Nuclear ground-state masses and deformations. *Atomic Data and Nuclear Data Tables*, 59(2):185 – 381, 1995.

[Moo64] F. L. Moore. New approach to separation of trivalent actinide elements from lanthanide elements. selective liquid-liquid extraction with tricaprylmethylammonium thiocyanate. *Analytical Chemistry*, 36(11):2158–2162, 1964.

[MP54] V. W. Meloche and A. F. Preuss. Analytical separation of rhenium and molybdenum by ion exchange. *Analytical Chemistry*, 26(12):1911–1914, 1954.

[MP64] F. Mitzel and H.S. Plendl. Messungen von (n, γ)-workungsquerschnitten und resonanzintegralen mit einem bleispektrometer. *Nukleonik*, 6(8):371 – 379, 1964.

[MPG06] S.G. Mashnik, R.E. Prael, and K.K. Gudima. Implementation of CEM03.01 into MCNP6 and its verification and validation running through MCNP6. CEM03.02 upgrade. Research Note X-3-RN(U)-07-03, Tech. Rep. LA-UR-06-8652, Los Alamos National Laboratory, 2006.

[MPS01] I. Muntian, Z. Patyk, and A. Sobiczewski. Sensitivity of calculated properties of superheavy nuclei to various changes. *Acta Physica Polonica B*, 32(3):691 – 697, 2001.

[MPS03] I. Muntian, Z. Patyk, and A. Sobiczewski. Calculated masses of heaviest nuclei. *Physics of Atomic Nuclei*, 66:1015–1019, 2003.

[MRH⁺84] G. Münzenberg, W. Reisdorf, S. Hofmann, Y. K. Agarwal, F. P. Heßberger,

K. Poppensieker, J. R. H. Schneider, W. F. W. Schneider, K. H. Schmidt, H. J. Schött, P. Armbruster, C. C. Sahm, and D. Vermeulen. Evidence for element 109 from one correlated decay sequence following the fusion ^{58}Fe with^{209}Bi. *Zeitschrift für Physik A Hadrons and Nuclei*, 315:145–158, 1984. 10.1007/BF01419373.

[MS74] W. D. Myers and W. J. Światecki. The nuclear droplet model for arbitrary shapes. *Annals of Physics*, 84(1-2):186 – 210, 1974.

[MS94] W.D. Myers and W. J. Światecki. Table of nuclear masses according to the 1994 Thomas-Fermi model. Tech. Rep. LBL-36803, Lawrence Berkeley National Laboratory, 1994. Available at `http://ie.lbl.gov/txt/ms.txt`.

[MSPG80] M T Magda, A Sandulescu, D G Popescu, and W Greiner. Heavy-ion fusion and the production of elements 103, 105 and 107. *Journal of Physics G: Nuclear Physics*, 6(2):221, 1980.

[MWH78] R. Michel, H. Weigel, and W. Herr. Proton-induced reactions on nickel with energies between 12 and 45 MeV. *Zeitschrift für Physik A*, 286:393–400, 1978.

[NAH$^+$02] Y. Nagame, M. Asai, H. Haba, S. Goto, K. Tsukada, I. Nishinaka, K. Nishio, S. Ichikawa, A. Toyoshima, K. Akiyama, H. Nakahara, M. Sakama, M. Schädel, J.V. Kratz, H.W. Gäggler, and A. Türler. Production cross sections of ^{261}Rf and ^{262}Db in bombardments of ^{248}Cm with ^{18}O and ^{19}F ions. *Journal of Nuclear and Radiochemical Sciences*, 3(1):85 – 88, 2002.

[NBSB91] Yoshihiro Nakagome, Robert C. Block, Rudolf E. Slovacek, and Edgar B. Bean. Neutron-induced fission cross section of ^{232}Th from 1 eV to 20 keV. *Phys. Rev. C*, 43(4):1824–1830, Apr 1991.

[ND68] V.S. Nikolaev and I.S. Dmitriev. On the equilibrium charge distribution in heavy element ion beams. *Physics Letters A*, 28(4):277 – 278, 1968.

[Ney37] J. Neyman. Outline of a theory of statistical estimation based on the classical theory of probability. *Phil. Trans. R. Soc. Lond. A*, 236:333 – 380, 1937.

[NHH$^+$06] K. Nishio, S. Hofmann, F. Heßberger, D. Ackermann, S. Antalic, V. Comas, Z. Gan, S. Heinz, J. Heredia, H. Ikezoe, J. Khuyagbaatar, B. Kindler, I. Kojouharov, P. Kuusiniemi, B. Lommel, R. Mann, M. Mazzocco, S. Mitsuoka, Y. Nagame, T. Ohtsuki, A. Popeko, S. Saro, H. Schött, B. Sulignano, A. Svirikhin, K. Tsukada, K. Tsuruta, and A. Yeremin. Measurement of evaporation residue cross-sections of the reaction ^{30}Si + ^{238}U at subbarrier energies. *The European Physical Journal A - Hadrons and Nuclei*, 29:281–287, 2006.

[NHH$^+$10] K. Nishio, S. Hofmann, F. P. Heßberger, D. Ackermann, S. Antalic, Y. Aritomo, V. F. Comas, Ch. E. Düllmann, A. Gorshkov, R. Graeger, K. Hagino, S. Heinz, J. A. Heredia, K. Hirose, H. Ikezoe, J. Khuyagbaatar, B. Kindler, I. Kojouharov, B. Lommel, R. Mann, S. Mitsuoka, Y. Nagame, I. Nishinaka, T. Ohtsuki, A. G. Popeko, S. Saro, M. Schädel, A. Türler, Y. Watanabe, A. Yakushev, and A. V. Yeremin. Nuclear orientation in the reaction ^{34}S+^{238}U and synthesis of the new isotope ^{268}Hs. *Phys. Rev. C*, 82(2):024611, Aug 2010.

[NK] M.N. Nikolaev and V.N. Koscheev. RUSsian File of evaluated Neutron Data (RUSFOND). Database and information available at `http://www.ippe.ru/podr/abbn/english/libr/rosfond.php`.

[NL00] D. Nayak and S. Lahiri. Separation of carrier-free cerium radionuclides from different target matrix produced by heavy ion beams. *Radiochimica Acta*, 88(2):115, 2000.

[OAB$^+$10] Yu. Ts. Oganessian, F. Sh. Abdullin, P. D. Bailey, D. E. Benker, M. E. Bennett, S. N. Dmitriev, J. G. Ezold, J. H. Hamilton, R. A. Henderson, M. G. Itkis, Yu. V. Lobanov, A. N. Mezentsev, K. J. Moody, S. L. Nelson, A. N. Polyakov, C. E. Porter, A. V. Ramayya, F. D. Riley, J. B. Roberto, M. A. Ryabinin, K. P. Rykaczewski, R. N. Sagaidak, D. A. Shaughnessy, I. V. Shirokovsky, M. A. Stoyer, V. G. Subbotin, R. Sudowe, A. M. Sukhov, Yu. S. Tsyganov, V. K. Utyonkov, A. A. Voinov, G. K. Vostokin, and P. A. Wilk. Synthesis of a new element with atomic number $Z = 117$. *Phys. Rev. Lett.*, 104(14):142502, Apr 2010.

[OBB$^+$78] Yu.Ts. Oganessian, H. Bruchertseifer, G.V. Buklanov, V.I. Chepigin, Choi Val Sek, B. Eichler, K.A. Gavrilov, H. Gaeggeler, Yu.S. Korotkin, O.A. Orlova, T. Reetz, W. Seidel, G.M. Ter-Akopian, S.P. Tretyakova, and I. Zvara. Experiments to produce isotopes of superheavy elements with atomic numbers 114-116 in ^{48}Ca ion reactions. *Nuclear Physics A*, 294(1-2):213 – 224, 1978.

[Oga07] Yuri Ts. Oganessian. Heaviest nuclei from ^{48}Ca-induced reactions. *Journal of Physics G: Nuclear and Particle Physics*, 34(4):R165, 2007.

[OIDT75] Yu. Ts. Oganessian, A. S. Iljinov, A. G. Demin, and S. P. Tretyakova. Experiments on the production of fermium neutron-deficient isotopes and new possibilities of synthesizing elements with Z ¿ 100. *Nuclear Physics A*, 239(2):353 – 364, 1975.

[ONT$^+$91] T. Ohtsuki, Y. Nagame, K. Tsukada, N. Shinohara, S. Baba, K. Hashimoto, I. Nishinaka, K. Sueki, Y. Hatsukawa, K. Hata, T. Sekine, I. Kanno, H. Ikezoe, and H. Nakahara. Mass yield curves in low-energy proton-induced fission of ^{233}U, ^{235}U, ^{236}U, ^{237}Np, ^{239}Pu, ^{242}Pu, ^{244}Pu, ^{241}Am, and ^{243}am. *Phys. Rev. C*, 44(4):1405–1423, Oct 1991.

[OUD$^+$05] Yu. Ts. Oganessian, V. K. Utyonkov, S. N. Dmitriev, Yu. V. Lobanov, M. G. Itkis, A. N. Polyakov, Yu. S. Tsyganov, A. N. Mezentsev, A. V. Yeremin, A. A. Voinov, E. A. Sokol, G. G. Gulbekian, S. L. Bogomolov, S. Iliev, V. G. Subbotin, A. M. Sukhov, G. V. Buklanov, S. V. Shishkin, V. I. Chepygin, G. K. Vostokin, N. V. Aksenov, M. Hussonnois, K. Subotic, V. I. Zagrebaev, K. J. Moody, J. B. Patin, J. F. Wild, M. A. Stoyer, N. J. Stoyer, D. A. Shaughnessy, J. M. Kenneally, P. A. Wilk, R. W. Lougheed, H. W. Gäggeler, D. Schumann, H. Bruchertseifer, and R. Eichler. Synthesis of elements 115 and 113 in the reaction ^{243}Am+^{48}Ca. *Phys. Rev. C*, 72(3):034611, Sep 2005.

[OUL+99] Yu. Ts. Oganessian, V. K. Utyonkov, Yu. V. Lobanov, F. Sh. Abdullin, A. N. Polyakov, I. V. Shirokovsky, Yu. S. Tsyganov, G. G. Gulbekian, S. L. Bogomolov, B. N. Gikal, A. N. Mezentsev, S. Iliev, V. G. Subbotin, A. M. Sukhov, G. V. Buklanov, K. Subotic, M. G. Itkis, K. J. Moody, J. F. Wild, N. J. Stoyer, M. A. Stoyer, and R. W. Lougheed. Synthesis of superheavy nuclei in the ^{48}Ca+ ^{244}Pu reaction. *Phys. Rev. Lett.*, 83(16):3154–3157, Oct 1999.

[OUL+00a] Yu. Ts. Oganessian, V. K. Utyonkov, Yu. V. Lobanov, F. Sh. Abdullin, A. N. Polyakov, I. V. Shirokovsky, Yu. S. Tsyganov, G. G. Gulbekian, S. L. Bogomolov, B. N. Gikal, A. N. Mezentsev, S. Iliev, V. G. Subbotin, A. M. Sukhov, O. V. Ivanov, G. V. Buklanov, K. Subotic, M. G. Itkis, K. J. Moody, J. F. Wild, N. J. Stoyer, M. A. Stoyer, and R. W. Lougheed. Synthesis of superheavy nuclei in the ^{48}Ca+^{244}Pu reaction: ^{288}114. *Phys. Rev. C*, 62(4):041604, Sep 2000.

[OUL+00b] Yu. Ts. Oganessian, V. K. Utyonkov, Yu. V. Lobanov, F. Sh. Abdullin, A. N. Polyakov, I. V. Shirokovsky, Yu. S. Tsyganov, G. G. Gulbekian, S. L. Bogomolov, B. N. Gikal, A. N. Mezentsev, S. Iliev, V. G. Subbotin, A. M. Sukhov, O. V. Ivanov, G. V. Buklanov, K. Subotic, M. G. Itkis, K. J. Moody, J. F. Wild, N. J. Stoyer, M. A. Stoyer, R. W. Lougheed, C. A. Laue, Ye. A. Karelin, and A. N. Tatarinov. Observation of the decay of ^{292}116. *Phys. Rev. C*, 63(1):011301, Dec 2000.

[OUL+04a] Yu. Ts. Oganessian, V. K. Utyonkov, Yu. V. Lobanov, F. Sh. Abdullin, A. N. Polyakov, I. V. Shirokovsky, Yu. S. Tsyganov, G. G. Gulbekian, S. L. Bogomolov, B. N. Gikal, A. N. Mezentsev, S. Iliev, V. G. Subbotin, A. M. Sukhov, A. A. Voinov, G. V. Buklanov, K. Subotic, V. I. Zagrebaev, M. G. Itkis, J. B. Patin, K. J. Moody, J. F. Wild, M. A. Stoyer, N. J. Stoyer, D. A. Shaughnessy, J. M. Kenneally, P. A. Wilk, R. W. Lougheed, R. I. Il'kaev, and S. P. Vesnovskii. Measurements of cross sections and decay properties of the isotopes of elements 112, 114, and 116 produced in the fusion reactions ^{233,238}U , ^{242}Pu , and ^{248}Cm+^{48}Ca. *Phys. Rev. C*, 70(6):064609, Dec 2004.

[OUL+04b] Yu. Ts. Oganessian, V. K. Utyonkov, Yu. V. Lobanov, F. Sh. Abdullin, A. N. Polyakov, I. V. Shirokovsky, Yu. S. Tsyganov, G. G. Gulbekian, S. L. Bogomolov, B. N. Gikal, A. N. Mezentsev, S. Iliev, V. G. Subbotin, A. M. Sukhov, A. A. Voinov, G. V. Buklanov, K. Subotic, V. I. Zagrebaev, M. G. Itkis, J. B. Patin, K. J. Moody, J. F. Wild, M. A. Stoyer, N. J. Stoyer, D. A. Shaughnessy, J. M. Kenneally, and R. W. Lougheed. Measurements of cross sections for the fusion-evaporation reactions ^{244}Pu(^{48}Ca,xn)$^{292-x}$114 and ^{245}Cm(^{48}Ca,xn)$^{293-x}$116. *Phys. Rev. C*, 69(5):054607, May 2004.

[OUL+06] Yu. Ts. Oganessian, V. K. Utyonkov, Yu. V. Lobanov, F. Sh. Abdullin, A. N. Polyakov, R. N. Sagaidak, I. V. Shirokovsky, Yu. S. Tsyganov, A. A. Voinov,

G. G. Gulbekian, S. L. Bogomolov, B. N. Gikal, A. N. Mezentsev, S. Iliev, V. G. Subbotin, A. M. Sukhov, K. Subotic, V. I. Zagrebaev, G. K. Vostokin, M. G. Itkis, K. J. Moody, J. B. Patin, D. A. Shaughnessy, M. A. Stoyer, N. J. Stoyer, P. A. Wilk, J. M. Kenneally, J. H. Landrum, J. F. Wild, and R. W. Lougheed. Synthesis of the isotopes of elements 118 and 116 in the ^{249}Cf and ^{245}Cm+^{48}Ca fusion reactions. *Phys. Rev. C*, 74(4):044602, Oct 2006.

[PFRPRL06] L. Poriel, A. Favre-Rguillon, S. Pellet-Rostaing, and M. Lemaire. Zirconium and hafnium separation, part 1. Liquid/liquid extraction in hydrochloric acid aqueous solution with Aliquat 336. *Separation Science & Technology*, 41(9):1927 – 1940, 2006.

[Pil86a] K. Pillay. The effects of ionizing radiations on synthetic organic ion exchangers. *Journal of Radioanalytical and Nuclear Chemistry*, 97:135–210, 1986. 10.1007/BF02060420.

[Pil86b] K. Pillay. A review of the radiation stability of ion exchange materials. *Journal of Radioanalytical and Nuclear Chemistry*, 102:247–268, 1986. 10.1007/BF02037966.

[PK60] R.A. Penneman and T.K. Keenan. The radiochemistry of americium and curium. Tech. Rep. NAS-NS 3006, National Academy of Sciences, National Research Council, 1960. Available at `http://library.lanl.gov/radiochemistry/index.htm`.

[PKS$^+$99] W. Paulus, J. Kratz, E. Strub, S. Zauner, W. Brüchle, V. Pershina, M. Schädel, B. Schausten, J. Adams, K. Gregorich, D. Hoffman, C. Laue, D. Lee, C. Mcgrath, D. Shaughnessy, D. Strellis, and E. Sylwester. Extraction of the fluoride-, chloride-, and bromide complexes of the elements Nb, Ta, Pa, and 105 into aliphatic amines. *Czechoslovak Journal of Physics*, 49:573–579, 1999.

[PPK$^+$07] G. Perdikakis, C. Papadopoulos, M. Kokkoris, R. Vlastou, S. Galanopoulos, A. Lagoyannis, A. Spyrou, G. Kalyva, and N. Patronis. Study of the $^{241}\mathrm{Am}(n,2n)^{240}$Am reaction cross section in the energy range of $En = 8.8?11.1$ MeV. *Journal of Radioanalytical and Nuclear Chemistry*, 272:223–226, 2007. 10.1007/s10967-007-0504-7.

[PPV$^+$06] G. Perdikakis, C. T. Papadopoulos, R. Vlastou, A. Lagoyannis, A. Spyrou, M. Kokkoris, S. Galanopoulos, N. Patronis, D. Karamanis, Ch. Zarkadas, G. Kalyva, and S. Kossionides. Measurement of the $^{241}\mathrm{Am}(n,2n)$ reaction cross section using the activation method. *Phys. Rev. C*, 73(6):067601, Jun 2006.

[Pra50] Wilhelm Prandtl. Johann Wolfgang Dobereiner, Goethe's chemical adviser. *Journal of Chemical Education*, 27(4):176, 1950.

[PS05] A. Parkhomenko and A. Sobiczewski. Phenomenological formula for α-decay half-lives of heaviest nuclei. *Acta Physica Polonica B*, 36(10):3095 – 3108, 2005.

[QHK$^+$09] J. Qian, A. Heinz, T. L. Khoo, R. V. F. Janssens, D. Peterson, D. Seweryniak, I. Ahmad, M. Asai, B. B. Back, M. P. Carpenter, A. B. Garnsworthy, J. P. Greene, A. A. Hecht, C. L. Jiang, F. G. Kondev, T. Lauritsen, C. J. Lister, A. Robinson, G. Savard, R. Scott, R. Vondrasek, X. Wang, R. Winkler, and S. Zhu. Spectroscopy of ^{257}Rf. *Phys. Rev. C*, 79(6):064319, Jun 2009.

[rBWK67] S. Bjørnholm, J. Borggreen, L. Westgaard, and V. A. Karnaukhov. Excitation energy of the spontaneously fissioning isomeric state in ^{240}Am. *Nuclear Physics A*, 95(3):513 – 525, 1967.

[RCW86] R.A. Roberts, G.R. Choppin, and J.F. Wild. The radiochemistry of uranium, neptunium, and plutonium – An updating. Tech. Rep. NAS-NS 3036, National Academy of Sciences, National Research Council, 1986. Available at `http://library.lanl.gov/radiochemistry/index.htm`.

[Rei81] W. Reisdorf. Analysis of fissionability data at high excitation energies. *Zeitschrift für Physik A Hadrons and Nuclei*, 300:227–238, 1981. 10.1007/BF01412298.

[RGH$^+$93] Barber R.C., N.N. Greenwood, A.Z. Hrynkiewicz, Y.P. Jeannin, M. Lefort, M. Sakai, I. Ulehla, A.H. Wapstra, and D.H. Wilkinson. Discovery of the transfermium elements. Part II: Introduction to discovery profiles. Part III: Discovery profiles of the transfermium elements. *Pure and Applied Chemistry*, 65(8):1757 – 1814, 1993.

[RHD$^+$05] D. Rochman, R.C. Haight, J.M. O' Donnell, A. Michaudon, S.A. Wender, D.J. Vieira, E.M. Bond, T.A. Bredeweg, A. Kronenberg, J.B. Wilhelmy, T. Ethvignot, T. Granier, M. Petit, and Y. Danon. Characteristics of a lead slowing-down spectrometer coupled to the lansce accelerator. *Nuclear Instruments and Methods in Physics Research Section A: Accelerators, Spectrometers, Detectors and Associated Equipment*, 550(1-2):397 – 413, 2005.

[RHOS06] D. Rochman, M. Herman, P. Oblozinský, and M. Sin. Modeling and neutron-induced fission cross sections for americium. *Nucl. Sci. Eng.*, 154(3):280–293, Nov 2006.

[RR68] L. Ruby and J.B. Rechen. A simpler approach to the geometrical efficiency of a parallel-disk source and detector system. *Nuclear Instruments and Methods*, 58(2):345 – 346, 1968.

[SanSS95] R. Smolańczuk, J. Skalski, and A. Sobiczewski. Spontaneous-fission half-lives of deformed superheavy nuclei. *Phys. Rev. C*, 52(4):1871–1880, Oct 1995.

[SB60] E.M. Scadden and N.E. Ballou. The radiochemistry of molybdenum. Tech. Rep. NAS-NS 3009, National Academy of Sciences, National Research Council, 1960. Available at `http://library.lanl.gov/radiochemistry/index.htm`.

[SB08] Balraj Singh and E. Browne. Nuclear data sheets for A = 240. *Nuclear Data Sheets*, 109(10):2439 – 2499, 2008. With permission from Elsevier.

[SBB$^+$09] A. Santamarina, D. Bernard, P. Blaise, M. Coste, A. Courcelle, T.D. Huynh,

C. Jouanne, P. Leconte, O. Litaize, S. Mengelle, G. Noguère, J.-M. Ruggiéri, O. Sérot, J. Tommasi, C. Vaglio, and J.-F. Vidal. The JEFF-3.1.1 nuclear data library. JEFF Report 22, Nuclear Energy Agency, Organisation for Economic Co-operation and Development, 2009.

[SC74] Mohamed Sawan and Robert W. Conn. Neutron pulses slowing down in heavy media analysis with applications of the lead spectrometer. *Nucl. Sci. Eng.*, 54:127 – 142, 1974.

[SCB+77] R.E. Slovacek, D.S. Cramer, E.B. Bean, J.R. Valentine, R.W. Hockenbury, and R.C. Block. $^{238}\mathrm{U}(n, f)$ measurements below 100 keV. *Nucl. Sci. Eng.*, 62:455 – 462, 1977.

[Sch06] Matthias Schädel. Chemistry of superheavy elements. *Angewandte Chemie International Edition*, 45(3):368–401, 2006.

[SDM+73] R. J. Silva, P. F. Dittner, M. L. Mallory, O. L. Keller, K. Eskola, P. Eskola, M. Nurmia, and A. Ghiorso. The new nuclide nobelium-259. *Nuclear Physics A*, 216(1):97 – 108, 1973.

[Sea46] Glenn T. Seaborg. The transuranium elements. *Science*, 104(2704):pp. 379–386, 1946.

[Seg77] E. Segré. *Nuclei and Particles: An Introduction to Nuclear and Subnuclear Physics*. Benjamin Cummings, 2nd edition, 1977.

[SGD+09] L. Stavsetra, K. E. Gregorich, J. Dvorak, P. A. Ellison, I. Dragojević, M. A. Garcia, and H. Nitsche. Independent verification of element 114 production in the $^{48}\mathrm{Ca}+^{242}\mathrm{Pu}$ reaction. *Phys. Rev. Lett.*, 103(13):132502, Sep 2009.

[SGH57] W. G. Smith, W. M. Gibson, and J. M. Hollander. Electron-capture decay of Am^{239} and Am^{240}. *Phys. Rev.*, 105(5):1514–1517, Mar 1957.

[SGN68] Torbjorn Sikkeland, Albert Ghiorso, and Matti J. Nurmia. Analysis of excitation functions in Cm(C,xn)No reactions. *Phys. Rev.*, 172(4):1232–1238, Aug 1968.

[SGS50] K. Street, A. Ghiorso, and G. T. Seaborg. The isotopes of americium. *Phys. Rev.*, 79(3):530–531, Aug 1950.

[SHS+98] M. Sonck, A. Hermanne, F. Szelecsényi, S. Takács, and F. Tárkányi. Study of the $^{\mathrm{nat}}\mathrm{Ni}(p, x)^{57}\mathrm{Ni}$ process up to 44-MeV for monitor purposes. *Applied Radiation and Isotopes*, 49(12):1533 – 1536, 1998.

[SIN+11] Keiichi Shibata, Osamu Iwamoto, Tsuneo Nakagawa, Nobuyuki Iwamoto, Akira Ichihara, Satoshi Kunieda, Satoshi Chiba, Kazuyoshi Furutaka, Naohiko Otuka, Takaaki Ohsawa, Toru Murata, Hiroyuki Matsunobu, Atsushi Zukeran, So Kamada, and Jun ichi Katakura. JENDL-4.0: A new library for nuclear science and engineering. *Journal of Nuclear Science and Technology*, 48(1):1–30, 2011.

[SJM49] G.T. Seaborg, R.A. James, and L.O. Morgan. The new element americium (atomic number 95). In G.T. Seaborg, J.J. Katz, and Manning W.M., editors, *The Transuranium Elements: Research Papers*, volume 14B of *National Nuclear Energy Series*, pages 1525–1553. McGraw-Hill Book Co., 1949.

[SKFK03] J.-Ch. Sublet, A.J. Koning, R.A. Forrest, and J. Kopecky. The JEFF-3.0/A neutron activation file - EAF-2003 into ENDF-6 format. Tech. Rep. JEFDOC-982, Commissariat à l'Energie Atomique, 2003.

[SLAB91] Bernard Shleien, Jr. Slaback Lester A., and Brian Birky. *Handbook of Health Physics and Radiological Health.* Lippencott Williams & Wilkins, 3rd edition, 1991.

[SMA07] F.S. Al Saleh, K.S. Al Mugren, and A. Azzam. Excitation functions of (p, x) reactions on natural nickel between proton energies of 2.7 and 27.5 MeV. *Applied Radiation and Isotopes*, 65(1):104 – 113, 2007.

[SPKF10] J.-Ch. Sublet, L.W. Packer, J. Kopecky, and R. Forrest. The European Activation File: EAF-2010 neutron-induced cross section library. Tech. Rep. CCFE-R (10) 05, 2010.

[SSPC84] K. H. Schmidt, C. C. Sahm, K. Pielenz, and H. G. Clerc. Some remarks on the error analysis in the case of poor statistics. *Zeitschrift für Physik A Hadrons and Nuclei*, 316:19–26, 1984.

[SSWW05] W. J. Światecki, K. Siwek-Wilczyńska, and J. Wilczyński. Fusion by diffusion. II. Synthesis of transfermium elements in cold fusion reactions. *Phys. Rev. C*, 71(1):014602, Jan 2005.

[SSWW08] W. J. Światecki, K. Siwek-Wilczyńska, and J. Wilczyński. Ratios of disintegration rates for distinct decay modes of an excited nucleus. *Phys. Rev. C*, 78(5):054604, Nov 2008.

[Ste60] Ellis P. Steinberg. The radiochemistry of zirconium and hafnium. Tech. Rep. NAS-NS 3011, National Academy of Sciences, National Research Council, 1960. Available at `http://library.lanl.gov/radiochemistry/index.htm`.

[Ste61] Ellis P. Steinberg. The radiochemistry of niobium and tantalum. Tech. Rep. NAS-NS 3039, National Academy of Sciences, National Research Council, 1961. Available at `http://library.lanl.gov/radiochemistry/index.htm`.

[STT$^+$01] F. Szelecsényi, F. Tárkányi, S. Takács, A. Hermanne, M. Sonck, Yu. Shubin, M. G. Mustafa, and Zhuang Youxiang. Excitation function for the $^{\mathrm{nat}}\mathrm{Ti}(p, x)^{48}\mathrm{V}$ nuclear process: Evaluation and new measurements for practical applications. *Nuclear Instruments and Methods in Physics Research Section B: Beam Interactions with Materials and Atoms*, 174(1-2):47 – 64, 2001.

[SW70] Taichi Sato and Hiroshi Watanabe. The extraction of zirconium(IV) from hydrochloric acid solutions by tricaprylmethylammonium chloride. *Analytica Chimica Acta*, 49(3):463 – 471, 1970.

[TAB$^+$08] A. P. Tonchev, C. T. Angell, M. Boswell, A. S. Crowell, B. Fallin, S. Hammond, C. R. Howell, A. Hutcheson, H. J. Karwowski, J. H. Kelley, R. S. Pedroni, W. Tornow, J. A. Becker, D. Dashdorj, J. Kenneally, R. A. Macri, M. A.

Stoyer, C. Y. Wu, E. Bond, M. B. Chadwick, J. Fitzpatrick, T. Kawano, R. S. Rundberg, A. Slemmons, D. J. Vieira, and J. B. Wilhelmy. Measurement of the ^{241}Am$(n, 2n)$ reaction cross section from 7.6 MeV to 14.5 MeV. *Phys. Rev. C*, 77(5):054610, May 2008.

[Tew55] Howard A. Tewes. Excitation functions for some proton-induced reactions of thorium. *Phys. Rev.*, 98(1):25–27, Apr 1955.

[THH$^+$10] A. P. Tonchev, S. L. Hammond, C. R. Howell, C. Huibregtse, A. Hutcheson, J. H. Kelley, E. Kwan, R. Raut, G. Rusev, W. Tornow, T. Kawano, D. J. Vieira, and J. B. Wilhelmy. Measurement of the ^{241}Am$(\gamma, n)^{240}$Am reaction in the giant dipole resonance region. *Phys. Rev. C*, 82(5):054620, Nov 2010.

[TSK91] F. Tárkányi, F. Szelecsényi, and P. Kopecky. Excitation functions of proton induced nuclear reactions on natural nickel for monitoring beam energy and intensity. *International Journal of Radiation Applications and Instrumentation. Part A. Applied Radiation and Isotopes*, 42(6):513 – 517, 1991.

[TTSH02] S. Takács, F. Tárkányi, M. Sonck, and A. Hermanne. New cross-sections and intercomparison of proton monitor reactions on Ti, Ni and Cu. *Nuclear Instruments and Methods in Physics Research Section B: Beam Interactions with Materials and Atoms*, 188(1-4):106 – 111, 2002.

[TvGL$^+$92] A. Türler, H. R. von Gunten, J. D. Leyba, D. C. Hoffman, D. M. Lee, K. E. Gregorich, D. A. Bennett, R. M. Chasteler, C. M. Gannett, H. L. Hall, R. A. Henderson, and M. J. Nurmia. Actinide production from the interactions of ^{40}C and ^{44}Ca with ^{248}Cm and a comparison with the ^{48}Ca $+^{248}$Cm system. *Phys. Rev. C*, 46(4):1364–1382, Oct 1992.

[Van77] R Vandenbosch. Spontaneously fissioning isomers. *Annual Review of Nuclear Science*, 27(1):1–35, 1977.

[vdM06] Steven C. van der Marck. Benchmarking ENDF/B-VII.0. *Nuclear Data Sheets*, 107(12):3061 – 3118, 2006. Evaluated Nuclear Data File ENDF/B-VII.0.

[Vie08] David J. Vieira. (private communication), 2008.

[WB73] Andrew B. Wittkower and Hans D. Betz. Equilibrium charge-state distributions of 2-15-MeV tantalum and uranium ions stripped in gases and solids. *Phys. Rev. A*, 7(1):159–167, Jan 1973.

[Wee33] Mary Elvira Weeks. The discovery of the elements. xxi. supplementary note on the discovery of phosphorus. *Journal of Chemical Education*, 10(5):302, 1933.

[WFS92] S. J. Watson, D. J. S. Findlay, and M. R. Sen. Photofission and photoneutron measurements on ^{241}Am between 5 and 10 MeV. *Nuclear Physics A*, 548(3):365 – 373, 1992.

[WGT$^+$00] P. A. Wilk, K. E. Gregorich, A. Türler, C. A. Laue, R. Eichler, V. Ninov, J. L. Adams, U. W. Kirbach, M. R. Lane, D. M. Lee, J. B. Patin, D. A. Shaughnessy, D. A. Strellis, H. Nitsche, and D. C. Hoffman. Evidence for new isotopes of element 107: ^{266}Bh and ^{267}Bh. *Phys. Rev. Lett.*, 85(13):2697–2700, Sep 2000.

[WMG+87] Robert B. Welch, Kenton J. Moody, Kenneth E. Gregorich, Diana Lee, and Glenn T. Seaborg. Dependence of actinide production on the mass number of the projectile: Xe +^{248}Cm. *Phys. Rev. C*, 35(1):204–212, Jan 1987.

[WSNN70] Hiroaki Wakabayashi, Akira Sekiguchi, Masaharu Nakazawa, and Osamu Nishino. Some new applications of neutron slowing down time spectrometry. *Journal of Nuclear Science and Technology*, 7(10):487–499, 1970.

[Xie98] Z. Q. Xie. Production of highly charged ion beams from electron cyclotron resonance ion sources (invited). *Review of Scientific Instruments*, 69(2):625–630, 1998.

[YB03] W. Younes and H. C. Britt. Neutron-induced fission cross sections simulated from (t, pf) results. *Phys. Rev. C*, 67(2):024610, Feb 2003.

[YBB04] W. Younes, H.C. Britt, and J.A. Becker. Estimated (n,f) cross sections for ^{236,236m,237,238}Np, ^{237,237m}Pu, and ^{240,241,242,242m,243,244,244m}Am isotopes. Tech. Rep. UCRL-TR-201913, Lawrence Livermore National Laboratory, 2004.

[YKK+93] Akihiro Yamanaka, Itsuro Kimura, Satoshi Kanazawa, Katsuhei Kobayashi, Shuji Yamamoto, Yoshihiro Nakagome, Yoshiaki Fujita, and Tadaharu Tamai. Measurement of fission cross section of neptunium-237 in resonance region with electron linac-driven lead spectrometer. *Journal of Nuclear Science and Technology*, 30(9):863–869, 1993.

[Zag04] V.I. Zagrebaev. Fusion-fission dynamics of super-heavy element formation and decay. *Nuclear Physics A*, 734:164 – 167, 2004.

[Zag10] Valery I. Zagrebaev. (private communication), 2010.

[ZAHA06] K. Zarie, N. Al-Hammad, and A. Azzam. Experimental study of excitation functions of some proton induced reactions on $^{\mathrm{nat}}$Ti for beam monitoring purposes. *Radiochimica Acta*, 94(12):795–799, 2006.

[ZHY+07] Ge Zhigang, Yu Hongwei, Zhuang Youxiang, Lie Tingjin, Zhang Jingshang, Liu Ping, Huang Xiaolong, Zhao Zhixiang, and Xia Haihong. The updated version of the Chinese Evaluated Nuclear Data Library (CENDL-3.1 and China nuclear data evaluation activities. In *Proceedings of the International Conference on Nuclear Data for Science and Technology 2007*, pages 753 – 757, Jeju-do, South Korea, 2007.

[Zie04] James F. Ziegler. SRIM-2003. *Nuclear Instruments and Methods in Physics Research Section B: Beam Interactions with Materials and Atoms*, 219-220:1027 – 1036, 2004. Proceedings of the Sixteenth International Conference on Ion Beam Analysis.

[ZIO03] V. Zagrebaev, M. Itkis, and Yu. Oganessian. Fusion-fission dynamics and perspectives of future experiments. *Physics of Atomic Nuclei*, 66:1033–1041, 2003.

Appendix A

^{242}Pu data sheet

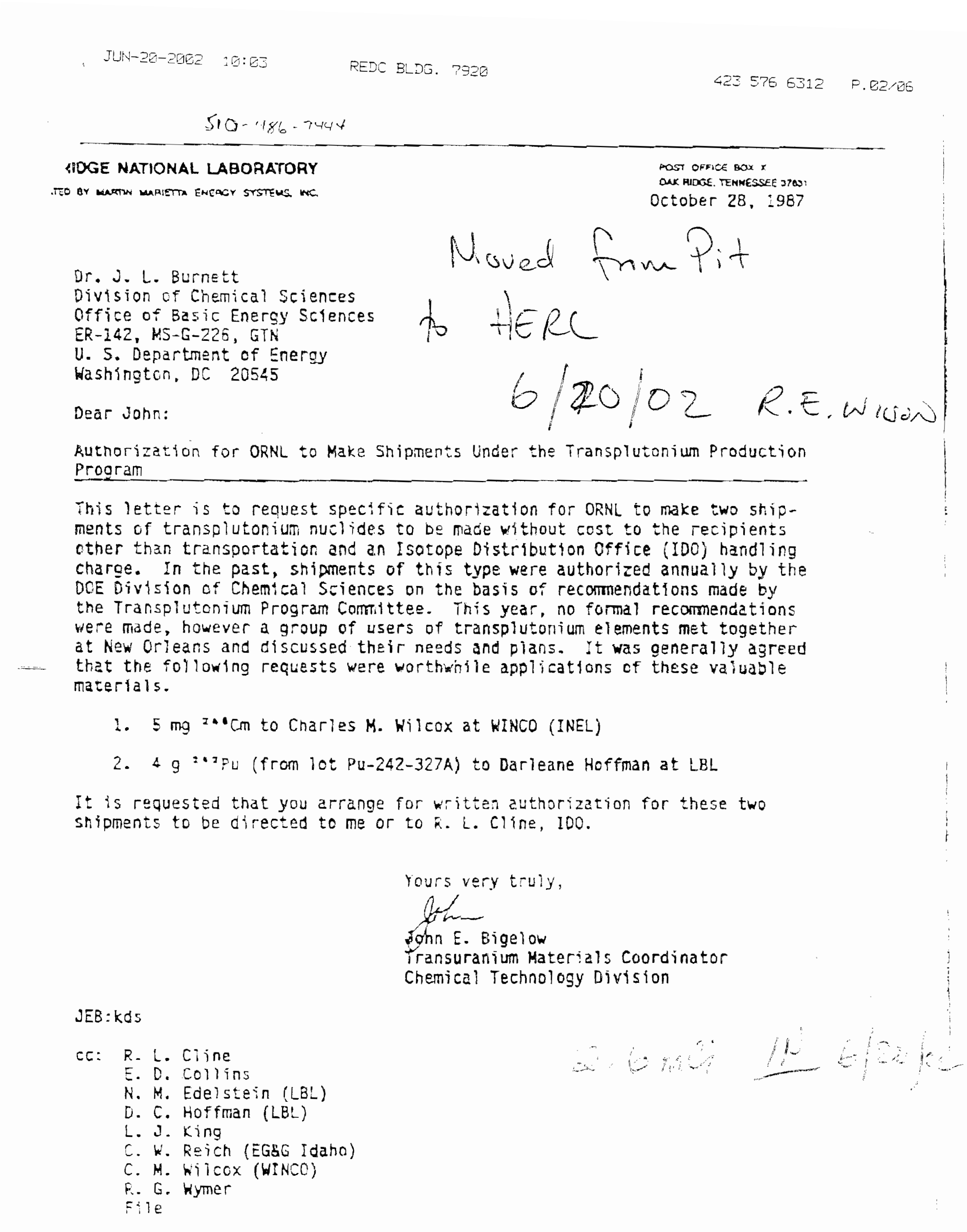

JUN-20-2002 10:03 REDC BLDG. 7920 423 576 6312 P.02/06

510-486-7444

IDGE NATIONAL LABORATORY
TED BY MARTIN MARIETTA ENERGY SYSTEMS, INC.

POST OFFICE BOX X
OAK RIDGE, TENNESSEE 37831

October 28, 1987

Moved from Pit
to HERC
6/20/02 R.E. Wilson

Dr. J. L. Burnett
Division of Chemical Sciences
Office of Basic Energy Sciences
ER-142, MS-G-226, GTN
U. S. Department of Energy
Washington, DC 20545

Dear John:

Authorization for ORNL to Make Shipments Under the Transplutonium Production Program

This letter is to request specific authorization for ORNL to make two shipments of transplutonium nuclides to be made without cost to the recipients other than transportation and an Isotope Distribution Office (IDO) handling charge. In the past, shipments of this type were authorized annually by the DOE Division of Chemical Sciences on the basis of recommendations made by the Transplutonium Program Committee. This year, no formal recommendations were made, however a group of users of transplutonium elements met together at New Orleans and discussed their needs and plans. It was generally agreed that the following requests were worthwhile applications of these valuable materials.

1. 5 mg ^{248}Cm to Charles M. Wilcox at WINCO (INEL)
2. 4 g ^{242}Pu (from lot Pu-242-327A) to Darleane Hoffman at LBL

It is requested that you arrange for written authorization for these two shipments to be directed to me or to R. L. Cline, IDO.

Yours very truly,

John E. Bigelow
Transuranium Materials Coordinator
Chemical Technology Division

JEB:kds

2.6 mCi [illegible] 6/22/[illegible]

cc: R. L. Cline
E. D. Collins
N. M. Edelstein (LBL)
D. C. Hoffman (LBL)
L. J. King
C. W. Reich (EG&G Idaho)
C. M. Wilcox (WINCO)
R. G. Wymer
File

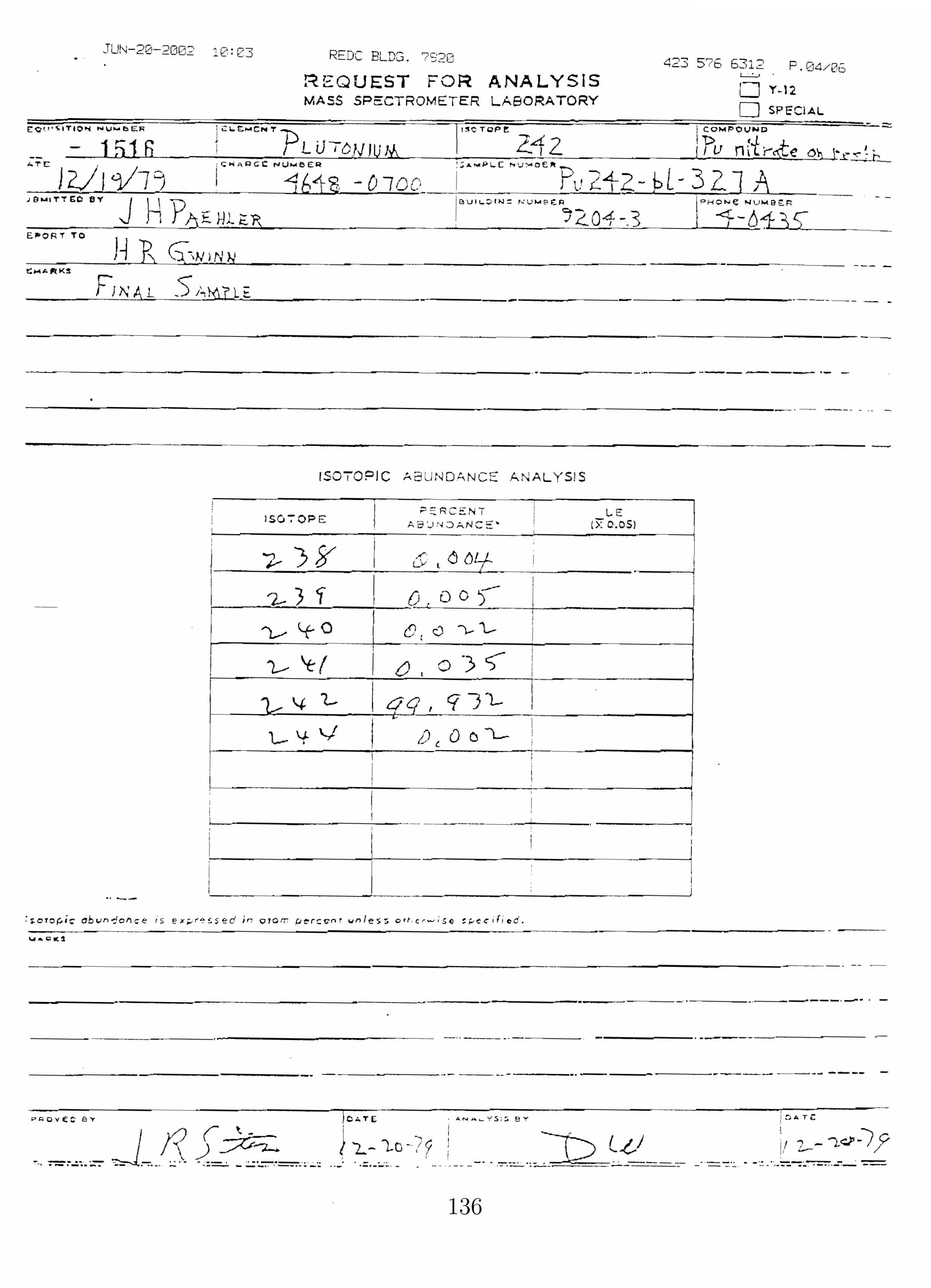

JUN-20-2002 10:03 REDC BLDG. 7920 423 576 6312 P.04/06

REQUEST FOR ANALYSIS
MASS SPECTROMETER LABORATORY

☐ Y-12
☐ SPECIAL

EQUISITION NUMBER - 1516	ELEMENT PLUTONIUM	ISOTOPE 242	COMPOUND Pu nitrate on resin
ATE 12/19/79	CHARGE NUMBER 4648 -0700	SAMPLE NUMBER Pu242-bl-327A	
JBMITTED BY J H PAEHLER		BUILDING NUMBER 9204-3	PHONE NUMBER 4-0435

EPORT TO H R GWINN

EMARKS FINAL SAMPLE

ISOTOPIC ABUNDANCE ANALYSIS

ISOTOPE	PERCENT ABUNDANCE*	LE ($\bar{X}$ 0.05)
238	0.004	
239	0.005	
240	0.022	
241	0.035	
242	99.932	
244	0.002	

*Isotopic abundance is expressed in atom percent unless otherwise specified.

MARKS

PROVED BY	DATE 12-20-79	ANALYSIS BY	DATE 12-20-79

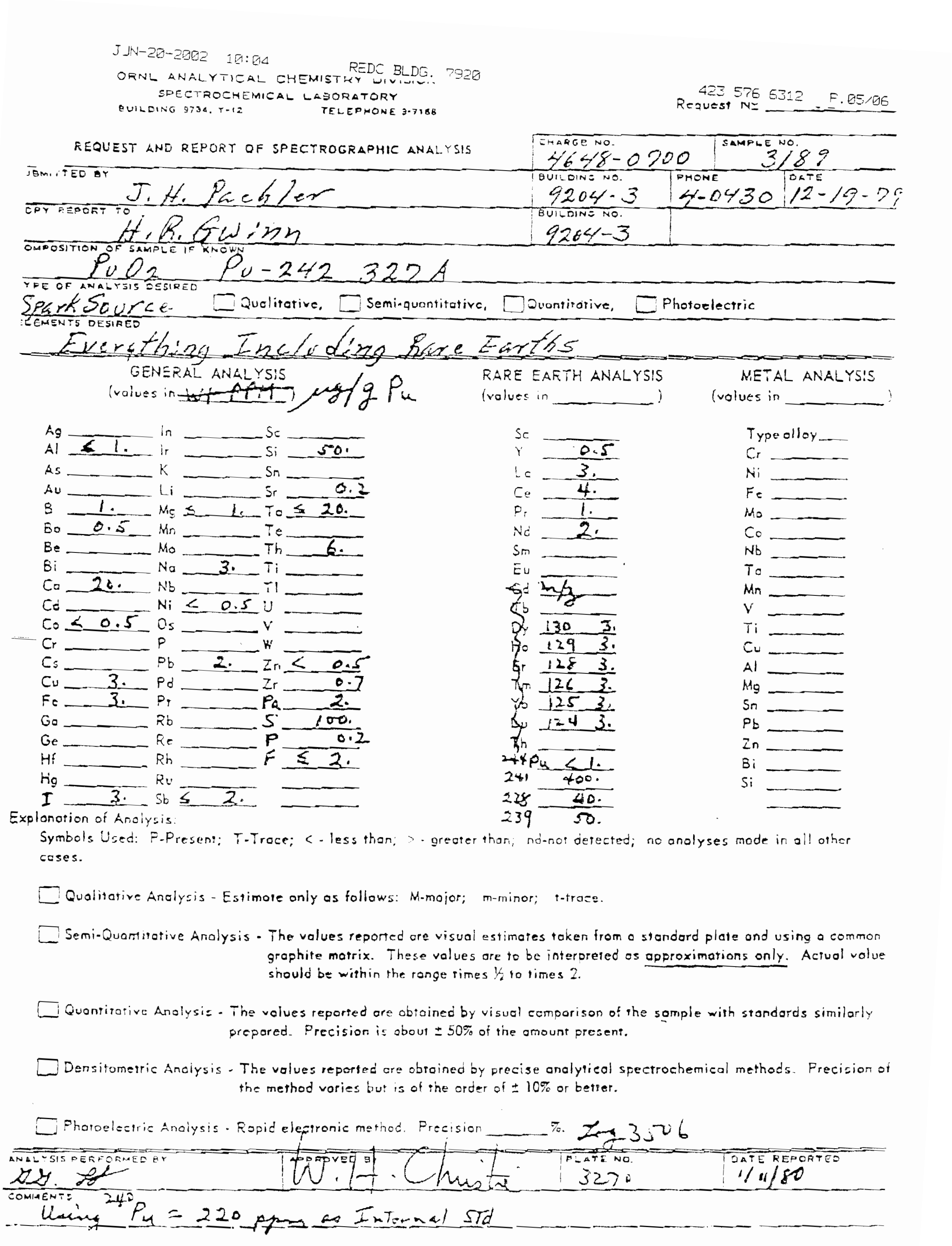

JUN-20-2002 10:04 REDC BLDG. 7920 423 576 6312 P.05/06

ORNL ANALYTICAL CHEMISTRY DIVISION
SPECTROCHEMICAL LABORATORY
BUILDING 9734, Y-12 TELEPHONE 3-7168

Request No

REQUEST AND REPORT OF SPECTROGRAPHIC ANALYSIS

CHARGE NO. 4648-0700
SAMPLE NO. 3189

SUBMITTED BY J. H. Pachler
BUILDING NO. 9204-3
PHONE 4-0430
DATE 12-19-79

COPY REPORT TO H. B. Gwinn
BUILDING NO. 9204-3

COMPOSITION OF SAMPLE IF KNOWN PuO2 Pu-242 322A

TYPE OF ANALYSIS DESIRED Spark Source ☐ Qualitative, ☐ Semi-quantitative, ☐ Quantitative, ☐ Photoelectric

ELEMENTS DESIRED Everything Including Rare Earths

GENERAL ANALYSIS
(values in ~~wt PPM~~) μg/g Pu

Ag		In		Sc	
Al	≤ 1.	Ir		Si	50.
As		K		Sn	
Au		Li		Sr	0.2
B	1.	Mg	≤ 1.	Ta	≤ 20.
Ba	0.5	Mn		Te	
Be		Mo		Th	6.
Bi		Na	3.	Ti	
Ca	20.	Nb		Tl	
Cd		Ni	< 0.5	U	
Co	< 0.5	Os		V	
Cr		P		W	
Cs		Pb	2.	Zn	< 0.5
Cu	3.	Pd		Zr	0.7
Fe	3.	Pt		Pa	2.
Ga		Rb		S	100.
Ge		Re		P	0.2
Hf		Rh		F	≤ 2.
Hg		Ru			
I	3.	Sb	≤ 2.		

RARE EARTH ANALYSIS
(values in)

Sc		
Y		0.5
La		3.
Ce		4.
Pr		1.
Nd		2.
Sm		
Eu		
~~Gd~~	m/z	
Tb		
Dy	130	3.
Ho	129	3.
Er	128	3.
Tm	126	3.
Yb	125	3.
Lu	124	3.
Th		
244Pu		< 1.
241		400.
238		40.
239		50.

METAL ANALYSIS
(values in)

Type alloy
Cr
Ni
Fe
Mo
Co
Nb
Ta
Mn
V
Ti
Cu
Al
Mg
Sn
Pb
Zn
Bi
Si

Explanation of Analysis:

Symbols Used: P-Present; T-Trace; < - less than; > - greater than; nd-not detected; no analyses made in all other cases.

☐ Qualitative Analysis - Estimate only as follows: M-major; m-minor; t-trace.

☐ Semi-Quantitative Analysis - The values reported are visual estimates taken from a standard plate and using a common graphite matrix. These values are to be interpreted as approximations only. Actual value should be within the range times ½ to times 2.

☐ Quantitative Analysis - The values reported are obtained by visual comparison of the sample with standards similarly prepared. Precision is about ± 50% of the amount present.

☐ Densitometric Analysis - The values reported are obtained by precise analytical spectrochemical methods. Precision of the method varies but is of the order of ± 10% or better.

☐ Photoelectric Analysis - Rapid electronic method. Precision ______%. Log 3506

ANALYSIS PERFORMED BY
APPROVED BY W. H. Christie
PLATE NO. 3270
DATE REPORTED 1/11/80

COMMENTS Using ^{240}Pu = 220 ppm as Internal STd

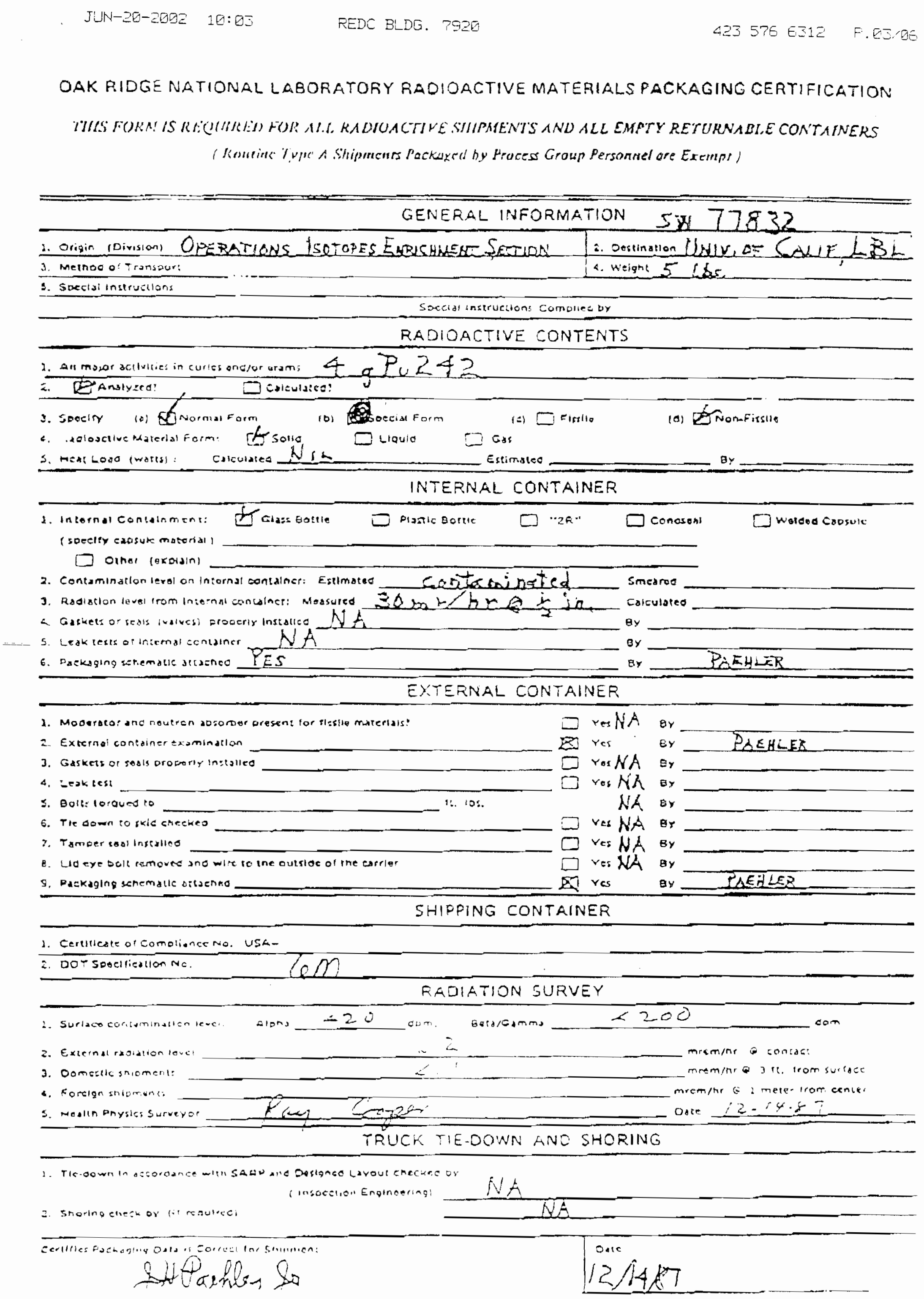

JUN-20-2002 10:03 REDC BLDG. 7920 423 576 6312 P.03/06

OAK RIDGE NATIONAL LABORATORY RADIOACTIVE MATERIALS PACKAGING CERTIFICATION

THIS FORM IS REQUIRED FOR ALL RADIOACTIVE SHIPMENTS AND ALL EMPTY RETURNABLE CONTAINERS

(Routine Type A Shipments Packaged by Process Group Personnel are Exempt)

GENERAL INFORMATION SW 77832

1. Origin (Division) OPERATIONS ISOTOPES ENRICHMENT SECTION
2. Destination UNIV. OF CALIF, LBL
3. Method of Transport
4. Weight 5 lbs.
5. Special Instructions

Special Instructions Complied by

RADIOACTIVE CONTENTS

1. All major activities in curies and/or grams 4 g Pu242
2. ☑ Analyzed? ☐ Calculated?
3. Specify (a) ☑ Normal Form (b) ☒ Special Form (c) ☐ Fissile (d) ☑ Non-Fissile
4. Radioactive Material Form: ☑ Solid ☐ Liquid ☐ Gas
5. Heat Load (watts) : Calculated Nil Estimated By

INTERNAL CONTAINER

1. Internal Containment: ☑ Glass Bottle ☐ Plastic Bottle ☐ "2R" ☐ Conoseal ☐ Welded Capsule
   (specify capsule material)
   ☐ Other (explain)
2. Contamination level on internal container: Estimated contaminated Smeared
3. Radiation level from internal container: Measured 30 mr/hr @ ½ in. Calculated
4. Gaskets or seals (valves) properly installed NA By
5. Leak tests of internal container NA By
6. Packaging schematic attached YES By PAEHLER

EXTERNAL CONTAINER

1. Moderator and neutron absorber present for fissile materials? ☐ Yes NA By
2. External container examination ☒ Yes By PAEHLER
3. Gaskets or seals properly installed ☐ Yes NA By
4. Leak test ☐ Yes NA By
5. Bolts torqued to ft. lbs. NA By
6. Tie down to skid checked ☐ Yes NA By
7. Tamper seal installed ☐ Yes NA By
8. Lid eye bolt removed and wire to the outside of the carrier ☐ Yes NA By
9. Packaging schematic attached ☒ Yes By PAEHLER

SHIPPING CONTAINER

1. Certificate of Compliance No. USA–
2. DOT Specification No. 6M

RADIATION SURVEY

1. Surface contamination level Alpha <20 dpm. Beta/Gamma <200 dpm
2. External radiation level ~2 mrem/hr @ contact
3. Domestic shipment: <1 mrem/hr @ 3 ft. from surface
4. Foreign shipment: mrem/hr @ 1 meter from center
5. Health Physics Surveyor Ray Cooper Date 12-14-87

TRUCK TIE-DOWN AND SHORING

1. Tie-down in accordance with SARP and Designed Layout checked by (Inspection Engineering) NA
2. Shoring check by (if required) NA

Certifies Packaging Data is Correct for Shipment: S H Paehler Jr

Date 12/14/87

SCHEMATIC PACKING

DETAILS FOR SW 77832

Order No. 41-0023

Pu242-327A

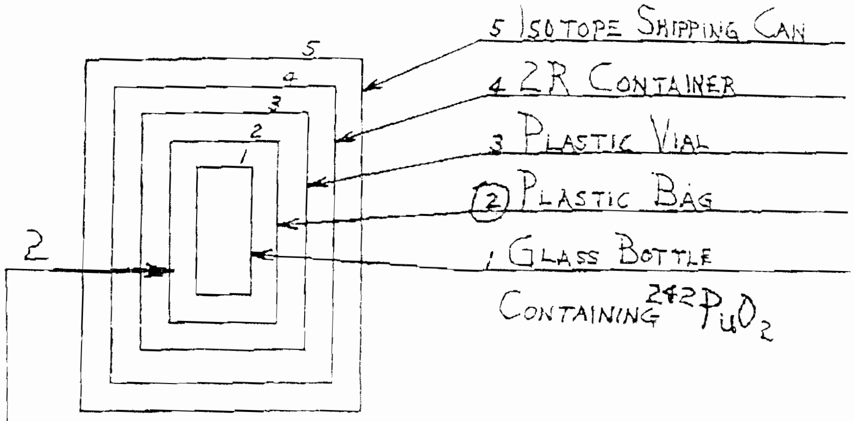

EXTRA COPY

When packed for shipment, the <u>inside</u> of this container (No. 2 in schematic) was contaminated with radioactive material. Therefore, this container should be opened using standard techniques of your plant for the handling of contaminated items (in glove box, etc.).

Date 12/14/87

By PAEHLER

TOTAL P.06

Appendix B

AutoCAD drawings of 6 mm circular target electrodeposition cell.

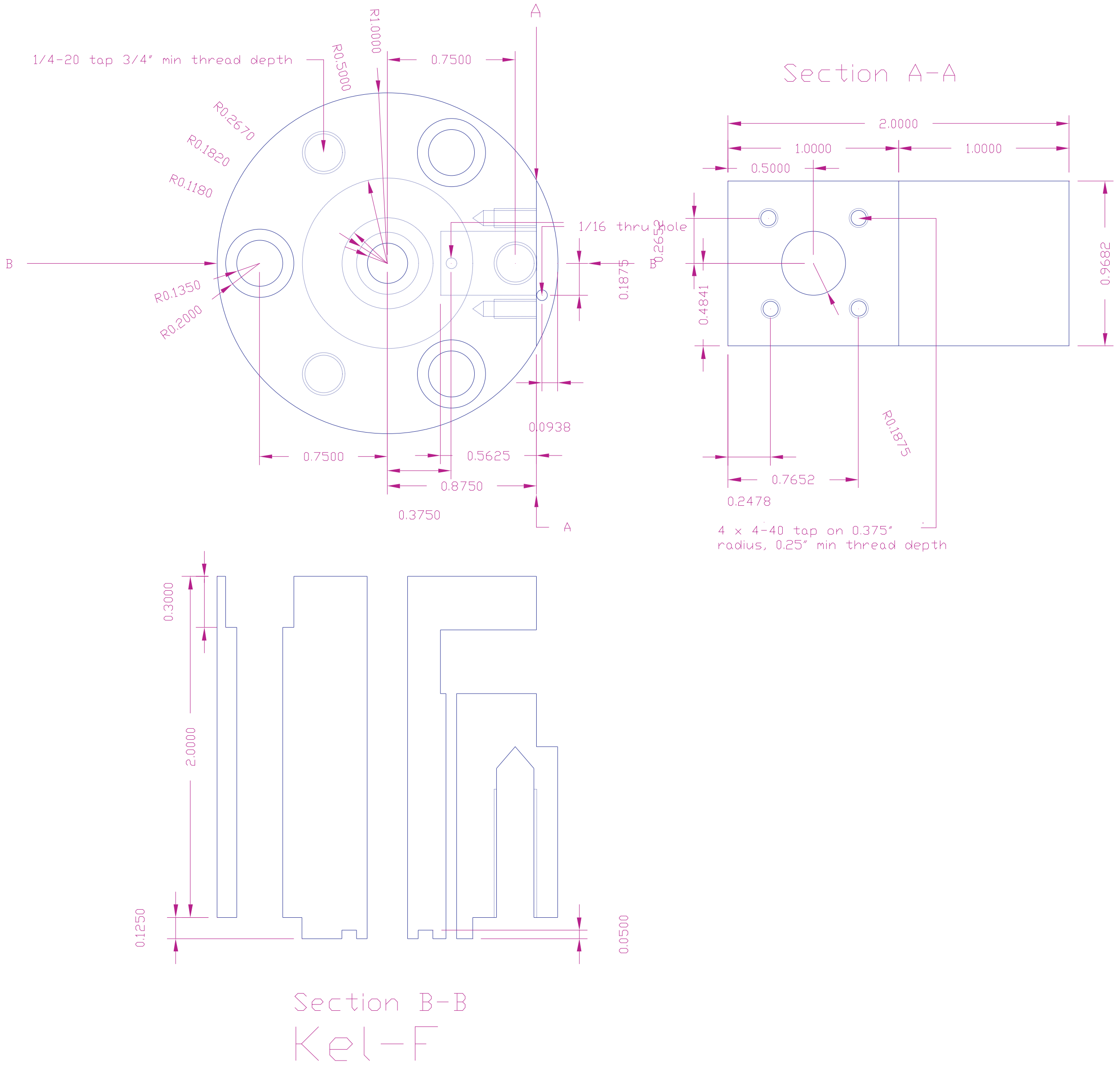

Kel-F top segment of plating cell

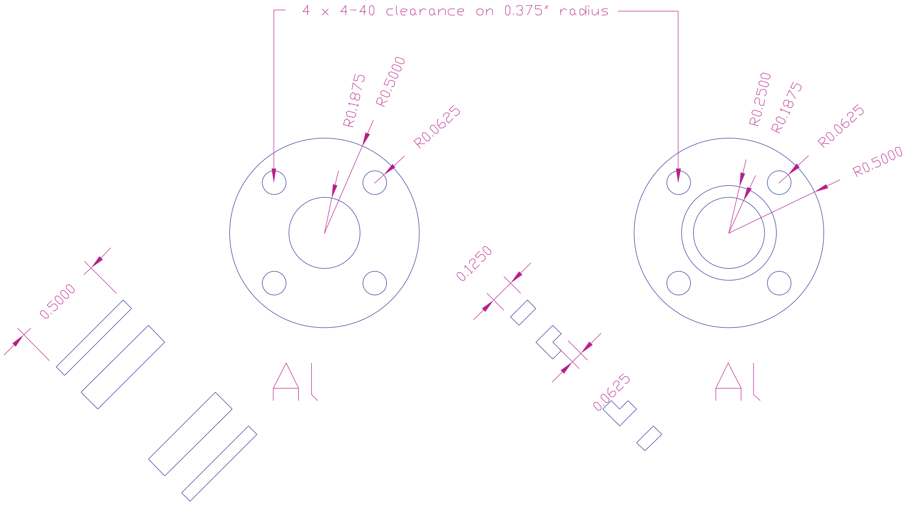

Aluminum SHV mounting bracket

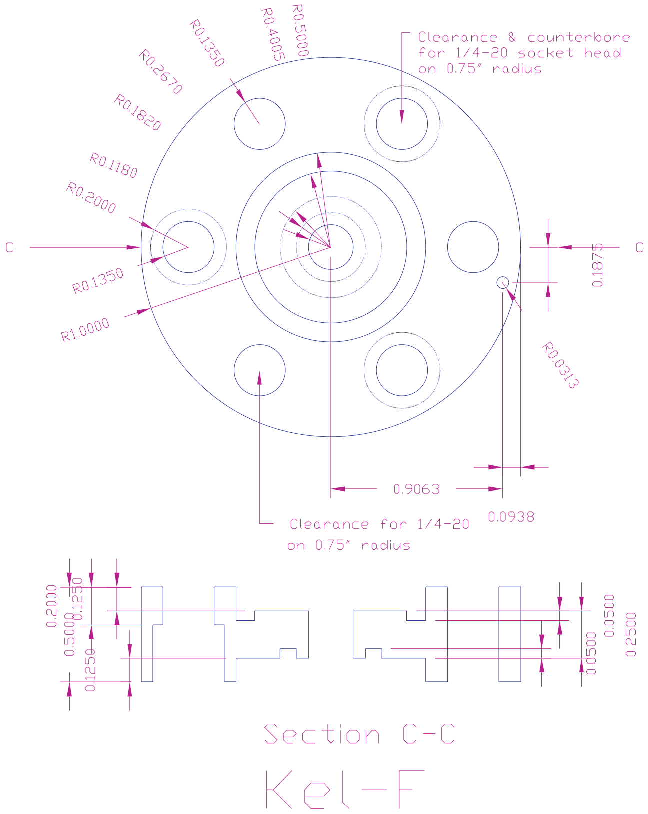

Kel-F middle segment of cell

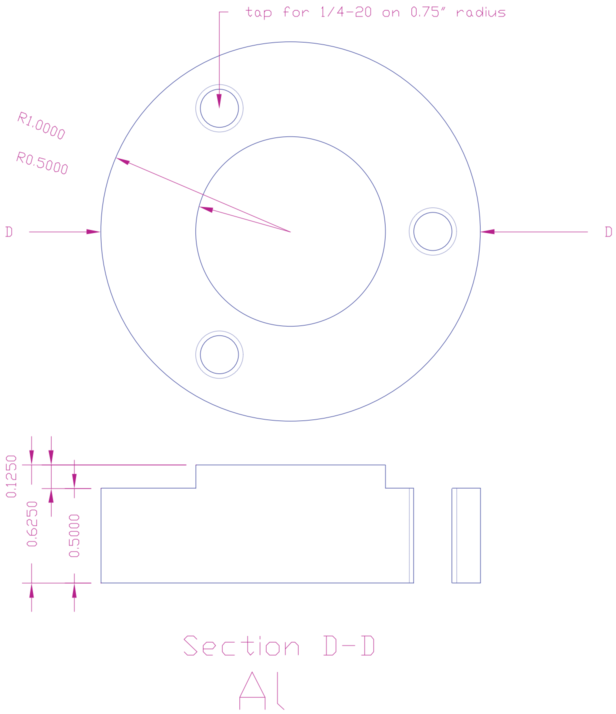

Aluminum base of cell

Appendix C

Summary of experimental warm and hot fusion nuclear reaction cross section data plotted in Figure 4.2.

Table C.1: Summary of experimental data plotted in Figure 4.2.

Z	Target	Projectile	Exit channel	Cross section (pb)	Ref.
104	^{238}U	^{26}Mg	$3n$	28^{92}_{-26}	[GGG$^+$08]
104	^{238}U	^{26}Mg	$4n$	180^{80}_{-60}	[GGG$^+$08]
104	^{238}U	^{26}Mg	$5n$	$(1.52 \pm 0.35) \times 10^3$	[GGG$^+$08]
104	^{244}Pu	^{22}Ne	$4n$	700	[LGL$^+$96]
104	^{248}Cm	^{28}O	$5n$	$(2.3 \pm 0.4) \times 10^4$	[HKK$^+$11]
104	^{249}Cf	^{12}C	$4n$	1×10^4	[GNH$^+$69]
105	^{241}Am	^{22}Ne	$4n$	$(1.6 \pm 1.2) \times 10^3$	[GQF$^+$01]
105	^{241}Am	^{22}Ne	$5n$	$(3.6 \pm 1.8) \times 10^3$	[GQF$^+$01]
105	^{243}Am	^{22}Ne	$4n$	250 ± 110	[LGL$^+$98]
105	^{248}Cm	^{19}F	$5n$	260^{150}_{90}	[DEJ$^+$99]
105	^{248}Cm	^{19}F	$5n$	$(1.3 \pm 0.4) \times 10^3$	[NAH$^+$02]
105	^{249}Bk	^{18}O	$4n$	$(10 \pm 6) \times 10^3$	[KGZ$^+$92]
105	^{249}Bk	^{18}O	$5n$	$(6 \pm 3) \times 10^3$	[KGZ$^+$92]
105	^{250}Cf	^{15}N	$4n$	510 ± 200	[LGL$^+$98]
106	^{238}U	^{30}Si	$3n$	$3.5^{+8.1}_{-2.9}$	[NHH$^+$06]
106	^{238}U	^{30}Si	$4n$	9^{+6}_{-4}	[GGD$^+$06]
106	^{238}U	^{30}Si	$5n$	54^{+51}_{-29}	[GGD$^+$06]
106	^{248}Cm	^{22}Ne	$4n$	80^{+160}_{-53}	[LLO$^+$94]

Continued on next page.

Table E.1, continued.

Z	Target	Projectile	Exit channel	Cross section (pb)	Ref.
106	^{248}Cm	^{22}Ne	$5n$	320^{+640}_{-210}	[LLO$^+$94]
107	^{248}Cm	^{23}Na	$5n$	50	[MMK$^+$09]
107	^{249}Bk	^{22}Ne	$4n$	96^{+55}_{-25}	[WGT$^+$00]
107	^{249}Bk	^{22}Ne	$5n$	140^{+110}_{-115}	[WGT$^+$00]
108	^{238}U	^{34}S	$4n$	$0.8^{+2.6}_{-0.7}$	[GAC$^+$10]
108	^{238}U	^{34}S	$4n$	$0.54^{+1.3}_{-0.45}$	[NHH$^+$10]
108	^{238}U	^{34}S	$5n$	$1.8^{+4.2}_{-1.5}$	[NHH$^+$10]
108	^{248}Cm	^{26}Mg	$3n$	$2.5^{+2.3}_{-1.5}$	[DBC$^+$08]
108	^{248}Cm	^{26}Mg	$4n$	$2.8^{+2.1}_{-1.4}$	[DBC$^+$08]
108	^{248}Cm	^{26}Mg	$5n$	$6.9^{+3.2}_{-2.6}$	[DBC$^+$08]
110	^{244}Pu	^{34}S	$5n$	$0.4^{+1.5}_{-0.3}$	[LLO$^+$96]
112	^{238}U	^{48}Ca	$3n$	$0.72^{+0.58}_{-0.35}$	[HAA$^+$07]
112	^{238}U	^{48}Ca	$3n$	$2.5^{+1.8}_{-1.1}$	[OUL$^+$04a]
112	^{238}U	^{48}Ca	$4n$	$0.6^{+1.6}_{-0.5}$	[OUL$^+$04a]
113	^{237}Np	^{48}Ca	$3n$	$0.9^{+1.6}_{-0.6}$	[Oga07]
114	^{242}Pu	^{48}Ca	$3n$	$3.6^{+3.4}_{-1.7}$	[OUL$^+$04a]
114	^{242}Pu	^{48}Ca	$4n$	$4.5^{+3.6}_{-1.9}$	[OUL$^+$04a]
114	^{242}Pu	^{48}Ca	$5n$	$0.6^{+1.5}_{-0.5}$	[EGB$^+$10]
114	^{244}Pu	^{48}Ca	$3n$	$8.0^{+7.4}_{-4.5}$	[DSY$^+$10]
114	^{244}Pu	^{48}Ca	$3n$	$1.7^{+2.5}_{-1.1}$	[OUL$^+$04b]
114	^{244}Pu	^{48}Ca	$4n$	$9.8^{+3.9}_{-3.1}$	[DSY$^+$10]
114	^{244}Pu	^{48}Ca	$4n$	$5.3^{+3.6}_{-2.1}$	[OUL$^+$04b]
114	^{244}Pu	^{48}Ca	$5n$	$1.1^{+2.6}_{-0.9}$	[OUL$^+$04b]
115	^{243}Am	^{48}Ca	$3n$	$3.7^{+1.3}_{-1.0}$	[OUD$^+$05]
115	^{243}Am	^{48}Ca	$4n$	$0.9^{+1.6}_{-0.6}$	[OUD$^+$05]
116	^{245}Cm	^{48}Ca	$3n$	$3.7^{+3.6}_{-1.8}$	[OUL$^+$06]
116	^{248}Cm	^{48}Ca	$4n$	$3.3^{+2.5}_{-1.4}$	[OUL$^+$04a]
117	^{249}Bk	^{48}Ca	$3n$	$1.3^{+1.5}_{-0.6}$	[OAB$^+$10]
118	^{249}Cf	^{48}Ca	$3n$	$0.5^{+1.6}_{-0.3}$	[OUL$^+$06]

Appendix D

Discussion of the calculation of low statistics error limits

In BGS experiments, there are often only a small number of events of interest recorded in a week- or month-long experiment. Understanding the error limits on these values is an important and non-trivial task. This appendix is dedicated to reviewing some of the literature and methods of calculating error on the following measurables:

- The number of observed events (and therefore cross section values)
- The branching ratio calculated from the number of two different types of events.
- The observed lifetime (and therefore half-life)

D.1 Classical vs. Bayesian Debate

In the various fields that focus on measurables with a small number of observed events there is quite a bit of debate as to the best way to estimate the error bars. The discussion is spread out over many decades (since at least the 1930's) and over many different scientific fields (very low cross section measurements in both low energy nuclear physics and high energy particle physics, and near background radioactive counting). The two main methods of error estimation are (i) the classical or frequentist method which estimates so-called "classical confidence intervals" and (ii) the Bayesian method which estimates so-called "Bayesian credible (or confidence) intervals". The two articles that directly relate these methods to low-energy nuclear physics cross section measurements are by Schmidt *et al.* [SSPC84] for the classical method and Brüchle [Brü03] for the Bayesian method.

The sections below give an overview of each of these methods and how to calculate confidence intervals for some of the measurables that we are interested in such as observed number of events, half-lives, and branching/common ratios.

D.1.1 Classical (or frequentist) method

The first method for estimating errors on the above mentioned measurables is the so-called Classical or Frequentist method. This method is notably used by K.-H. Schmidt *et al.* to construct confidence intervals [Brü03] for low energy nuclear science experiments with a small number of events. While this article does a good job of relating the method to several measurables of interest to low energy nuclear science, it does not address the overarching classical/bayesian debate or discuss the basis of the method. An excellent article outlining the classical method and comparing it with the Bayesian method is by Feldman and Cousins [FC98]. This frequently cited article is from the field of high energy particle physics measurements, but is very easily relate-able to our field. Much of the following overview section is motivated by this article.

Summary of the classical method

The classical method was first formulated by Jerzy Neyman in the 1930s [Ney37]. This paper is written as a mathematics paper and is quite hard to interpret. However, Feldman and Cousins do a good job of translating it into a more physical language.

At the heart of the classical confidence interval method is the construction of a confidence interval or belt. Suppose it is our goal to make a measurement of some actual average parameter μ by measuring an observable K which depends on μ according to the probability distribution function: $P(K|\mu)$. Then it is possible for every value of μ to find an interval of K such that $P(K \in [K_{ll}, K_{ul}]|\mu) = CI$. That is, the probability that K is greater than or equal K_{ll} and less than or equal to K_{ul} is equal to CI. If these horizontal acceptance intervals ($[K_{ll}, K_{ul}]$) are plotted as horizontal lines as a function of μ on a μ vs K plot, it will give Feldman and Cousins' Figure 1 [FC98] (notice Feldman and Cousins' variable x is my variable K).

Once this confidence belt is constructed, it can be used to generate a the classical confidence interval of μ for an observed K_{obs} by drawing a vertical line over the confidence belt and measuring the lower limit of its intersection with the belt (μ_{ll}) and its upper limit of the intersection (μ_{ul}). It can be seen (and if you think about it enough, makes intuitive sense) that these limits can be mathematically calculated by solving the following equations for μ_{ll} and μ_{ul} for an observed K_{obs}:

$$\int_{K_{obs}}^{\infty} P(K|\mu_{ll})\, dK = \frac{1-CI}{2}$$

$$\int_{0}^{K_{obs}} P(K|\mu_{ul})\, dK = \frac{1-CI}{2}$$

where CI is the confidence interval one wishes to know μ. The above method calculates the classical central confidence interval where μ is within $[\mu_{ll}, \mu_{ul}]$ with a confidence of CI and above μ_{ul} with $(1 - CI)/2$ and below μ_{ll} with $(1 - CI)/2$.

When the function $P(K|\mu)$ is not continuous as a function of K, such as the case of the binomial and poisson distributions, the classical method can still be used. However, because of the discrete nature of these distributions, it is not possible for every μ to find a horizontal acceptance interval such that $P(K \in [K_{ll}, K_{ul}]|\mu) = CI$. To work around this fact, we must add some degree of conservativeness to determining the intervals by looking for K_{ll} and K_{ul} such that $P(K > K_{ul}) \leq (1 - CI)/2$ and $P(K < K_{ll}) \leq (1 - CI)/2$. By fulfilling these inequalities, we see that $P(K \in [K_{ll}, K_{ul}]|\mu) \geq CI$ is fulfilled. The amount which the left hand side of this equation is larger than CI varies depending on K_{ll} and K_{ul} and is a thoroughly undesirable, but necessary part of using the classical method on probability functions that are discrete with respect to K.

Using these methods , confidence belts can be made for discrete K probability functions in the same way as described above. For a poisson distribution with a known background of 3.0, it will give us the Figure 6 from [FC98] (in this case, Feldman and Cousins' variable n is my variable K).

Once the confidence belt is made, the confidence interval of μ can be determined by drawing a vertical line at the observed K_{obs} and finding its intersection with all the lines formed by the above defined horizontal acceptance intervals. The classical confidence interval is then defined as the set of all μ intersection points (μ_{ll}, μ_{ul}). (The parentheses around the μ limits mean it's a non-inclusive limit, meaning μ_{ll} and μ_{ul} are actually outside the interval. It can be seen (and if you think about it hard enough, makes intuitive sense) that these limits can be mathematically calculated by solving the following equations for μ_{ll} and μ_{ul} for an observed K_{obs}:

$$\sum_{K=K_{obs}}^{\infty} P(K|\mu_{ll}) = \frac{1 - CI}{2}$$

$$\sum_{K=0}^{K_{obs}} P(K|\mu_{ul}) = \frac{1 - CI}{2}$$

These properties on the confidence of μ come about as a result of the choices we made for the horizontal acceptance intervals for x, i.e. finding K_{ll} and K_{ul} such that $P(K > K_{ul}) \leq (1 - CI)/2$ and $P(K < K_{ll}) \leq (1 - CI)/2$. There are other ways of defining the horizontal acceptance intervals to account for some problems. One way that this is done is based on an ordering principle based on likelihood ratios as described in [FC98].

Classical confidence intervals in the number of observed events with and without background

In experiments where only a small number of events are observed, then the number of observed events is determined by a Poisson distribution about the number expected from the actual average count rate. The equation for this is given by:

$$P(K|\mu) = \frac{\mu^K e^{-\mu}}{K!}$$

where K is the number of observed events and μ is the number expected from the actual average count rate. As such, we must use the method described above for a probability distribution function with discrete values of K. Thus, the classical confidence interval (μ_{ll}, μ_{ul}) can be calculated by solving the following two equations:

$$\sum_{K=K_{obs}}^{\infty} \frac{\mu_{ll}^K e^{-\mu_{ll}}}{K!} = 1 - \sum_{K=0}^{K_{obs-1}} \frac{\mu_{ll}^K e^{-\mu_{ll}}}{K!} = \frac{1-CI}{2}$$

$$\sum_{K=0}^{K_{obs}} \frac{\mu_{ul}^K e^{-\mu_{ul}}}{K!} = \frac{1-CI}{2}$$

If there is a known background rate producing an expected background of bkd events, then the equations are

$$\sum_{K=K_{obs}}^{\infty} \frac{(\mu_{ll}+bkd)^K e^{-(\mu_{ll}+bkd)}}{K!} = 1 - \sum_{K=0}^{K_{obs-1}} \frac{(\mu_{ll}+bkd)^K e^{-(\mu_{ll}+bkd)}}{K!} = \frac{1-CI}{2}$$

$$\sum_{K=0}^{K_{obs}} \frac{(\mu_{ul}+bkd)^K e^{-(\mu_{ul}+bkd)}}{K!} = \frac{1-CI}{2}$$

Calculating these classical confidence intervals can be performed in MathCAD. Figure D.1 shows the commented MathCAD sheet to accomplish this.

Classical confidence intervals of the lifetime of an observed radioactive decay

As discussed by Schmidt [SSPC84], one can use the classical method to calculate the confidence intervals on the observed lifetime of a radioactive decay as a function of the average lifetime and the number of observed events. The following section will elaborate upon and derive the equations within section 7 of his paper.

Given an actual lifetime of τ, the probability function of observing an average lifetime $\bar{t}$ with a total of n events is given by integrating the product of the individual probabilities for each lifetime observation $(t_1, t_2, ..., t_n)$ with the constraint that the average of the individual lifetime observations is $\bar{t}$. The normalized individual probability distribution function is given by:

$$P(t_i|\tau)\,dt_i = \frac{e^{-t_i/\tau} dt_i}{\int_0^\infty e^{-t_i/\tau}\,dt_i} = \frac{1}{\tau} e^{-t_i/\tau}\,dt_i$$

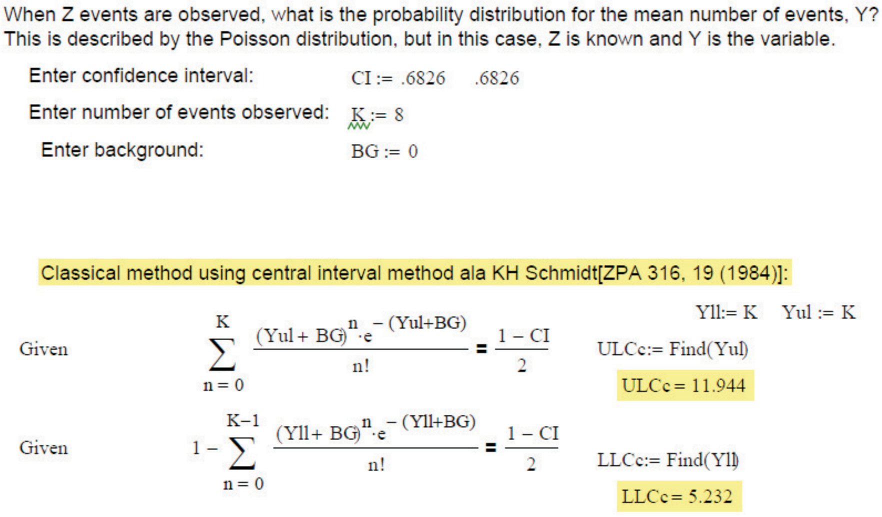

When Z events are observed, what is the probability distribution for the mean number of events, Y?
This is described by the Poisson distribution, but in this case, Z is known and Y is the variable.

Enter confidence interval: CI := .6826 .6826

Enter number of events observed: K := 8

Enter background: BG := 0

Classical method using central interval method ala KH Schmidt[ZPA 316, 19 (1984)]:

Yll:= K Yul := K

Given $\sum_{n=0}^{K} \frac{(Yul+BG)^{n} \cdot e^{-(Yul+BG)}}{n!} = \frac{1-CI}{2}$

ULCc:= Find(Yul)

ULCc = 11.944

Given $1 - \sum_{n=0}^{K-1} \frac{(Yll+BG)^{n} \cdot e^{-(Yll+BG)}}{n!} = \frac{1-CI}{2}$

LLCc:= Find(Yll)

LLCc = 5.232

Figure D.1 Commented MathCAD spreadsheet for calculating classical confidence intervals for the number of events with and without background.

and the probability distribution function for $\bar{t}$ is:

$$P(\bar{t}|\tau) = \int_0^{\infty} \cdots \int_0^{\infty} \prod_{i=1}^{n} \left[\frac{1}{\tau} e^{-t_i/\tau} \right] \delta\left(\bar{t} - \frac{1}{n} \sum_{j=1}^{n} t_j \right) dt_1\, dt_2 \ldots dt_n$$

where $\delta(x)$ is the dirac delta function which is equal to infinity when $x = 0$ and zero when $x \neq 0$. This function also has some important properties that we will take advantage of in the following mathematics. One property is that $\delta(\alpha x) = \frac{1}{\alpha}\delta(x)$ and the other is that $\int_0^{\infty} f(x)\delta(x - x_0)\, dx = f(x_0)$. Using this first property, we see that

$$\delta\left(\bar{t} - \frac{1}{n} \sum_{j=1}^{n} t_j \right) = \delta\left(\frac{1}{n} \left(\bar{t} - \frac{1}{n} \sum_{j=1}^{n} t_j \right) \right) = n\, \delta\left(n\bar{t} - \sum_{j=1}^{n} t_j \right)$$

Making this substitution, we see:

$$P(\bar{t}|\tau) = \int_0^{\infty} \cdots \int_0^{\infty} \prod_{i=1}^{n} \left[\frac{1}{\tau} e^{-t_i/\tau} \right] n\, \delta\left(n\bar{t} - \sum_{j=1}^{n} t_j \right) dt_1\, dt_2 \ldots dt_n$$

$$= \int_0^{\infty} \cdots \int_0^{\infty} \prod_{i=1}^{n-1} \left[\frac{1}{\tau} e^{-t_i/\tau} \right] \frac{1}{\tau} e^{-t_n/\tau}\, n\, \delta\left(n\bar{t} - \sum_{j=1}^{n-1} (t_j) - t_n \right) dt_1\, dt_2 \ldots dt_n$$

$$= \frac{n}{\tau^n} \int_0^\infty \cdots \int_0^\infty \prod_{i=1}^{n-1} \left[e^{-t_i/\tau} \right] e^{-t_n/\tau} \delta\left(n\bar{t} - \sum_{j=1}^{n-1} (t_j) - t_n \right) dt_1\, dt_2 \ldots\, dt_n$$

We can then integrate over t_n to eliminate the dirac delta function and get the following expression and the following algebraic simplifications:

$$P(\bar{t}|\tau) = \frac{n}{\tau^n} \int_0^\infty \cdots \int_0^\infty \prod_{i=1}^{n-1} \left[e^{-t_i/\tau} \right] e^{-(n\bar{t} - \sum_{j=1}^{n-1}(t_j))/\tau}\, dt_1\, dt_2 \ldots\, dt_{n-1}$$

$$= \frac{n}{\tau^n} \int_0^\infty \cdots \int_0^\infty \prod_{i=1}^{n-1} \left[e^{-t_i/\tau} \right] e^{-n\bar{t}/\tau} e^{\sum_{j=1}^{n-1}(t_j)/\tau}\, dt_1\, dt_2 \ldots\, dt_{n-1}$$

$$= \frac{n}{\tau^n} \int_0^\infty \cdots \int_0^\infty \prod_{i=1}^{n-1} \left[e^{-t_i/\tau} \right] e^{-n\bar{t}/\tau} \prod_{j=1}^{n-1} \left[e^{t_j/\tau} \right] dt_1\, dt_2 \ldots\, dt_{n-1}$$

$$= \frac{n}{\tau^n} \int_0^\infty \cdots \int_0^\infty e^{-n\bar{t}/\tau}\, dt_1\, dt_2 \ldots\, dt_{n-1}$$

$$P(\bar{t}|\tau) = \frac{ne^{-n\bar{t}}}{\tau^n} \int_0^\infty \cdots \int_0^\infty dt_1\, dt_2 \ldots\, dt_{n-1}$$

We must now work our way through the $n-1$ integrals, which at first seems like it would give an infinite answer. However, upon further thinking about the subject, we see that if we have $t_n = n\bar{t} - \sum_{i=1}^{n-1}(t_i)$, then $t_{n-1} \in [0, n\bar{t} - \sum_{i=1}^{n-2}(t_i)]$, $t_{n-2} \in [0, n\bar{t} - \sum_{i=1}^{n-3}(t_i)]$, ... , $t_2 \in [0, n\bar{t} - t_1]$, and $t_1 \in [0, n\bar{t}]$. Thus, we can put non-infinite bounds on our integrals and start integrating over dt_{n-1}:

$$P(\bar{t}|\tau) = \frac{ne^{-n\bar{t}/\tau}}{\tau^n} \int_0^{n\bar{t}} \cdots \int_0^{n\bar{t} - \sum_{i=1}^{n-2} t_i} dt_{n-1} dt_{n-2} \ldots dt_2 dt_1$$

$$= \frac{ne^{-n\bar{t}/\tau}}{\tau^n} \int_0^{n\bar{t}} \cdots \int_0^{n\bar{t} - \sum_{i=1}^{n-3} t_i} \left[n\bar{t} - \sum_{i=1}^{n-2} t_i \right] dt_{n-2} dt_{n-3} \ldots dt_2 dt_1$$

$$= \frac{ne^{-n\bar{t}/\tau}}{\tau^n} \int_0^{n\bar{t}} \cdots \int_0^{n\bar{t} - \sum_{i=1}^{n-3} t_i} \left[n\bar{t} - \sum_{i=1}^{n-3} t_i - t_{n-2} \right] dt_{n-2} dt_{n-3} \ldots dt_2 dt_1$$

If we then keep subsequently integrating over t_{n-2}, t_{n-3}, ... down to t_1, we see the following trend:

$$P(\bar{t}|\tau) = \frac{ne^{-n\bar{t}/\tau}}{\tau^n} \int_0^{n\bar{t}} \cdots \int_0^{n\bar{t} - \sum_{i=1}^{n-3} t_i} \left[n\bar{t} - \sum_{i=1}^{n-3} t_i - t_{n-2} \right] dt_{n-2} dt_{n-3} \ldots dt_2 dt_1$$

$$= \frac{ne^{-n\bar{t}/\tau}}{\tau^n} \int_0^{n\bar{t}} \cdots \int_0^{n\bar{t}-\sum_{i=1}^{n-4} t_i} \frac{1}{2}\left[n\bar{t} - \sum_{i=1}^{n-4} t_i - t_{n-3}\right]^2 dt_{n-3} dt_{n-4} \ldots dt_2 dt_1$$

$$= \frac{ne^{-n\bar{t}/\tau}}{\tau^n} \int_0^{n\bar{t}} \cdots \int_0^{n\bar{t}-\sum_{i=1}^{n-5} t_i} \frac{1}{2}\frac{1}{3}\left[n\bar{t} - \sum_{i=1}^{n-5} t_i - t_{n-4}\right]^3 dt_{n-4} dt_{n-5} \ldots dt_2 dt_1$$

$$\cdots$$

$$= \frac{ne^{-n\bar{t}/\tau}}{\tau^n} \int_0^{n\bar{t}} \int_0^{n\bar{t}-t_1} \frac{1}{(n-3)!}\left[n\bar{t} - t_1 - t_2\right]^{n-3} dt_2 dt_1$$

$$= \frac{ne^{-n\bar{t}/\tau}}{\tau^n} \int_0^{n\bar{t}} \frac{1}{(n-2)!}\left[n\bar{t} - t_1\right]^{n-2} dt_1$$

$$= \frac{ne^{-n\bar{t}/\tau}}{\tau^n} \frac{1}{(n-1)!}[n\bar{t}]^{n-1}$$

$$= \frac{n^n\, \bar{t}^{n-1}}{\tau^n (n-1)!} e^{-n\bar{t}/\tau}$$

$$= \frac{n^{n+1}\, \bar{t}^{n-1}}{\tau^n (n)!} e^{-n\bar{t}/\tau}$$

$$P(\bar{t}|\tau) = \frac{n^{n+1}}{(n)!} \frac{\bar{t}^{n-1}}{\tau^n} e^{-n\bar{t}/\tau}$$

As discussed above about continuous probability distributions of K for a given μ, the classical confidence intervals for τ are found by solving the following equations:

$$\int_{\bar{t_m}}^{\infty} P(\bar{t}|\tau_{ll})\, d\bar{t} = \frac{1-CI}{2}$$

$$\int_0^{\bar{t_m}} P(\bar{t}|\tau_{ul})\, d\bar{t} = \frac{1-CI}{2}$$

where $\bar{t_m}$ is the measured average lifetime. Thus, the confidence intervals are found by solving the following calculations

$$\int_{\bar{t_m}}^{\infty} P(\bar{t}|\tau_{ll})\, d\bar{t} = \int_{\bar{t_m}}^{\infty} \frac{n^{n+1}}{(n)!} \frac{\bar{t}^{n-1}}{\tau^n} e^{-n\bar{t}/\tau}\, d\bar{t} = \frac{1-CI}{2}$$

and

$$\int_0^{\bar{t_m}} P(\bar{t}|\tau_{ul})\, d\bar{t} = \int_0^{\bar{t_m}} \frac{n^{n+1}}{(n)!} \frac{\bar{t}^{n-1}}{\tau^n} e^{-n\bar{t}/\tau}\, d\bar{t} = \frac{1-CI}{2}$$

The easiest way to perform these integrals is by substituting $x = \frac{n\bar{t}_m}{\tau}$, then $dx = \frac{n}{\tau}d\bar{t}_m$ such that $\bar{t}_m = \frac{x\tau}{n}$ and $d\bar{t}_m = \frac{\tau}{m}dx$. Let $x_m = n\bar{t}_m/\tau$. The the first of the above equations simplifies to:

$$\begin{aligned}
\frac{1-CI}{2} &= \int_{\bar{t}_m}^{\infty} \frac{n^{n+1}}{n!}\frac{\bar{t}^{n-1}}{\tau^n}e^{-n\bar{t}/\tau}\,d\bar{t} \\
&= \frac{n^{n+1}}{n!\tau^n}\int_{x_m}^{\infty}\left(\frac{x\tau}{n}\right)^{n-1}e^{-x}\left(\frac{\tau}{n}\right)dx \\
&= \frac{n^{n+1}}{n!\tau^n}\left(\frac{x\tau}{n}\right)^{n}\int_{x_m}^{\infty}x^{n-1}e^{-x}\,dx \\
&= \frac{n\,(n-1)!}{n!}\int_{x_m}^{\infty}\frac{x^{n-1}e^{-x}}{(n-1)!}\,dx = \int_{x_m}^{\infty}\frac{x^{n-1}e^{-x}}{(n-1)!}\,dx
\end{aligned}$$

The bounded integral that we must now take is a normalized Poisson distribution. It's solution can be found by integration by parts. To remind you about this integration method, this is how it works: $\int u\,dv = uv - \int v\,du$. To use this method on the above integral, take $u = x^{n-1}$, then $du = (n-1)x^{x-2}\,dx$. Also, $dv = e^{-x}\,dx$, giving $v = -e^{-x}$. Then we see that:

$$\int_{x_m}^{\infty}\frac{x^{n-1}e^{-x}}{(n-1)!}\,dx = \frac{1}{(n-1)!}\left[-x^{n-1}e^{-1}\Big|_{x=x_m}^{\infty} + (n-1)\int_{x_m}^{\infty}x^{n-2}e^{-x}\,dx\right]$$

Integration by parts must then be performed $n-3$ more times ($n-2$ times total), as demonstrated in the following:

$$= \frac{1}{(n-1)!}\left[\Big(-x^{n-1}e^{-1}\Big)\Big|_{x=x_m}^{\infty} + (n-1)\int_{x_m}^{\infty}x^{n-2}e^{-x}\,dx\right]$$

$$= \frac{1}{(n-1)!}\left[\Big(-x^{n-1}e^{-1}\Big)\Big|_{x=x_m}^{\infty} + (n-1)\Big(-x^{n-2}e^{-1}\Big)\Big|_{x=x_m}^{\infty} + (n-1)(n-2)\int_{x_m}^{\infty}x^{n-3}e^{-x}\,dx\right]$$

$$= \frac{1}{(n-1)!}\Bigg[\Big(-x^{n-1}e^{-1}\Big)\Big|_{x=x_m}^{\infty} + (n-1)\Big(-x^{n-2}e^{-1}\Big)\Big|_{x=x_m}^{\infty} + (n-1)(n-2)\Big(-x^{n-3}e^{-1}\Big)\Big|_{x=x_m}^{\infty} + (n-1)(n-2)(n-3)\int_{x_m}^{\infty}x^{n-4}e^{-x}\,dx\Bigg]$$

$$\cdots$$

$$= \sum_{i=0}^{n-1}\left(\frac{-x^{i}e^{-x}}{i!}\Big|_{x_m}^{\infty}\right) = \sum_{i=0}^{n-1}\frac{{x_m}^{i}e^{-x_m}}{i!}$$

Thus, substituting x_m back out, that

$$\int_{\bar{t}_m}^{\infty}P(\bar{t}|\tau_{ll})\,d\bar{t} = \frac{1-CI}{2} = \sum_{i=0}^{n-1}\left(\frac{n\bar{t}_m}{\tau_{ll}}\right)^{i}\frac{1}{i!}e^{-(n\bar{t}_m)/\tau_{ll}}$$

To perform the same calculation for the upper limit, we must perform the above derived integration with the integration bounds of 0 to τ_{ul}. The integration process is all the same, so we see:

$$\int_0^{\bar{t_m}} P(\bar{t}|\tau_{ul})\, d\bar{t} = \frac{1-CI}{2} = \sum_{i=0}^{n-1} \left(\frac{-x^i e^{-x}}{i!} \Big|_0^{x_m} \right)$$
$$= \sum_{i=0}^{n-1} \left(\frac{-{x_m}^i e^{-x_m}}{i!} \right) + 1$$

Thus we see

$$\int_0^{\bar{t_m}} P(\bar{t}|\tau_{ul})\, d\bar{t} = \frac{1-CI}{2} = 1 - \sum_{i=0}^{n-1} \left(\frac{n\bar{t}_m}{\tau_{ul}} \right)^i \frac{1}{i!} e^{-(n\bar{t}_m)/\tau_{ul}}$$

So, in the end, the central confidence interval (τ_{ll}, τ_{ul}) for the observed lifetime of a radioactive decay process $\bar{t}_m$ where n events have been observed is given by the solutions to the following equations:

$$\frac{1-CI}{2} = \sum_{i=0}^{n-1} \left(\frac{n\bar{t}_m}{\tau_{ll}} \right)^i \frac{1}{i!} e^{-(n\bar{t}_m)/\tau_{ll}}$$
$$= 1 - \sum_{i=0}^{n-1} \left(\frac{n\bar{t}_m}{\tau_{ul}} \right)^i \frac{1}{i!} e^{-(n\bar{t}_m)/\tau_{ul}}$$

It should be noted that these equations are slightly different from the equations quoted in section 7 of [SSPC84] for the confidence interval (τ_{ll}, τ_{ul}). This must be due to a typo in this paper, as the equations in the paper are not solvable. These classical confidence intervals can be calculated using MathCAD. Figure D.2 shows the commented MathCAD sheet to accomplish this.

D.1.2 Bayesian Method

Another method for estimating the errors on some of these events is using the so-called Bayesian method. The following section will begin by summarizing the method and its criticisms and then continue with several sections as to how to use this method to estimate error in the number of observed events with and without background and a non-100% efficiency and branching and regular ratios.

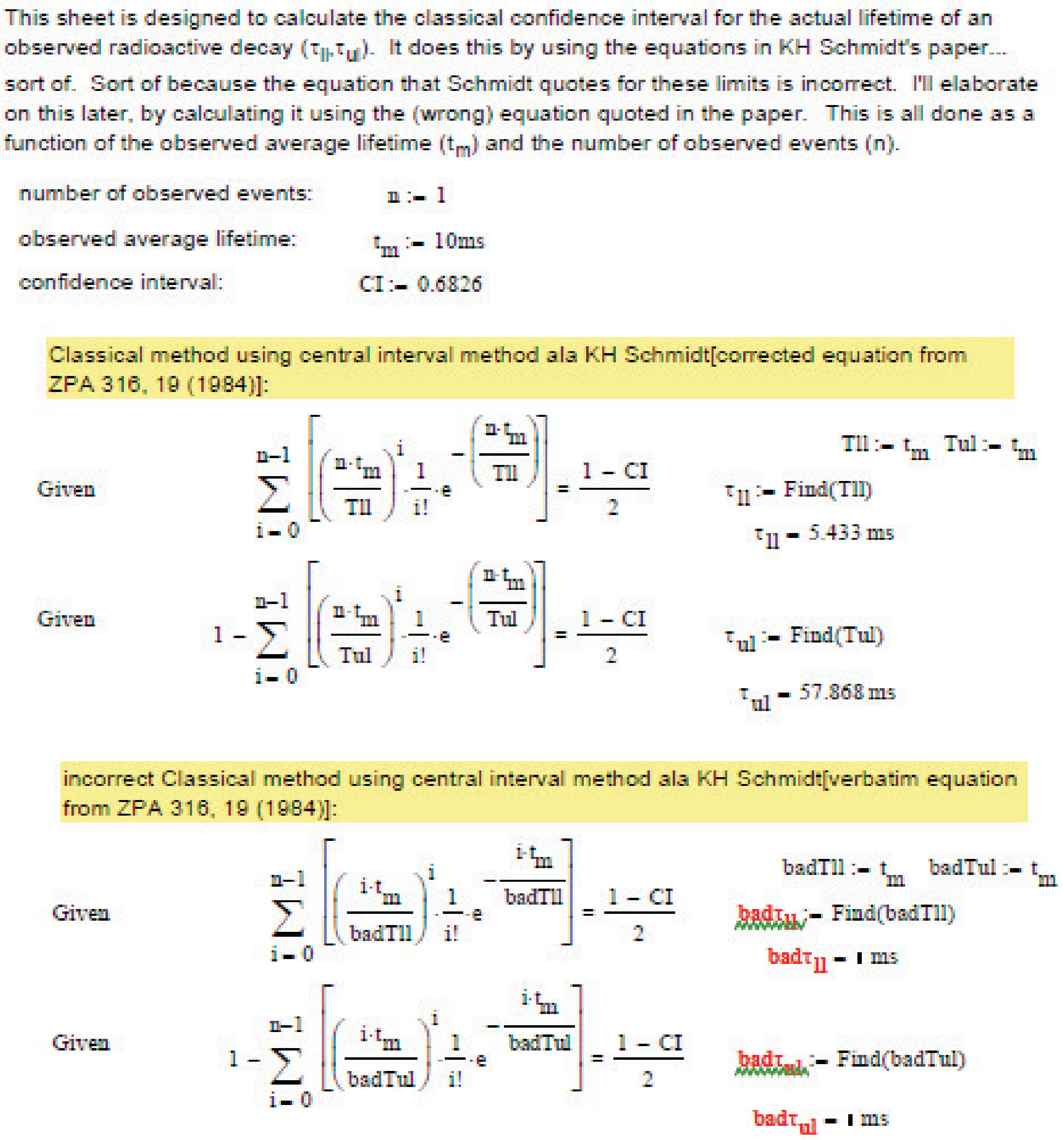

This sheet is designed to calculate the classical confidence interval for the actual lifetime of an observed radioactive decay (τ_{ll}, τ_{ul}). It does this by using the equations in KH Schmidt's paper... sort of. Sort of because the equation that Schmidt quotes for these limits is incorrect. I'll elaborate on this later, by calculating it using the (wrong) equation quoted in the paper. This is all done as a function of the observed average lifetime (t_m) and the number of observed events (n).

number of observed events: $n := 1$

observed average lifetime: $t_m := 10\text{ms}$

confidence interval: $CI := 0.6826$

Classical method using central interval method ala KH Schmidt[corrected equation from ZPA 316, 19 (1984)]:

Given

$$\sum_{i=0}^{n-1}\left[\left(\frac{n\cdot t_m}{Tll}\right)^i\cdot\frac{1}{i!}\cdot e^{-\left(\frac{n\cdot t_m}{Tll}\right)}\right] = \frac{1-CI}{2}$$

$Tll := t_m$ $Tul := t_m$

$\tau_{ll} := \text{Find}(Tll)$

$\tau_{ll} = 5.433\text{ ms}$

Given

$$1-\sum_{i=0}^{n-1}\left[\left(\frac{n\cdot t_m}{Tul}\right)^i\cdot\frac{1}{i!}\cdot e^{-\left(\frac{n\cdot t_m}{Tul}\right)}\right] = \frac{1-CI}{2}$$

$\tau_{ul} := \text{Find}(Tul)$

$\tau_{ul} = 57.868\text{ ms}$

incorrect Classical method using central interval method ala KH Schmidt[verbatim equation from ZPA 316, 19 (1984)]:

Given

$$\sum_{i=0}^{n-1}\left[\left(\frac{i\cdot t_m}{badTll}\right)^i\cdot\frac{1}{i!}\cdot e^{-\frac{i\cdot t_m}{badTll}}\right] = \frac{1-CI}{2}$$

$badTll := t_m$ $badTul := t_m$

$bad\tau_{ll} := \text{Find}(badTll)$

$bad\tau_{ll} = \blacksquare\text{ ms}$

Given

$$1-\sum_{i=0}^{n-1}\left[\left(\frac{i\cdot t_m}{badTul}\right)^i\cdot\frac{1}{i!}\cdot e^{-\frac{i\cdot t_m}{badTul}}\right] = \frac{1-CI}{2}$$

$bad\tau_{ul} := \text{Find}(badTul)$

$bad\tau_{ul} = \blacksquare\text{ ms}$

Figure D.2 Commented MathCAD spreadsheet for calculating classical confidence intervals for the measured lifetime of a radioactively decaying nuclide.

Summary of the Bayesian method

Assume it is the goal to make a measurement of some actual average parameter μ by measuring an observable K. Also, suppose the observable K depends on μ according to the probability distribution function: $P(K|\mu)$. Using the Bayesian method, we can relate this probability distribution function with the probability distribution function of μ given the observation of K events. These two distributions are related by the following equation:

$$P(\mu|K)\,P(K) = P(K|\mu)\,P(\mu)$$

$$P(\mu|K) = \frac{P(K|\mu)\,P(\mu)}{P(K)}$$

The $P(K)$ in the denominator of the bottom equation, which is not a function of μ, is typically just a normalization constant. In the literature, $P(\mu|K)$ is sometimes called the “posterior” probability distribution function and $P(\mu)$ is called the “prior” probability function. This “prior” function allows the user of the Bayesian method to incorporate knowledge about μ, along with previous experimental measurements. When this is done, it’s called using a *subjective* prior function and it allows contradictory or non-physical values of μ to be given a low priority.

If no information is known about the parameter μ, it is desirable to make an *objective* prior which only conveys the user’s prior ignorance. The prior function to use in this case seems to be well debated. Brüchle [Brü03] and Helene [Hel84] advocate the use of a ”uniform” prior distribution by setting the prior equal to one. Several articles disagree with this usage, calling it ”naive” and recommend the usage of $P(\mu) = 1/\mu$ such as James [Jam85], Feldman and Cousins [FC98], and Jaynes [Jay68].

Once one has a probability distribution function for the actual average value of a parameter ($P(\mu|K)$), once can calculate the Bayesian confidence intervals for the parameter. As discussed in [Brü03], confidence limits can be extracted several ways by integration. The two main ways confidence limits can be extracted are illustrated by Figure 3 of this paper.

The sections that follow outline calculations of Bayesian $P(\mu|K)$ probability distribution function for the number of observed events, number of events with background, number of events with efficiency, the branching ratio of two types of events, and the ratio of two types of events. These Bayesian probability distribution functions ($P(\mu|K)$) can then be integrated to determine the Bayesian confidence intervals for each of these parameters. The confidence intervals are calculated in MathCAD for both the uniform prior and $1/\mu$ prior.

Bayesian credible interval limits in the number of observed events

In experiments where only a small number of events are observed, then the number of observed events is determined by a Poisson distribution about the number expected from the actual average count rate. The equation for this is given by:

$$P(K|\mu) = \frac{\mu^K e^{-\mu}}{K!}$$

where K is the number of observed events and μ is the number expected from the actual average count rate. Using the Bayesian approach, we can manipulate this equation to become a continuous function of μ and determine the error from the probability distribution function $P(\mu|K)$. We see then that we get:

$$P(\mu|K) = \frac{\frac{\mu^K e^{-\mu}}{K!} P(\mu)}{P(K)}$$

with $P(\mu)$ the prior function and $P(K)$ a normalization function. Different references use different values for this prior probability function. The two that I have seen most mentioned are a uniform prior distribution of $P(\mu) = 1$ (in which case $P(K) = 1$, obvious cause Poisson dist. is normalized) and the $1/\mu$ distribution where $P(\mu) = 1/\mu$ (in which case $P(K) = 1/K$, trust me or do the integration yourself).

We thus get the two Bayesian probability distributions for the actual average number of expected events to be

$$P(\mu|K) = \frac{\mu^K e^{-\mu}}{K!}$$

for a uniform prior distribution and

$$P(\mu|K) = \frac{\mu^{K-1} e^{-\mu}}{(K-1)!}$$

for a $1/\mu$ prior distribution.

These Bayesian confidence intervals using uniform and $1/\mu$ prior probability distribution functions for the number of events can be calculated with a MathCAD such as that shown in Figure D.3 shows the commented MathCAD sheet to accomplish this.

Bayesian credible interval limits in the number of observed events with a given efficiency

Bruechle [Brü03] also discusses how the probability distribution of the actual number of events varies as a function of both the number of observed decays K and the efficiency for detecting the decays θ. The paper does this with a combination of the aboved discussed Bayesian methods with the binomial distribution. Specifically, we know that if we have K observed decays, that we can write the probability that N decays produced these K observed decays by the binomial distribution where:

$$P(N|K, \theta) = \binom{N}{K} \theta^K (1 - \theta^{N-K})$$

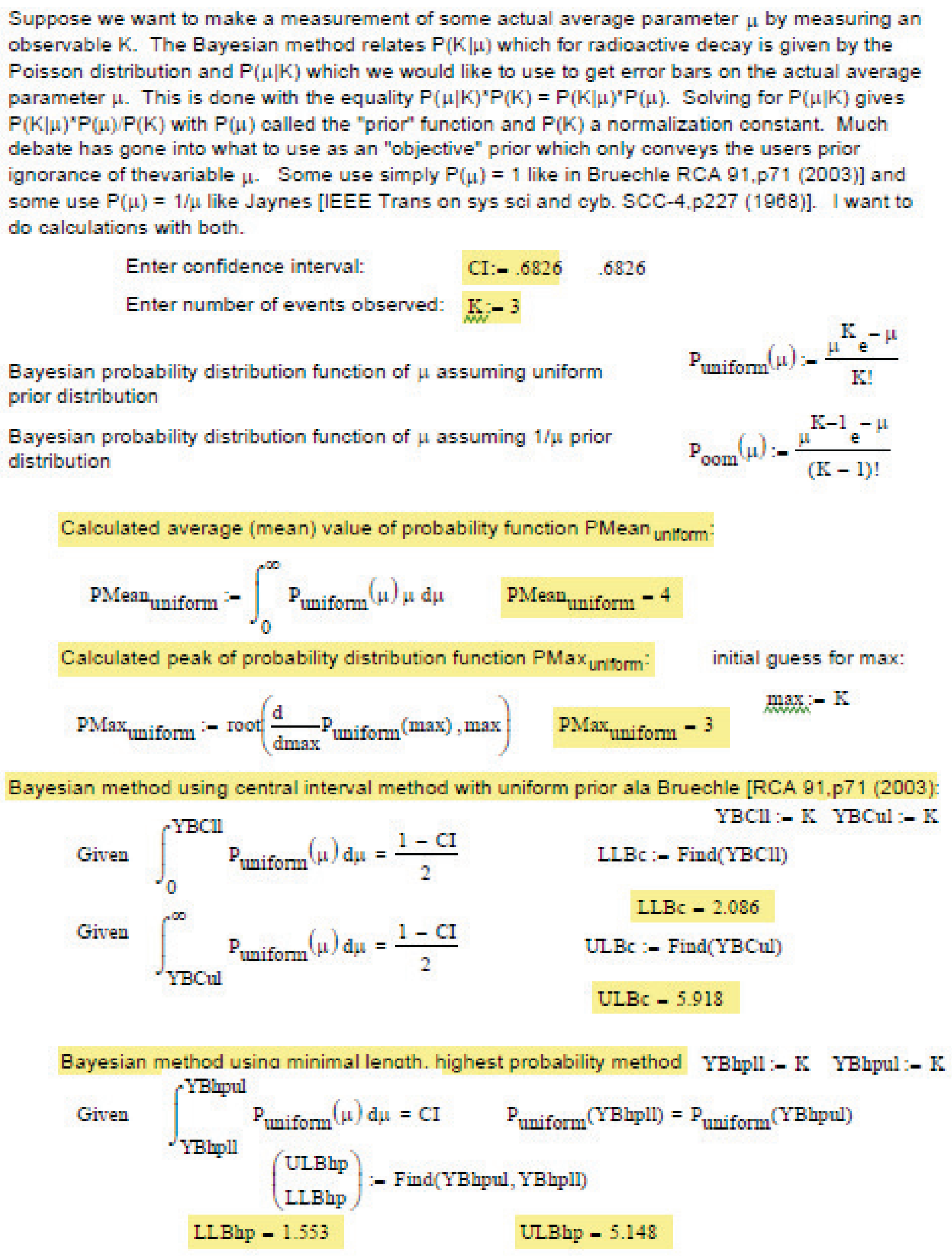

Suppose we want to make a measurement of some actual average parameter μ by measuring an observable K. The Bayesian method relates P(K|μ) which for radioactive decay is given by the Poisson distribution and P(μ|K) which we would like to use to get error bars on the actual average parameter μ. This is done with the equality P(μ|K)*P(K) = P(K|μ)*P(μ). Solving for P(μ|K) gives P(K|μ)*P(μ)/P(K) with P(μ) called the "prior" function and P(K) a normalization constant. Much debate has gone into what to use as an "objective" prior which only conveys the users prior ignorance of thevariable μ. Some use simply P(μ) = 1 like in Bruechle RCA 91,p71 (2003)] and some use P(μ) = 1/μ like Jaynes [IEEE Trans on sys sci and cyb. SCC-4,p227 (1968)]. I want to do calculations with both.

Enter confidence interval: $CI := .6826$ .6826

Enter number of events observed: $K := 3$

Bayesian probability distribution function of μ assuming uniform prior distribution $P_{uniform}(\mu) := \frac{\mu^{K} e^{-\mu}}{K!}$

Bayesian probability distribution function of μ assuming 1/μ prior distribution $P_{oom}(\mu) := \frac{\mu^{K-1} e^{-\mu}}{(K-1)!}$

Calculated average (mean) value of probability function PMean$_{uniform}$:

$PMean_{uniform} := \int_0^{\infty} P_{uniform}(\mu)\,\mu\,d\mu$ $PMean_{uniform} = 4$

Calculated peak of probability distribution function PMax$_{uniform}$:

initial guess for max:

$max := K$

$PMax_{uniform} := root\left(\frac{d}{dmax}P_{uniform}(max), max\right)$ $PMax_{uniform} = 3$

Bayesian method using central interval method with uniform prior ala Bruechle [RCA 91,p71 (2003):

$YBCll := K$ $YBCul := K$

Given $\int_0^{YBCll} P_{uniform}(\mu)\,d\mu = \frac{1-CI}{2}$

$LLBc := Find(YBCll)$

$LLBc = 2.086$

Given $\int_{YBCul}^{\infty} P_{uniform}(\mu)\,d\mu = \frac{1-CI}{2}$

$ULBc := Find(YBCul)$

$ULBc = 5.918$

Bayesian method using minimal length, highest probability method $YBhpll := K$ $YBhpul := K$

Given $\int_{YBhpll}^{YBhpul} P_{uniform}(\mu)\,d\mu = CI$ $P_{uniform}(YBhpll) = P_{uniform}(YBhpul)$

$\begin{pmatrix} ULBhp \\ LLBhp \end{pmatrix} := Find(YBhpul, YBhpll)$

$LLBhp = 1.553$ $ULBhp = 5.148$

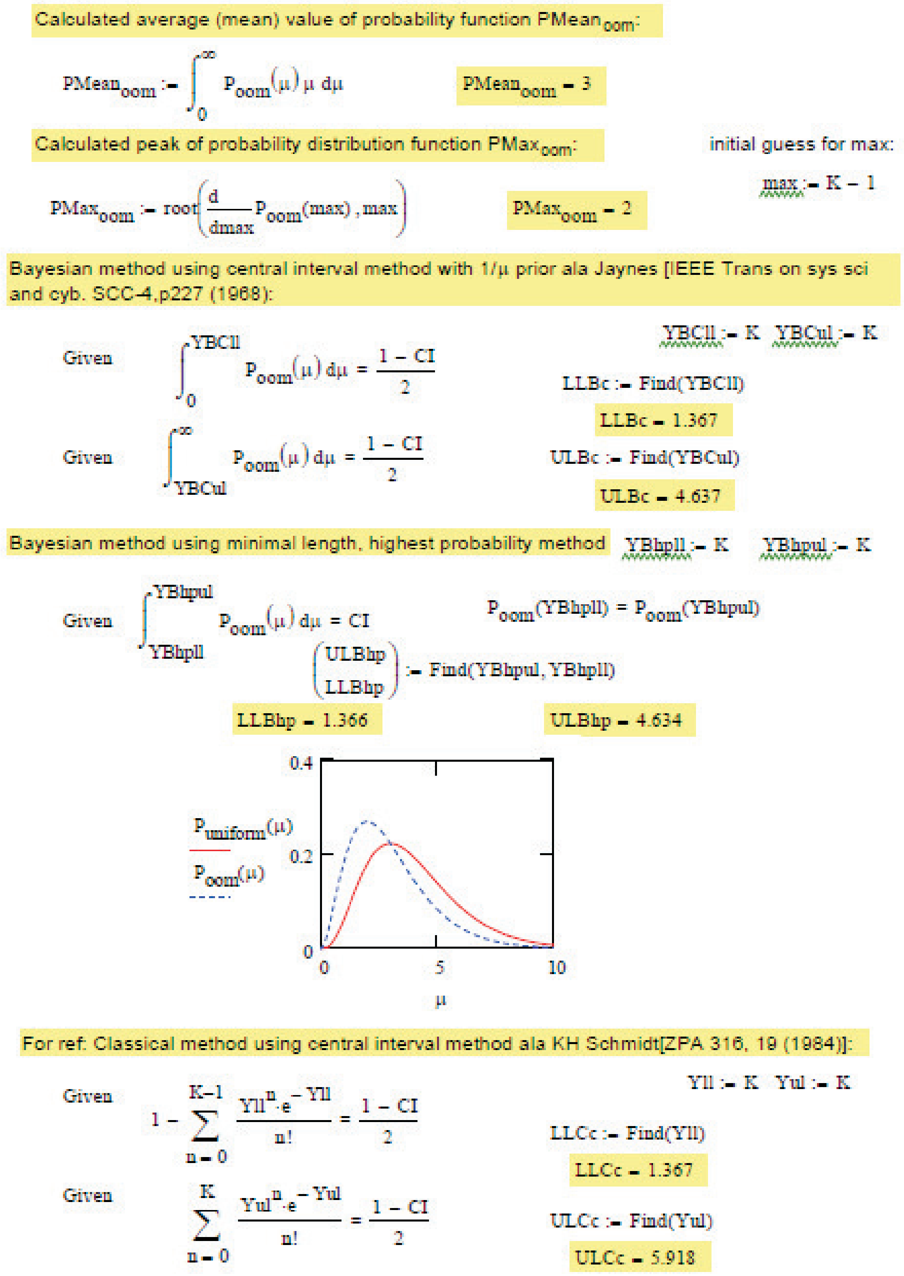

Calculated average (mean) value of probability function $PMean_{oom}$:

$PMean_{oom} := \int_0^\infty P_{oom}(\mu)\,\mu\,d\mu$ $\quad PMean_{oom} = 3$

Calculated peak of probability distribution function $PMax_{oom}$:

initial guess for max:

$max := K - 1$

$PMax_{oom} := root\left(\frac{d}{dmax}P_{oom}(max), max\right)$ $\quad PMax_{oom} = 2$

Bayesian method using central interval method with 1/μ prior ala Jaynes [IEEE Trans on sys sci and cyb. SCC-4,p227 (1968):

$YBCll := K \quad YBCul := K$

Given $\int_0^{YBCll} P_{oom}(\mu)\,d\mu = \frac{1 - CI}{2}$

$LLBc := Find(YBCll)$

$LLBc = 1.367$

Given $\int_{YBCul}^{\infty} P_{oom}(\mu)\,d\mu = \frac{1 - CI}{2}$

$ULBc := Find(YBCul)$

$ULBc = 4.637$

Bayesian method using minimal length, highest probability method $\quad YBhpll := K \quad YBhpul := K$

Given $\int_{YBhpll}^{YBhpul} P_{oom}(\mu)\,d\mu = CI$ $\quad P_{oom}(YBhpll) = P_{oom}(YBhpul)$

$\begin{pmatrix} ULBhp \\ LLBhp \end{pmatrix} := Find(YBhpul, YBhpll)$

$LLBhp = 1.366 \quad ULBhp = 4.634$

For ref: Classical method using central interval method ala KH Schmidt[ZPA 316, 19 (1984)]:

$Yll := K \quad Yul := K$

Given $1 - \sum_{n=0}^{K-1} \frac{Yll^n \cdot e^{-Yll}}{n!} = \frac{1 - CI}{2}$

$LLCc := Find(Yll)$

$LLCc = 1.367$

Given $\sum_{n=0}^{K} \frac{Yul^n \cdot e^{-Yul}}{n!} = \frac{1 - CI}{2}$

$ULCc := Find(Yul)$

$ULCc = 5.918$

Figure D.3 Commented MathCAD spreadsheet for calculating Bayesian confidence intervals for the number of events.

To normalize this function, we must sum from $N = K$ to infinity. This is because with K observed events, N can be as low as K (we saw all events that happened) up to infinity (we barely saw any). Thus, to normalize this probability function need to divide by:

$$\sum_{N=K}^{\infty} \binom{N}{K} \theta^K (1 - \theta^{N-K})$$

It can be show (like it is [Brü03]) that this normalization factor is equal to $1/\theta$.

Thus, to get the probability distribution function for the number expected from the actual average count rate, μ, given the number of observed events K and the efficiency for observing them θ, we can do a bayesian "integral method" of poisson distributions for each possible number of events that occured N. That is, for all $N \geq K$, we want to take $P(\mu|N) = \frac{\mu^N e^{-\mu}}{N!}$ and then weigh it by the normalized probability that there was N decays that caused the observed K events. Then the normalized probability function of the number of expected decays from the actual average count rate as a function of the number of observed decays and the known efficiency is just the sum over all possible values of N. Thus, putting it all together in terms of μ (actual average number of decays), K (measured number of events) and θ (efficiency):

$$P_{uni}(\mu|(K, \theta)) = \sum_{N=K}^{\infty} \frac{\binom{N}{K}\theta^K (1 - \theta^{N-K})}{1/\theta} \frac{\mu^N e^{-\mu}}{N!}$$

for a uniform prior distribution and

$$P_{oom}(\mu|(K, \theta)) = \sum_{N=K}^{\infty} \frac{\binom{N}{K}\theta^K (1 - \theta^{N-K})}{1/\theta} \frac{\mu^{N-1} e^{-\mu}}{(N-1)!}$$

for a $1/\mu$ prior distribution.

These Bayesian confidence intervals using the uniform prior probability distribution functions for the number of events given a certain detection effiiency can be calculated with a MathCAD such as that shown in Figure D.4 shows the commented MathCAD sheet to accomplish this.

Bayesian credible interval limits in the number of observed events with a given known background rate

Bruechle [Brü03] also discusses how to calculate the probability distribution function of the average actual number of events given an observed number of events K and a known average background rate of BG. The paper does this by first estimating the probability that K-B events are real events given K observed and an average background rate of BG. It contents that:

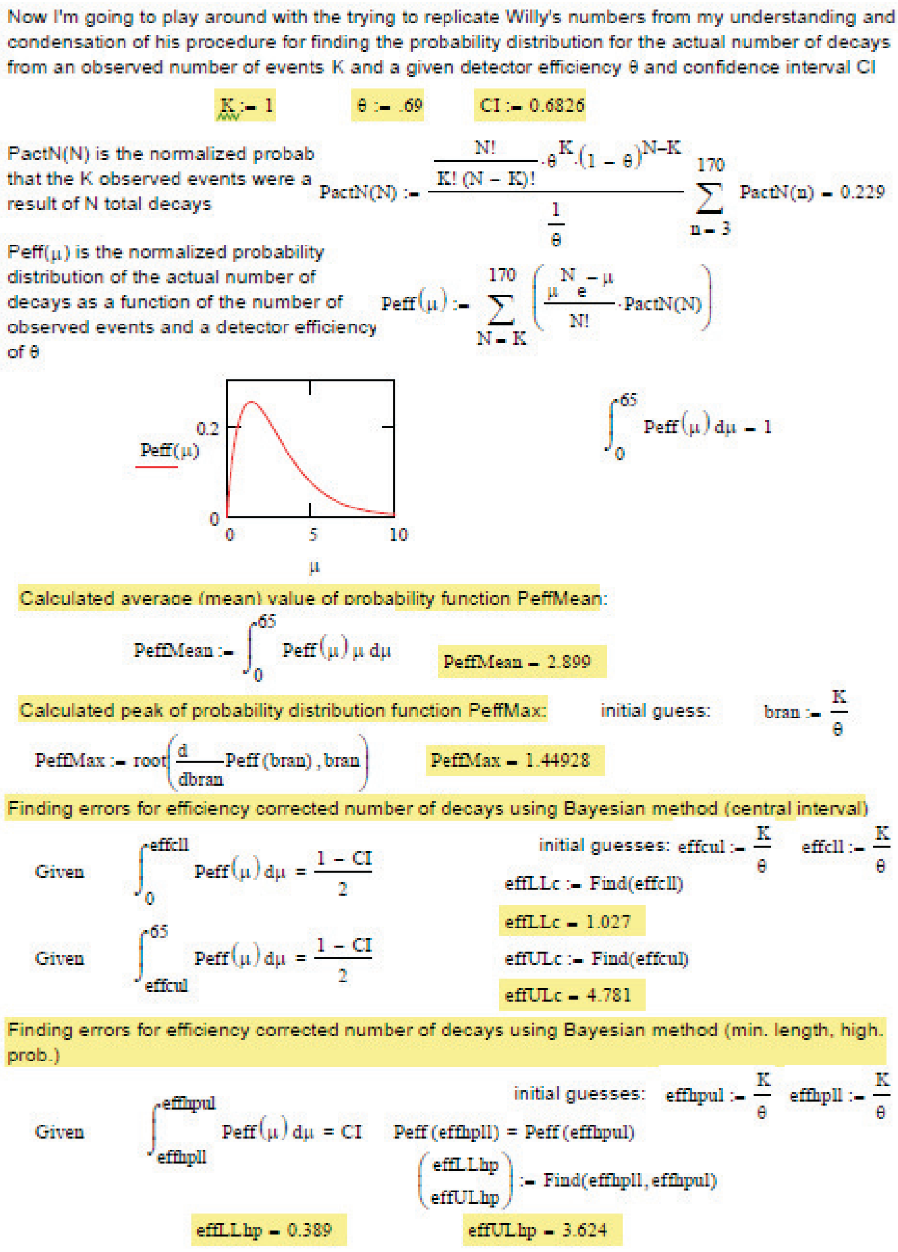

Now I'm going to play around with the trying to replicate Willy's numbers from my understanding and condensation of his procedure for finding the probability distribution for the actual number of decays from an observed number of events K and a given detector efficiency θ and confidence interval CI

$K := 1$ $\theta := .69$ $CI := 0.6826$

PactN(N) is the normalized probab that the K observed events were a result of N total decays

$$PactN(N) := \frac{\frac{N!}{K!\,(N-K)!}\cdot\theta^{K}\cdot(1-\theta)^{N-K}}{\frac{1}{\theta}} \qquad \sum_{n=3}^{170} PactN(n) = 0.229$$

Peff(μ) is the normalized probability distribution of the actual number of decays as a function of the number of observed events and a detector efficiency of θ

$$Peff(\mu) := \sum_{N=K}^{170}\left(\frac{\mu^{N}\,e^{-\mu}}{N!}\cdot PactN(N)\right)$$

$$\int_{0}^{65} Peff(\mu)\,d\mu = 1$$

Calculated average (mean) value of probability function PeffMean:

$$PeffMean := \int_{0}^{65} Peff(\mu)\,\mu\,d\mu \qquad PeffMean = 2.899$$

Calculated peak of probability distribution function PeffMax: initial guess: $bran := \frac{K}{\theta}$

$$PeffMax := root\left(\frac{d}{dbran}Peff(bran), bran\right) \qquad PeffMax = 1.44928$$

Finding errors for efficiency corrected number of decays using Bayesian method (central interval)

initial guesses: $effcul := \frac{K}{\theta}$ $effcll := \frac{K}{\theta}$

Given $\int_{0}^{effcll} Peff(\mu)\,d\mu = \frac{1-CI}{2}$

$effLLc := Find(effcll)$

$effLLc = 1.027$

Given $\int_{effcul}^{65} Peff(\mu)\,d\mu = \frac{1-CI}{2}$

$effULc := Find(effcul)$

$effULc = 4.781$

Finding errors for efficiency corrected number of decays using Bayesian method (min. length, high. prob.)

initial guesses: $effhpul := \frac{K}{\theta}$ $effhpll := \frac{K}{\theta}$

Given $\int_{effhpll}^{effhpul} Peff(\mu)\,d\mu = CI$ $Peff(effhpll) = Peff(effhpul)$

$$\begin{pmatrix} effLLhp \\ effULhp \end{pmatrix} := Find(effhpll, effhpul)$$

$effLLhp = 0.389$ $effULhp = 3.624$

Figure D.4 Commented MathCAD spreadsheet for calculating Bayesian confidence intervals for the number of events detected with a given efficiency.

$$P(K-B|(K,BG)) = P(B|(K,BG)) = \frac{\frac{BG^{B}e^{-BG}}{B!}}{\sum_{n=0}^{K}\frac{BG^{B}e^{-BG}}{B!}}$$

This equation is normalized by the fact that $B \leq K$ because the observed number of events due to background can be any number less than or equal to the number of observed events.

Then we can sum over each possible number of real observed events (x), scaling them by $P(K-B|(K,BG)) = P(B|(K,BG))$ to get the overall probability distribution function for the average actual number of events $P(\mu|(K,BG))$. Thus,

$$P_{uni}(\mu|(K,BG)) = \sum_{x=0}^{K}\frac{\mu^{x}e^{-\mu}}{x!}\frac{\frac{BG^{K-x}e^{-BG}}{(K-x)!}}{\sum_{n=0}^{K}\frac{BG^{K-x}e^{-BG}}{(K-x)!}}$$

for a uniform prior distribution and

$$P_{oom}(\mu|(K,BG)) = \sum_{x=0}^{K}\frac{\mu^{x-1}e^{-\mu}}{(x-1)!}\frac{\frac{BG^{K-x}e^{-BG}}{(K-x)!}}{\sum_{n=0}^{K}\frac{BG^{K-x}e^{-BG}}{(K-x)!}}$$

for a $1/\mu$ prior distribution.

These Bayesian confidence intervals using the uniform prior probability distribution functions for the number of events given a known background can be calculated with a MathCAD such as that shown in Figure D.5 shows the commented MathCAD sheet to accomplish this.

Bayesian credible interval limits for the branching ratio of two observed decay modes

When studying superheavy elements, the nuclides will often have two competing decay modes. For example, this could be a competition between alpha decay and spontaneous fission decay. The following discusses my method for calculating the probability distribution for the actual branching ratio as a function of the number of observed events for two Poissonian processes. I know this probability distribution is given by the product of Poisson distributions. Thus,

$$P(\mu_x,\mu_y|(K_x,K_y))\,d\mu_x\,d\mu_y = P(\mu_x|K_x)\,P(\mu_y|K_y)\,d\mu_x\,d\mu_y$$

For the case of a uniform prior distribution we see:

$$P_{uni}(\mu_x,\mu_y|(K_x,K_y))\,d\mu_x\,d\mu_y = \frac{\mu_x^{K_x}e^{-\mu_x}}{K_x!}\frac{\mu_y^{K_y}e^{-\mu_y}}{K_y!}\,d\mu_x\,d\mu_y$$

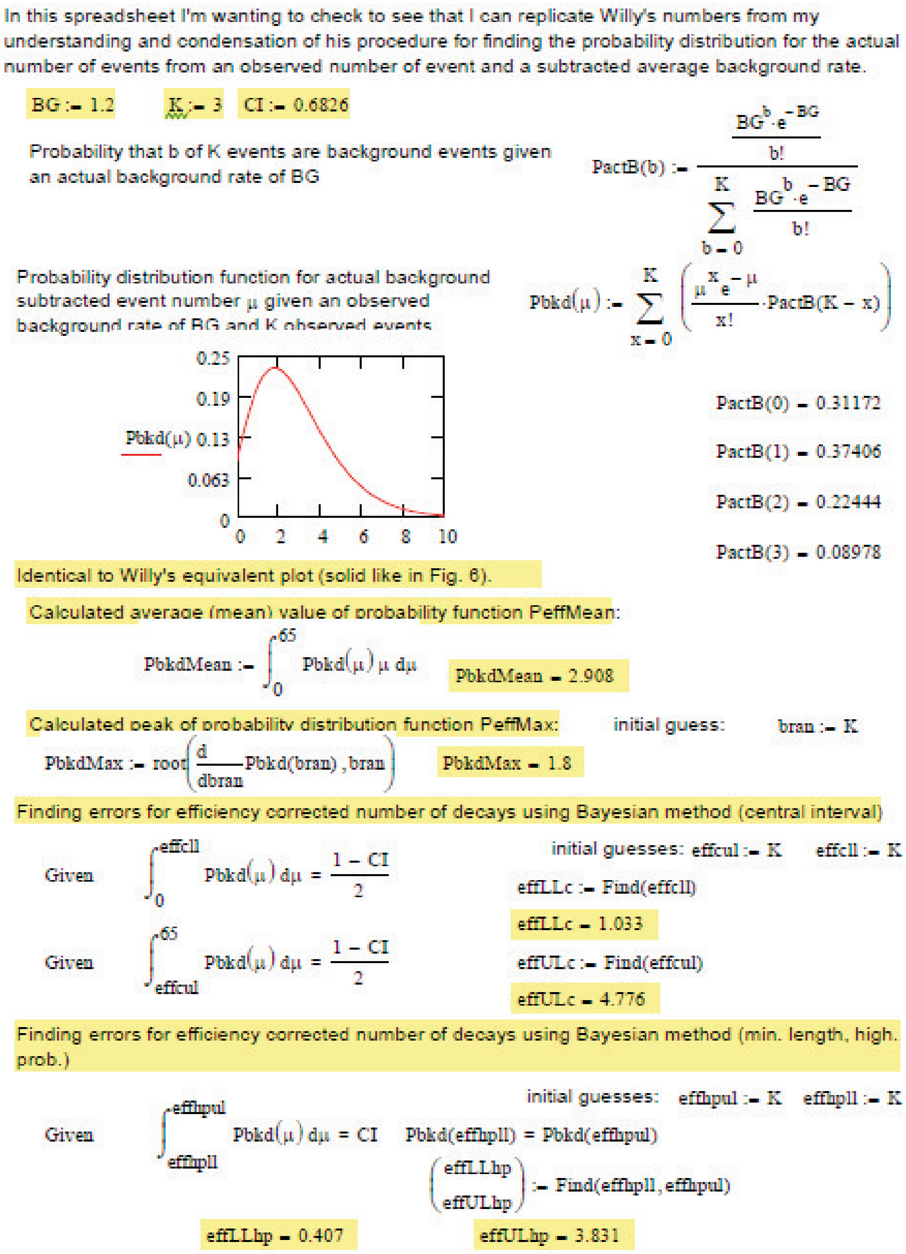

In this spreadsheet I'm wanting to check to see that I can replicate Willy's numbers from my understanding and condensation of his procedure for finding the probability distribution for the actual number of events from an observed number of event and a subtracted average background rate.

$BG := 1.2$ $K := 3$ $CI := 0.6826$

Probability that b of K events are background events given an actual background rate of BG

$$PactB(b) := \frac{\dfrac{BG^{b} \cdot e^{-BG}}{b!}}{\displaystyle\sum_{b=0}^{K} \frac{BG^{b} \cdot e^{-BG}}{b!}}$$

Probability distribution function for actual background subtracted event number μ given an observed background rate of BG and K observed events

$$Pbkd(\mu) := \sum_{x=0}^{K} \left(\frac{\mu^{x} e^{-\mu}}{x!} \cdot PactB(K-x) \right)$$

$PactB(0) = 0.31172$

$PactB(1) = 0.37406$

$PactB(2) = 0.22444$

$PactB(3) = 0.08978$

Identical to Willy's equivalent plot (solid like in Fig. 6).

Calculated average (mean) value of probability function PeffMean:

$$PbkdMean := \int_{0}^{65} Pbkd(\mu)\,\mu\,d\mu \qquad PbkdMean = 2.908$$

Calculated peak of probability distribution function PeffMax: initial guess: $bran := K$

$$PbkdMax := root\left(\frac{d}{dbran}Pbkd(bran), bran\right) \qquad PbkdMax = 1.8$$

Finding errors for efficiency corrected number of decays using Bayesian method (central interval)

initial guesses: $effcul := K$ $effcll := K$

$$\text{Given} \qquad \int_{0}^{effcll} Pbkd(\mu)\,d\mu = \frac{1-CI}{2}$$

$effLLc := Find(effcll)$

$effLLc = 1.033$

$$\text{Given} \qquad \int_{effcul}^{65} Pbkd(\mu)\,d\mu = \frac{1-CI}{2}$$

$effULc := Find(effcul)$

$effULc = 4.776$

Finding errors for efficiency corrected number of decays using Bayesian method (min. length, high. prob.)

initial guesses: $effhpul := K$ $effhpll := K$

$$\text{Given} \qquad \int_{effhpll}^{effhpul} Pbkd(\mu)\,d\mu = CI \qquad Pbkd(effhpll) = Pbkd(effhpul)$$

$$\begin{pmatrix} effLLhp \\ effULhp \end{pmatrix} := Find(effhpll, effhpul)$$

$effLLhp = 0.407$ $effULhp = 3.831$

Figure D.5 Commented MathCAD spreadsheet for calculating Bayesian confidence intervals for the number of events detected with a known background.

with K_x and K_y being the number of observed events and μ_x and μ_y being the number expected from the actual average count rate. We would like to take the above equation, make some substitutions, and then get out a probability distribution as a function of the branching ratio (b). The following definitions of branching ratio are important:

$$b = \frac{\mu_x}{(\mu_x + \mu_y)}$$

$$db = \frac{-\mu_x}{(\mu_x + \mu_y)}\, d\mu_y = -\frac{b^2}{\mu_x}\, d\mu_y$$

These equations can be rearranged to give μ_y and its differential as a function of μ_x and b and their differentials:

$$\mu_y = \frac{\mu_x}{b} - \mu_x = \mu_x\Big(\frac{1}{b} - 1\Big)$$

$$d\mu_y = -\frac{\mu_x}{b^2}\, db$$

Substituting these into the probability distribution function gives:

$$P_{uni}(b, \mu_x|(K_x, K_y))\, db\, d\mu_x = \frac{\mu_x^{K_x} e^{-\mu_x}}{K_x!} \frac{\mu_x^{K_y}\left(\frac{1}{b} - 1\right)^{K_y} e^{-\left(\frac{\mu_x}{b} - \mu_x\right)}}{K_y!} \Big(- \frac{\mu_x}{b^2}\Big)\, db\ d\mu_x$$

$$= -\frac{\mu_x^{K_x+K_y+1}\ e^{-\frac{\mu_x}{b}} \left(\frac{1}{b} - 1\right)^{K_y}}{b^2\, K_x!\, K_y!}\, d\mu_x\, db$$

If you're clever, you can see a normalized Poisson distribution inside there that's itching to get integrated to -1. Here, look in the second bracket of the algebraic rearrangement shown below:

$$P_{uni}(b, \mu_x|(K_x, K_y))\, db\, d\mu_x = \left[- \frac{\left(\frac{1}{b} - 1\right)^{K_y}}{b^2\, K_x!\, K_y!}\right] \left[\mu_x^{1+K_x+K_y}\ e^{-\frac{\mu_x}{b}}\ d\mu_x \right] db$$

To integrate this out, we need to do some more changes including a substitution of $d\mu_x/b = d(\mu_x/b)$.

$$P_{uni}(b, \mu_x|(K_x, K_y))\, db\, d\mu_x = \left[- \frac{\left(\frac{1}{b} - 1\right)^{K_y}}{b^2\, K_x!\, K_y!}\right] \left[b^{2+K_x+K_y}\, (1 + K_x + K_y)! \left[\frac{\left(\frac{\mu_x}{b}\right)^{1+K_x+K_y}\ e^{-\frac{\mu_x}{b}}}{(1 + K_x + K_y)!}\, d\Big(\frac{\mu_x}{b}\Big)\right]\right] db$$

We can see in the equation above that its portion inside the inner right brackets is a normalized poisson distribution which integrates to -1. The portion of the formula outside the inner brackets on the right was added to balance the equality. By integrating μ_x from 0 to infinity, we get the equality as a function of only b, i.e.,

$$P_{uni}(b|(K_x, K_y))\, db = \frac{b^{2+K_x+K_y}\left(\frac{1}{b} - 1\right)^{K_y} \left(1 + K_x + K_y\right)!}{b^2\, K_x!\, K_y!}\, db$$

$$= \frac{b^{K_x+K_y}\left(\frac{1-b}{b}\right)^{K_y}(1+K_x+K_y)!}{K_x!\,K_y!}\,db$$

By doing one final round of simplification, we get the equation below which is the probability distribution for the actual branching ratio as a function of the number of observed events for two Poissonian processes assuming a uniform prior distribution.

$$P_{uni}(b|(K_x,K_y))\,db = \frac{b^{K_x}(1-b)^{K_y}(1+K_x+K_y)!}{K_x!\,K_y!}\,db$$

A similar expression can be derived assuming a $1/\mu$ prior distribution and is shown below:

$$P_{oom}(b|(K_x,K_y))\,db = \frac{b^{K_x-1}(1-b)^{K_y-1}(K_x+K_y-1)!}{(K_x-1)!\,(K_y-1)!}\,db$$

These Bayesian confidence intervals using the uniform and $1/\mu$ prior probability distribution functions for the branching ratio of two observed decay modes can be calculated with a MathCAD such as that shown in Figure D.6 shows the commented MathCAD sheet to accomplish this.

Bayesian credible interval limits in the ratio of two observed decay modes

The above procedure can also be performed exactly the same way, except instead getting the ending probability as a function of $r = \mu_N/\mu_D$ instead of $b = \mu_x/(\mu_x+\mu_y)$.

The goal is to get the probability distribution function of the product of two Poisson-distributed variables as a function of $r = \mu_N/\mu_D$, beginning with the distribution below,

$$P(\mu_n,\mu_d|(K_n,K_d))\,d\mu_d\,d\mu_n = P(\mu_n|K_n)\,P(\mu_d|K_d)\,d\mu_n\,d\mu_d$$

For the case of a uniform prior distribution we see:

$$P_{uni}(\mu_n,\mu_d|(K_n,K_d))\,d\mu_n\,d\mu_d = \frac{\mu_n^{K_n}e^{-\mu_n}}{K_n!}\frac{\mu_d^{K_d}e^{-\mu_d}}{K_d!}\,d\mu_n\,d\mu_d$$

with K_n and K_d being the number of observed events and μ_n and μ_d being the number expected from the actual average count rate. We would like to take the above equation, make some substitutions, and then get out a probability distribution as a function of their ratio (r). The following definitions of the ratio are important:

$$r = \frac{\mu_n}{(\mu_d)}$$

$$dr = \frac{1}{(\mu_d)}\,d\mu_n$$

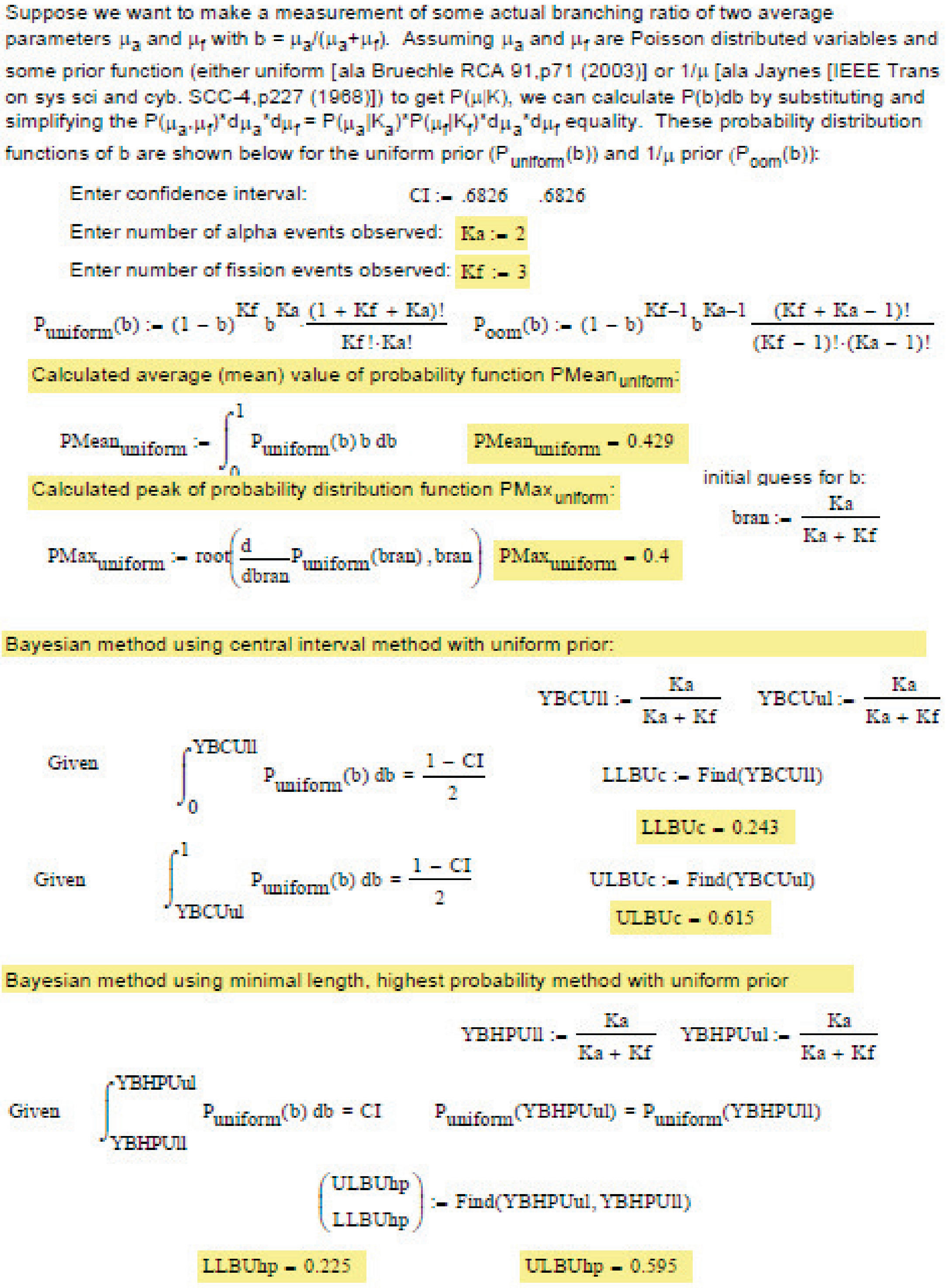

Suppose we want to make a measurement of some actual branching ratio of two average parameters μ_a and μ_f with $b = \mu_a/(\mu_a+\mu_f)$. Assuming μ_a and μ_f are Poisson distributed variables and some prior function (either uniform [ala Bruechle RCA 91,p71 (2003)] or 1/µ [ala Jaynes [IEEE Trans on sys sci and cyb. SCC-4,p227 (1968)]) to get P(µ|K), we can calculate P(b)db by substituting and simplifying the $P(\mu_a,\mu_f)*d\mu_a*d\mu_f = P(\mu_a|K_a)*P(\mu_f|K_f)*d\mu_a*d\mu_f$ equality. These probability distribution functions of b are shown below for the uniform prior ($P_{uniform}(b)$) and 1/µ prior ($P_{oom}(b)$):

Enter confidence interval: $CI := .6826$ $\quad .6826$

Enter number of alpha events observed: $Ka := 2$

Enter number of fission events observed: $Kf := 3$

$$P_{uniform}(b) := (1-b)^{Kf}\, b^{Ka} \cdot \frac{(1+Kf+Ka)!}{Kf!\cdot Ka!} \qquad P_{oom}(b) := (1-b)^{Kf-1}\, b^{Ka-1} \frac{(Kf+Ka-1)!}{(Kf-1)!\cdot(Ka-1)!}$$

Calculated average (mean) value of probability function $PMean_{uniform}$:

$$PMean_{uniform} := \int_0^1 P_{uniform}(b)\, b\, db \qquad PMean_{uniform} = 0.429$$

Calculated peak of probability distribution function $PMax_{uniform}$:

initial guess for b:

$$bran := \frac{Ka}{Ka+Kf}$$

$$PMax_{uniform} := root\left(\frac{d}{dbran} P_{uniform}(bran), bran\right) \qquad PMax_{uniform} = 0.4$$

Bayesian method using central interval method with uniform prior:

$$YBCUll := \frac{Ka}{Ka+Kf} \qquad YBCUul := \frac{Ka}{Ka+Kf}$$

Given $$\int_0^{YBCUll} P_{uniform}(b)\, db = \frac{1-CI}{2}$$

$LLBUc := Find(YBCUll)$

$LLBUc = 0.243$

Given $$\int_{YBCUul}^1 P_{uniform}(b)\, db = \frac{1-CI}{2}$$

$ULBUc := Find(YBCUul)$

$ULBUc = 0.615$

Bayesian method using minimal length, highest probability method with uniform prior

$$YBHPUll := \frac{Ka}{Ka+Kf} \qquad YBHPUul := \frac{Ka}{Ka+Kf}$$

Given $$\int_{YBHPUll}^{YBHPUul} P_{uniform}(b)\, db = CI \qquad P_{uniform}(YBHPUul) = P_{uniform}(YBHPUll)$$

$$\begin{pmatrix} ULBUhp \\ LLBUhp \end{pmatrix} := Find(YBHPUul, YBHPUll)$$

$LLBUhp = 0.225$ $\qquad ULBUhp = 0.595$

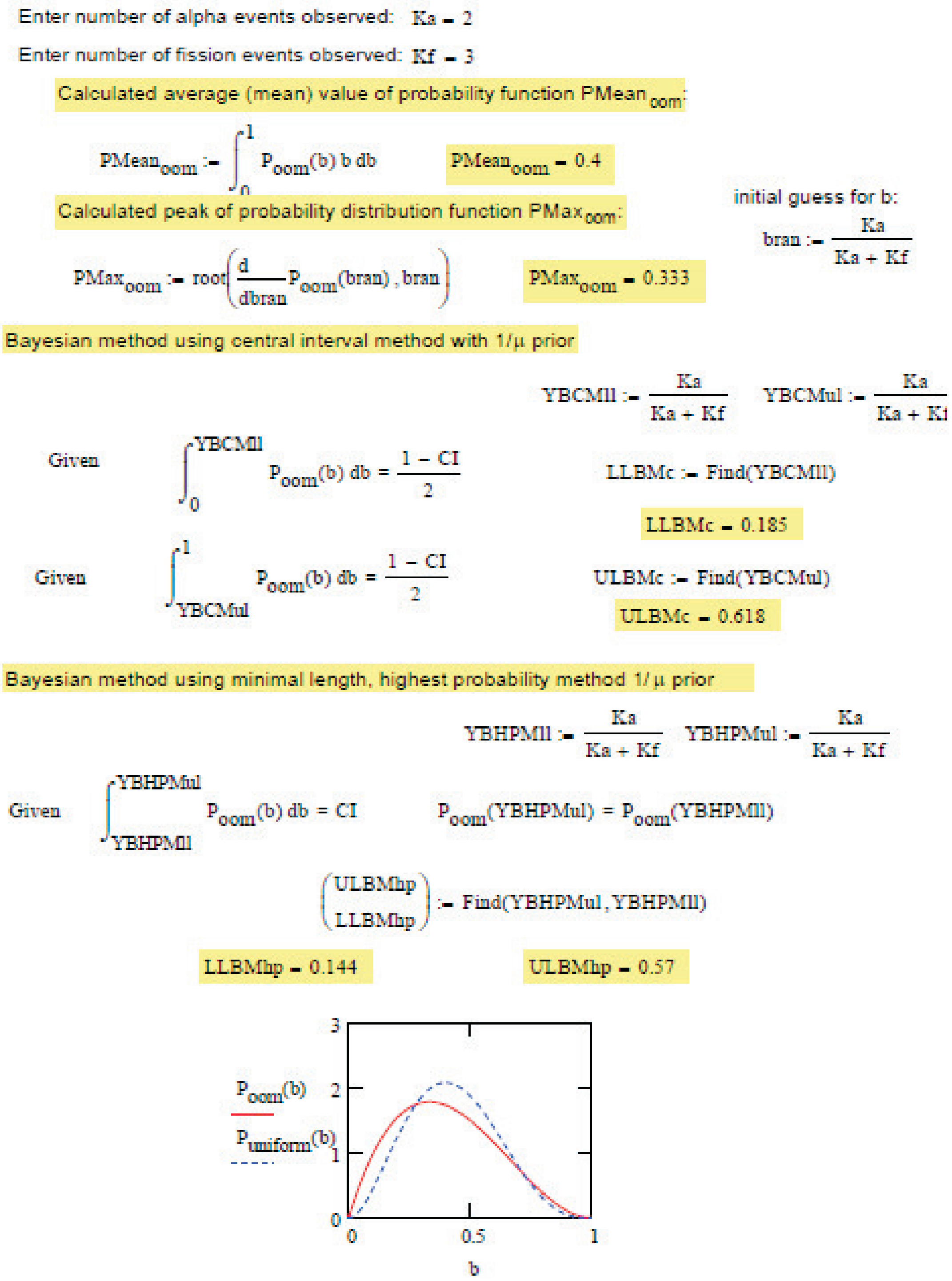

Enter number of alpha events observed: $Ka = 2$

Enter number of fission events observed: $Kf = 3$

Calculated average (mean) value of probability function $PMean_{oom}$:

$$PMean_{oom} := \int_0^1 P_{oom}(b)\, b\, db \qquad PMean_{oom} = 0.4$$

Calculated peak of probability distribution function $PMax_{oom}$:

initial guess for b:

$$bran := \frac{Ka}{Ka + Kf}$$

$$PMax_{oom} := root\left(\frac{d}{dbran} P_{oom}(bran), bran\right) \qquad PMax_{oom} = 0.333$$

Bayesian method using central interval method with 1/µ prior

$$YBCMll := \frac{Ka}{Ka + Kf} \qquad YBCMul := \frac{Ka}{Ka + Kf}$$

Given $\displaystyle\int_0^{YBCMll} P_{oom}(b)\, db = \frac{1 - CI}{2}$

$$LLBMc := Find(YBCMll)$$

$$LLBMc = 0.185$$

Given $\displaystyle\int_{YBCMul}^{1} P_{oom}(b)\, db = \frac{1 - CI}{2}$

$$ULBMc := Find(YBCMul)$$

$$ULBMc = 0.618$$

Bayesian method using minimal length, highest probability method 1/µ prior

$$YBHPMll := \frac{Ka}{Ka + Kf} \qquad YBHPMul := \frac{Ka}{Ka + Kf}$$

Given $\displaystyle\int_{YBHPMll}^{YBHPMul} P_{oom}(b)\, db = CI \qquad P_{oom}(YBHPMul) = P_{oom}(YBHPMll)$

$$\begin{pmatrix} ULBMhp \\ LLBMhp \end{pmatrix} := Find(YBHPMul, YBHPMll)$$

$$LLBMhp = 0.144 \qquad ULBMhp = 0.57$$

Figure D.6 Commented MathCAD spreadsheet for calculating Bayesian confidence intervals for the branching ratio of two observed decay modes.

These equations can be rearranged to give μ_n and its differential as a function of μ_d and r and their differentials:

$$\mu_n = r\,\mu_d$$

$$d\mu_n = \mu_d\,dr$$

Substituting these into the probability distribution function gives:

$$P_{uni}(r, \mu_d|(K_n, K_d))\,dr\,d\mu_d = \frac{(r\mu_d)^{K_n} e^{-r\mu_d}}{K_n!} \frac{\mu_d^{K_d} e^{-\mu_d}}{K_d!} \mu_d\,dr\,d\mu_d$$

$$= \frac{r^{K_n} \mu_d^{K_n+K_d+1} e^{-\mu_d(r+1)}}{K_n! K_d!}\,dr\,d\mu_d$$

If you're clever, you can see a normalized Poisson distribution inside there that's itching to get integrated to -1. Here, look in the second bracket of the algebraic rearrangement shown below:

$$P_{uni}(r, \mu_x|(K_n, K_d))\,dr\,d\mu_x = \left[\frac{r^{K_n}}{K_n! K_d!}\right] \left[\mu_d^{K_n+K_d+1} e^{-\mu_d(r+1)}\,d\mu_d\right] dr$$

To integrate this out, we need to do some more changes including a substitution of $d\mu_d = d(\mu_d(r+1))/r+1$.

$$P_{uni}(r, \mu_x|(K_n, K_d))\,dr\,d\mu_x = \left[\frac{r^{K_n}}{K_n! K_d!}\right] \left[\frac{(K_n+K_d+1)!}{(r+1)^{K_n+K_d+1}(r+1)}\right] \left[\frac{(\mu_d(r+1))^{K_n+K_d+1} e^{-\mu_d(r+1)}}{(K_n+K_d+1)!}\,d(\mu_d(r+1))\right] dr$$

We can see in the equation above that its portion inside the inner right brackets is a normalized poisson distribution which integrates to 1. The portion of the formula outside the inner brackets on the right was added to balance the equality. By integrating μ_d from 0 to infinity, we get the equality as a function of only r, i.e.,

$$P_{uni}(r|(K_n, K_d))\,dr = \frac{(K_n+K_d+1)!}{K_n! K_d!} \frac{r^{K_n}}{(r+1)^{K_n+K_d+2}}\,dr$$

The equation above is the probability distribution for the actual ratio as a function of the number of observed events for two Poissonian processes with assuming a uniform prior distribution. A similar expression can be derived assuming a $1/\mu$ prior distribution and is shown below:

$$P_{oom}(r|(K_n, K_d))\,dr = \frac{(K_n+K_d-1)!}{(K_n-1)!(K_d-1)!} \frac{r^{(K_n-1)}}{(r+1)^{K_n+K_d}}\,dr$$

These Bayesian confidence intervals using the uniform and $1/\mu$ prior probability distribution functions for the ratio of two observed decay modes can be calculated with a MathCAD such as that shown in Figure D.8 shows the commented MathCAD sheet to accomplish this.

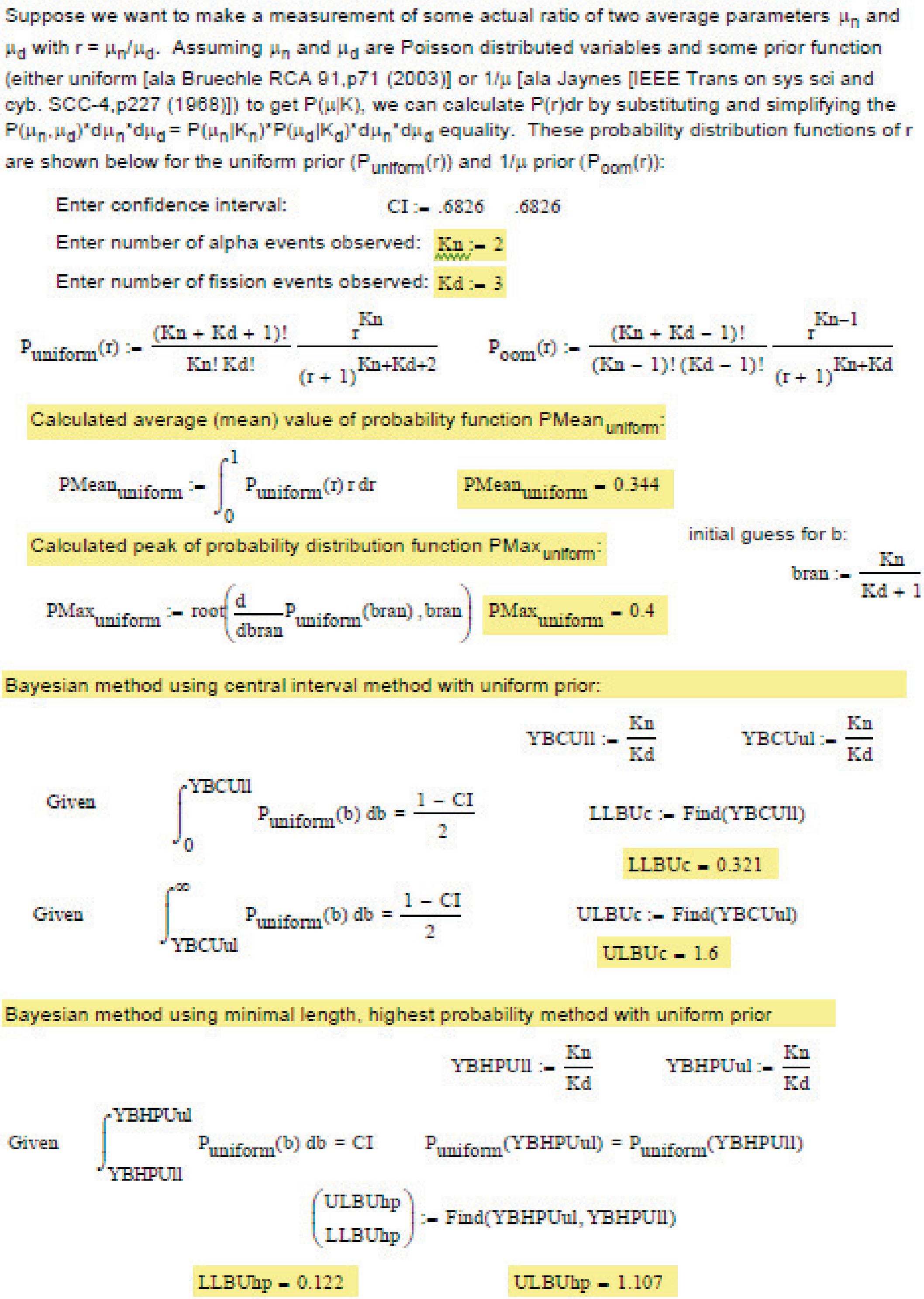

Suppose we want to make a measurement of some actual ratio of two average parameters μ_n and μ_d with $r = \mu_n/\mu_d$. Assuming μ_n and μ_d are Poisson distributed variables and some prior function (either uniform [ala Bruechle RCA 91,p71 (2003)] or 1/μ [ala Jaynes [IEEE Trans on sys sci and cyb. SCC-4,p227 (1968)]) to get P(μ|K), we can calculate P(r)dr by substituting and simplifying the $P(\mu_n,\mu_d)*d\mu_n*d\mu_d = P(\mu_n|K_n)*P(\mu_d|K_d)*d\mu_n*d\mu_d$ equality. These probability distribution functions of r are shown below for the uniform prior ($P_{uniform}(r)$) and 1/μ prior ($P_{oom}(r)$):

Enter confidence interval: $CI := .6826 \quad .6826$

Enter number of alpha events observed: $Kn := 2$

Enter number of fission events observed: $Kd := 3$

$$P_{uniform}(r) := \frac{(Kn + Kd + 1)!}{Kn!\,Kd!}\,\frac{r^{Kn}}{(r+1)^{Kn+Kd+2}} \qquad P_{oom}(r) := \frac{(Kn + Kd - 1)!}{(Kn-1)!\,(Kd-1)!}\,\frac{r^{Kn-1}}{(r+1)^{Kn+Kd}}$$

Calculated average (mean) value of probability function $PMean_{uniform}$:

$$PMean_{uniform} := \int_0^1 P_{uniform}(r)\,r\,dr \qquad PMean_{uniform} = 0.344$$

Calculated peak of probability distribution function $PMax_{uniform}$:

initial guess for b: $bran := \frac{Kn}{Kd + 1}$

$$PMax_{uniform} := root\left(\frac{d}{dbran}P_{uniform}(bran), bran\right) \qquad PMax_{uniform} = 0.4$$

Bayesian method using central interval method with uniform prior:

$$YBCUll := \frac{Kn}{Kd} \qquad YBCUul := \frac{Kn}{Kd}$$

Given $\displaystyle\int_0^{YBCUll} P_{uniform}(b)\,db = \frac{1 - CI}{2}$ $\quad LLBUc := Find(YBCUll)$

$LLBUc = 0.321$

Given $\displaystyle\int_{YBCUul}^{\infty} P_{uniform}(b)\,db = \frac{1 - CI}{2}$ $\quad ULBUc := Find(YBCUul)$

$ULBUc = 1.6$

Bayesian method using minimal length, highest probability method with uniform prior

$$YBHPUll := \frac{Kn}{Kd} \qquad YBHPUul := \frac{Kn}{Kd}$$

Given $\displaystyle\int_{YBHPUll}^{YBHPUul} P_{uniform}(b)\,db = CI$ $\quad P_{uniform}(YBHPUul) = P_{uniform}(YBHPUll)$

$$\begin{pmatrix} ULBUhp \\ LLBUhp \end{pmatrix} := Find(YBHPUul, YBHPUll)$$

$LLBUhp = 0.122$ $\qquad ULBUhp = 1.107$

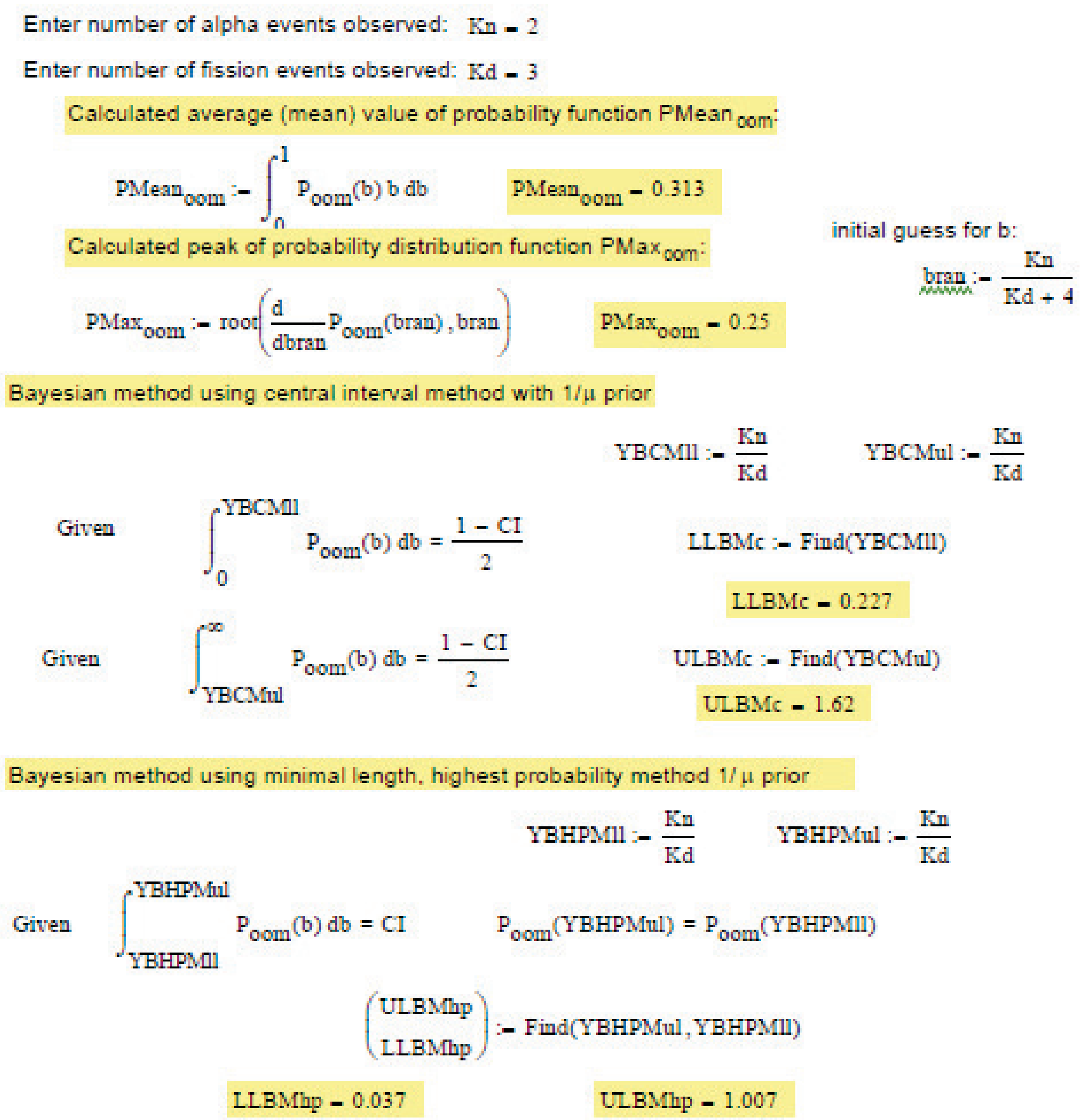

Enter number of alpha events observed: $Kn = 2$

Enter number of fission events observed: $Kd = 3$

Calculated average (mean) value of probability function $PMean_{oom}$:

$$PMean_{oom} := \int_0^1 P_{oom}(b)\, b\, db \qquad PMean_{oom} = 0.313$$

Calculated peak of probability distribution function $PMax_{oom}$:

initial guess for b:

$$bran := \frac{Kn}{Kd + 4}$$

$$PMax_{oom} := \mathrm{root}\left(\frac{d}{dbran} P_{oom}(bran), bran\right) \qquad PMax_{oom} = 0.25$$

Bayesian method using central interval method with 1/µ prior

$$YBCMll := \frac{Kn}{Kd} \qquad YBCMul := \frac{Kn}{Kd}$$

Given $\displaystyle\int_0^{YBCMll} P_{oom}(b)\, db = \frac{1 - CI}{2}$ $\qquad LLBMc := \mathrm{Find}(YBCMll)$

$$LLBMc = 0.227$$

Given $\displaystyle\int_{YBCMul}^{\infty} P_{oom}(b)\, db = \frac{1 - CI}{2}$ $\qquad ULBMc := \mathrm{Find}(YBCMul)$

$$ULBMc = 1.62$$

Bayesian method using minimal length, highest probability method 1/µ prior

$$YBHPMll := \frac{Kn}{Kd} \qquad YBHPMul := \frac{Kn}{Kd}$$

Given $\displaystyle\int_{YBHPMll}^{YBHPMul} P_{oom}(b)\, db = CI$ $\qquad P_{oom}(YBHPMul) = P_{oom}(YBHPMll)$

$$\begin{pmatrix} ULBMhp \\ LLBMhp \end{pmatrix} := \mathrm{Find}(YBHPMul, YBHPMll)$$

$$LLBMhp = 0.037 \qquad ULBMhp = 1.007$$

Figure D.7 Commented MathCAD spreadsheet for calculating Bayesian confidence intervals for the ratio of two observed decay modes.

Bayesian credible interval limits in the lifetime of an observed radioactive decay

Given an actual lifetime of τ, the probability function of observing an average lifetime $\bar{t}$ with a total of n events is derived in the above section titled "Classical confidence intervals of the lifetime of an observed radioactive decay" to be:

$$P(\bar{t}|\tau)d\bar{t} = \frac{n^{n+1}}{(n)!}\frac{\bar{t}^{n-1}}{\tau^n}e^{-n\bar{t}/\tau}$$

Using the Bayesian method, we can get the probability distribution of the actual lifetime τ as a function of the observed average lifetime $\bar{t}$ and the number of observed events n by:

$$P(\tau|\bar{t})d\tau = \frac{P(\bar{t}|\tau)P(\tau)\,d\tau}{\int_0^\infty P(\bar{t}|\tau)P(\tau)\,d\tau}$$

We calculate the normalization integral for a uniform prior ($P(\tau) = 1$) distribution below:

$$\int_0^\infty P(\bar{t}|\tau)P(\tau)\,d\tau = \int_0^\infty P(\bar{t}|\tau)\,d\tau = \int_0^\infty \frac{n^{n+1}}{n!}\frac{\bar{t}^{n-1}}{\tau^n}e^{-n\bar{t}/\tau}\,d\tau = \frac{n^{n+1}}{n!}\bar{t}^{n-1}\int_0^\infty \tau^{-n}e^{-n\bar{t}/\tau}\,d\tau$$

Let $x = n\bar{t}/\tau$, then $\tau = n\bar{t}/x$, $dx = \frac{-n\bar{t}}{\tau^2}\,d\tau$, and $d\tau = \frac{-\tau^2}{n\bar{t}}dx = \frac{-n\bar{t}}{x^2}dx$. Then, we see

$$\int_0^\infty P(\bar{t}|\tau)P(\tau)\,d\tau = \frac{n^{n+1}}{n!}\bar{t}^{n-1}\int_0^\infty \left(\frac{n\bar{t}}{x}\right)^{-n}e^{-x}\left(\frac{-n\bar{t}}{-x^2}\right)dx$$

$$= \frac{n^{n+1}}{n!}\bar{t}^{n-1}\left(\frac{1}{n\bar{t}}\right)^{n-1}\int_0^\infty x^{n-2}e^{-x}\,dx$$

$$= \frac{n^{n+1}}{n!}\bar{t}^{n-1}\left(\frac{1}{n\bar{t}}\right)^{n-1}(n-2)!\int_0^\infty \frac{x^{n-2}e^{-x}}{(n-2)!}\,dx$$

The integral is now a normalized Poisson function and integrates to 1, so we see

$$\int_0^\infty P(\bar{t}|\tau)\,d\tau = \frac{n^{n+1}}{n!}\bar{t}^{n-1}\left(\frac{1}{n\bar{t}}\right)^{n-1}(n-2)!\,dx$$

$$= \frac{n^2}{n!}(n-2)! = \frac{n}{n-1}$$

Thus, the Bayesian method with a uniform prior states that the probability distribution function for the actual lifetime τ as a function of the observed lifetime $\bar{t}$ in n events is:

$$P_{uni}(\tau|\bar{t})d\tau = \frac{n-1}{n}\frac{n^{n+1}}{n!}\frac{\bar{t}^{n-1}}{\tau^n}e^{-n\bar{t}/\tau}\,d\tau$$

$$P_{uni}(\tau|\bar{t})d\tau = \frac{(n\bar{t})^{n-1}}{\tau^n(n-2)!}e^{-n\bar{t}/\tau}\,d\tau$$

A similar derivation shows that the Bayesian method with a prior function equal to $P(\tau) = 1/\tau$ gives the following equations:

$$P_{oot}(\tau|\bar{t})d\tau = \frac{P(\bar{t}|\tau)(1/\tau)\,d\tau}{\int_0^\infty P(\bar{t}|\tau)(1/\tau)\,d\tau} = \frac{\frac{n^{n+1}}{n!}\frac{\bar{t}^{n-1}}{\tau^n}e^{-n\bar{t}/\tau}\left(\frac{1}{\tau}\right)\,d\tau}{1/\bar{t}}$$

$$P_{oot}(\tau|\bar{t})d\tau = \frac{n^{n+1}}{n!}\frac{\bar{t}^n}{\tau^{n+1}}e^{-n\bar{t}/\tau}\,d\tau$$

These Bayesian confidence intervals using the uniform and $1/\mu$ prior probability distribution functions for the lifetime can be calculated with a MathCAD such as that shown in Figure D.8 shows the commented MathCAD sheet to accomplish this.

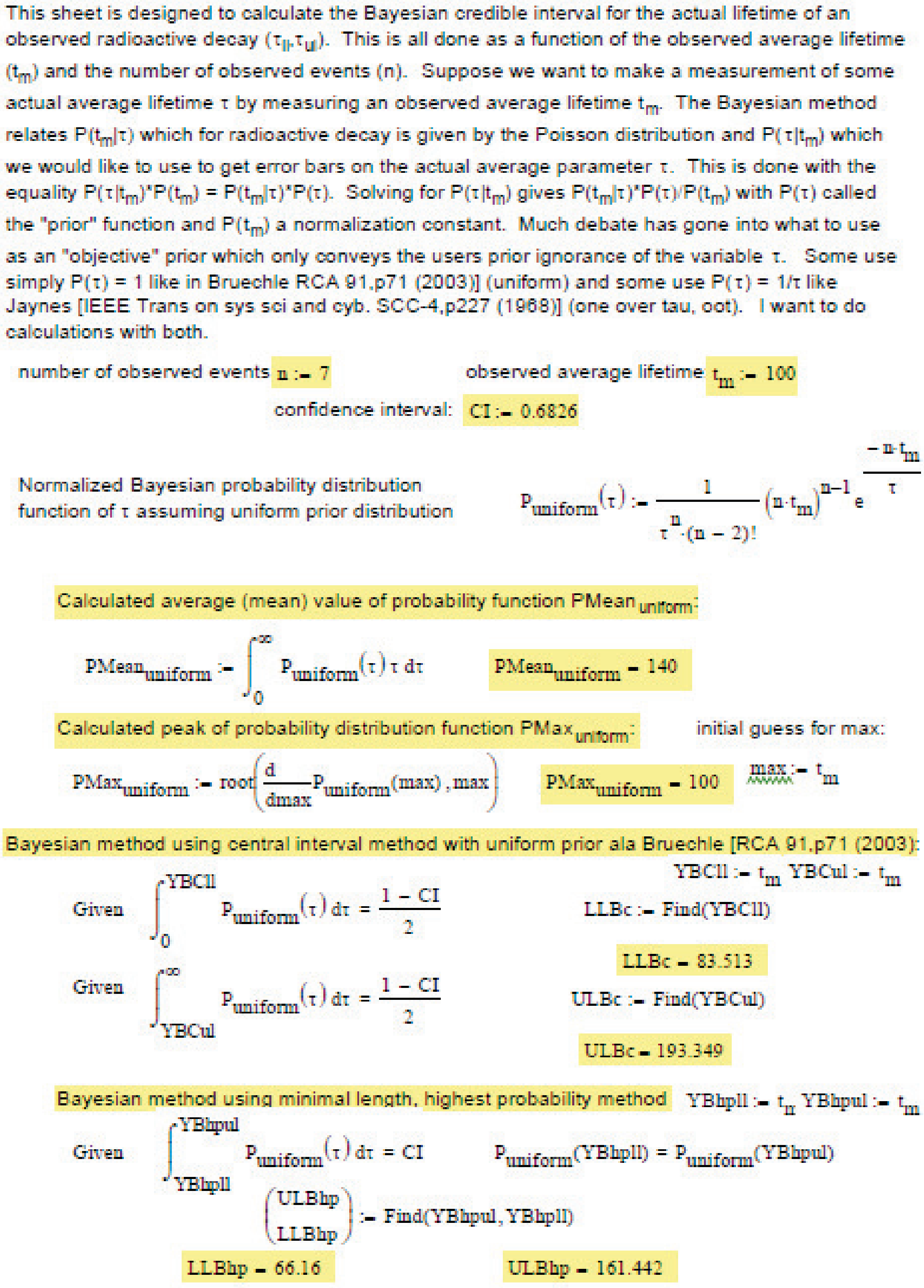

This sheet is designed to calculate the Bayesian credible interval for the actual lifetime of an observed radioactive decay (τ_{ll},τ_{ul}). This is all done as a function of the observed average lifetime (t_m) and the number of observed events (n). Suppose we want to make a measurement of some actual average lifetime τ by measuring an observed average lifetime t_m. The Bayesian method relates P(t_m|τ) which for radioactive decay is given by the Poisson distribution and P(τ|t_m) which we would like to use to get error bars on the actual average parameter τ. This is done with the equality P(τ|t_m)*P(t_m) = P(t_m|τ)*P(τ). Solving for P(τ|t_m) gives P(t_m|τ)*P(τ)/P(t_m) with P(τ) called the "prior" function and P(t_m) a normalization constant. Much debate has gone into what to use as an "objective" prior which only conveys the users prior ignorance of the variable τ. Some use simply P(τ) = 1 like in Bruechle RCA 91,p71 (2003)] (uniform) and some use P(τ) = 1/τ like Jaynes [IEEE Trans on sys sci and cyb. SCC-4,p227 (1968)] (one over tau, oot). I want to do calculations with both.

number of observed events $n := 7$ observed average lifetime $t_m := 100$

confidence interval: $CI := 0.6826$

Normalized Bayesian probability distribution function of τ assuming uniform prior distribution

$$P_{uniform}(\tau) := \frac{1}{\tau^{n}\cdot(n-2)!}\left(n\cdot t_m\right)^{n-1} e^{\frac{-n\cdot t_m}{\tau}}$$

Calculated average (mean) value of probability function PMean$_{uniform}$:

$$PMean_{uniform} := \int_0^{\infty} P_{uniform}(\tau)\,\tau\,d\tau \qquad PMean_{uniform} = 140$$

Calculated peak of probability distribution function PMax$_{uniform}$: initial guess for max:

$$PMax_{uniform} := root\left(\frac{d}{dmax}P_{uniform}(max), max\right) \qquad PMax_{uniform} = 100 \qquad max := t_m$$

Bayesian method using central interval method with uniform prior ala Bruechle [RCA 91,p71 (2003):

$YBCll := t_m$ $YBCul := t_m$

$$\text{Given} \quad \int_0^{YBCll} P_{uniform}(\tau)\,d\tau = \frac{1-CI}{2} \qquad LLBc := Find(YBCll)$$

$$LLBc = 83.513$$

$$\text{Given} \quad \int_{YBCul}^{\infty} P_{uniform}(\tau)\,d\tau = \frac{1-CI}{2} \qquad ULBc := Find(YBCul)$$

$$ULBc = 193.349$$

Bayesian method using minimal length, highest probability method $YBhpll := t_m$ $YBhpul := t_m$

$$\text{Given} \quad \int_{YBhpll}^{YBhpul} P_{uniform}(\tau)\,d\tau = CI \qquad P_{uniform}(YBhpll) = P_{uniform}(YBhpul)$$

$$\begin{pmatrix} ULBhp \\ LLBhp \end{pmatrix} := Find(YBhpul, YBhpll)$$

$$LLBhp = 66.16 \qquad ULBhp = 161.442$$

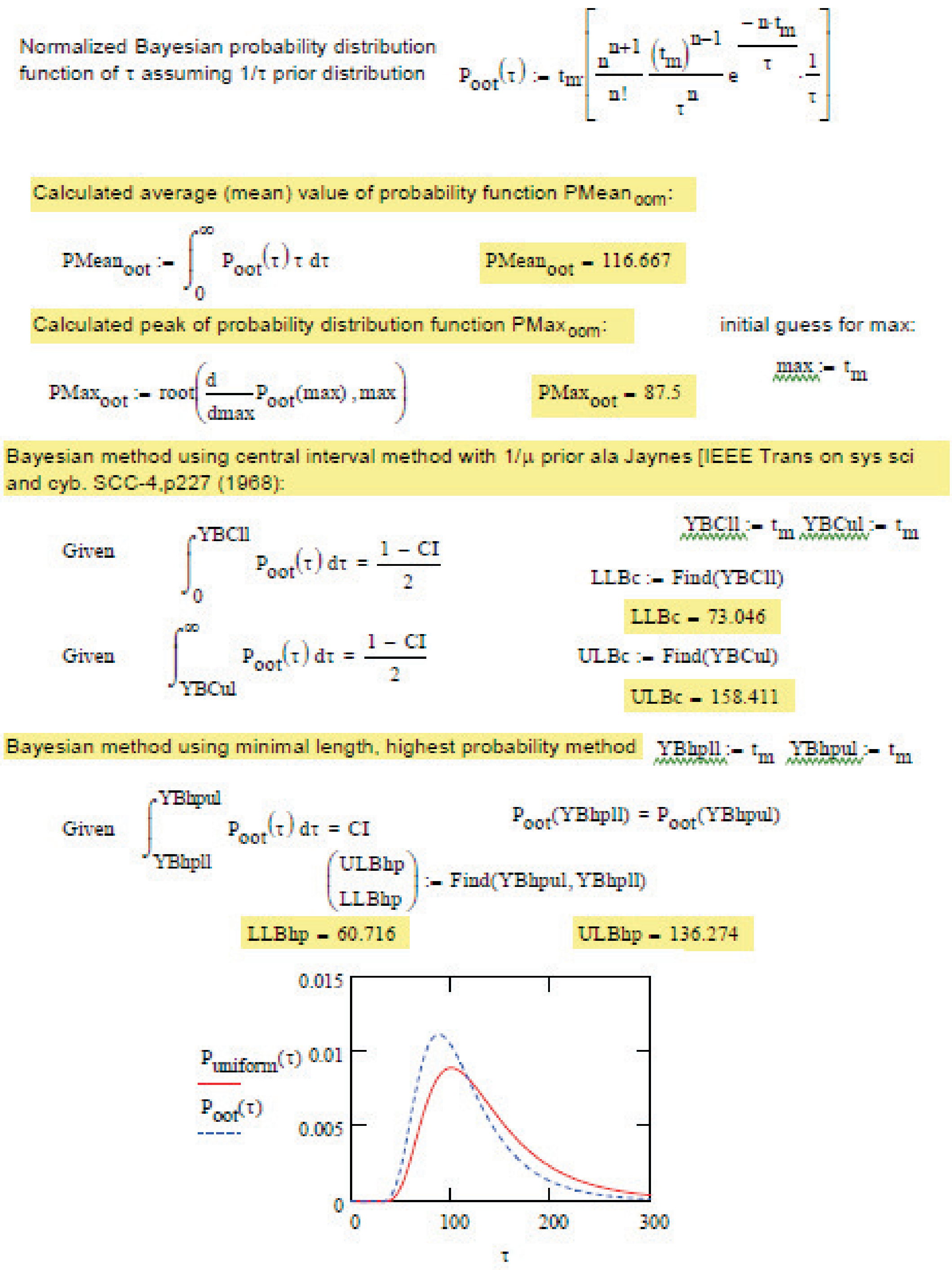

Normalized Bayesian probability distribution function of τ assuming 1/τ prior distribution

$$P_{oot}(\tau) := t_m \left[\frac{n^{n+1}}{n!} \cdot \frac{(t_m)^{n-1}}{\tau^{n}} \cdot e^{\frac{-n \cdot t_m}{\tau}} \cdot \frac{1}{\tau} \right]$$

Calculated average (mean) value of probability function $PMean_{oom}$:

$$PMean_{oot} := \int_{0}^{\infty} P_{oot}(\tau)\,\tau\, d\tau \qquad PMean_{oot} = 116.667$$

Calculated peak of probability distribution function $PMax_{oom}$:

initial guess for max:

$$max := t_m$$

$$PMax_{oot} := root\left(\frac{d}{dmax} P_{oot}(max), max\right) \qquad PMax_{oot} = 87.5$$

Bayesian method using central interval method with 1/μ prior ala Jaynes [IEEE Trans on sys sci and cyb. SCC-4,p227 (1968):

$YBCll := t_m$ $YBCul := t_m$

Given $\int_{0}^{YBCll} P_{oot}(\tau)\, d\tau = \frac{1 - CI}{2}$

$LLBc := Find(YBCll)$

$LLBc = 73.046$

Given $\int_{YBCul}^{\infty} P_{oot}(\tau)\, d\tau = \frac{1 - CI}{2}$

$ULBc := Find(YBCul)$

$ULBc = 158.411$

Bayesian method using minimal length, highest probability method

$YBhpll := t_m$ $YBhpul := t_m$

Given $\int_{YBhpll}^{YBhpul} P_{oot}(\tau)\, d\tau = CI$

$P_{oot}(YBhpll) = P_{oot}(YBhpul)$

$$\begin{pmatrix} ULBhp \\ LLBhp \end{pmatrix} := Find(YBhpul, YBhpll)$$

$LLBhp = 60.716$ $ULBhp = 136.274$

Figure D.8 Commented MathCAD spreadsheet for calculating Bayesian confidence intervals for the lifetime of a radioactively decaying nuclide.

Appendix E

Summary of experimental Q_α data plotted in Figure 6.3.

Table E.1: Summary of experimental data plotted in Figure 6.3.

Z	A	Type of study	Q_α (MeV)	Ref.
118	294	Recoil-corrected E_α[1]	11.81	[Oga07]
116	293	Recoil-corrected E_α[1]	10.69	[Oga07]
	292	Recoil-corrected E_α[1]	10.80	[Oga07]
	291	Recoil-corrected E_α[1]	10.89	[Oga07]
	290	Recoil-corrected E_α[1]	11.00	[Oga07]
114	289	Recoil-corrected E_α[1]	9.96	[Oga07]
	288	Recoil-corrected E_α[1]	10.08	[Oga07]
	287	Recoil-corrected E_α[1]	10.16	[Oga07]
	286	Recoil-corrected E_α[1]	10.33	[Oga07]
	285	Recoil-corrected E_α[1]	10.54	[EGB^{+}10]
112	285	Recoil-corrected E_α[1]	9.28	[Oga07]
	284	Recoil-corrected E_α limit[2]	<9.88	[Oga07, DSY^{+}10]
	283	Recoil-corrected E_α[1]	9.67	[Oga07]
	282	Recoil-corrected E_α limit[2]	<10.79	[Oga07, EGB^{+}10, SGD^{+}09]
	281	Recoil-corrected E_α[1]	10.46	[Oga07]
	277	Recoil-corrected E_α[1]	11.62	[HHA^{+}02]
110	281	Recoil-corrected E_α[1]	8.86	[EGB^{+}10]
	279	Recoil-corrected E_α[1]	9.84	[Oga07]
	277	Recoil-corrected E_α[1]	10.72	[DSY^{+}10]
	273	Recoil-corrected E_α[1]	11.37	[HHA^{+}02]
	271	Recoil-corrected E_α[1]	10.93	[FGD^{+}04]

Continued on next page.

Table E.1, continued.

Z	A	Type of study	Q_α (MeV)	Ref.
	270	Recoil-corrected $E_\alpha{}^1$	11.16	[HHA+01]
	269	Recoil-corrected $E_\alpha{}^1$	11.30	[HNH+95b]
108	277	Recoil-corrected E_α limit^2	<10.75	[DSY+10]
	275	Recoil-corrected $E_\alpha{}^1$	9.44	[Oga07]
	273	Recoil-corrected $E_\alpha{}^1$	9.73	[EGB+10]
	271	Recoil-corrected $E_\alpha{}^1$	9.44	[DBC+06, DBC+08]
	270	Recoil-corrected $E_\alpha{}^1$	9.01	[DBC+06, DBC+08]
	269	Recoil-corrected $E_\alpha{}^1$	9.27	[DBC+06, DBC+08]
	267	Recoil-corrected $E_\alpha{}^1$	10.04	[FGD+04]
	266	Recoil-corrected $E_\alpha{}^1$	10.35	[HHA+01]
	265	Recoil-corrected $E_\alpha{}^1$	10.73	[HNH+95b]
	264	Recoil-corrected $E_\alpha{}^1$	10.59	[Heß10]
	263	Recoil-corrected $E_\alpha{}^1$	11.08	[DacGD+09]
106	271	Recoil-corrected $E_\alpha{}^1$	8.67	[Oga07]
	269	Recoil-corrected $E_\alpha{}^1$	8.69	[EGB+10]
	267	Recoil-corrected $E_\alpha{}^1$	8.32	[DBC+06, DBC+08]
	266	Recoil-corrected E_α limit^2	<9.17	[DBC+06, DBC+08]
	265	Recoil-corrected $E_\alpha{}^1$	8.82	[DBC+06, DBC+08]
	264	Recoil-corrected $E_\alpha{}^1$ limit	<9.54	[GGD+06]
	263	Recoil-corrected $E_\alpha{}^1$	9.43	[GGD+06]
	262	Recoil-corrected E_α limit^2	<9.53	[HHA+01, GGD+06]
	261	Recoil-corrected $E_\alpha{}^1$	9.70	[HNH+95b]
	260	Recoil-corrected $E_\alpha{}^1$	9.90	[HHS+09]
	259	Recoil-corrected $E_\alpha{}^1$	9.84	[HHS+09]
104	267	Recoil-corrected E_α limit^2	<8.07	[Oga07]
	265	Recoil-corrected E_α limit^2	<8.07	[EGB+10]
	263	Recoil-corrected E_α limit^2	<8.07	[DBC+06, DBC+08]
	261	Recoil-corrected $E_\alpha{}^1$	8.42	[DBC+06, DBC+08]
	259	Recoil-corrected $E_\alpha{}^1$	9.05	[FGD+04]
	258	Recoil-corrected $E_\alpha{}^1$	9.19	[GGG+08]
	257	α-electron coincidence study^3	9.084	[QHK+09]
	256	Recoil-corrected $E_\alpha{}^1$	8.93	[HHN+97]
	255	Recoil-corrected $E_\alpha{}^1$	8.56	[DacGD+09]
102	259	Recoil-corrected $E_\alpha{}^1$	7.81	[SDM+73]
	257	Recoil-corrected $E_\alpha{}^1$	8.38	[GSN67]
	256	Recoil-corrected $E_\alpha{}^1$	8.56	[GSN67]

Continued on next page.

Table E.1, continued.

Z	A	Type of study	Q_α (MeV)	Ref.
	255	Recoil-corrected E_α[1]	8.24	[GSN67]
	254	Recoil-corrected E_α[1]	8.23	[GSN67]
	253	α-gamma coincidence study[3]	8.41	[HHA$^+$04]
	252	Recoil-corrected E_α[1]	8.55	[GSN67]
	251	α-gamma coincidence study[3]	8.75	[HHA$^+$04]

[1] Recoil-corrected α-decay values were calculated by multiplying the highest full energy α particle by the mass of the parent nuclide and dividing by the mass of the daughter nuclide. For even-Z/even-N nuclides this value is equal to the actual α-decay Q-value. For even-Z/odd-N nuclides where α decay often populates an excited state of the daughter nuclide, the recoil-corrected E_α value is likely smaller than the actual Q_α.

[2] Upper limits for the recoil-corrected α-decay energies were calculated for nuclides where only spontaneous fission has been observed. A Bayesian upper limit for the α-decay branching ratio was calculated as a function of the number of observed spontaneous fission events. This limit was used along with the observed half-life to calculate an 84% confidence lower limit for the α-decay partial half-life. This was used along with the α-decay systematics outlined by [PS05] to calculate the 84% confidence upper limits for the recoil-correccted α-decay energy.

[3] In the alpha-gamma and alpha-conversion electron coincidence studies, nuclear level schemes of daughter nuclides have been elucidated by observing electron and photon radiation coincident to alpha decay events. The Q_{alpha} reported in the table is calculated using these nuclear level schemes to be the energy difference between the ground state of the parent and the ground state of the daughter.